U.S.NRC
United States Nuclear Regulatory Commission
Protecting People and the Environment

Aging of Post-tensioned Concrete Containment Vessels with Emphasis on Concrete Creep and Creep Rupture

Manuscript Completed: August 2021
Date Published: March 2022

Prepared by:

J. Hogancamp[1]
C. Jones[2]
M. Sircar[3]
R. Gascot[3]
B. Dameron[4]
P. Chang[4]
E. Kjolsing[5]
R. James[6]

[1]Sandia National Laboratories
1515 Eubank Blvd SE
Albuquerque, NM 87123

[2]Kansas State University
Manhattan, KS 66506

[3]US Nuclear Regulatory Commission
Washington, DC 20555-0001

[4]Moffatt & Nichol
4225 E. Conant Street
Long Beach CA 90808

[5]Karagozian & Case, Inc.
700 N Brand Blvd., Suite 700
Glendale, CA 91203

[6]Structural Solutions Consulting, LLC

Research Information Letter
Office of Nuclear Regulatory Research

Disclaimer

Legally binding regulatory requirements are stated only in laws, NRC regulations, licenses, including technical specifications, or orders; not in Research Information Letters (RILs). A RIL is not regulatory guidance, although NRC's regulatory offices may consider the information in a RIL to determine whether any regulatory actions are warranted.

ABSTRACT

This document reviews aging and degradation mechanisms in post-tensioned reinforced concrete containment vessels (PCCVs) with emphasis on concrete creep effects. Background context is provided from regulatory and technical perspectives. Aging and degradation mechanisms in post-tensioned reinforced concrete structures, including PCCVs as well as others, are discussed for their significance. Material degradation modes with emphasis on concrete creep are described and analyzed for their impact on the integrity of PCCVs. Case studies are presented describing concrete creep effects in nuclear and non-nuclear post-tensioned concrete structures. A thorough literature review of concrete creep rupture is presented that indicates that concrete subjected to stresses either in compression or tension above 70% of ultimate uniaxial capacity (in compression or tension, respectively) may be susceptible to creep rupture.

Simulations and analyses of a 1:3-scale PCCV mockup constructed and tested by Électricité de France (EDF) were conducted as part of this study. The EDF project titled VeRCoRs consisted of physical examination and modeling, including pre-test analyses of time-varying strains in the mockup and comparing the model simulation results to experimental data. The entire mockup was modeled including concrete geometry, rebar geometry, post-tensioning (PT) tendons geometry, concrete creep and drying shrinkage, rebar and tendon elastic response, and internal pressurization tests. Simulation results conducted in ABAQUS revealed that simulation of concrete creep and drying shrinkage were required for agreement with the experimental data. Concrete creep was analyzed using the Bažant B3 model improved by updating with creep test data and implemented into ABAQUS utilizing a Prony series. Concrete drying shrinkage was implemented into ABAQUS using a Fick's 2nd Law approach to simulate moisture diffusion. Both models showed excellent agreement with separate effects' experimental data and overall PCCV behavior. A smaller simulation with higher discretization representative of the mockup was conducted to study the radial tensile stresses and strains created by hoop-tendon PT. The smaller simulation with higher discretization clearly indicates development of radial tensile stresses and radial creep strains in the wall of the PCCV.

Current and experimental nondestructive evaluation and structural monitoring techniques that can be used in PCCVs are presented and described. Of note are the digital twin techniques used in the VeRCoRs mockup. Current pertinent research at the universities is also presented. This research involves post-tensioned wall experiments, both for straight slabs and for curved walls, as well as concrete creep prediction experiments utilizing time-temperature superposition principles. For the conditions of one set of experiments, wall delamination cracks initiated at circumferential compressive wall stresses between $0.13f'_c$ and $0.23f'_c$, which is significantly less than the allowable $0.35f'_c$ limit at initial prestress (before losses) provided in the American Society of Mechanical Engineers Boiler & Pressure Vessel Code, Section III, Division 2, Part CC-3431.

FOREWORD

This report documents a research project sponsored by the U.S. Nuclear Regulatory Commission to study degradation modes of post-tensioned concrete containment vessels with emphasis on concrete creep and creep fracture. Sandia National Laboratories conducted the study with support from its subcontractors Structural Integrity Associates, Structural Solutions Consulting, and Moffatt & Nichol.

The goal of this study was to address a knowledge gap identified in the Expanded Material Degradation Assessment (EMDA) Report, NUREG/CR-7153 Vol. 4, "Aging of Concrete and Civil Structures," published in October 2014. The EMDA report identifies low knowledge but high significance issues in concrete and concrete degradation related to nuclear power plants (NPPs) long term operation. Concrete creep and potential creep fracture are issues that have been identified for prestressed concrete containment vessels (PCCVs) with sustained, multi-axial loading. NPPs were originally licensed for 40 years of operation. Since then, most plants have undergone a license renewal process to extend the plant operation to 60 years and presently the NPPs have started license renewal for operation up to 80 years.

This project evaluated concrete aging and degradation effects on PCCVs by taking advantage of an international activity (VeRCoRs) being conducted under the auspices of the Nuclear Energy Agency. VERCORS is a multi-year (*2015-2025*) experimental study aimed at understanding concrete aging effects including creep and shrinkage using a 1/3-scale model of a PCCV. Extensive related laboratory testing, instrumentation, and non-destructive examination (NDE) are also parts of this international research.

To address the EMDA knowledge gap, the study used literature reviews, modeling and simulations, and expert analyses to:

- Describe concrete creep and creep rupture phenomenology

- Review PCCV material and systematic degradation mechanisms

- Describe the implementation of complex concrete material properties including those related to creep and shrinkage into finite element simulations and subsequent comparisons to experimental data

- Analyze PCCVs for susceptibility to concrete creep effects via calculations and simulations

- Describe state-of-the-art nondestructive evaluation and monitoring techniques that could be used in PCCVs

- Describe other pertinent and recent research into concrete creep and post-tensioned concrete structures

TABLE OF CONTENTS

LIST OF FIGURES

LIST OF TABLES

EXECUTIVE SUMMARY

This document reviews aging and degradation mechanisms in post-tensioned reinforced concrete containment vessels (PCCVs) with emphasis on concrete creep effects. Nuclear power plants (NPPs) were originally licensed for 40 years of operation. The majority of the plants have undergone a license renewal process to extend the plant operation to 60 years, and many are applying for a subsequent license renewal (SLR) to extend operation to 80 years. The Expanded Material Degradation Assessment (EMDA) Report, NUREG/CR-7153 Vol. 4, "Aging of Concrete and Civil Structures," published in October 2014, identifies low-knowledge but high significance concrete and concrete degradation issues related to operation up to 80 years. Creep and potential creep fracture are identified issues that are applicable for PCCVs owing to the sustained multi-axial loading from the post-tensioning (PT) system. This is more relevant for containment structures without reinforcement in the radial direction (a significant number in the U.S. fleet) and/or when pre-stressing systems require adjustment such as modifications for steam generator replacement. This research reviews results and progress of activities being done by universities, industry (primarily the Electric Power Research Institute (EPRI)), and the Department of Energy (DOE) as well as related research being done abroad with the goal of comprehensively characterizing the state of the art for creep and crack/fracture testing and modeling in concrete as relevant for PCCVs. Creep and creep-fracture can interact with other degradation mechanisms (e.g., corrosion, alkali-silica reaction, and freeze-thaw), but those interactions are not part of this research.

Section 2 is a review and analysis of PCCV degradation mechanisms with weighted emphasis on concrete creep and creep fracture. A summary on concrete, rebar, tendon, and PCCV systemic degradation mechanisms is presented in Section 2.2, which also provides references for more detailed information. A detailed analysis of concrete creep, concrete creep effects in post-tensioned structures, and concrete rupture is discussed in Section 2.3. A growing database of creep in post-tensioned concrete bridges shows that many bridges experience more creep in late service life (25+ years of operation) than was predicted at the time of design by the designers. Some structures fail from excessive deflections that result in unplanned stress distributions, excessive strains, loss of post-tensioning stress, and excessive cracking.

Concrete creep and concrete creep rupture are discussed in detail in Section 2.3.4 . Existing research indicates that concrete follows standard creep behavior: primary, secondary, and tertiary creep phases followed by rupture (depending on applied load). Design practices intend to limit the stresses in concrete, and these limits are all below what is required for concrete rupture. Tertiary creep and creep rupture will not occur if the concrete stress remains below a specific threshold. Concrete creep rupture is more probable at 70%, and significantly more probable at stresses above 75%, of ultimate uniaxial capacity in either compression or tension.

In addition to the EMDA report, referenced above, the Organization of Economic Cooperation and Development / Committee on the Safety of Nuclear Installations (OECD/CSNI) has identified aging effects for PCCVs in a CSNI Activity Proposal Sheet (CAPS). Creep, shrinkage, drying, and moisture transport are identified as significant aging topics for study. The CAPS focuses on the VeRCoRs (In French: Vérification réaliste du confinement des réacteurs, In English: Realistic verification of the reactor containment) benchmark activities as an opportunity to study the life cycle of a realistic containment structure within a compressed timeframe. VeRCoRs is an Électricité de France (EDF) funded and executed multiyear, comprehensive study of a 1/3-scale PCCV that focuses on aging effects and computational modeling. This mockup is designed such that 1 year of aging in the mockup is equivalent to 9 years of aging in

a full-scale PCCV. The 1:9-time scale is a result of the rate at which drying occurs. Drying in concrete walls is directly proportional to the wall thickness squared; hence, reducing the size of the containment by a factor of 3 increases the rate of drying by a factor of $3^2=9$. The increased drying rate increases cracking and creep in the containment. Until 2020, VeRCoRs was funded by EDF, and for the next 4 years it has been included as a part of the ACES project which is funded by Euratom/Horizon2020. The ACES project has been established with the goal towards improved Assessment of safety performance for long-term operation of nuclear Civil Engineering Structures.

Section 3 describes simulations and analyses of the VeRCoRs 1/3-scale mockup performed by Sandia National Laboratories (SNL) and Moffatt & Nichol, and a separate limited scope study on delayed creep effects on PCCVs by Structural Integrity Associates (SIA) and Structural Solutions Consulting (SSC). Section 3.1 has a detailed description of the mockup. SNL's analysis of the mockup is presented in Section 3.2. Section 3.2.1 includes geometry, mesh, and boundary condition information. Effects from initial PT stressing were considered with separate simulations; the details of which are in Section 3.2.2. Material properties including concrete creep and concrete drying shrinkage implementation are described in Section 3.2.3. Significant detail is provided to describe the concrete creep and concrete drying shrinkage models, both of which are required to achieve better agreement of the VeRCoRs simulation results with experimental data. Section 3.2.4 has the simulation timeline and Section 3.2.5 compares simulation results to experimental VeRCoRs data. An analysis of the VeRCoRs mockup by Moffatt & Nichol is presented in Section 3.3 which found that tensile radial strains develop in the containment wall but were below those required for fracturing of the concrete. Moffat & Nichol recommended an analysis with finer discretization. To assess the effect of a refined discretization, a representative thin-slice geometry from the PCCV is described in Section 3.4 for investigating the radial tensile stresses and strains developed from PT hoop tendons in the PCCV. Section 3.5 presents creep effects in PCCVs performed by SIA and SSC. SIA has a proprietary concrete model called ANACAP that includes creep effects, nonlinear compressive stress-strain behavior of concrete, modeling of concrete cracking and shear degradation due to cracking, and interaction between concrete and reinforcement. Section 3.6 presents the simulation and analyses conclusions. A conclusion of the analyses is that radial tensile strains and stresses can develop in PCCVs but not necessarily delamination. Additional research including improved material model and secondary creep effects can better determine the conditions in which the radial strains could lead to initiation of delamination cracking.

Section 4 describes and reviews non-destructive evaluation (NDE) technologies including those used and studied in the VeRCoRs project. The US NPP industry lacks the experience of using sensors and instruments to monitor structural responses and aging effects. The use of sensors and instruments to monitor the structural performance, and any degradation thereof, is common in French NPPs. Monitoring by instrumentations and sensors is common in bridge industry in US and other countries. This monitoring data is expected to provide valuable insight for the evaluation of aging structures and the US nuclear power industry has started investigating the use of various types of sensors. EPRI has installed sensors in VeRCoRs mockup. As a part of the VeRCoRs project, promising NDE and digital twin technologies are evaluated in Section 4.

Section 4.1 briefly describes current PCCV nondestructive evaluation (NDE) and monitoring techniques, though the reader is pointed to other references for more information. Section 4.2 describes proposed and experimental NDE and monitoring techniques from EPRI and from the VeRCoRs project.

Section 5 describes select current research into concrete creep and into post-tensioned concrete structures. Section 5.1 describes post-tensioned curved reinforced concrete wall experiments performed at the University of Texas at Austin. For the conditions of one set of experiments, wall delamination cracks initiated at circumferential compressive wall stresses between $0.13f'_c$ and $0.23f'_c$, which is significantly less than the allowable $0.35f'_c$ limit at initial prestress (before losses) provided in the American Society of Mechanical Engineers Boiler & Pressure Vessel Code, Section III, Division 2, Part CC-3431.

Section 5.2 describes two types of concrete creep experiments performed at Texas A&M University. The first—post-tensioned concrete slab experiments—indicate that wall thickness is extremely important in determining whether concrete creep or concrete drying shrinkage will be the prominent volume change phenomenon. The second—concrete creep material experiments—indicate time-temperature superposition principles apply to concrete; these concrete creep experiments indicate that creep can be predicted for significantly longer time frames by extrapolating the response of similar specimens at different temperatures.

The overall conclusions of the report are as follows:

- The U.S. NPP fleet is aging and is subject to material and systemic degradation.

- Concrete creep follows general material creep trends: primary, secondary, and tertiary creep stages potentially followed by creep rupture under specific conditions.

- Concrete tertiary creep and creep rupture are possible if the concrete is subject to a stress above a specific threshold. Concrete creep rupture is more probable at 70%, and significantly more probably at stresses above 75%, of ultimate uniaxial capacity in either compression or tension.

- Concrete creep and concrete drying shrinkage models were required for better agreement of the VeRCoRs simulation results with experimental data. The models implemented in this report were successful in matching experimental data.

- Radial tensile stresses and strains develop due to PT in the hoop tendons. A conclusion of the analyses is that radial tensile strains and stresses develop in PCCVs but not necessarily delamination. Additional research including improved material model and secondary creep effects can better determine the conditions in which the radial strains could lead to initiation of delamination cracking.

- There are several NDEs, monitoring methods, and digital twin technology that can be applied to current and future PCCVs.

ABBREVIATIONS AND ACRONYMS

AAR	Alkali-aggregate reaction
AASHTO	American Association of State Highway and Transportation Officials
ACES	Assessment of safety performance for long-term operation of nuclear Civil Engineering Structures
ACI	American Concrete Institute
AEA	Air-entraining admixture
ASME	American Society of Mechanical Engineers
BPVC	Boiler & Pressure Vessel Code
CAPS	CSNI Activity Proposal Sheet
CEB-FIP	International Federation for Structural Concrete (Fédération Internationale du Béton)
CR3	Crystal River 3
CSNI	Committee on the Safety of Nuclear Installations
CV	Containment vessel
DAQ	Data acquisition unit
DOE	Department of Energy
EDF	Électricité de FranceE
EMDA	Expanded Material Degradation Assessment
ENDE	Non-Destructive Evaluation of Containment Nuclear Plant Structures
EPRI	Electric Power Research Institute
ILRT	Integrated leak rate test
KB	Koror-Babeldaob
LRFD	Load and resistance factor design
LVDT	Linear variable differential transformer
NDE	non-destructive examination
NPP	Nuclear power plant
NRC	U.S. Nuclear Regulatory Commission
NTP	Normal temperature and pressure: temperature 20°C (68°F) and pressure 1 atm
OECD	Organization of Economic Co-operation and Development
PCCV	Post-tensioned or prestressed concrete containment vessel
PT	Post-tensioning
PWR	Pressurized water reactor

REBAR   Mild steel reinforcement
RES   NRC Office of Nuclear Regulatory Research
RH   Relative humidity
RG   Regulatory Guide

SIA   Structural Integrity Associates
SIT   structural integrity test
SLR   Subsequent license renewal
SNL   Sandia National Laboratories
SSC   Structral Solutions Consulting

TSs   Technical Specifications

VeRCoRs   Vérification Réaliste du Confinement des Réacteurs

1 HISTORICAL AND REGULATORY CONTEXT

1.1 Regulatory Context

Nuclear power plants (NPPs) were originally licensed for 40 years of operation. Since then, the majority of the plants have undergone a license renewal process to extend the plant operation to 60 years and most other remaining NPPs are planning to do the same. Currently, subsequent license renewal (SLR) from 60 to 80 years have started.

The Expanded Material Degradation Assessment (EMDA) Report, NUREG/CR-7153 Vol. 4, "Aging of Concrete and Civil Structures," published in October 2014, identifies low-knowledge but high significance for concrete and concrete degradation issues related to SLR (US Nuclear Regulatory Commission, 2014). Creep and potential creep fracture are issues cited in the EMDA that are applicable for Prestressed Concrete Containment Vessels (PCCVs) owing to the sustained multi-axial loading. This is most relevant for containment structures without reinforcement in the radial direction (of which there is a significant number in the US fleet) and/or when pre-stressing systems require adjustment such as modifications for steam generator replacement (US Nuclear Regulatory Commission, 2010), repair, or loss of pre-stress. This research will perform a literature search for the results and progress of activities being done by the industry, namely the Electric Power Research Institute (EPRI), and the Department of Energy (DOE) as well as related research being done abroad with the goal of comprehensively characterizing the state of the art for creep and crack/fracture testing and modeling in concrete. It is also important to note that creep and creep-fracture may interact with other degradation mechanisms (e.g., corrosion, alkali-silica reaction, freeze-thaw) and study of creep and creep-fracture may necessarily involve the study of other related mechanisms or vice-versa.

In addition to the EMDA report, referenced above, the Organization of Economic Cooperation and Development / Committee on the Safety of Nuclear Installations (OECD/CSNI) has identified aging effects for concrete containment structures in a CSNI Activity Proposal Sheet (CAPS). Creep, shrinkage, drying, and moisture transport are specifically identified as some of the several significant aging topics for study. This CAPS specifically focuses on the VeRCoRs (In French: Vérification réaliste du confinement des réacteurs, In English: Realistic verification of the reactor containment) benchmark activities as an opportunity to study the long term aging (drying and creep) of a realistic containment structure within a compressed timeframe, drying effects are about 9 times faster on the mock up because of scale effects. VeRCoRs is an Électricité de France (EDF) funded and executed multiyear, comprehensive study of a 1/3 scale PCCV that focuses on gaining insight into aging effects and computational modeling. Additionally, the proposed VeRCoRs activity includes many varied research activities with varying applicability to U.S. Nuclear Regulatory Commission's (NRC's) mission and work scope. Participation in the VeRCoRs benchmark activity provided information to address research questions aimed at improved understanding and characterization of creep and shrinkage in PCCVs of regulatory interest.

The research under this agreement addresses technical issues related to ageing, shrinkage, creep, and their effects on PCCVs in the light of 80-year operating life. The scope of the research also includes independent confirmatory assessments of results by industry and other countries to provide additional insights to inform review guidance. It is expected that this study will contribute to maintaining and strengthening competence and improving practices for assessing aging effects for PCCVs. This research also gathers information on various

nondestructive methods and sensors that are included in VeRCoRs activity. EDF considers VeRCoRs as digital twins for structural evaluation and maintaining safety.

There is limited technical basis regarding aging management of pre-stressing systems. Regulatory Guide (RG) 1.90, *In-service Inspection of Pre-stressed Concrete Containment Structures with Grouted Tendons* was recently updated based on literature search (2012), not on analytical or experimental results (US Nuclear Regulatory Commission, 2012). Similarly, RG 1.35.1, *Determining Pre-stressing Forces for Inspection of Pre-stressed Concrete Containments* was reviewed in 2013 (US Nuclear Regulatory Commission, 2013). The current RG relies on experimental data from 1960s/70s. Knowledge gained from this project can support the update to RG 1.35.1.

1.2   Technical Context

Containment integrity and containment degradation research sponsored by the NRC at Sandia National Laboratories (SNL) and other DOE laboratories over the last three decades, which included various international and multi-organizational collaborative research programs, provided a good understanding of the performance of containments such as those used in U.S. NPPs under severe (beyond design-basis) accident conditions (US Nuclear Regulatory Commission, 2006) . Evaluating the performance of containment behavior in the extended timeframe is a current area of interest.

There is need for review and improvement in the technical basis for evaluating creep, creep-fracture, and other aging related concrete phenomena. Since the issuance of the EMDA report, joint research roadmaps have been created to coordinate activities between DOE, NRC, and industry. The most up-to-date roadmap for concrete creep and creep-fracture research lists several research gaps for the 2017-2021 timeframe. In the research roadmap the EDF funded and executed VeRCoRs benchmark is identified as the primary large-scale engineering validation effort. Strategic participation in this project can bring valuable knowledge for NRC's work and enhance the understanding related to concrete in the context of long-term operation.

In addition, the VeRCoRs benchmark endeavors to investigate the effect of temperature on the accident response of the containment. While computational models have been created to explore these effects in OECD/CSNI International Standard Problem #48 on containment Capacity and under USNRC-AERB Nuclear Safety Co-Operation Program, Standard Problem Exercise – 3 (www.sandia.gov/spe3/), there has been no experimental validation of these models.

Furthermore, the US NPP industry lacks the experience of using sensors and instruments to monitor structural responses and ageing effects. The use of sensors and instruments to monitor the structural performance, and any degradation thereof, is common in French NPPs. Monitoring by instrumentations and sensors is common in bridge industry in U.S. and other countries. This monitoring data is expected to provide valuable insight for the evaluation of aging structures and the U.S. industry has started investigating the use of various types of sensors. EPRI have installed sensors in the VeRCoRs mockup. In addition, promising NDE technologies will be evaluated as a part of the VeRCoRs project.

In addition to ageing, the effects of possible large-scale repair, modification activities for steam generator replacement, detensioning and retensioning, and replacing pre-stressing tendon systems over 80 years of operating life should be investigated.

1.3   NPP Operation Notable Issues

This section lists NPP containment buildings that have reported issues with the post-tensioning (PT) systems and describes the issues. A complete list of operational plants with PCCVs is listed in Appendix B. A more detailed list of reactors and concrete component degradation occurrences can be found in Appendix C.

1.3.1   Calvert Cliffs

Each of the containments at the Calvert Cliffs NPP has a total of 876 tendons: 204 vertical, 468 hoop, and 204 dome. In 1997, during a 20-year surveillance test, broken wires were discovered in Unit 1. The licensee also found a low liftoff value compared to the prestressing force for one of the three randomly selected vertical tendons. The low liftoff value was attributed to uneven shim stack heights on the two opposing sides of the anchor- head. In accordance with the requirement in the plant's Technical Specifications (TSs), the licensee tested two additional vertical tendons adjacent to this tendon. During liftoff testing of one of these tendons, a noise was heard—indicating tendon wires might have ruptured. A visual examination of the tendon showed three broken wires 5-7 inches below the bottom of the button-heads. Further examination of the wires at the top of other vertical tendons revealed additional wire breakage. The licensee expanded the liftoff testing and visual examination to 100 percent of the vertical tendons—revealing similar degradation of additional vertical tendons. As part of its corrective action, the licensee replaced 63 of the 202 vertical tendons in Unit 1 and 64 of the 204 vertical tendons in Unit 2. (US Nuclear Regulatory Commission, 1999).

During a periodic tendon surveillance in 2008, five hoop tendons were found with a lift-off force below the lower limit expected value in Unit 1. All tendons were re-tensioned to acceptable values. No signs of abnormal degradation of the end anchorage or adjacent concrete surface of the containment had been found in any of these areas. No water was found, nor broken/missing wires that have not been previously noted. Despite lift-off force levels being lower than expected, all have been above the design basis accident load for each tendon. Therefore, the containment remained operable. (Baltimore Gas and Electric Company, 1997)

1.3.2   LaSalle

Each of the containment buildings at LaSalle NPP has a total of 308 tendons: 188 hoop and 120 verticals. In 2003, seven tendons had failed, six were degraded with broken wires, and eight had internal corrosion. The observed damage was due to water-induced corrosion caused by failure of the water intrusion barrier gaskets and aided by a loss of the corrosion protective grease. Over the course of the containments' (Unit 1 and Unit 2) life, vertical tendon liftoff forces have been found to be decreasing over time; however, the forces are still above design values. (Exelon Generation, 2016)

1.3.3   Oconee

In summer 1995, the licensee of the Oconee Nuclear Station, Duke Power Company, performed the sixth tendon surveillance of Oconee Unit 3. The licensee, using the averages of the liftoff forces obtained to that date, concluded that the mean liftoff force for each group fell below the required values. A subsequent trending analysis on the basis of individual liftoff forces indicated that the dome tendon force began to fall below the minimum required force about eight years after the structural integrity test (SIT). For other tendon groups in Unit 3, the tendon forces were not predicted to fall below the minimum required value until 40 years or more after the SIT.

Since Oconee Units 1 and 2 are identical to Oconee Unit 3, the licensee performed a trend analysis for each of these units and found that the vertical tendon forces in Unit 1 and Unit 2 were predicted to fall below the minimum value at 30 years and 10 years after the SIT, respectively. The cause of these results is attributed to the repeated use of the same tendons for liftoff testing subjecting the tendons to cyclic loading. As a result, the tendons subjected to repeated liftoff tests are no longer considered representative of the tendon population. As part of its corrective action, the licensee reanalyzed the containment structure using state-of-the-art analysis techniques and committed to random tendon selection for future tendon surveillance in accordance with Regulatory Guide 1.35.

In 1997, inspections precursory conditions of abnormal tendon degradation were observed. These conditions included higher than normal water content in tendon filler grease, presence of free water, grease leakage from the reactor building, lower than expected tendon elongation, and low filler grease reserve alkalinity. The engineering evaluation concluded that these precursor conditions did not result in loss of tendon prestress, and that the examined tendons were capable of performing their intended functions. (US Nuclear Regulatory Commission, 2000)

1.3.4   South Texas

In 2004, six reactor containment building tendons (three vertical and three horizontal) were inspected for the surveillance. Excessive grease voids (11.4% and 19.8%) were found in two of the vertical tendons.

By 2010, 140 liftoff tests had been conducted. All but two of these were acceptable (>95% of predicted force). The other two occurred in year 1 (Unit 2) and year 5 (Unit 1), both at 94% of predicted force. In years 10, 15, and 20 all tested tendons were found to be above the acceptance limit. Thus, no observations to date indicate unacceptable rates of degradation. (South Texas Projct Nuclear Operating Company, 2013)

2 POST-TENSIONED CONCRETE CONTAINMENT VESSEL DEGRADATION MODES

A major design consideration of PCCVs is the protection of the post-tensioning system from degradation. Grouted or bonded tendons are used in many PCCVs in several countries including France, Belgium, South Korea, China, and Canada. Some of these containments do not have steel liners while the United States use steel liners as protection for leakage of radiation products. Only two PCCVs in the United States have bonded prestressing systems with the rest using unbonded tendons coated with corrosion-inhibiting wax or grease, enabling the tendons to be examined, retensioned, and replaced as necessary. PCCVs also have conventional reinforcement in addition to pre- and post-tensioning systems, but reinforcement congestion is an issue around equipment hatch openings.

The first prestressed containment facilities (R.E. Ginna in 1969) included only vertical prestressing, but biaxially prestressed containments quickly became the primary PCCV type. Because these containments have nearly 1000 tendons anchored at a variety of locations on the structure, the installation, tensioning, and corrosion-proofing of the prestressing system was a time-consuming process. A typical cement used in PCCVs is Type II Portland cement due to its resistance to sulfate attack and low heat of hydration. PCCV concrete design often uses air-entraining admixtures (AEA) and curing agents to prevent common modes of degradation. Each concrete containment in the United States has an interior steel liner (0.25-0.5 in thick) to serve as a leak tight vapor barrier; its strength is neglected in design.

2.1 Post-Tensioning System Description

Post-tensioned concrete structures use tension cables or tendons to introduce large compressive stresses in the concrete material. In the case of a nuclear plant, the reactor and the steam generators are contained in a large strong containment structure designed to contain possible radioactive material release under various postulated design loading combinations. The two typical approaches are to use reinforced concrete or to use post-tensioned concrete. PCCVs use tendons to carry a significant portion of the hoop stresses generated from internal pressure under accident conditions while reinforced concrete containments use primarily rebar.

Excessive vertical and hoop tensioning can exaggerate the radial tension between the plane of the hoop tendons and outer surface of the concrete, which is of special concern for PCCV designs without radial tie bars. Figure 2-1 demonstrates the tensile stress that develops from hoop tensioning. The 2019 American Society of Mechanical Engineers (ASME) Boiler & Pressure Vessel Code (BPVC) Section III requires radial reinforcing steel and/or radial stirrups (see Figure 2-2) in the containment cylinder by prohibiting the reliance on concrete tensile strength to resist the external loads and moments or the forces and moments resulting from internal self-constraint (ASME, Boiler Pressure Vessel Code Section III, 2019). However, the radial reinforcement steel requirement was not required prior to 2019. Only a few NPPs have radial reinforcements in the containment cylinder, namely Farley, Vogtle, Summer, South Texas, Calvert Cliffs, Wolf Creek, and San Onofre (US Nuclear Regulatory Commission, 2010). It is very common to have radial reinforcements in containment domes because:

1. Tendons are located closer to the inner radius.
2. There are often three sets of intersecting tendons.
3. The dome is thinner than the cylinder.

4. Radial stresses caused by prestress are even higher in domes than in cylinders.
5. The ASME BPVC required radial reinforcement in concrete structures with double curvature (e.g., domes).
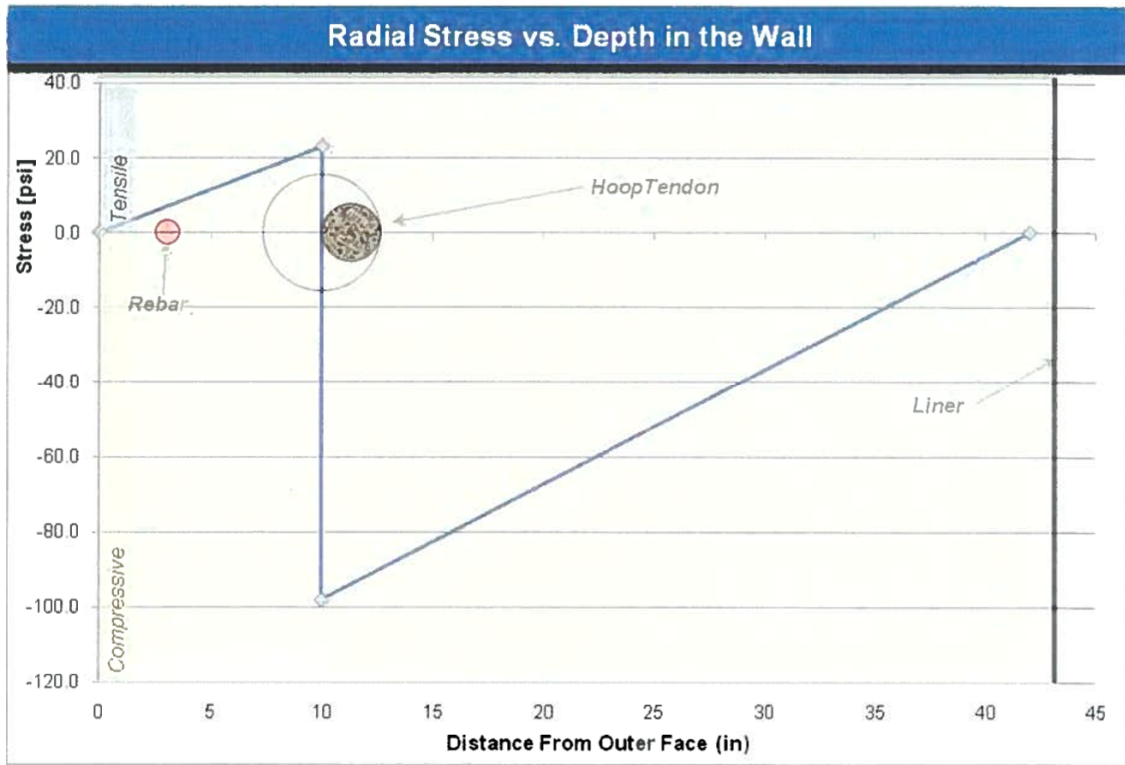
Figure 2-1   Tensile and compressive stresses in concrete wall cross-section due to horizontal hoop tendons. (US Nuclear Regulatory Commission, 2010)
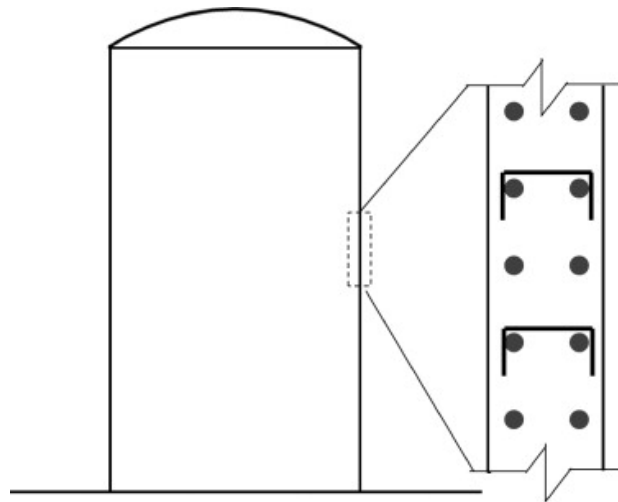
Figure 2-2   PCCV structure (left) with a schematic of horizontal tendons and radial reinforcement (right). (Wang & Munshi, 2013)

Radial stresses in the containment wall are designed such that the tensile stress of the concrete is not exceeded. However, over-tensioning of hoop tendons or improper installation techniques could initiate delamination-type cracking in the wall of the containment. Over time and in combination with other operating conditions, such as ambient thermal cycling, this cracking could degrade the ultimate capacity to withstand pressurization and also render the PCCV more vulnerable to issues with structural modifications. Excessive vertical and hoop tensioning can also induce additional compressive creep strains (over that assumed in design). Under constant load, this additional compressive creep strain is generally not a problem and tends to relax the stress, but it could potentially contribute to structural issues if there is a change in loading, for example, de-tensioning for structural modifications. Upon load removal from de-tensioning, these compressive creep strains start to slowly dissipate (viscoelastic behavior). Excessive tensioning also means higher stress in tendons and, along with compressive creep in the concrete, will lead to a more rapid decay in the design prestress conditions. This can usually be corrected for PCCV designs with un-grouted tendons through scheduled inspection and re-tensioning. However, repeated cycles of this can increase the risk for delamination cracking and generate additional compressive creep strains. It is also noted that the creep rate in concrete is generally sensitive to change in loading, that is, if the change is significant enough, the higher primary creep rate (consistent with the age of the concrete) can initiate. Repeated cycles of over tensioning would incrementally increase the age integrated total creep strains with corresponding changes in the rate of creep beyond that accounted for in the design leading to additional risks in detensioning.

2.2   Brief Summaries of Material Degradation Modes

Material degradation modes in PCCVs are covered in great detail in (US Nuclear Regulatory Commission, 2014), (American Concrete Institute, 2018), and (Electric Power Research Institute, 2015). Brief summaries are presented here for the reader's convenience.

2.2.1   Concrete

Concrete is susceptible to chemical attack and physical attack. The information presented in this section is summarized from (Mindess, Young, & Darwin, 2003) for the reader's convenience.

- Chemical attack:
    - Leaching and efflorescence
    - Sulfate attack
    - Alkali-aggregate reaction (AAR)

- Physical attack:
    - Freezing and thawing
    - Wetting and drying
    - Temperature changes
    - Wear and abrasion

Efflorescence in concrete is a whitish colored powdered deposition of salts on the concrete surface that is formed due to evaporation of water from the concrete. It is caused when water-soluble salts present in the concrete material come on to the surface and water evaporates from

the concrete. Efflorescence, in itself, is an aesthetic rather than durability problem. However, it does indicate that substantial leaching is occurring within the concrete. Extensive leaching of salts, namely calcium hydroxide, from the interior of the concrete causes an increase in porosity, lowering the strength of the concrete and increasing the permeability, thereby increasing its vulnerability to aggressive chemicals. Leaching is most prevalent when the water can seep through the concrete, particularly under pressure. Concrete is not significantly leached by water flowing over its surface unless accompanied by physical abrasion from suspended solid matter.

One of the most common forms of concrete chemical attack is the action of sulfates on concrete. Sulfates are often present in groundwaters, particularly when high proportions of clay are present in the soil, and seawater has sulfates as a major constituent. Sulfates present in rainwater from air pollution, or produced by biological growths, may cause slow deterioration even in concrete above ground. The damage caused by sulfate attack may involve cracking and expansion of concrete as a whole, as well as softening and disintegration of cement paste. Sulfate attack is a complex process that may involve all hydration products produced by Portland cement. Portland cement hydration products contain a compound called monosulfoaluminate. When additional sulfates are supplied to the pore water, the monosulfoaluminate converts to ettringite: long, needle-like crystals. The conversion is accompanied by a 55% increase in solid volume of the compound, causing a volume expansion within the paste that generates internal stresses and ultimately leads to cracking. Some sulfate attacks can weaken the cement paste without large volume changes or cracking; these attacks result in significant softening and disintegration of the primary hydration product calcium-silicate-hydrate (C-S-H), leaving the cement paste in a puttylike state. The type of sulfate attack largely depends on the particular sulfates involved.

AAR is a concrete degradation mode due to expansions caused by a chemical reaction between the alkalis contained in the cement paste and certain reactive forms of silica within the aggregate. The reaction between the silica and cement paste causes the formation of a 'gel layer' on the exterior of the aggregates; the gel layer has a larger volume than the constituents, causing internal stresses and eventually cracking and spalling. Various forms of silica have different reactivities, depending of the degree of crystallinity, internal porosity, crystallite size, and internal crystal strain. Different aggregates react at different rates, and damage due to AAR may not be apparent for many years after a structure is put into service. AAR has a significant effect on concrete compressive strength, tensile strength, and elastic modulus: all are reduced by up to 50% depending on the severity of the AAR (Trent, 2018).

Porous materials containing moisture are susceptible to damage under repeated cycles of freezing and thawing. Hardened cement paste, which has a high porosity, is particularly susceptible to such conditions and can be destroyed in a single winter in northern climates. Fortunately, AEAs have proven to be an effective and reliable means of protecting concrete from freeze-thaw damage. PCCVs use AEAs to prevent freeze-thaw damage in the hardened cement paste. Porous aggregates can also be susceptible to freeze-thaw damage and are therefore not recommended for use in high-risk structures that are exposed to freezing temperatures. Further information on NRC recommendations for loss of material and cracking due to freeze-thaw damage can be found in (US Nuclear Regulatory Commission, 2010) (US Nuclear Regulatory Commission, 2017). For plants located in moderate to severe weathering conditions (weathering index >100 day-inch/year), a plant-specific program is not required if documented evidence confirms that the existing concrete had air content of 3 percent to 8 percent (including tolerance) and subsequent inspection of accessible areas did not exhibit degradation related to freeze-thaw.

2.2.2 Rebar

The information presented in this section is summarized from (Mindess, Young, & Darwin, 2003) (McCormac & Brown, 2009) for the reader's convenience.

The corrosion of reinforcing steel in concrete structures that are regularly exposed to salts is one of the most acute durability problems in North America. Bridge decks exposed to deicing salts and structures exposed to seawater, both in fluid form and brought to the structure by winds, are most at risk. Salts will penetrate into the pores or cracks of the concrete and slowly diffuse down to the reinforcement. Chloride ions, notably from NaCl, reduce the pH of the pore solution in concrete. The chloride ions penetrate the passive protective layer on steel reinforcement. Without the protective layer, water reacts with the steel to cause oxidation (rust). Oxidized iron has a larger volume than non-oxidized, causing severe volumetric expansion. The iron expansion causes concrete internal stress, and eventually concrete cracking and spalling. This reduces the concrete cover for the steel, accelerating corrosion. Also, the bond of the concrete to the steel is reduced, degrading the structural integrity.

2.2.3 Tendons

Unbonded tendons, as used in the U.S., are generally protected by a ferrous duct and anticorrosive grease around the strand. However, corrosion in steel prestressing (or post-tensioning, the terms are used alternatively) tendons can occur due to pitting corrosion, general steel rusting, hydrogen embrittlement, stress-corrosion cracking, fretting fatigue, or corrosion fatigue. Tendons are typically subjected to a continuous applied stress level of no greater than 70% of ultimate tensile strength.

Stress relaxation occurs in post-tensioning strands and is a significant portion of the predicted stress losses in a PCCV (with concrete creep another major contributor). Tendon stress relaxation can often be predicted during design prior to construction, but concrete creep and total prestressing system stress losses is significantly more difficult to predict.

Water penetrating the protective sheath and anticorrosive grease can cause the steel tendons to rust, lowering the effective cross-sectional area of the tendon and therefore its strength. Water buildup inside the tendon sheaths can also enable microbial attack on the anticorrosion grease, resulting in acid buildup that degrades the tendons.

The susceptibility of steel to stress-corrosion cracking and hydrogen embrittlement generally increases with increasing strength. Hydrogen embrittlement is defined as the reduction in ductility due to the absorption of atomic hydrogen into the metal lattice. Hydrogen embrittlement can occur at any point in the components of the prestressing system's life, even before installation.

For stress-corrosion cracking to occur, the metal should be under tensile stress and simultaneously exposed to a corrosive environment. Corrosion products and weight loss at or near the failure may be negligible. The cracking takes the form of transgranular or intergranular cracking. Hydrogen embrittlement and stress-corrosion cracking manifest in similar ways: both occur by brittle fracture and may both have the same appearance (little necking).

2.2.4 PCCV System Degradation

Outside of specific material degradations, PCCVs are also subject to system-wide degradation.

The effects of elevated temperatures and freeze-thaw cycles on hardened concrete can alter (typically reduce) structural integrity by reducing the strength of concrete and the reinforcing steel and potentially permanently modifying the microstructure of PT tendons and concrete. Increased temperature can increase the creep rate of concrete as well as increase the stress relaxation in the tendons. Thermal load cycles can induce fatigue effects into the structure as well. Freeze-thaw cycles can result in eventual cracking, scaling, or disintegration of concrete if highly saturated concrete has insufficient entrained air in the cement paste or has highly porous aggregates.

The containment inner steel liner and its anchorages are often 6 mm -13 mm (0.25 in - 0.5 in) thick, so there is little tolerance for material loss. In addition, the liner is an air-tight seal, so corrosion holes are functionally safety significant. Containment liners typically receive a protective coating on the exposed inner surface, but the surface in contact with the concrete is untreated.

2.3   Concrete Creep and Creep Rupture

This section provides a brief review of creep and creep rupture in metals, an overview of creep in concrete, a few examples of excessive creep in post-tensioned concrete structures, and a detailed literature review of creep rupture in concrete. Creep and creep rupture in metals is a rigorously studied field, so a review is provided to familiarize the reader with common mechanics of general creep and creep rupture. A review of creep in concrete is also provided to the reader to demonstrate how creep in concrete is similar to and differs from creep in metals. As this document is primarily focused on determining the effects of creep in post-tensioned concrete, a few examples of post-tensioned concrete structural failures related to creep are described. A brief review of the state of creep research in post-tensioned concrete containment vessels in the nuclear power industry is also presented. Finally, an extensive literature review on creep rupture in concrete is presented. The general conclusions are:

- Concrete creep follows the common three-phase creep progression. The third phase, if stress conditions trigger its initiation, manifests in a drastically increasing creep rate potentially followed by rupture. If excessive creep is expected in any portion of a post-tensioned concrete structure, monitoring systems are recommended.

- Concrete creep rupture does not typically manifest below 60% of the ultimate uniaxial stress in either compression or tension. Concrete design codes in the U.S. limit the stresses in concrete, and these limits are below tertiary creep and creep rupture thresholds. However, if structural circumstances cause excessive deformations, the threshold stress for the onset of tertiary creep and subsequent creep rupture in either compression or tension may be exceeded.

- Temperature effects on concrete creep rupture have not been studied; however, increased temperature does increase concrete creep strains.

2.3.1   Introduction to Creep

Materials are often placed in service at elevated temperatures and/or exposed to static mechanical stresses (e.g., turbine rotors in jet engines, steam generators that experience centrifugal stresses, and concrete structures subjected to constant dead weights or post-tensioning forces). Deformation over time under such circumstances is termed creep. Defined

as the time-dependent and permanent deformation[1] of materials when subjected to a constant load or stress, creep is normally an undesirable phenomenon and is often the limiting factor in the lifetime of a part, especially for mechanical systems. It is observed in all material types; for metals it becomes important only for temperatures greater than about $0.4 T_m$ (T_m is the absolute melting temperature in Kelvin) (William D. Callister, 2007). Amorphous polymers, which include plastics and rubbers, are especially sensitive to creep deformation. If creep deformation advances too far, the material can rupture, or fracture, into multiple pieces. This phenomenon is termed creep rupture (or creep fracture, the terms are used interchangeably).

One prominent example of long-term deformations from sustained or repeated loads is rutting in asphalt[2] pavements. As heavy vehicles such as cargo trucks or aircraft repeatedly traverse the same area of pavement, the pavement under the highest stresses slowly deforms as shown in Figure 2-3.

Figure 2-3   Asphalt pavement rutting on a primary highway. (Pavement Tools Cosortium, n.d.)

The manifestation of concrete creep is similar to asphalt, but typically to a lesser order of magnitude. Asphalt binders are considered a plastic, fluid-like material while hydrated Portland cement is considered a brittle solid. That being said, concrete creep is an important consideration in structural concrete engineering. Concrete structures are typically designed for approximately 50 years of service life (Medeiros-Junior, de Lima, & de Medeiros, 2015), and structural concrete codes require designers to account for concrete creep effects. Increasingly, for major bridges, service life requirements are being set by bridge owners to 100 years or even longer (California Department of Transportation (CalTrans), 2000) (Port of Long Beach, 2010). Concrete elements under sustained loads such as beams, columns, or prestressed members are subject to significant creep over their service life. As creep advances, the stress state of the concrete elements, and of their reinforcement, can change. These altered stress states can sometimes alleviate danger zones by redistributing high stress from one area into neighboring

---

[1] Some, but not all, creep deformation is recoverable.
[2] Technically asphalt pavement is "asphalt concrete." Portland cement concrete is the usually grey material that most people label "concrete." The term "concrete" in this document refers to Portland cement concrete.

elements. However, advanced creep could also reduce the capacity of concrete elements or add stress to neighboring elements that should not accrue more.

While concrete creep is a well-studied phenomenon, there is a distinct knowledge gap in the field of concrete creep rupture (US Nuclear Regulatory Commission, 2014). Structural concrete elements include reinforcing elements, typically steel reinforcing bars. While concrete performance can be degraded due to creep rupture at elevated stresses and temperatures, there is no mention of concrete creep rupture in the structural concrete design code for the United States (American Concrete Institute, 2014).

2.3.2   Creep Review

Creep in concrete is an intricate topic due to the complexities of hydrated Portland cement (e.g., porosity and hydration states in the material). Therefore, before discussing creep in concrete, a brief introduction of creep and creep rupture of metals is presented. Creep and creep rupture of metals represents a more simplistic case of creep and is a more established field of study. An overview is beneficial to considering it for cement and concrete.

2.3.2.1   *Creep of Metals*

A typical creep test for metals (ASTM) consists of subjecting a specimen to a constant load or stress while maintaining the temperature constant; deformation or strain is measured and plotted as a function of elapsed time.

Figure 2-4 is a schematic representation of the typical constant load creep behavior of metals; Figure 2-5 is a schematic representation of the typical creep rate vs time. Upon application of the load there is an instantaneous deformation, as indicated in the figure, which is mostly elastic. The resulting creep curve consists of three regions, each of which has its own distinctive strain-time feature. Primary or transient creep occurs first, typified by a continuously decreasing creep rate; that is, the slope of the curve diminishes with time. This suggests that the material is experiencing an increase in creep resistance or strain hardening—deformation becomes more difficult as the material is strained. For secondary creep, sometimes termed steady-state creep, the rate is constant; that is, the plot becomes linear. This stage of creep often has the longest duration. The constant rate of creep in this regime is explained based on a balance between the competing processes of strain hardening and recovery, recovery being the process whereby a material becomes softer and retains its ability to experience deformation. Finally, for tertiary creep, there is an acceleration of the creep rate and then ultimate failure. This failure is frequently termed rupture and results from microstructural and/or metallurgical changes, for example, grain boundary separation, and the formation of internal cracks, cavities, and voids. Also, for tensile loads in metals, a neck may form at some point within the deformation region. These all lead to a decrease in the effective cross-sectional area and an increase in strain rate.
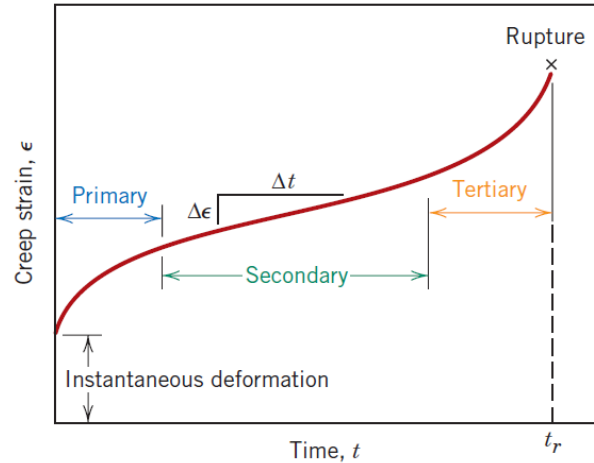
Figure 2-4   Typical creep curve of strain vs time at a constant stress and constant temperature. The minimum creep rate $\Delta\epsilon/\Delta t$ is the slope of the linear segment in the secondary region. Rupture lifetime t_r is the total time to rupture. (William D. Callister, 2007)
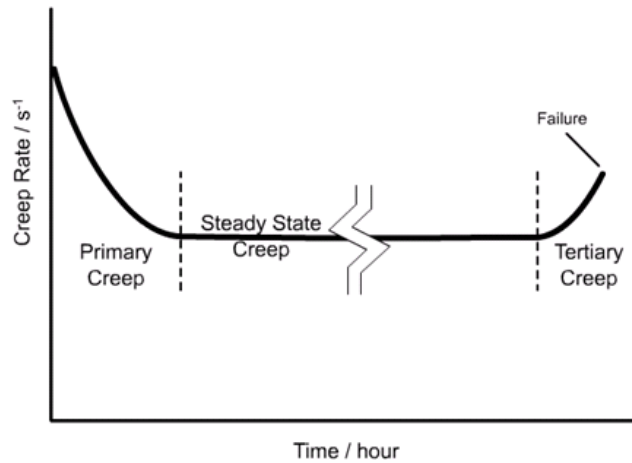
Figure 2-5   Typical creep rate vs time graph with primary, secondary, and tertiary phases.

In metals, most creep tests are conducted in uniaxial tension using a specimen having the same geometry as for tensile tests. On the other hand, uniaxial compression tests are more appropriate for brittle materials; these provide a better measure of the intrinsic creep properties as there is not stress amplification and crack propagation, as with tensile loads. Compressive test specimens are usually right cylinders or parallelepipeds having length-to-diameter ratios ranging from about 2 to 4. For most materials creep properties are virtually independent of loading direction.

Possibly the most important parameter from a creep test is the slope of the secondary portion of the creep curve ($\Delta\epsilon/\Delta t$ in Figure 2-4); this is often called the minimum or steady-state creep rate $\dot{\epsilon}_s$. It is the engineering design parameter that is considered for long-life applications, such as a

NPP component that is scheduled to operate for several decades, and when failure or too much strain lead to loss of function. On the other hand, for many relatively short-life creep situations (e.g., turbine blades in military aircraft and rocket motor nozzles (William D. Callister, 2007)), time to rupture, or the rupture lifetime t_r, is the dominant design consideration (also indicated in Figure 2-4). Of course, for t_r determination, creep tests must be conducted to the point of failure.

2.3.2.2   Stress and Temperature Effects in Metals

Both temperature and the level of the applied stress influence the creep characteristics (Figure 2-6 and Figure 2-7). At a temperature substantially below $0.4T_m$, and after the initial deformation, the strain in metals is virtually independent of time. With either increasing stress or temperature the following will be noted:

- The instantaneous strain at the time of stress application increases,
- The steady-state creep rate is increased,
- The rupture lifetime is diminished.

The results of creep rupture tests are most commonly presented as the logarithm of stress versus the logarithm of rupture lifetime. Figure 2-8 is one such plot for a nickel alloy in which a linear relationship can be seen to exist at each temperature. For some alloys and over relatively large stress ranges, nonlinearity in these curves is observed.

A thorough treatment of creep rupture for weld material, and the original reference defining the rupture criteria for liner plate material can be found in (Manjoine, 1982).
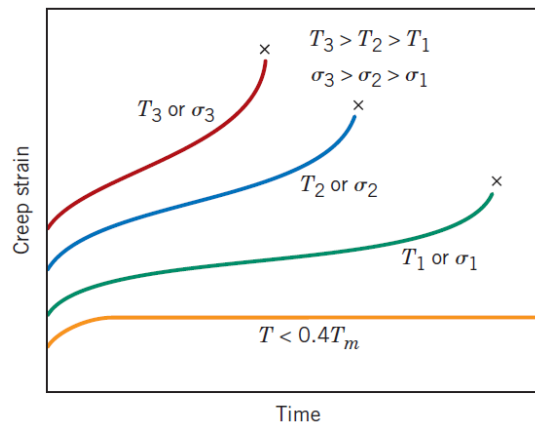
Figure 2-6   **Schematic of influence of stress σ and temperature T on creep behavior. (William D. Callister, 2007)**
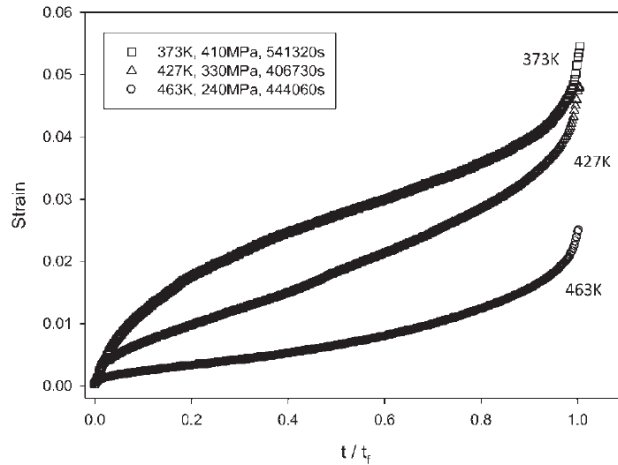
Figure 2-7   Experimental creep-strain time curves recorded for different stresses at 373, 427, and 463 K for Al 2124. (Williams, Bache, & Wilshire, 2010)
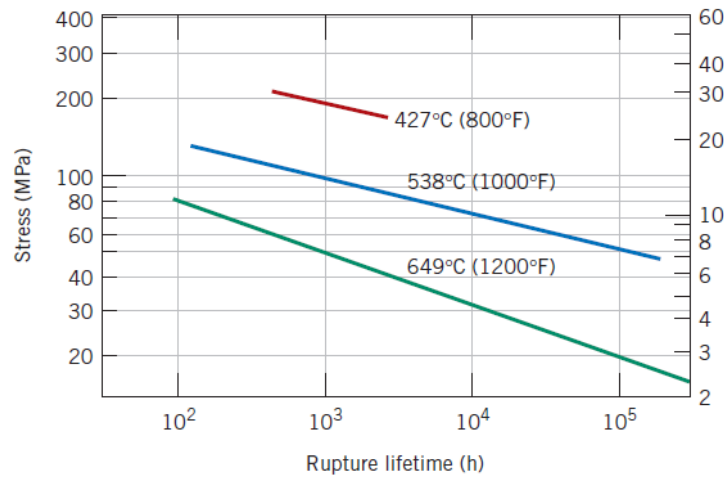
Figure 2-8   Stress (logarithmic scale) versus rupture lifetime (logarithmic scale) for a low carbon-nickel alloy at three temperatures. (Benjamin (Senior Editor), 1980)

2.3.2.3   Creep of Concrete

Although all materials undergo time-dependent deformation under load, ceramics and metals have an almost negligible creep at room temperature. The fundamental origins for creep of concrete must be quite different, since significant volume changes occur at ambient temperatures and the variations in presence of moisture in the material play a major role.

Portland cement concrete is comprised of a matrix of cement, sand, and aggregate; the cement part of the hardened matrix is referred to as the 'paste'. It is commonly stated that concrete creep and drying shrinkage are interrelated phenomena because there are a number of similarities between the two. The strain-time curves are very similar, experimental parameters affect creep in much the same way as shrinkage, the magnitudes of the strains are the same,

and they include a considerable amount of irreversibility. Like shrinkage, creep is a paste property, and the aggregate in concrete serves to act as a restraint (Boresi & Schmidt, 2003).

A typical concrete creep curve for concrete in compression is given in Figure 2-9. When a specimen is unloaded, the instantaneous recovery is approximately the same as the instantaneous strain on the first application of the load, but creep recovery, although it occurs more rapidly than creep, is by no means complete. A considerable portion of the total creep is irreversible (irrecoverable). Under typical service conditions such as columns or walls, concrete is most likely drying while under load, and it has been found that creep deformations are greater under such conditions than if the concrete is dried prior to loading. Terminology has been developed to consider this fact and is illustrated in Figure 2-10. If the free shrinkage (ε_{sh}, determined while the specimen is unloaded but subjected to the same drying conditions) and basic creep (ε_{bc}, determined while specimen is loaded but not drying) are added together, their sum is less than the total strain (ε_{tot}) determined during simultaneous loading and drying. The excess deformation is called drying creep (ε_{dc}).
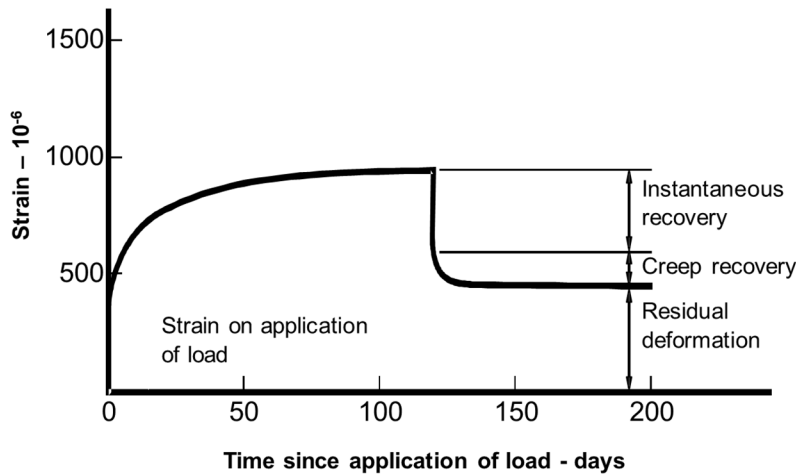
Figure 2-9   Typical creep curve for plain concrete.
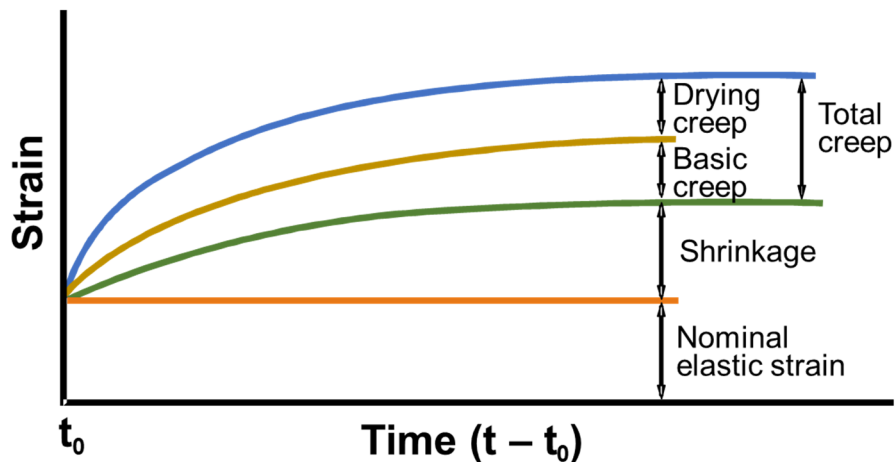
Figure 2-10   Creep of concrete under simultaneous loading and drying.

2-12

Several factors influence concrete creep and are summarized below.

- Creep increases nonlinearly with stress as shown in Figure 2-11, though an approximate linear relationship can be assumed in the stress range typical in structures.

- Increased time of moist curing decreases specific creep.

- Specific creep increases with increasing water-to-cement ratio (w/c ratio).

- Specific creep decreases with increasing concrete strength.

- Total creep increases for samples of concrete at higher temperatures compared to samples of the same mixture (and same load) at lower temperature.

- Creep increases with increased amounts of non-evaporable water in the cement pores.

- Aggregate content and modulus of elasticity are the most important factors affecting creep of concrete. Increased aggregate content and/or aggregate stiffness decrease creep. Increased modulus of elasticity decreases creep.

- The magnitude of creep strains in tension is greater compared to compression for any given load.

- Flexural creep is complicated by the fact that part of the concrete is in compression and part in tension.

- Under a uniaxial compressive stress, some lateral creep also occurs due to the lateral tension associated with Poisson's ratio stress.
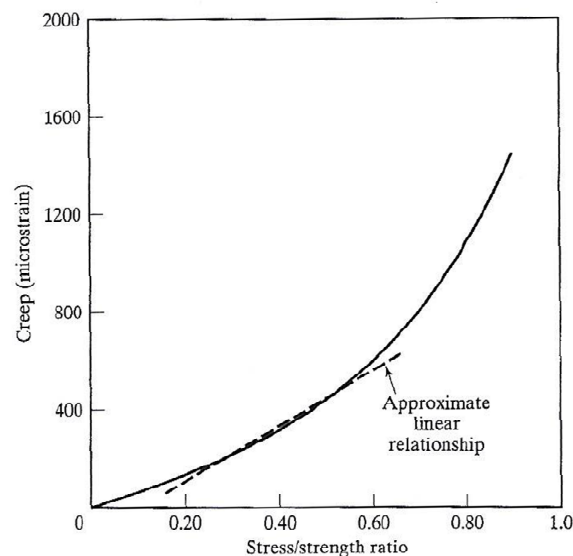
Figure 2-11   Creep-stress relationship for concrete. (Mindess, Young, & Darwin, 2003)

Important to note in the description of concrete creep is that concrete does not creep at the same rate in different loading conditions. Concrete creep under compression is the "slowest" creep with creep under bending, tension, and shear being significantly "faster". Work performed by (Kim, Park, & Lee, 2019) indicate that concrete bending creep and tensile creep are ~3x and ~4x greater than compressive concrete creep, respectively (Figure 2-12). Work performed by (Mhamankar & Jones, 2019) indicate that concrete shear creep is ~13x greater than concrete compressive creep as shown in Figure 2-13.
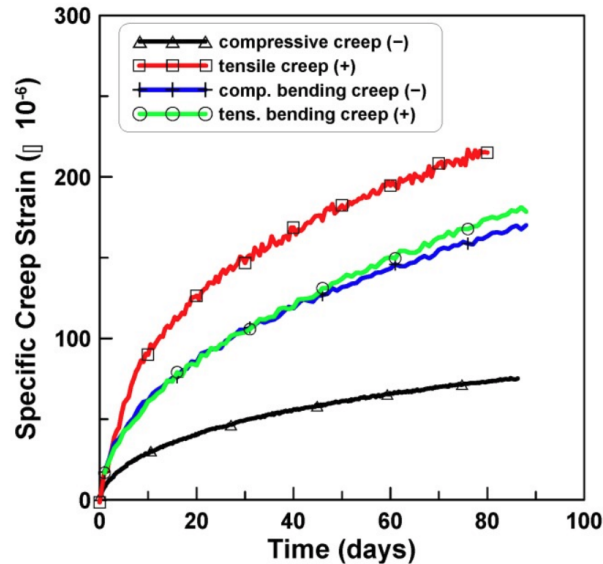
Figure 2-12   Comparison of specific creep in compression, tension, and bending. (Kim, Park, & Lee, 2019)
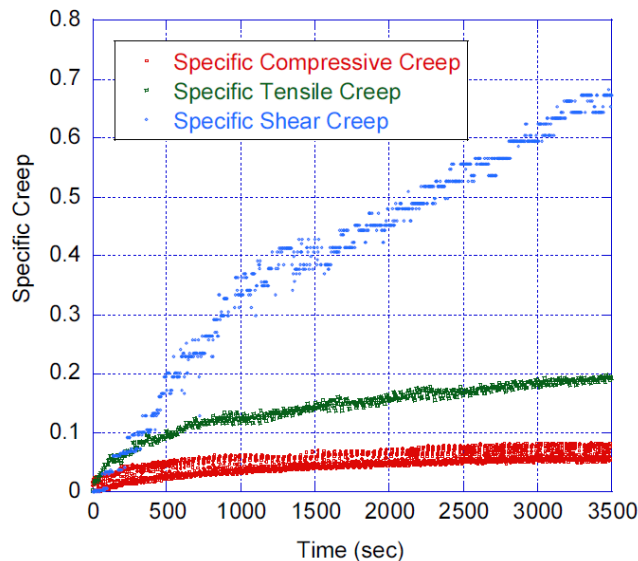
Figure 2-13   Compressive, tensile, and shear specific creep plot. Figure courtesy of IASMiRT. (Mhamankar & Jones, 2019)

The reader should note that, while these factors are listed separately, many are coupled in certain circumstances. For example, increasing the time of moist curing and decreasing the w/c ratio often increases concrete strength, decreases specific creep, and decreases internal concrete porosity. A more detailed discussion on each factor and how they relate to each other can be found in (Mindess, Young, & Darwin, 2003).

Zdenek Bažant states the following about concrete creep (Bažant Z. P., Creep and Shrinkage of Concrete, 1975):

> "The most obvious effect of creep to be considered in design is the growth of deflections, which is of concern, e.g., in large-span prestressed concrete bridges. Cases of deflections over one foot in excess of the predicted values have been experienced in some early long-span bridges. In concrete columns, compressed walls, and thin shells, creep magnifies the buckling deflections and internal forces due to unavoidable imperfections and leads to long-time instability under a load several times less than the short-time stability limit. In many structures, creep causes extensive redistributions of internal forces and, together with stresses induced by shrinkage and thermal dilations, may produce severe cracking and overload of some structural parts. A typical example is a bridge span whose halves are cast by cantilever method with the same slip form, one after the other; the younger half tends to deflect more but, because of the connection at midspan, produces a shear force. In all prestressed structures, creep and shrinkage cause a significant loss of prestressing force. In statically indeterminate structures, creep can be beneficial in reducing the forces induced by shrinkage, or the internal forces due to displacements imposed during the construction by jacks to rectify previous undesirable deflections or internal forces in the structure, or the forces due to differential settlements of the structure."

Bažant's statements summarize creep analysis in general concrete engineering practice: creep can relieve some internal stresses in a structure, but creep can also cause problems in prestressed structures or in structures built in pieces over a long time period.

For design of bridges for which creep effects are particularly important to assess accurately, the two most prevalent Codes in USA design practice are AASHTO and the CEB-FIP (American Association of State Highway and Transportation Officials, September 2017) (International Federation for Structural Concrete, October 2013).

2.3.2.4   Effect of Temperature on Concrete Creep

The properties of Portland cement concrete at elevated temperatures have been studied for decades. Extensive research exists analyzing concrete creep at elevated temperatures (Gross, 1975) (Bazant, Theory of Creep and Shrinkage in Concrete Structures: A Precis of Recent Developments, 1975) (Bazant, Cusatis, & Cedolin, Temperature Effect of Concrete Creep Modeled by Microprestress-Solidification Theory, June 2004). A few select graphs and conclusions are presented here that summarize the general trend of concrete creep at elevated temperatures.

As with metals, concrete subjected to elevated temperatures is susceptible to increased creep (Kodur, 2014). However, the mechanism of increased concrete creep in concrete is not the same as in metals. Under temperature ranges between ~20°C and 100°C, creep in concrete is affected by moisture movement in the cement matrix. The presence of water in the pores

creates a complicated creep strain response. At temperatures up to 160°F (71°C), concrete creep increases by a factor of ~3.5 (compared to creep at 70°F). Above 160°F (71°C), Nasser & Neville suggest that moisture evaporation from the cement gel pores increases the capillary suction effect in the cementitious matrix, causing a reduction in creep to a factor of ~1.7 (Figure 2-14, (Nasser & Neville, 1966)).
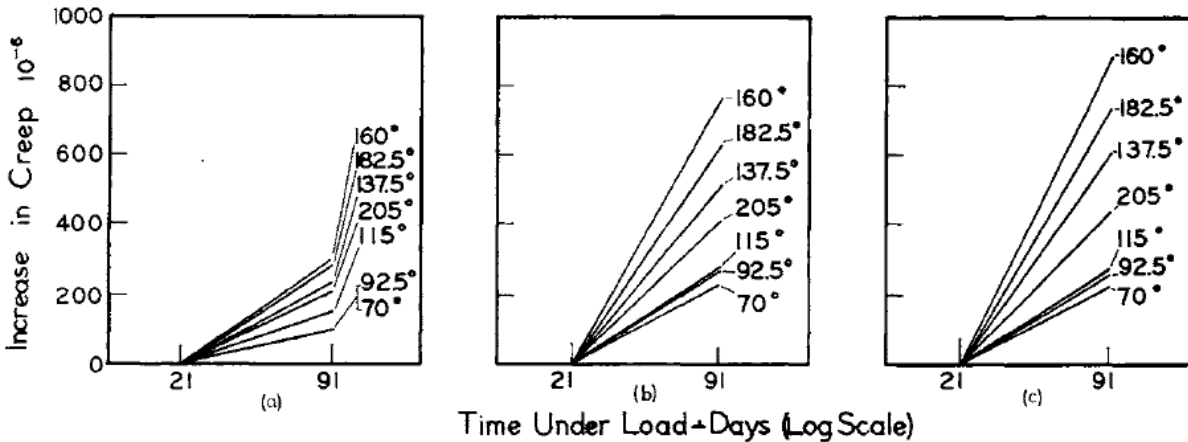
Figure 2-14   Increase in creep above the 21-day creep for different temperatures and stress-strength ratios of (a) 35%; (b) 60%; and (c) 70%. Temperature is in °F. (Nasser & Neville, 1966)

Concrete creep at temperatures above 100°C (the boiling point of water) becomes increasingly more severe with higher temperatures as shown in Figure 2-15 and Figure 2-16. There are two creep effects in concrete at elevated temperatures: transient creep and creep at elevated temperatures. Transient creep occurs during the first time that concrete is heated at constant rate under load. Transient creep does not occur during subsequent cooling or immediate re-heating to the same maximum temperature (The International Union of Laboratories and Experts in Construction Materials, Systems and Structures (RILEM), June 1998). Concrete creep at elevated temperatures is generated upon maintaining a certain level of temperature for a certain amount of time.

Yoon et al. in (Yoon, et al., 2017) determined that the amount of creep of high-strength concrete at elevated temperatures showed similar results at respective heating temperature levels regardless of the compressive strength. Increasing the temperature from 100°C to 600°C (212°F to 1112°F) increased creep strains by a factor of ~2 (compared to the strains at 100°C). Further increasing the temperature to 700-800°C (1292-1472°F) increased the creep strain by a factor of ~5 (compared to the strains at 100°C).
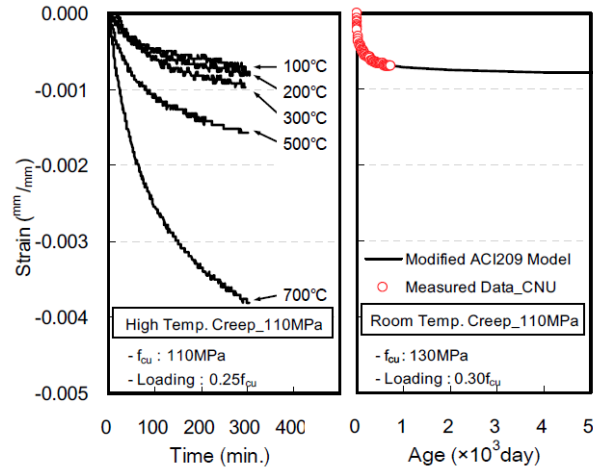
Figure 2-15   Creep strain of high-strength concrete at ambient and elevated temperatures. (Yoon, et al., 2017)
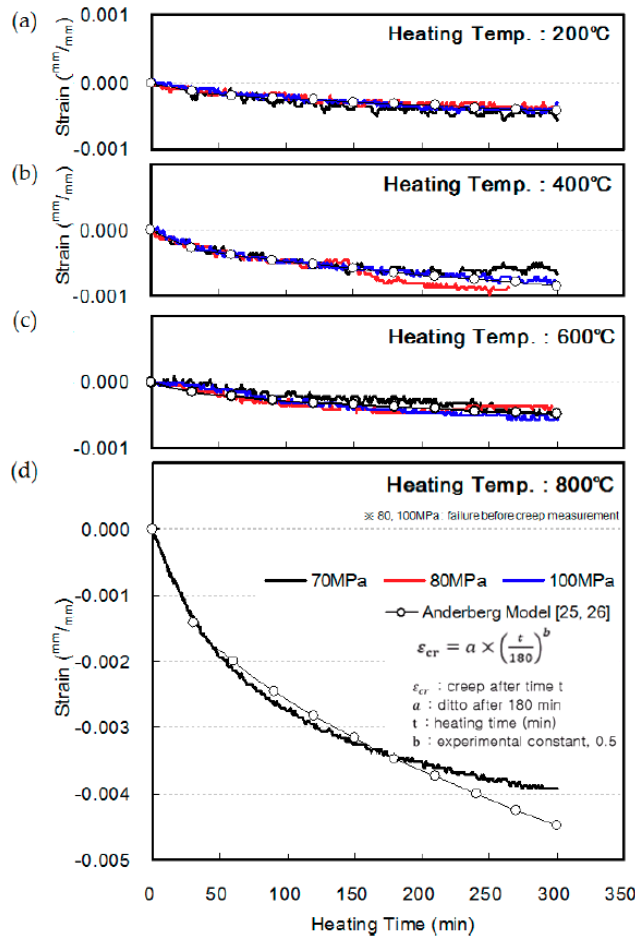
Figure 2-16   Creep of high-strength concrete at elevated temperature: (a) 200°C (392°F); (b) 400°C (752°F); (c) 600°C (1112°F); (d) 800°C (1472°F). Test specimens with f'_c of 80 MPa and 100 MPa at 800°C fractured before creep could be measured. (Yoon, et al., 2017)

As a general conclusion, concrete creep increases significantly until 71°C (160°F). Between 71-100°C (160-212°F), moisture evaporation effects cause the creep to slightly reduce (but still be greater than creep at normal temperature and pressure[3] (NTP)). Above 100°C, concrete creep increases with increasing temperatures. A significant increase in creep strain occurs between 700-800°C (1292-1472°F).

2.3.3   Examples of Creep in Post-tensioned Concrete Structures

Post-tensioning (or prestressing) can be defined in general terms as the preloading of a structure, before application of the service loads, to improve its performance in specific ways. Post-tensioning of concrete involves application of a compressive loading so that concrete tensile stresses that would otherwise occur are reduced or eliminated. The deflection of a member may also be controlled. Beams may be designed to have zero deflection at a specific combination of post-tensioning and external loading. Post-tensioned concrete is common in infrastructure with applications in slabs, floor beams, bridge decks and/or girders, and structures such as stadiums or airport terminals.

2.3.3.1   Post-tensioned Concrete Non-Nuclear Structures

One of the most widely used applications of concrete post-tensioning is in bridges. Furthermore, there is a growing database on creep in pre- or post-tensioned concrete bridges. Bažant has collected data from more than 60 bridges worldwide; most of these bridges deflected much more than predicted by calculation models in the design specifications (Bažant, Hubler, & Yu, 2011) (Bažant, Hubler, & Yu, Pervasiveness of Excessive Segmental Bridge Deflections: Wake-Up Call for Creep, 2011) (Bažant, Qiang, & Guang-Hua, Excessive Long-Time Deflections of Prestressed Box Girders. I: Record-Span Bridge in Palau and Other Paradigms, 2011). The data suggests no evidence of a finite asymptotic bound for concrete creep. Concrete creep becomes logarithmic after about 1000 days but does not exhibit asymptotic behavior. Most of the 60 bridges had already crossed their predicted 100-year maximum creep deflection, some within only 25 years of service. Excessive unexpected creep can result in uncomfortable riding conditions, excessive concrete cracking, service failure, or structural failure (collapse).

---

[3] Normal temperature and pressure: temperature 20°C (68°F) and pressure 1 atm. (National Institute of Standards and Technology (NIST), 2020)
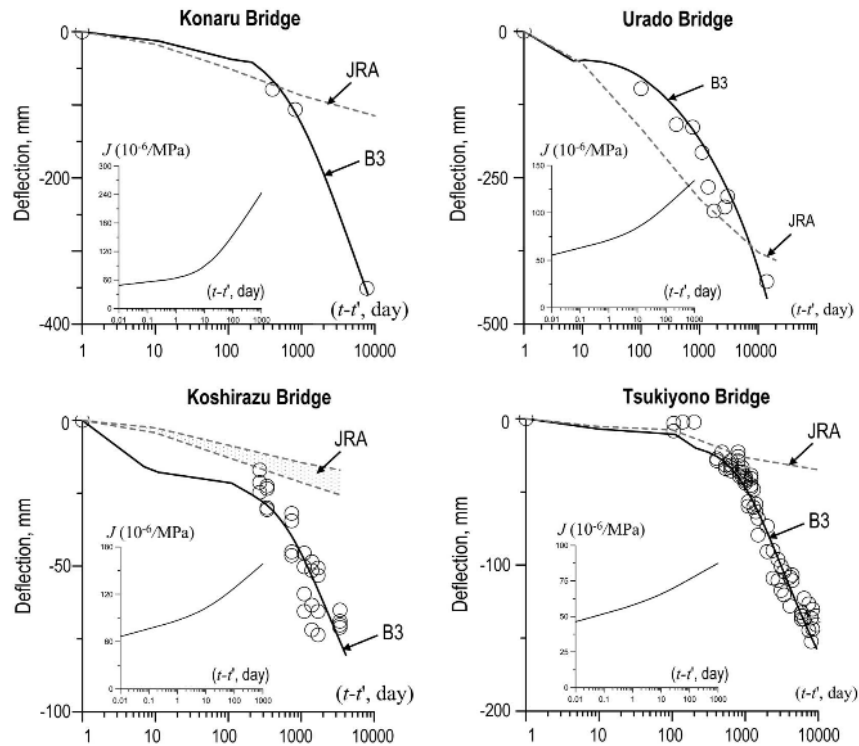
Figure 2-17   Excessive deflections observed in four bridges in Japan. JRA represents the Japanese Road Association predicted deflection while B3 represents Bažant's B3 creep model. (Bažant, Qiang, & Guang-Hua, Excessive Long-Time Deflections of Prestressed Box Girders. I: Record-Span Bridge in Palau and Other Paradigms, 2011). With permission from ASCE.[4]

As an example of the severity of excess deformations, Figure 2-18 shows creep effects visible to the naked eye on the Savines Bridge in France (Sellin, Barthélémy, Bondonet, & Cauvin, 2015). Built in 1960, the Savines Bridge was one of the first post-tensioned concrete bridges constructed in France. At 40 years, Eurocode Standard EN1992-1-1 predicted a maximum deflection of ~50 mm while EN1992-2 without silica fume predicted a maximum deflection of ~90 mm. The actual deflections of the bridge measured from 120-170 mm (Sellin, Barthélémy, Bondonet, & Cauvin, 2015).

Figure 2-18   Present-day view of the Savines Bridge in France. (Sellin, Barthélémy, Bondonet, & Cauvin, 2015)

One of the more severe cases, the Koror-Babeldaob (KB) Bridge in Palau, developed a midspan deflection of 1.61 m (5.3 ft) after 18 years. Completed in 1977, the KB Bridge was a cantilevered prestressed girder bridge with a 120.4 m (395 ft) long main-span cantilever. Mid-span deflections were noticed to exceed predictions as early as 1985—8 years after construction. A remedial prestressing repair was completed in 1996 in an attempt to save the bridge. The bridge collapsed three months after completion of the repairs (Bažant, Qiang, & Guang-Hua, Excessive Long-Time Deflections of Prestressed Box Girders. I: Record-Span Bridge in Palau and Other Paradigms, 2011) (Tang, 2014). One popular theory as to how the bridge collapsed includes many factors, the primary of which are listed here:

- Excessive concrete creep led to increased deflections across the span.

- The prestressing tendons were found to have only 50% of the design stress. The minimum safety margin for the tendons was 90% of the design stress.

- Excessive deflections from creep and loss of prestressing led to cracking in the top portion of the concrete girder, further reducing the girder stiffness.

It is worth noting that forensic analysis of the KB bridge indicated that the prestressing tendon ducts in the top layer of the bridge may have delaminated from the concrete. There were about 300 tendons in the top slab near the main pier of the bridge. They were arranged in four layers. Each tendon was placed inside a 47 mm (1.9 in) diameter metal duct. Bonding of these ducts to the concrete is usually weaker at the underside of the ducts (Figure 2-19). Due to the Poisson's effect, a high compressive stress in the longitudinal direction after the repair could have accelerated the separation of the concrete from the tendon ducts. As a result, the concrete in this area might have formed layers between the rolls of ducts, and as such could not perform as a monolithic material as designed.
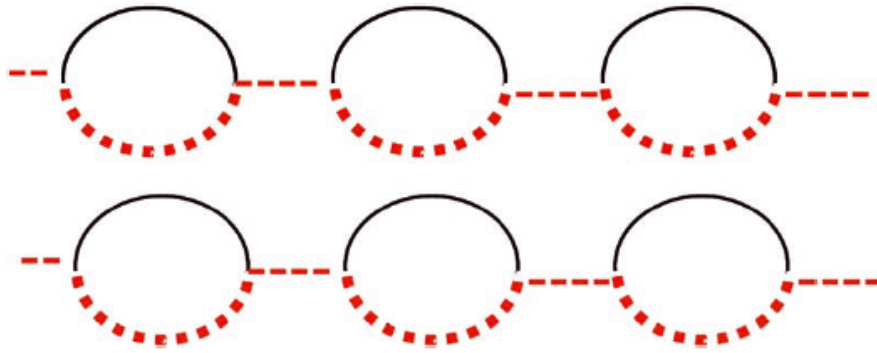
Figure 2-19   Possible delamination of the bottom of tendon ducts from concrete. (Tang, 2014)

A bridge in Cheviré, France also experienced unexpected excessive creep deformations (Raphael, Zgheib, & Chateauneauf, Experimental investigations and sensitivity analysis to explain the large creep of concrete deformations in the bridge of Cheviré, 2018). Built between 1988 and 1991, the bridge consists of two viaducts of concrete formed over 22 spans, the largest of which is 242 m (794 ft) long. The 242 m span consists of a 162 m (531 ft) steel span connected to two 40 m (131 ft) concrete viaducts. A composite steel-prestressed concrete is used to build the deck. The deck has a depth varying between 4.55 m (15.0 ft) and 9 m (29.5 ft) and a width of 24.6 m (80.7 ft). A schematic of the bridge is shown in Figure 2-20.

The vertical displacement of the free-end cantilever has been measured and monitored since 1994. The predicted deflection during design for 3200 days of service was 3.01 cm (1.18 in); the measured deflection after 3200 days of service was 18.2 cm (7.17 in). Both major European design codes at the time of construction (BPEL and Eurocode 2) drastically underestimated creep. No major structural repercussions have occurred, but the bridge is being closely monitored.
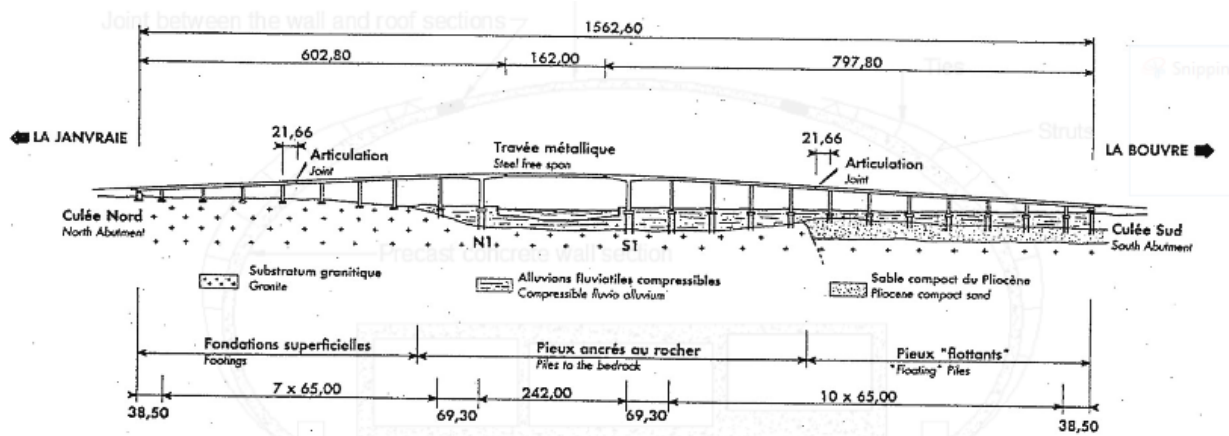
Figure 2-20   Elevation view of the bridge of Cheviré. (Raphael, Zgheib, & Chateauneauf, Experimental investigations and sensitivity analysis to explain the large creep of concrete deformations in the bridge of Cheviré, 2018)

The Parrotts Ferry Bridge in California, USA, was built between 1976 and 1979 and is a three-span prestressed concrete continuous rigid frame bridge that is experiencing excessive deflections from creep at midspan. At 195 m (640 ft), the main span is one of the longest prestressed concrete beam bridges ever built in the United States. The central span sagged nearly 30 cm (12 in) five months after opening and up to 63.5 cm (25 in) as of 2015 (HighestBridges.com, 2009) (Chen, Yang, & Liu, 2015).

Figure 2-21   Parrotts Ferry Bridge showing deflection at midspan (inside the red circle). (HighestBridges.com, 2009)

Figure 2-22   Parrotts Ferry Bridge with a nearly 2-foot (61 cm) sag in the center. (HighestBridges.com, 2009)

Figure 2-23   Brace installed on Parrotts Ferry Bridge (indicated by arrow) more than 10 years after construction to support the center. (HighestBridges.com, 2009)

Another U.S. bridge that is experiencing excessive creep deformations is the Robert E. Lee Memorial Bridge in Richmond, VA. This precast concrete stringer bridge was completed in 1989, provides six (6) lanes of vehicular traffic, and includes an underslung pedestrian suspension bridge as shown in Figure 2-24. Figure 2-25 shows the effect of creep between Pier 8 and Pier 9. As of 2011, the bridge span at the expansion joint had sagged a total of 25 cm (0.82 ft) since its construction, bringing the expansion joint 14 cm (0.46 ft) below the reference line (Theryo, 2011).

Figure 2-24   Robert E. Lee Memorial Bridge in Richmond, VA. Photograph shows the piers, underside, and pedestrian suspension bridge. (BridgeHunter.com, 2017)
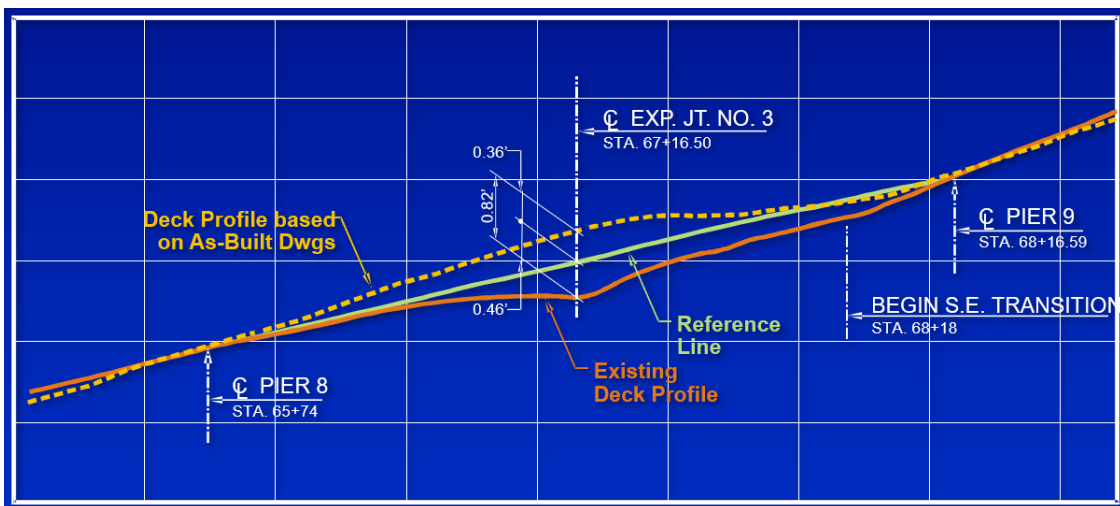
Figure 2-25   Robert E. Lee Memorial Bridge deck profile on the east face of the curb showing the as-built and existing deck profiles relative to the reference line. (Theryo, 2011)

Design practice for long span post-tensioned cantilever (segmentally erected) bridges for which creep is particularly important to correctly assess, is well described in (Takacs, 2002). Discussion of post-tensioned bridge design and creep calculation in USA Bridge Design Practice can be found in (Goodyear & Smith, 1988).

An example of structural failure outside of bridges due in part to excess creep is the collapse of Terminal 2E at Roissy-CDG airport in 2004 (Daou, Salha, Raphael, & Chateauneuf, 2019). The collapse occurred eleven months after its inauguration and caused four casualties. The failure of the terminal was investigated several studies (El Kamari, Raphael, & Chateauneuf, 2015) (Raphael, Faddoul, Feghaly, & Chateauneuf, 2012). A schematic of the terminal is shown in Figure 2-26. Studies indicate that:

- The stresses and efforts calculated in the design phase were inaccurate; the load applied at the ultimate limit state was 4.5 times greater than the maximum permissible load.

- Hasty construction practices lacked appropriate monitoring techniques.

- Long-term concrete creep caused excessive unpredicted deformations that resulted in excessive forces in the struts that led to shear punching in the shell.

- The maximum deflection occurred in the local area where the crash occurred.

- Excessive deformation was a major cause of the structural damage, and thus, led to the terminal failure.
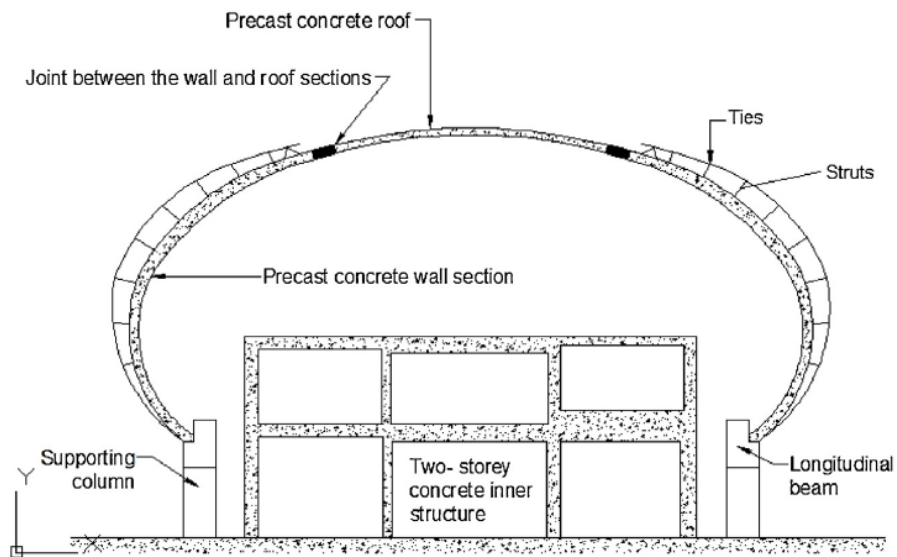
Figure 2-26   Typical section of boarding area of a terminal at Roissy-CDG airport. (Daou, Salha, Raphael, & Chateauneuf, 2019)

2.3.3.2   *Concrete Nuclear Containment Structures*

Concrete nuclear containment structures in the U.S., were initially licensed for 40-year of operating life. However, many NPPs have been granted permission to continue operating to up

to 60 years, and some are expected to request a SLR to continue operations to 80 years. Most pressurized water reactor containment systems use PCCVs (KEPRI, 2000) (Pandey, 1997) (Lundqvist & Nilsson, 2011). As the PCCVs are subject to post-tensioning stresses for their entire operating life cycle (with brief detensioning allowed for inspections or equipment replacement as needed), concrete creep and creep-cracking has been identified as one of the aging effects (US Nuclear Regulatory Commission, 2014). In addition, the interior surface of the PCCVs are subject to elevated temperatures from reactor operations and sometimes external surface may be exposed to hot desert type climate. As discussed in 2.3.2.4, elevated temperatures accelerate creep rates in concrete. While extensive research has been performed to study corrosion effects in PCCVs (US Nuclear Regulatory Commission, 2015) (Dunn, Pulvirenti, & Hiser, 2011) (Petti, et al., 2011) (Pensado, et al., 2013) (US Nuclear Regulatory Commission, 1999) (US Nuclear Regulatory Commission, 2011) (Installations, NPP Containment Prestress Loss Summary Statement, 1999) (Installations, Bonded or Unbonded Technologies for Nuclear Reactor Prestressed Concrete Containments, 2015), little is known about the direct effects of creep in PCCVs.

A delamination failure at Crystal River Nuclear Power Plant in 2009 indicated that creep may be an issue in long-term PCCV operations (US Nuclear Regulatory Commission, 2010). During a planned shutdown and after tendon detensioning, an opening was cut in the PCCV to replace a steam generator. While creating this opening, workers saw that there was a gap, or separation, affecting the outer layer of concrete in the building wall. This gap or separation in concrete is commonly referred to as a delamination. The delamination occurred on the plane formed by the post-tensioning tendon ducts, see Figure 2-27. The delamination occurred in an hourglass shape across the structure as presented in Figure 2-28.This plane is an area where the concrete stress state changes from pure compression to a state involving tension (US Nuclear Regulatory Commission, 2015). The delamination is a source for discontinuities in the cross-section of the PCCV wall, effectively decoupling the in-plane compressive forces from the PT with the interior portions of the wall, thereby allowing for a multitude of problems to occur that could damage and failure to an extent requiring decommissioning of the PCCV. While several issues contributed to the delamination event, the importance of creep could not be determined.

Figure 2-27   Photograph of delamination crack running from horizontal tendon to horizontal tendon, parallel to the wall surface, approximately 10 inches from the exterior surface of the concrete. (US Nuclear Regulatory Commission, 2010)
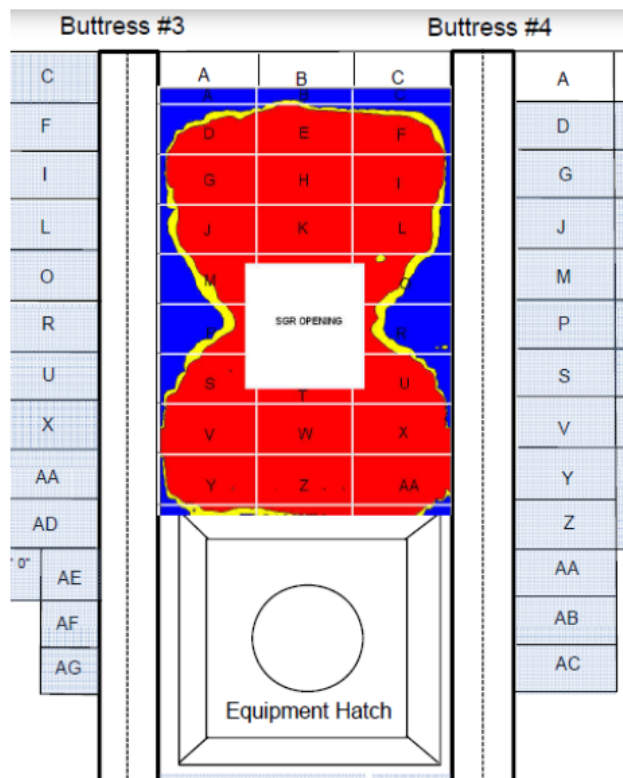
Figure 2-28   Crystal River structure (top) and extent of delamination (bottom). (US Nuclear Regulatory Commission, 2010)

Leak tightness in PCCVs is assured in the United States by using steel liners inside the concrete containment. In a loss-of-coolant accident, prestressing tendons through the concrete theoretically maintain a compressive stress throughout the structure even if the interior is pressurized.

Common practice in the U.S. is to use greased, or sheathed, tendon ducts. The tendon ducts are installed into the structure prior to concrete placement, and then the PT tendons are pulled through the ducts after the concrete hardens. The tendons are greased, tensioned, and locked off. The ducts are filled with grease for corrosion resistance. This method allows the tendons to be individually removed, inspected, and re-tensioned as needed throughout the life of the structure. Another practice in France and some other countries is to grout the tendons into the tendon ducts, filling the ducts with cementitious material. This method more thoroughly protects the tendons from corrosion, but the tendons cannot be re-tensioned if needed. More information can be found in (US Nuclear Regulatory Commission, 2015).

In the past, concrete creep was not given much attention beyond design consideration for loss of prestress associated with uniaxial concrete stress; however, studies show that concrete creep in PCCVs is a complex and important design aspect that can have severe consequences on the structure (Bažant, Carreira, & Walser, Creep and Shrinkage in Reactor Containment Shells, 1975) (Bažant Z. P., Creep and Shrinkage Effects in Nuclear Reactor Containment Shells, 1974). More recent literature confirms that concrete creep is one of the, if not the, biggest time-dependent prestress loss mechanisms (Song, Kim, Byun, & Song, 2002) (Hu & Lin, 2016) (Lundqvist & Nilsson, 2011). Some researchers have found that the creep-prediction equations in AASHTO LRFD, ACI Committee 209, the CEB/FIB-90 model code, and the BP Model all show a general tendency to decrease creep strain according to the loading ages and underestimate the creep of the reactor concrete (Song, Kim, Byun, & Song, 2002). However, other literature suggests that current models can overestimate total losses when concrete creep predictions are combined with concrete shrinkage and tendon relaxation (Lundqvist & Nilsson, 2011).

Concrete in PCCVs is typically in a biaxial or even triaxial stress state, but designers often use data from creep experiments in a uniaxial stress state (Lee, Song, & Han, 2004). According to (Mindess, Young, & Darwin, 2003), the behavior of concrete under multiaxial stress states is still not completely understood. Concrete under hydrostatic pressure, as exemplified in Figure 2-29, has a higher uniaxial compressive strength. Concrete under combined stress states such as compression-compression or compression-tension behaves as shown in Figure 2-30. Concrete under a 2:1 compressive biaxial stress condition has an approximately 30% increase in compressive capacity. Concrete under tension has a reduced compressive capacity; for example, concrete under 50% of its ultimate tensile capacity has approximately 50% reduced compressive capacity. However, if concrete is under biaxial compressive stress, the tensile capacity of the concrete in the third axial stress direction is unknown.
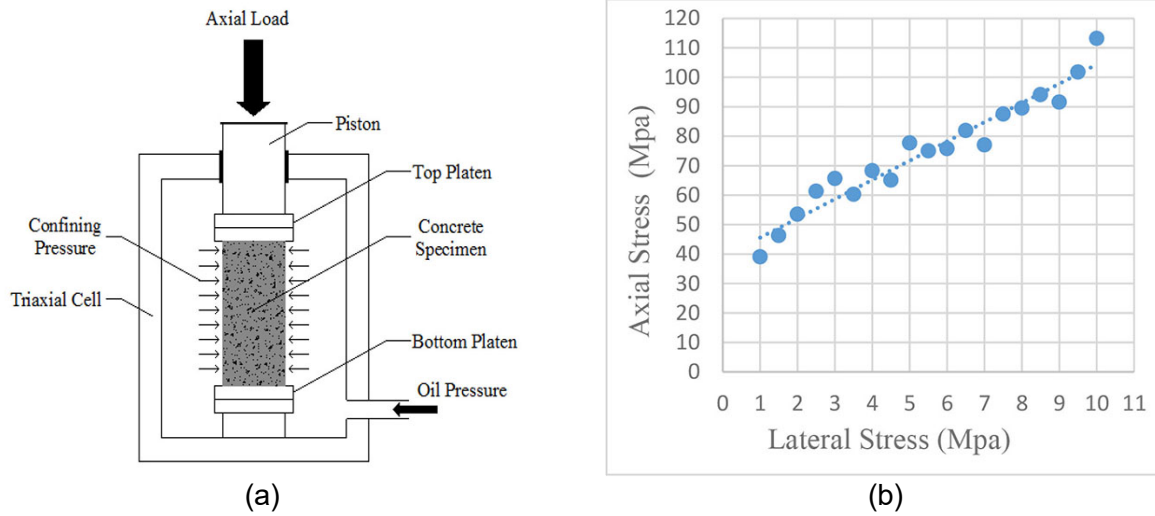
Figure 2-29 **(a) Example concrete cylinder triaxial stress compressive test; (b) Ultimate axial stress vs applied lateral stress. (Javanmardi, 2020)**
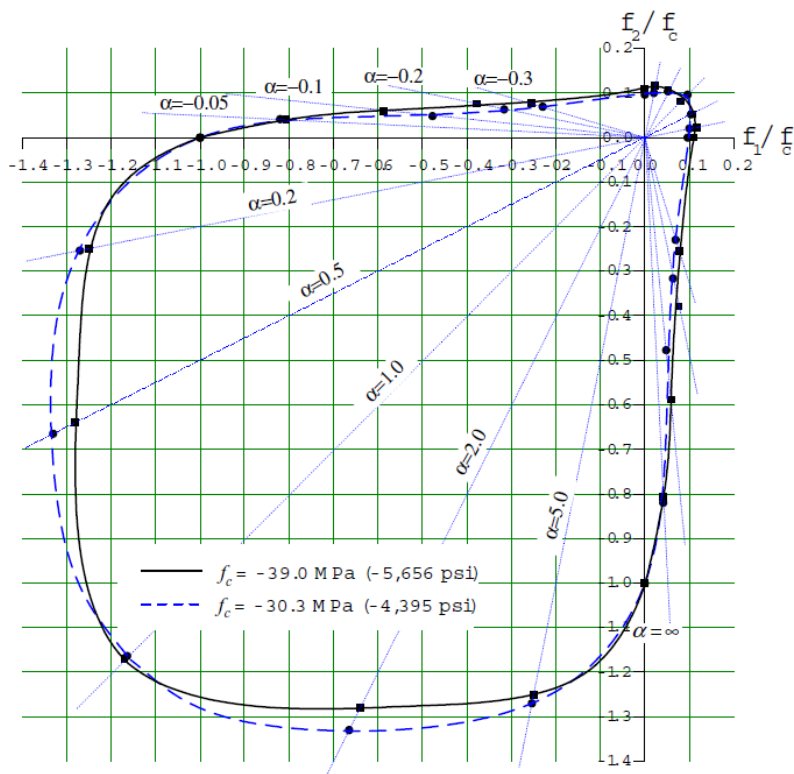
Figure 2-30 **Biaxial strength envelopes for two different types of concrete under biaxial stress. (Lee, Song, & Han, 2004)**

Due to creep and shrinkage of the concrete and the relaxation of the prestressing steel, tendon forces decrease with time. Since the safety of the structure depends on these forces, being able to monitor or at least estimate the prestress losses is of utmost importance. Tendon relaxation can typically be predicted with a good measure of certainty, but concrete creep is much more difficult to predict.

Creep and other concrete degradation mechanisms such as shrinkage or thermal effects are important in the early-age behavior of concrete nuclear containments and for large repairs and modifications. Benboudjema and Torrenti clearly outline cases in which differential strains occur between (1) concrete and reinforcement or (2) older and newer lifts of concrete (Benboudjema & Torrenti, 2008). Concrete lifts in PCCVs are often around 3 m (9.8 ft). Thick layers of an older concrete have different material properties such as strength and stiffness compared to a new layer of concrete. Shrinkage or thermal effects between the layers, with layers having different material properties in early age (within around 10 days), can cause cracks. However, early-age creep strains may relax internal differential stresses. Accounting for early-age creep-age is essential to predict induced stresses if autogenous shrinkage or thermal strains are restrained.

2.3.4   Creep Rupture in Concrete

Concrete creep is a well-defined phenomenon, though it is difficult to predict, and experts are still unsure exactly how concrete creeps. However, creep rupture in concrete is a little-studied field. Experts are not sure if structures subject to PT forces for their entire service lives are susceptible to concrete creep rupture (US Nuclear Regulatory Commission, 2014). It is known that concrete is susceptible to creep rupture, but as mentioned previously in this report, there is no mention of concrete creep rupture in the structural concrete design code in the United States (American Concrete Institute, 2014). The following documents from the American Concrete Institute (ACI) discuss creep and how to predict losses from concrete creep, but none mention creep rupture: Guide for Modeling and Calculating Shrinkage and Creep in Hardened Concrete (American Concrete Institute, 2008), Building Code Requirements for Structural Concrete (American Concrete Institute, 2014), Report on Evaluation and Repair of Existing Nuclear Safety-Related Concrete Structures (American Concrete Institute, 2005), and Code Requirements for Safety-Related Concrete Structures and Commentary (American Concrete Institute, 2013).

Carpinteri et al. (Carpinteri, Valente, Zhou, Ferrara, & Melchiorri, Tensile and flexural creep rupture tests on partially damaged concrete specimens, 1997) performed extensive tensile and flexural creep tests until rupture on partially-damaged unreinforced concrete specimens. As was the case with the creep rupture of metals in sustained loading tests, the creep curves for concrete also display a three-stage process, according to the change of creep rate. Creep rate decreases gradually in the primary stage, is almost constant in the secondary stage, and increases rapidly until failure in the tertiary stage. Figure 2-31 and Figure 2-32 show results of concrete tensile creep tests. The flexural creep tests in the same paper showed similar three-phase creep curve trends (primary, secondary, and tertiary). As the paper also performs tests on partially damaged specimens, one major conclusion is that concrete's capability of resisting creep rupture under sustained loading decreases with increasing damage and decreasing load-carrying capacity. Another document by Carpinteri analyzes concrete flexure creep rupture tests and develops a phenomenological model to predict creep curves as shown in Figure 2-33 (Carpinteri, Valente, & Zhou, Crack Propagation in Concrete Specimens Subjected ot Stustained Loads, 1995).
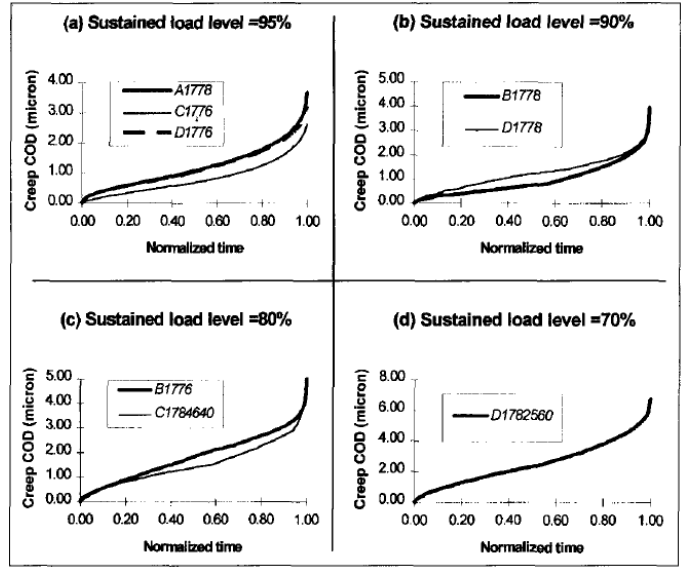
Figure 2-31   Creep curves till rupture in tensile creep tests. (Carpinteri, Valente, Zhou, Ferrara, & Melchiorri, Tensile and flexural creep rupture tests on partially damaged concrete specimens, 1997)
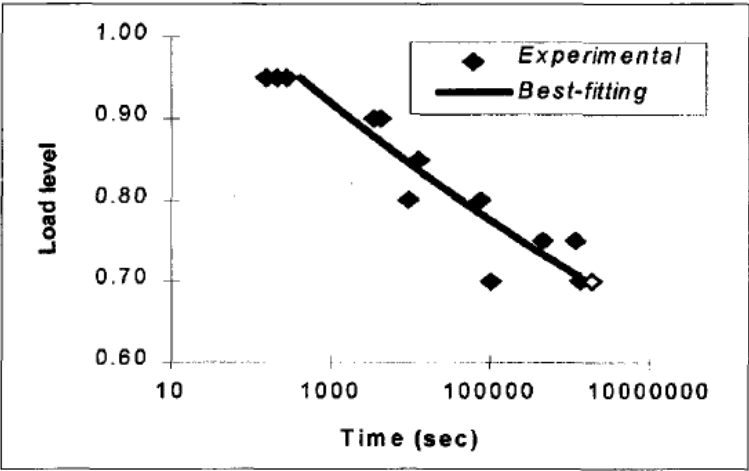
Figure 2-32   Sustained load level versus time to rupture in tensile creep tests. The hollow diamond dot denotes one test that did not reach final creep rupture. (Carpinteri, Valente, Zhou, Ferrara, & Melchiorri, Tensile and flexural creep rupture tests on partially damaged concrete specimens, 1997)
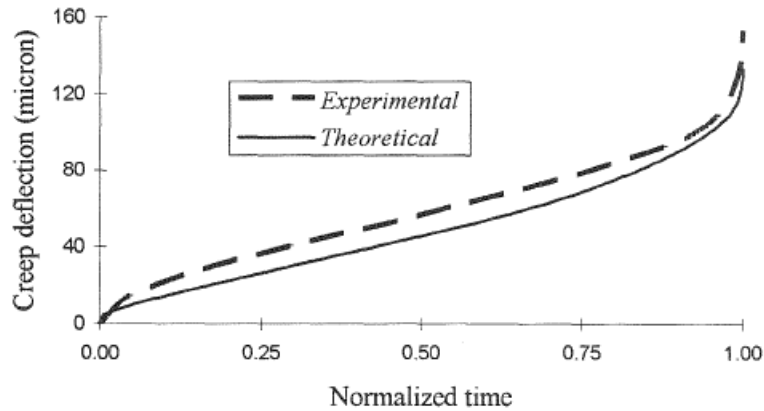
Figure 2-33   Mean experimental and simulated creep curves until rupture for a sustained load level of 80% of peak flexural strength. (Carpinteri, Valente, & Zhou, 1995)

A paper by Mazzotti indicates that short-term uniaxial compression creep tests at low, medium, high, and very high stress levels leads to different material behaviors (Mazzotti & Savoia, 2002). For medium stress levels, creep strains can be much greater than those predicted by linear viscoelasticity; for very high stresses (more than 80-90% of short-term compression strength f'_c), failure is reached by tertiary creep. Poisson's ratio also varies with stress. For low stresses, it is a constant value; for medium to high stress levels, it varies during the loading phase and is almost constant during creep deformation; and very high stress levels cause a significant increase of Poisson's ratio both in the loading and creep phases. Another paper by Mazzotti attempts to develop a model that can cover the whole range of concrete creep from viscoelastic behavior at low stress levels up to tertiary creep and creep rupture at high stress levels as shown in Figure 3-35 (Mazzotti & Savoia, Nonlinear Creep Damage Model for Concrete under Uniaxial Compression, 2003).
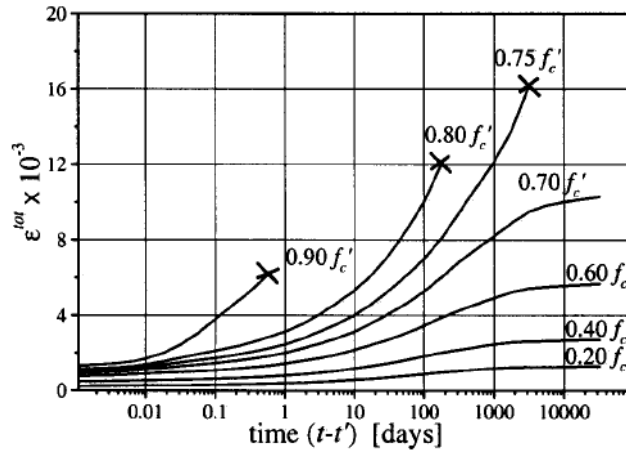
Figure 2-34   Simulation of compression creep tests at different stress levels (7-day age of concrete at loading). Data lines with an "X" at the end denote rupture. (Mazzotti & Savoia, Nonlinear Creep Damage Model for Concrete under Uniaxial Compression, 2003). With permission from ASCE.[5]

Concrete creep rupture is not limited to concrete specimens with no reinforcement. Naguib and Mirmiran have developed a model to predict creep and shrinkage in concrete filled tubes (Naguib & Mirmiran, 2003) (Terrey, Bradford, & Gilbert, 1994). Their study of concrete-filled steel tubes in compression, both if the concrete is bonded (BCFT) or not bonded (unbonded, UCFT) to the steel, found that the concrete in BCFTs and UCFTs are both susceptible to creep rupture at high stress. The authors find that, for the same magnitude of sustained loads, BCFT is much more durable for creep rupture than its equivalent UCFT for diameter/thickness ratios of 40 or less.

A dissertation by Zhou looked at concrete creep rupture in flexure and tension in unreinforced specimens, among other things (Zhou, Time-Dependent Crack Growth and Fracture in Concrete, 1992). Figure 2-35 shows creep rupture results for flexure specimens without or with a notch. The results indicate a log-trend similar to all other creep rupture tests presented in this review. Figure 2-36 shows the familiar three-stage creep rupture data for a notched specimen.
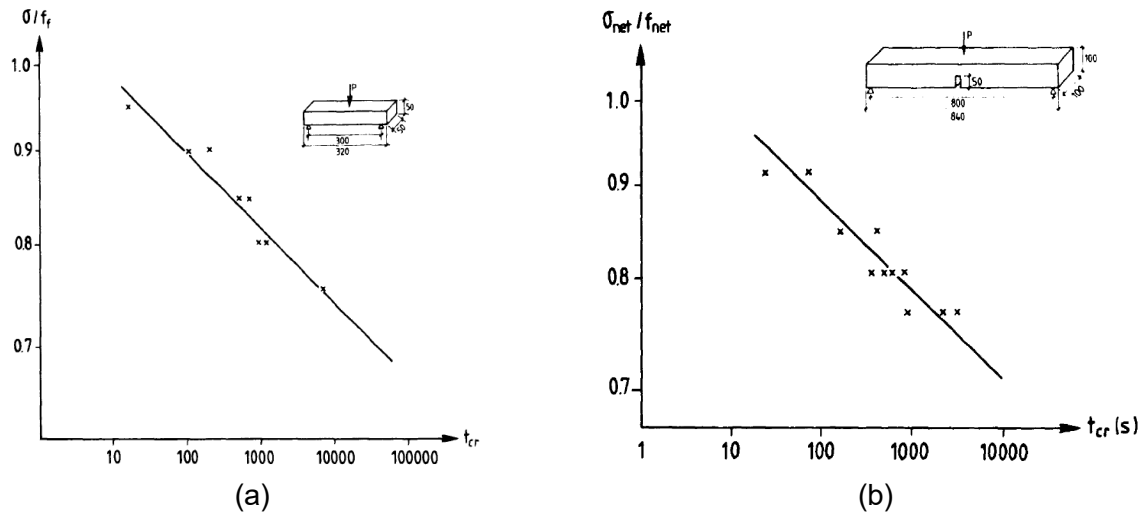
Figure 2-35 Flexure concrete creep rupture applied stress vs time until rupture for (a) unnotched beams and (b) notched beams. (Zhou, Time-Dependent Crack Growth and Fracture in Concrete, 1992)
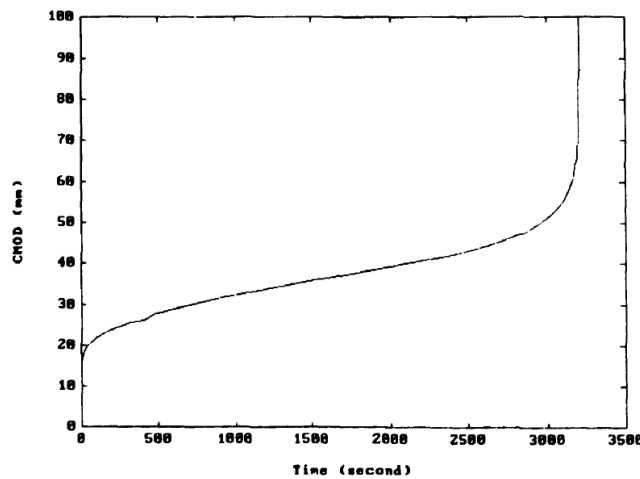
Figure 2-36 Crack mouth opening displacement (CMOD) time until rupture curve under a sustained load. (Zhou, Time-Dependent Crack Growth and Fracture in Concrete, 1992)

For concrete stressed more than 50% of the ultimate strength of the concrete, accumulated creep strain can drive existing microcracks into macrocracks that may in turn lead to failure (Mindess, Young, & Darwin, 2003). Micro-cracks develop due to various material degradation mechanisms, and continuing creep can turn these microcracks into full-fledged cracks over decades of structure service (Illston, 1965). In the anchor zones, this phenomenon is of somewhat less concern for grouted tendons than ungrouted tendons. Typically, in PCCVs, early-age concrete creep is avoided by waiting until the concrete has sufficiently aged before tensioning tendons. (US Nuclear Regulatory Commission, 2015)

To the authors' knowledge, there are no examples of reinforced concrete structures failing specifically from concrete creep rupture. Concrete structure failures that involve creep typically fail from excessive deformations that reorient or redistribute stresses in the structure such that the stresses exceed capacity. However, it is unknown if creep rupture may be involved in said failures. Research has shown (e.g., Figure 2-32, Figure 2-34, and Figure 2-35) that concrete under large sustained stresses can have increased creep rates and significantly shorter times until creep rupture. Thus, structures experiencing excessive deformations and redistributed stresses may demonstrate creep rupture phenomena. Monitoring can provide opportunity to mitigate degradation and potentially prevent failure due to excessive deformations under such conditions. Given the primary, secondary, and tertiary phases of concrete creep rupture, monitoring a structure for increasing creep rate is suggested.

Research summarized in this section indicates that concrete suffers creep rupture primarily when exposed to stresses above 70% of its ultimate uniaxial stress in either tension or compression. ACI 318 limits the maximum concrete compressive stress in flexure specimens immediately after transfer of post-tensioning at 60% of its maximum uniaxial compressive stress f'c (American Concrete Institute, 2014); the compressive stress is expected to reduce with time due to tendon steel relaxation and concrete creep (Nilson, 1987). ACI 318 also limits the maximum concrete tensile stress in flexure specimens immediately after transfer of post-tensioning to $3\sqrt{f_c'}$. Concrete ultimate tensile stress in bending is typically estimated at $7.5\sqrt{f_c'}$ (sometimes referred to as the Modulus of Rupture), so the tensile stress of the concrete is limited in design to ~40% of the ultimate uniaxial tensile stress. It should be noted, however, that in direct tension, many references report the direct uniaxial tensile capacity of concrete is approximately $4\sqrt{f_c'}$. ACI 349 (written for nuclear structures) makes no change to ACI 318 in these respects (American Concrete Institute, 2013). ASME BPVC (ASME, Boiler Pressure Vessel Code Section III, 2019) Div. 2 Figure CC-3421-1 limits primary membrane stresses and primary membrane plus bending stresses to $0.60f_c'$ and $0.75f_c'$, respectively. Additionally, primary plus secondary stresses in the membrane and membrane stresses plus bending are limited to $0.75f_c'$ and $0.85f_c'$, respectively.

If continuing concrete creep from a sustained load causes excessive deformations, the maximum stress (that could cause onset of tertiary creep) may be exceeded in either compression or tension.

2.3.5   Concrete Creep Rupture Conclusions

The objectives of this section were to provide an overview on general material creep, general material creep rupture, creep in concrete structures, and creep rupture in concrete. Section 2.3.2 reviews creep behavior in metals including the three phases of general material creep and stress and temperature effects. Section 2.3.2 also reviews general creep behavior in concrete.

Section 2.3.3 provides examples of unexpectedly high amounts of creep in post-tensioned concrete structures. A growing database of creep in post-tensioned concrete bridges shows that many bridges experience more creep in late service life (25+ years of operation) than was predicted by designers. Some structures fail from excessive deflections that result in unplanned stress distributions, excessive strains, loss of post-tensioning stress, and excessive cracking. Excessive creep can often be seen visually or by instrumented monitoring in bridges and massive structures. Section 2.3.3 also discusses how creep in concrete nuclear containment structures is a major concern for regulators as the structures are continuing to operate beyond

their design life. Research on the effects of creep in PCCVs is critical to extending the operation of the U.S. NPP infrastructure.

Section 2.3.4 demonstrates that concrete creep rupture is a little-studied field. Design practices limit the stresses in concrete to below stresses required for concrete rupture. Tertiary creep and creep rupture will not occur if the concrete stress remains below a specific threshold. However, if continuing concrete creep causes excessive deformations, the threshold stress may be exceeded. Concrete creep rupture is significantly more probable at stresses above 70%, and almost guaranteed at stresses above 75%, of ultimate uniaxial capacity in either compression or tension.

To the author's knowledge, temperature effects on concrete creep rupture have not been studied. Little data, if any, exists analyzing concrete creep rupture at elevated temperatures. However, Section 2.3.2.4 indicates that concrete creep at temperatures above 100°C (212°F) increases with increasing temperature, up to a factor of ~5 at 800°C (1472°F). Concrete creep at temperatures between normal temperature and pressure (NTP) and 100°C can increase by a factor of up to ~2.5.

2.4   Other Prominent Failure Modes of PCCVs

The Crystal River 3 (CR3) delamination event in October 2009, as described in (US Nuclear Regulatory Commission, 2010), included a list of seventy-five (75) PCCV failure modes that were investigated to identify the cause of failure. 'Failure modes' is defined as a mode of performance loss that could contribute to structural functional failure. SNL published a report that analyzes each of the PCCV failure modes listed for applicability to PCCVs beyond the age of 40 years (Hogancamp, Flores, James, Dameron, & Jones, 2019). The main conclusions from the SNL report are included herein.

The failure modes discussed in this section are related to issues that affect strength or integrity of the concrete, particularly in tension. For aging large civil infrastructure facilities, degradations are often coexistent, sometimes linked, and are cumulative. Looking at concrete, some failure modes contribute to demand (i.e., increased tensile stress), and others contribute to diminished capacity (e.g., age and wear-and-tear created microcracking). Combinations of failure modes will typically result in exaggerated damage and earlier performance loss; however, a very few combinations of failure modes can result in a net zero change in functional capacity. For example, tendon over-tensioning can cause high localized stresses, but concrete creep over time can redistribute the high localized stresses to the surrounding area and lower the stresses to a manageable level.

An important note in this section is that the list of failure modes from CR3 does not include liner failure. Many PCCVs around the world, including all in the United States, require a steel air-tight liner on the inside of the PCCV that doubles as the inner formwork of the structure. The list of 75 failure modes from CR3 does not include liner failure since the concrete delamination event would not be directly associated with a liner degradation mechanism. However, under slow pressurization the following event path can lead to functional failure of concrete containments with a steel liner:

- Increased deformation associated with overstress or damage to a strength element of the containment wall;
- Excess straining of the liner in the region of the increased deformation;

- Through-wall cracking of the concrete;

- Local tearing of the liner and thus leakage through the liner and concrete.

The failure mode most prominently analyzed in this report is described in Section 2.1 (e.g., Figure 2-1). The hoop tendons create a radial tensile zone in the containment, and the delamination layer in the concrete at CR3 occurred directly along this zone. The risk from the tensile zone, particularly in containments with no radial reinforcement, can be exacerbated in the presence of other aging effects in the wall, such as AAR or delayed ettringite formation. AAR and delayed ettringite formation cause swelling of the concrete and create internal tensile stresses. If one of these degradation mechanisms (or both) are active in the containment wall, their development of internal tensile stresses will combine with the radial tensile zone created by the hoop tendons to potentially cause a delamination event. Section 3.5 discusses the effects of local defects (e.g., a small crack or void) on cascading delamination events in a PCCV.

Modification or cutting of a PCCV structure may lead to unintended damage to the containment. All portions of the entire process incur risk—including de-tensioning tendons, the modifications, possible repairs, and tendon re-tensioning. Placing new concrete in contact with old concrete is worth noting as such a difference in contiguous/adjacent materials is a structural discontinuity and provides opportunities for stress concentrations, irregularities, and/or localized failure mechanisms. Any major modification is cause for some concern of long-term performance, and thus assessments are needed to ensure that the PCCV has either returned to a state compatible with the original design and/or is capable of operating within the applicable codes and regulatory limits for the extended operation timeline under consideration.

Regarding monitoring and analysis, aging PCCVs are subject to failure modes that require time to develop (e.g., alkali aggregate reactions, sulfate attack, thermal fatigue, other forms of corrosion, etc). Many degradation modes can be detected via visual inspection if the degradation is progressing to a point where it needs repair. An adequate monitoring/maintenance system does not in itself guarantee that all problems will be detected in advance of any failure(s). However, inadequate monitoring and maintenance would more likely fail to detect damage progression that could otherwise have been mitigated, if not avoided all together.

In every instance that a monitoring and inspection program detects a potential issue, the PCCV should be analyzed by an expert to determine the severity of the situation.

2.5 PCCV Degradation Modes Conclusions

- The effects of concrete creep and particularly concrete creep rupture on aging PCCVs have been little studied before this report. This report presents a thorough review of concrete creep, concrete creep rupture, and case summaries of post-tensioned concrete structures that have suffered from concrete creep effects.

- Post-tensioned concrete structures are susceptible to creep effects that may not have been adequately predicted during design.

- Design practices attempt to limit the stresses in concrete to stresses below what required for the occurrence of concrete rupture. Tertiary creep and creep rupture will not occur if the concrete stress remains below a specific threshold. However, if continuing concrete creep or other mechanism cause excessive deformations, the threshold stress in either

compression or tension may be exceeded. Concrete creep rupture is more probable at 70%, and significantly more probable at stresses above 75% of ultimate uniaxial capacity in either compression or tension.

- As of this publication, there is little research or literature on temperature effects on concrete creep rupture.

- The ASME BPVC Section III Division 2 (ASME, Boiler Pressure Vessel Code Section III, 2019) prohibits the reliance on concrete tensile strength to resist the external loads and moments or the forces and moments resulting from internal self-constraint. However, no radial reinforcement was required in the PCCV wall prior to 2019, leaving the concrete unreinforced in an area subject to tensile stresses.

- PCCVs are subject to many degradation mechanisms ranging from individual material phenomena to system-wide issues. Every instance of a potential issue in a PCCV should be analyzed by an expert to determine the severity of the situation.

- Liner is not a structural element, but excessive liner deformation may be an indication of issues related to containment structure.

3 SIMULATIONS AND ANALYSES

As mentioned in Section 1.2 , the purpose of the research documented in this report was to study the effect of creep, creep-fracture, and other aging related concrete phenomena on the structural integrity of PCCVs. Particularly, the tensile creep strain immediately on the outside of the hoop tendons as described in Figure 2-1 was to be evaluated. Performing finite element (FE) analyses on PCCV structural models requires detailed material information, especially for the concrete. Therefore, NRC and SNL participated in an international PCCV experimental project sponsored by Électricité de France under the OECD/CSNI IAGE. The project provided participants with detailed experimental material information as well as PCCV structural monitoring data.

Sections 3.1 to 3.4 describe the PCCV experiment, SNL's simulation, comparisons of SNL's simulation results with experimental data, analyses by Moffatt & Nichol, and an analysis of a thin-slice representative volume of a PCCV with finer discretization for additional insights. Section 3.5 summarizes the limited scope analyses performed by Structural Integrity Associates (SIA) and Structural Solutions Consulting (SSC) to examine the issue of creep in PCCVs in relation to the development of tensile strains adjacent to the outside of the hoop tendons and their potential to initiate delamination. These analyses used a finite element model based on the Crystal River Unit 3 PCCV and examined effects of de-tensioning of tendons associated with the cutting of a containment wall for steam generator replacement. Appendix C includes the SIA and SSC analyses.

3.1   VeRCoRs Description

The VeRCoRs project, properly titled Vérification Réaliste du Confinement des Réacteurs, was sponsored by Électricité de France (EDF). As part of EDF's continuous effort on the safety and life extension of its NPP infrastructure, an experimental mock-up of a reactor containment building at 1/3 scale was built at the "Les Renardières" EDF Laboratory near Paris, France. The mockup shown in Figure 3-1 was finely instrumented and its behavior has been monitored from the beginning of construction. More than 700 sensors and 2 km of optic fiber cables were embedded in the concrete. Several measurements are collected every day on each sensor. Hundreds of samples of concrete have been prepared and tested to determine their material behaviors and properties, including, but not limited to, hydration, strength, fracture energy and elastic properties, drying, shrinkage (autogenous and drying), creep (basic and drying), and permeability. The VeRCoRs structure includes an outer containment structure to protect the interior from the environment and an inner PCCV 1/3 scale experimental mockup.
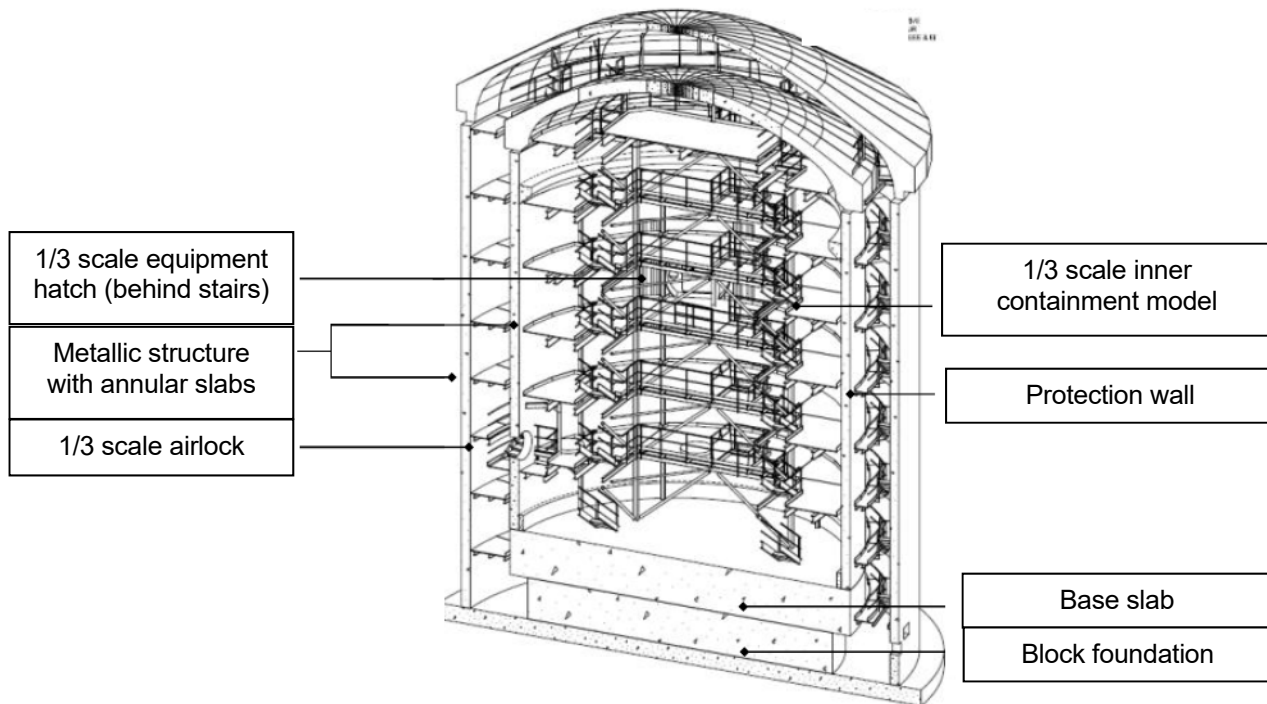
Figure 3-1   VeRCoRs mockup structure. In this image, the equipment hatch is located behind the interior stairs. (Corbin, 2018)

The main objectives of the project were to study the following:

- The behavior of the mockup at early age.

- The evolution of the leak tightness under the effect of aging (drying effects are about 9 times faster on the mock up because of scale effects); This mockup is designed such that one year of aging in the mockup is equivalent to nine years of aging in a full-scale PCCV. The 1:9 time scale is a result of the rate at which drying occurs. Drying in concrete walls is directly proportional to the wall thickness squared; hence, reducing the size of the containment by a factor of 3 increases the rate of drying by a factor of $3^2=9$. The increased drying rate increases cracking and creep in the containment.

- The behavior under severe accident conditions for which the thermo-mechanical loading is maintained for several days.

The experimental campaign consisted of a daily measurement of all sensors and of a periodic air pressure test of the mockup. During this test, the containment was pressurized to 5.2 bar absolute (4.2 bar relative to standard atmospheric pressure). The containment was pressurized at 200 mbar/h, and a plateau at 5.2 bar absolute was held for 12 hours before deflation at 150 millibar/hour. All sensors were interrogated every 30 minutes and the leakage was measured. The design pressure of the containment vessel is 5.2 bar absolute.

A schematic of the VeRCoRs mockup is shown in Figure 3-2, Figure 3-3, and Figure 3-4. The PCCV was constructed as a monolithic structure in concrete lifts with rebar spanning all lifts.

The slab was continuous with the pedestal. Rebars spanned all lift junctions, and there were no expansion joints. Areas of primary interest were labeled as the dome, the wall, the equipment hatch area, and the gusset. General dimensions and information are as follows:

- Height including dome and base mat: 22.30 m

- Inner radius: 7.30 m

- External radius: 7.70 m

- Inner volume: 3161 m^3

- Inner surface area: 1026 m^2

- Concrete volume: 463 m^3

- Cylinder wall thickness (standard section): 0.40 m

- Base mat thickness (standard section): 1.50 m

- Dome thickness (standard section): 0.30 m

- Annular space between the inner and outer containments: 1.80 m

- Four penetrations with diameters of 0.36 m, 0.5 m, 1.209 m, and 2.643 m (equipment hatch).

- Two buttresses at 180°.
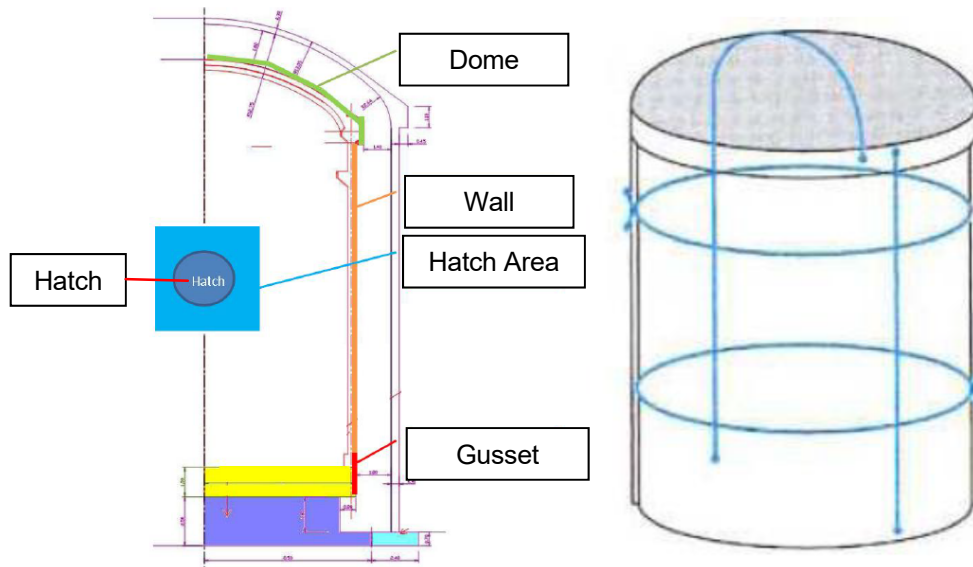
Figure 3-2 **(Left) VeRCoRs outline showing primary areas of focus; and (Right) post-tensioning tendon schematic. Dimensions are listed prior to the figure. (Corbin, 2018)**
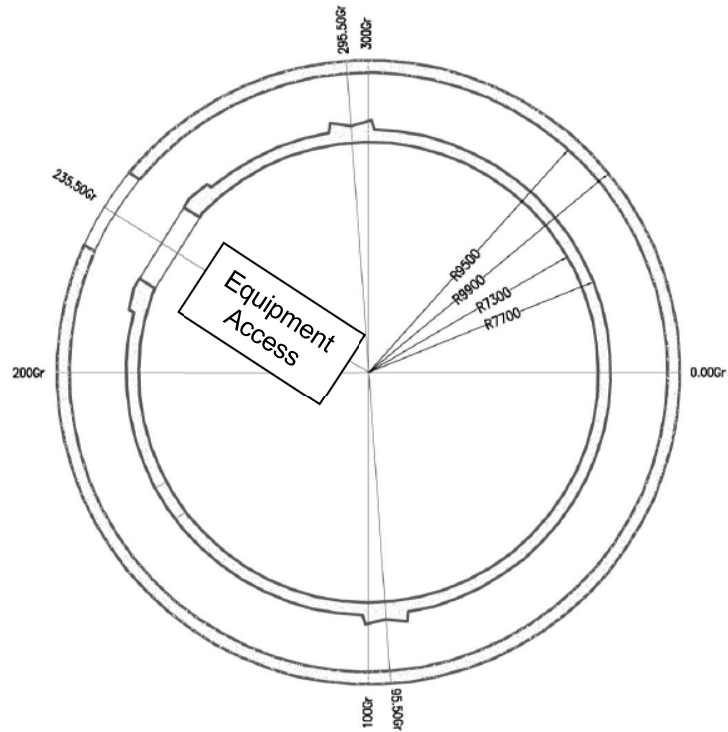
Figure 3-3   Plan view at level 8.72 m and showing a schematic of the inner and outer containment walls as well as the equipment access openings. (Électricité de France, 2018)
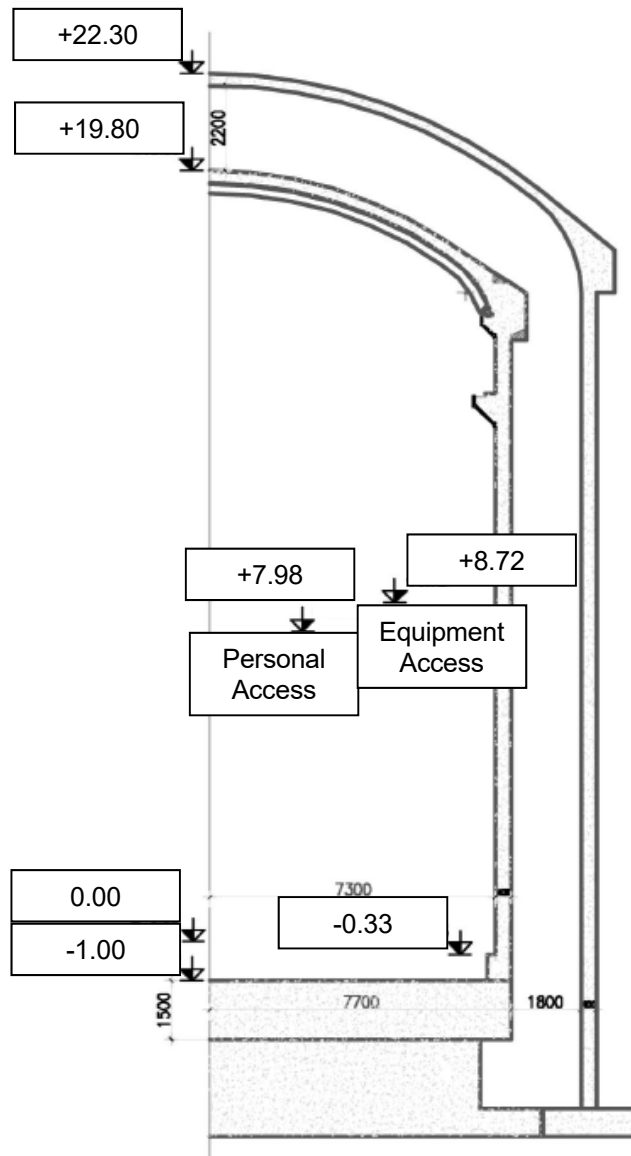
Figure 3-4   Side cut profile of the VeRCoRs mockup showing both inner and outer containments. (Électricité de France, 2018)

The primary dates for VeRCoRs activities are listed in Table 3-1.

Table 3-1   Primary dates for VeRCoRs activities. Times are listed as 24-hour clock system.

Raft concreting	24 July 2014		
End of construction	06 May 2015		
End of prestressing	17 August 2015		
Reference date for strains ($\varepsilon = 0$)	02 November 2015		
	0 bar	4.2 bar (relative)	0 bar
1st Pressure test 'Pre-op'	04 November 2015 06:05	05 November 2015 01:15	06 November 2015 10:31
2nd Pressure test 'VC1'	25 January 2016 16:01	26 January 2016 19:35	29 January 2016 12:11
Start of ambient air heating	12 April 2016		
3rd Pressure test 'VD1'	14 March 2017 06:35	15 March 2017 09:05	21 March 2017 07:06
4th Pressure test 'VD1 bis'	21 Marth 2017 07:06	22 March 2017 09:06	23 March 17 22:05
5th Pressure test 'VD2'	02 April 2018 07:00	03 April 2018 09:00	Not given

The following pages describe the monitoring system and layout of the VeRCoRs mockup. The strain gages used to measure strains in the concrete were SG1 extensometer gauges manufactured by Geo Instrumentation. The gages were embedded in the concrete. In general, strain gages are named following the examples in Table 3-2. Each gage includes a local gage name, a local gage location (e.g., near the interior or exterior surface of the concrete), and a local gage measuring direction (e.g., the gage is measuring vertical or tangential strains). In this report, "tangential" strains are the same as "hoop" strains. Strain gages located in the center of the mockup, e.g., C95R, C195R, I94EM, I194EM, (in Table 3-4) measure in two directions separated by 90° (or 100 Gr).

Table 3-2   Examples of strain gage names in the cylinder wall or the dome.

Full Gage Name	Local Gage Name	Local Gage Location	Local Gage Measuring Direction
P2IV	P2	I: internal	V: vertical
P1ET	P1	E: external	T: tangential*
J2IT	J2	I: internal	T: tangential*
H5EV	H5	E: external	V: vertical
J2EM:	J2	E: external	M: meridional

*In the cylinder wall, tangential strains are equivalent to hoop strains.

The air conditions were controlled and monitored inside the mockup, both inside the experimental containment vessel and in the annular space between the experimental containment vessel and

its protective structure. Relative humidity (RH) was intended to be measured throughout the experiment. The RH measurements are particularly important due to the significant effect of concrete drying shrinkage on the experiment. In actual PCCVs, the annular space is held at a low vacuum and is effectively at a constant 0% RH. The temperature was measured using 30 PT100 class A thermometers. Four plumb lines were included in the instrumentation program, each on its own vertical line and each with three tables at different heights measuring horizontal deflection of the PCCV walls.
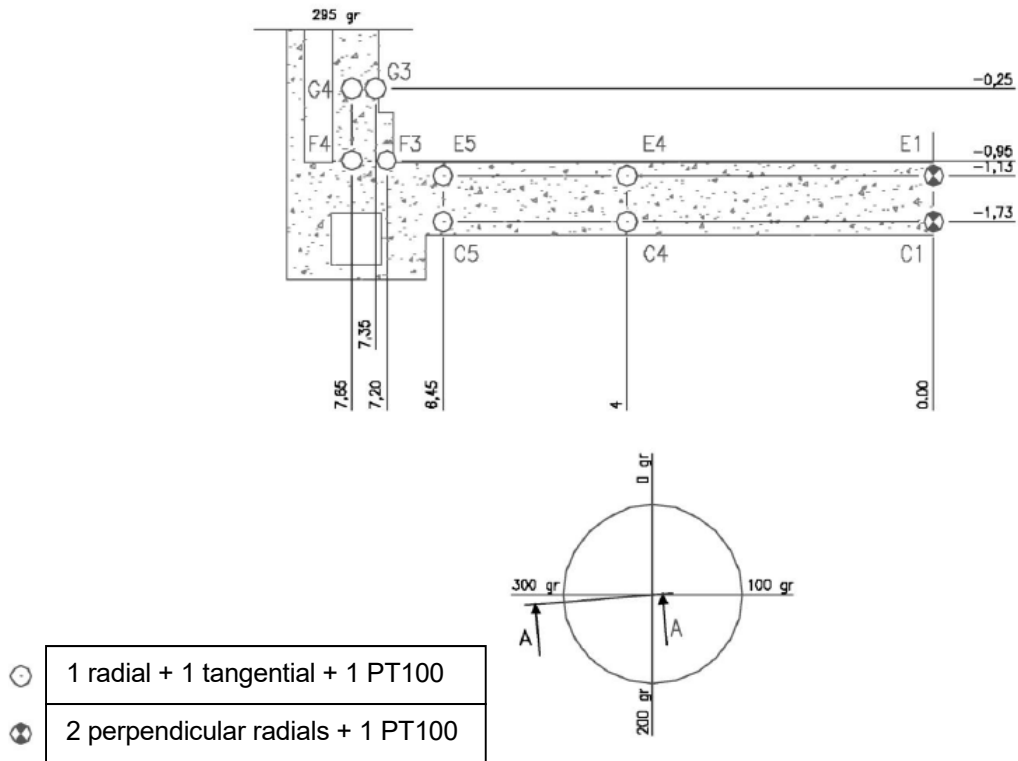
Figure 3-5   **Strain gauges and thermometers in the base slab. The shape of the base slab is given as an indication. There is no gallery in the base slab of the mockup. Please see Figure 3-4 for the real shape of the base slab. (Électricité de France, 2018)**
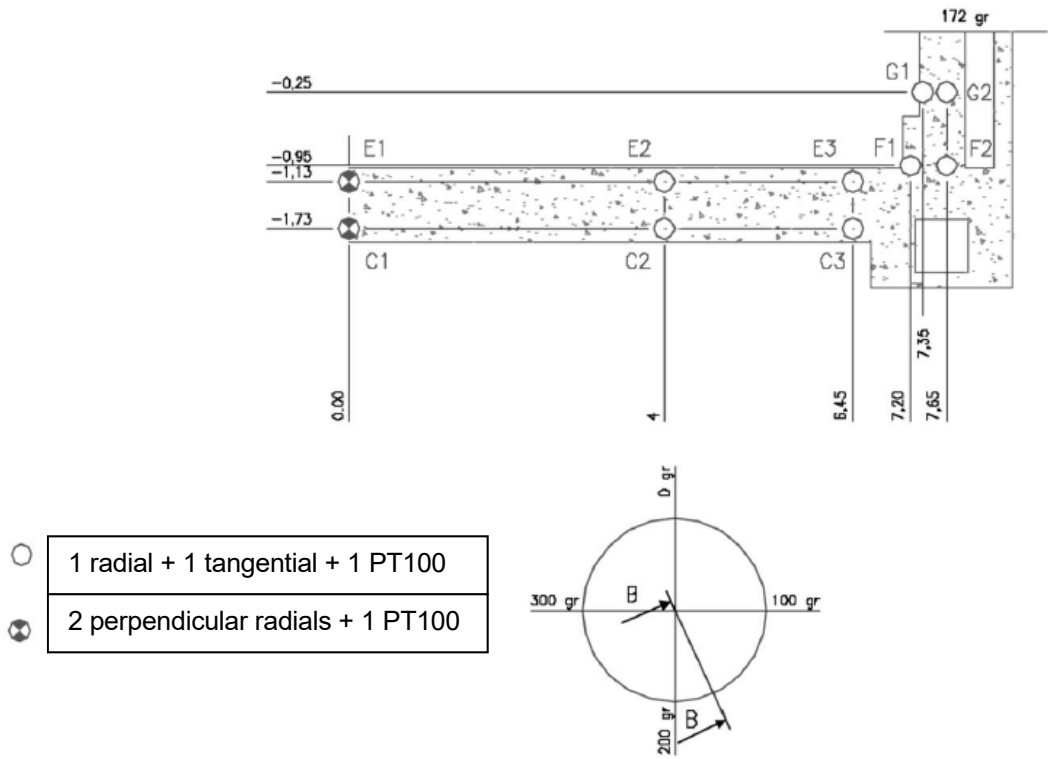
Figure 3-6   Strain gauges and thermometers in the base slab. The shape of the base slab is given as an indication. There is no gallery in the base slab of the mockup. Please see Figure 3-4 for the real shape of the base slab. (Électricité de France, 2018)
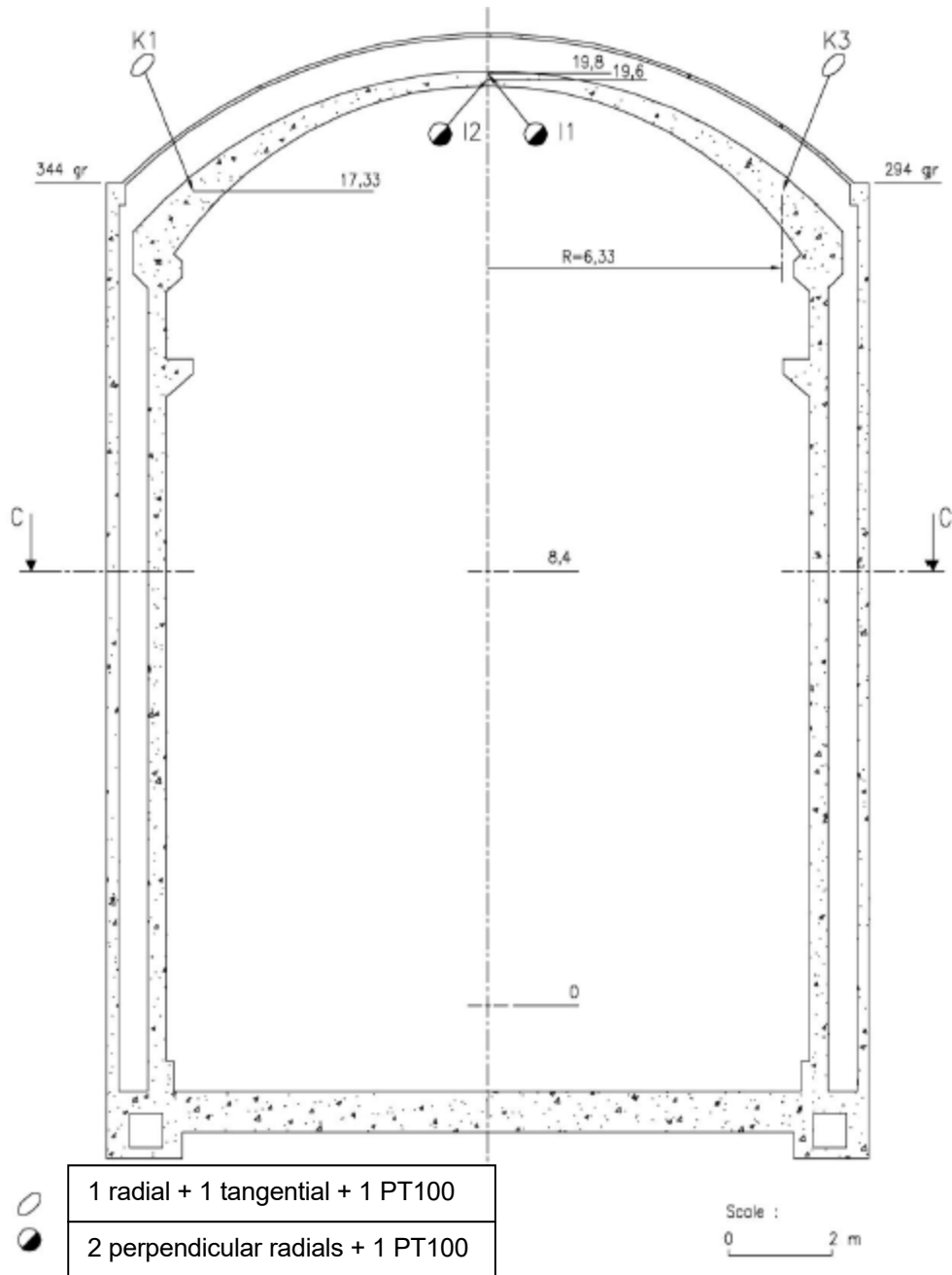
Figure 3-7 **Strain gages and thermometers in the cylindrical part and dome. The shape of the base slab is given as an indication. There is no gallery in the base slab of the mockup. Please see Figure 3-4 for the real shape of the base slab. (Électricité de France, 2018)**
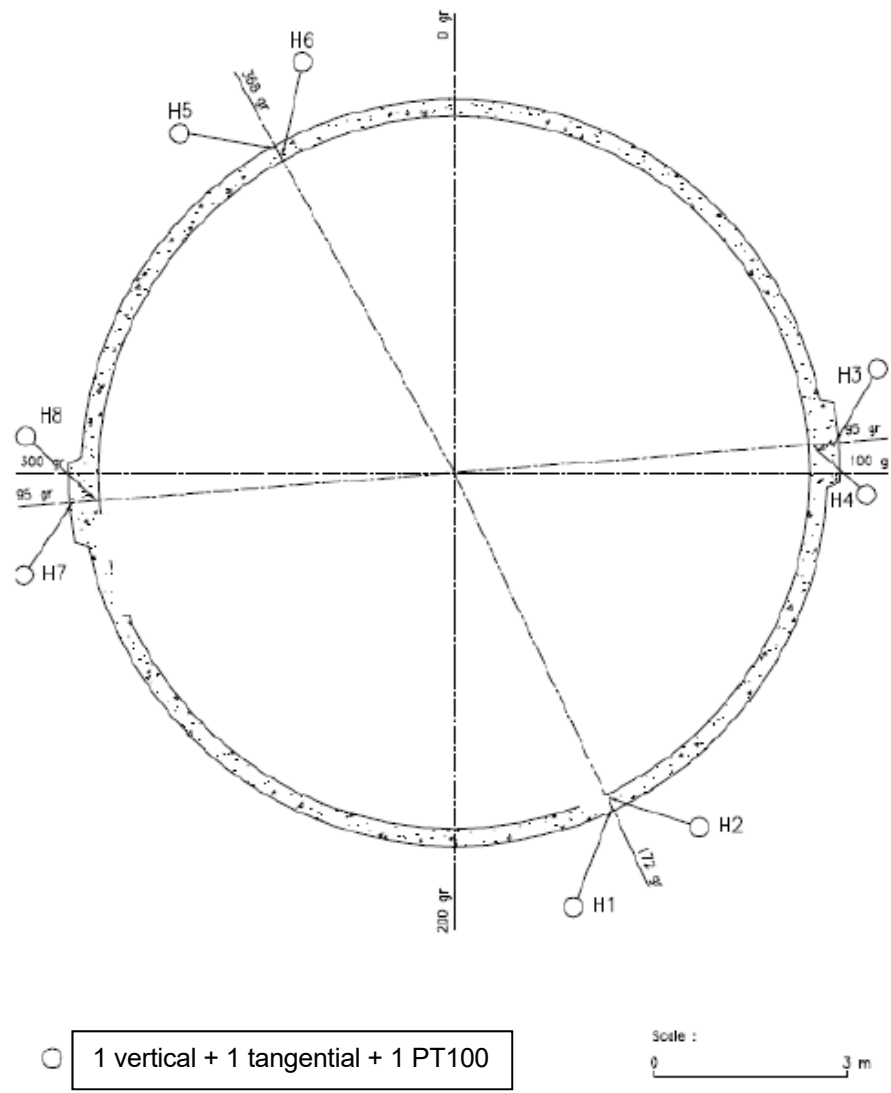
Figure 3-8 **Strain gages and thermometers at Section CC as described in Figure 3-7. (Électricité de France, 2018)**
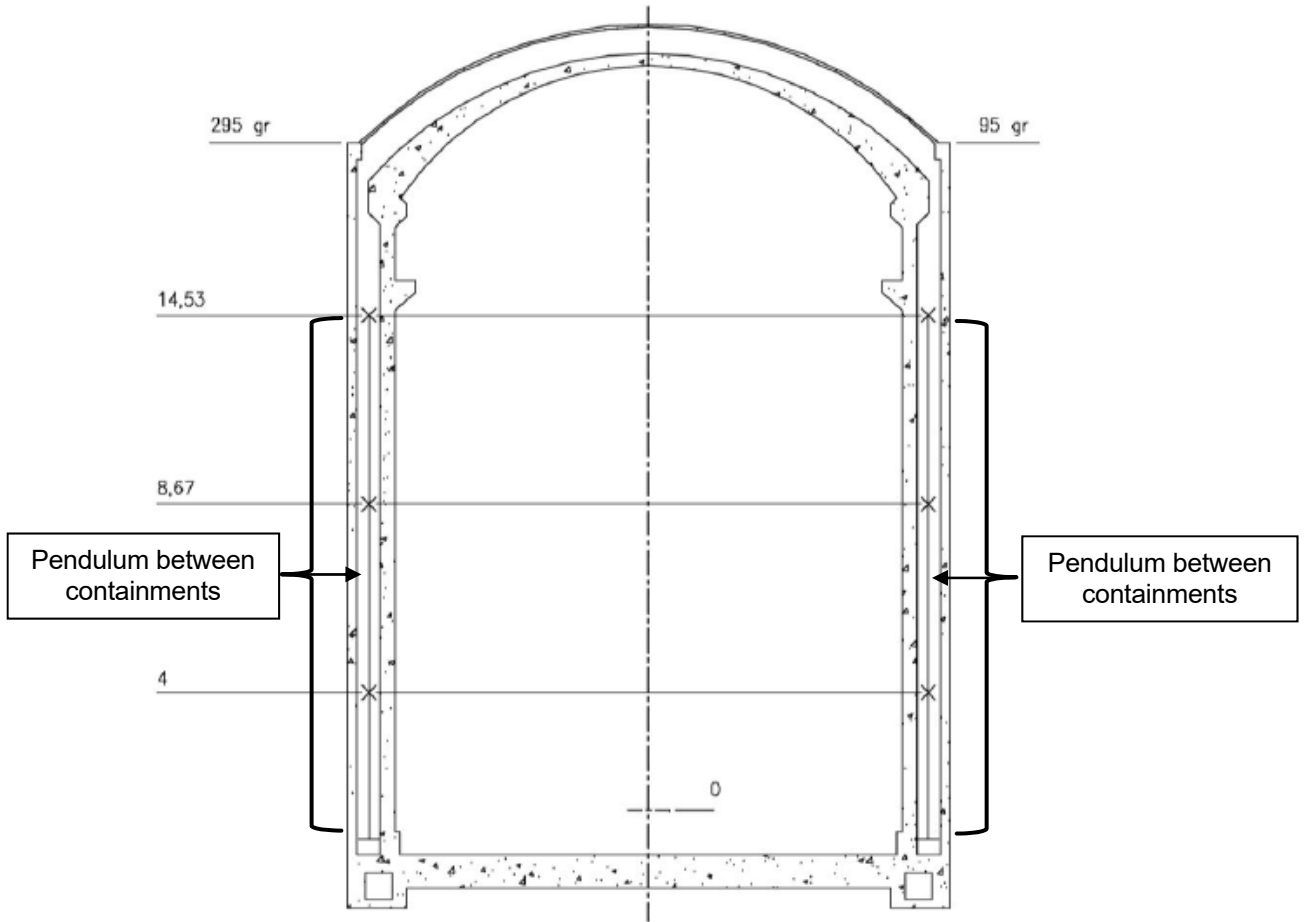
Figure 3-9 **Pendulums and Invar wires located between the inner and outer containments. The top of the pendulum is at 14.53 m. See Table 3-3 for more information. The shape of the base slab is given as an indication. There is no gallery in the base slab of the mockup. Please see Figure 3-4 for the real shape of the base slab. (Électricité de France, 2018)**

Table 3-3   Pendulum and Invar Wire Information (See Figure 3-9 for more information).

Types	Lines (gradians)	Measure's Level (m)
Invar wire		14.53
Pendulums	95	14.53
		8.86
		4
Invar wire		14.53
Pendulums	170	14.53
		8.67
		4
Invar wire		14.53
Pendulums	295	14.53
		8.67
		4

Types	Lines (gradians)	Measure's Level (m)
Invar wire		14.53
Pendulums	370	14.53
		8.67
		4

Table 3-4   VeRCoRs strain gage location descriptions.

Zone	Strain gauge	Radius (m)	Height (m)	Angle (gr)	Direction
Raft	C1_CENTRE_95_R (C95R)	0	-1.73	95.0	Radial
	C1_CENTRE_195_R (C195R)	0		195.0	Radial
	E1_CENTRE_95_R (E95R)	0	-1.15	95.0	Radial
	E1_CENTRE_195_R (E195R)	0		195.0	Radial
Gusset	F1IV	7.24	-0.88	172.0	Vertical
	FIIT	7.24		172.0	Tangential
	F2EV	7.58	-0.90	172.3	Vertical
	F2ET	7.58		172.3	Tangential
	G1IV	7.40	-0.25	172.2	Vertical
	G1IT	7.40		172.2	Tangential
	G2EV	7.61	-0.25	172.3	Vertical
	G2ET	7.61		172.3	Tangential
Cylindrical part (mid-height)	P1EV	7.65	8.01	389.3	Vertical
	P1ET	7.65		389.3	Tangential
	P2IV	7.31	8.01	387.8	Vertical
	P2IT	7.31		387.8	Tangential
	H1EV	7.58	8.43	172.0	Vertical
	H1ET	7.58		172.0	Tangential
	H2IV	7.42	8.43	172.0	Vertical
	H2IT	7.42		172.0	Tangential
	H5EV	7.65	8.00	369.0	Vertical
	H5ET	7.65		369.0	Tangential
	H6IV	7.40	7.99	367.7	Vertical
	H6IT	7.40		367.7	Tangential
Equipment hatch	M3EV	7.75	8.70	222.0	Vertical
	M3ET	7.75		222.0	Tangential
	M4IV	7.39	8.69	222.2	Vertical
	M4IT	7.39		222.2	Tangential
	M7EV	7.63	10.40	232.1	Vertical
	M7ET	7.63		232.1	Tangential

	M8IV	7.38	10.40	232.1	Vertical
	M8IT	7.38		232.1	Tangential
DOME	I1_194_EM (I194EM)	0	19.75	194	Radial
	I1_94_EM (I94EM)	0		94	Radial
	I2_194_IM (I194IM)	0	19.60	194	Radial
	I2_94_IM (I94IM)	0		94	Radial
	J1EM	5.93	17.80	344	Meridian
	J1ET	5.93		344.0	Tangential
	J2IM	6.00	17.73	344	Meridian
	J2IT	6.00		344.0	Tangential
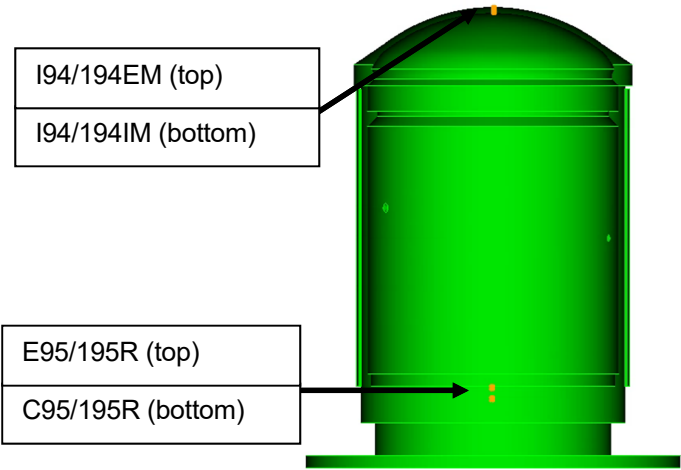
Figure 3-10   Strain gages C95/195R, E95/195R, I94/194EM, and I94/194IM.
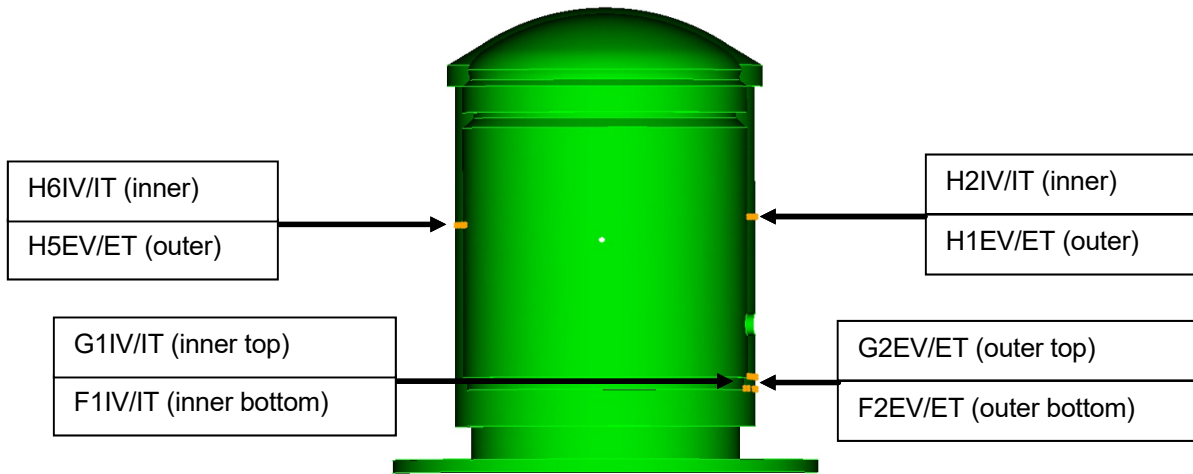
Figure 3-11   Strain gages F1IV/IT, F2EV/ET, G1IV/IT, G2EV/ET, H1EV/ET, H2IV/IT, H5EV/E, and H6IV/IT.
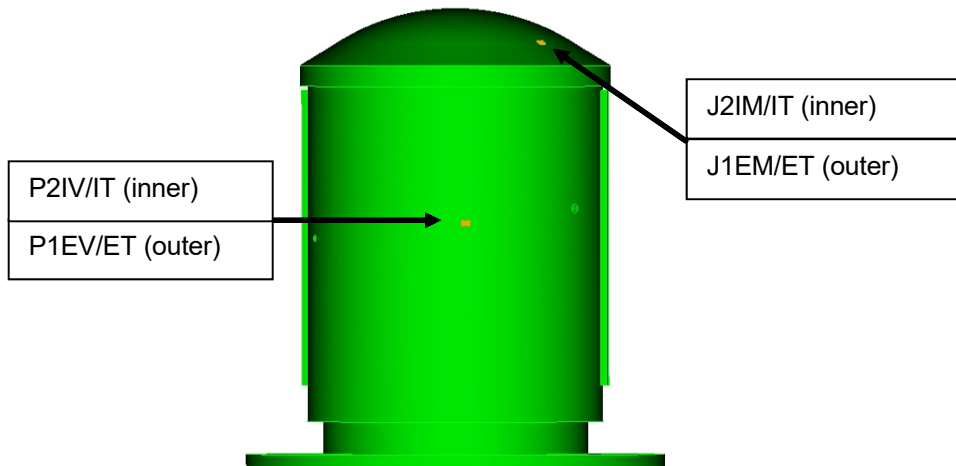
Figure 3-12   Strain gages P1EV/ET, P2IV/IT, J1EM/ET, and J2IM/IT.
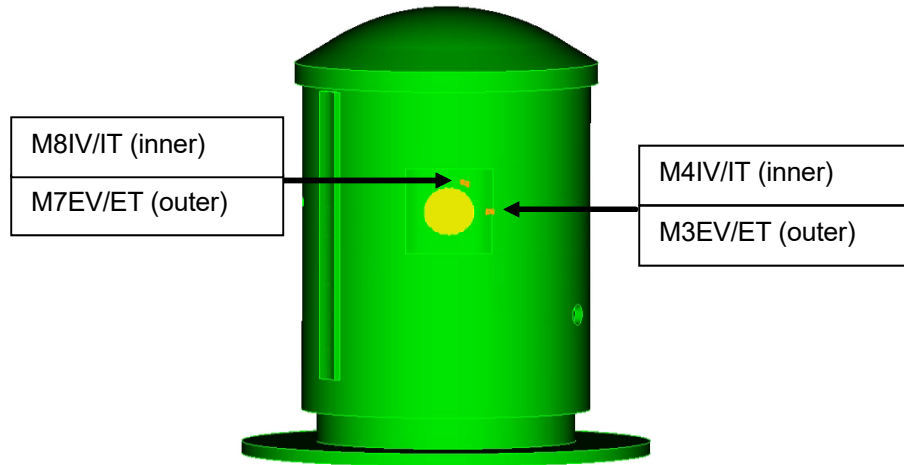
Figure 3-13   Strain gages M3EV/ET, M4IV/IT, M7IV/IT, and M8IV/IT.

3.2   SNL VeRCoRs Simulation

This section describes the VeRCoRs simulation created by SNL and its results compared to experimental data from EDF.

3.2.1   Geometry and Mesh

A 3D computer animated design geometry of VeRCoRs PCCV, including the concrete and PT tendons, was given to VeRCoRs participants. The FE meshes of the concrete and the PT tendons were developed by SNL. The rebar geometry and mesh were developed by SNL with reference to the VeRCoRs design drawings. The following sections detail the specifics of the FE mesh.

The geometry and mesh were modeled with Cubit 15.5. The FE analysis simulation was performed using ABAQUS 2019.

3.2.1.1   Concrete Containment Vessel

The concrete containment vessel (CV) geometry with a 'coarse' mesh is shown in Figure 3-14 and Figure 3-15. The CV was modeled using 8-noded hexahedral elements throughout. The 'coarse' CV mesh included 138,384 elements with element edge lengths varying from ~0.09 m to ~0.41 m. The 'coarse' CV mesh included 3 elements through the thickness of the cylinder wall and the dome. The 'fine' cv mesh includes 1,463,472 elements and is shown (cut-view) in Figure 3-16. The cylinder wall and the dome were refined to include 9 elements through the thickness. The minimum element edge length in the 'fine' CV mesh was ~0.048 m. The elements in the pedestal, base, and buttresses were not refined in the 'fine' mesh; while this decision created a transition at the intersection between 'fine' elements and 'coarse' elements, the areas of interest were not affected.
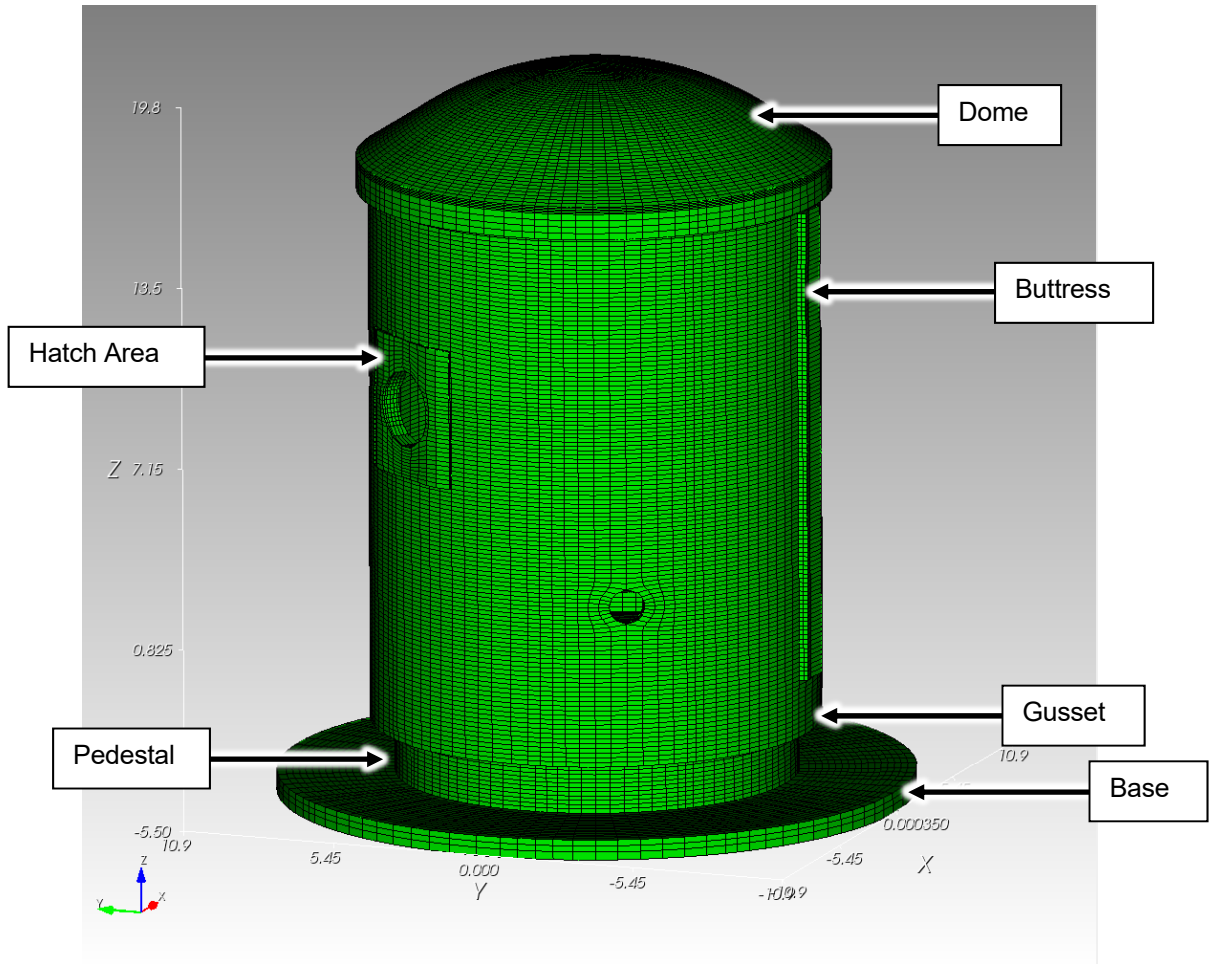
Figure 3-14   PCCV with 'coarse' mesh. Units are in m.
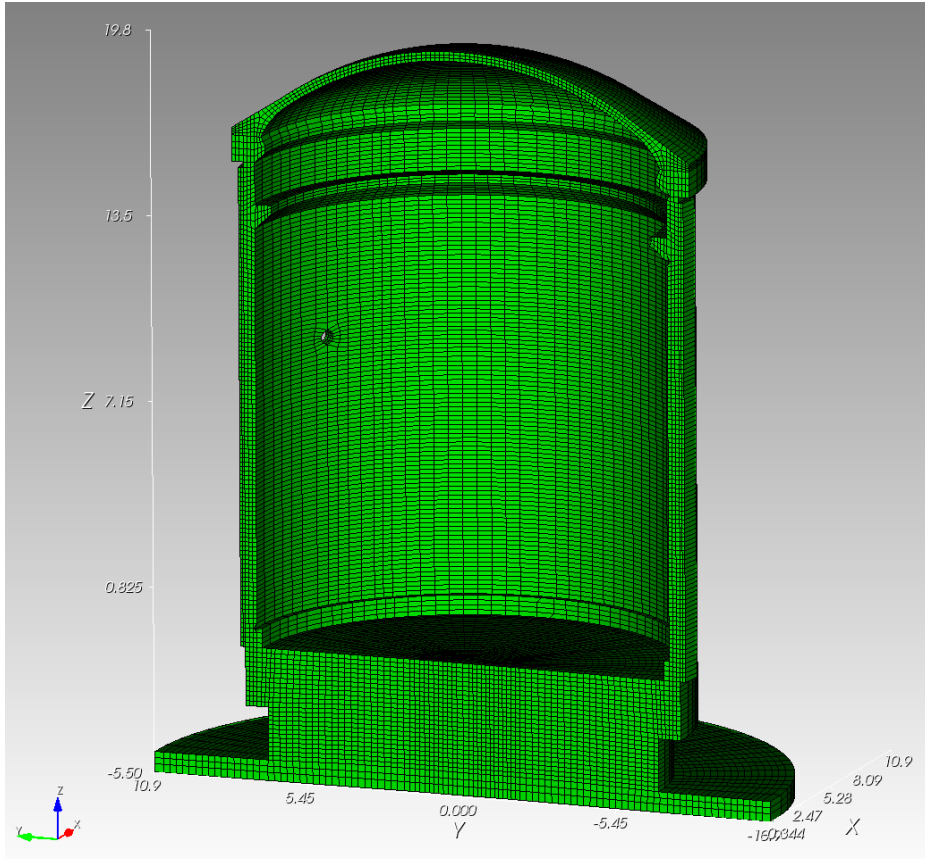
Figure 3-15   Cut view of the PCCV with 'coarse' mesh. Units are in m.
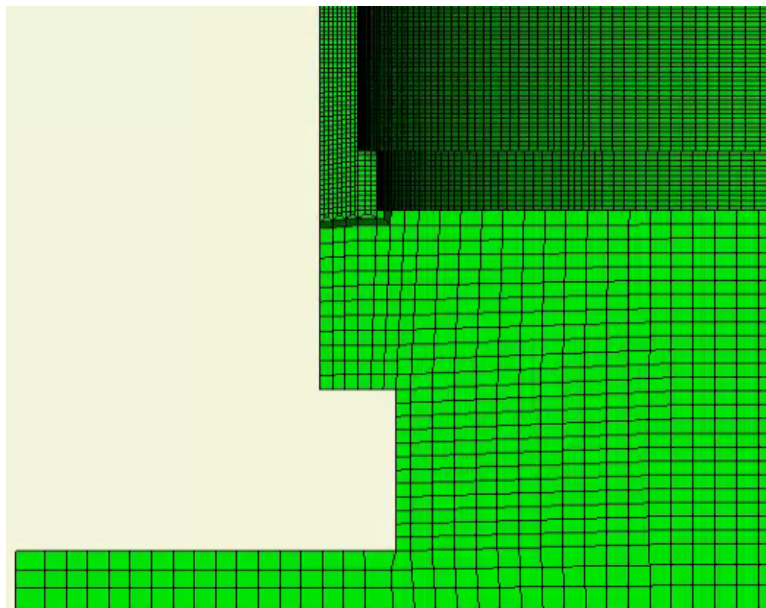
Figure 3-16   Cut view of the PCCV with 'fine' mesh showing the transition between coarse elements (in the basemat) and fine elements (in walls and dome).

Each penetration in the geometry included a single node at its center. These central nodes were tied to the interior nodes of the surrounding penetration as shown in Figure 3-17. Each node had an applied force during pressurizations in the simulation to account for the pressure that would be applied to the material passing through the penetration. This force boundary condition is described in more detail in Section 3.2.1.4 .
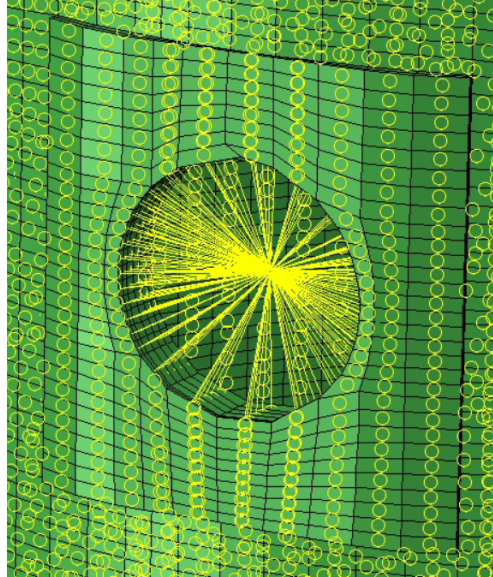
Figure 3-17   Equipment hatch penetration central node tied to the surrounding faces.

3.2.1.2   Rebar

The rebar mesh consists of 35,172 4-noded surface elements as shown in Figure 3-18. The surface layers are geometric placeholders for the rebar. The elements associated with the rebar are called by ABAQUS as "surface elements" and are designed to be used in conjunction with the command *Rebar Layers in ABAQUS. The rebar layers are represented in ABAQUS as surface elements with potentially orthotropic properties depending on reinforcement ratios in each direction. The rebar layers have been added throughout the CV based on drawings provided by EDF. Each concrete surface in the CV has a corresponding internal rebar layer 0.040 m inside the surface, and the pedestal contains several mats of rebar corresponding to actual rebar in the CV. Openings in the CV, such as the hatch door, are surrounded by an additional layer of rebar extending 0.75 times of diameter beyond the opening to account for the additional reinforcement. CV wall rebar, including the additional rebar around openings, consists of both hoop and vertical bars. Pedestal floor mat rebar and dome rebar consists of rebar layers in an X-Y grid.
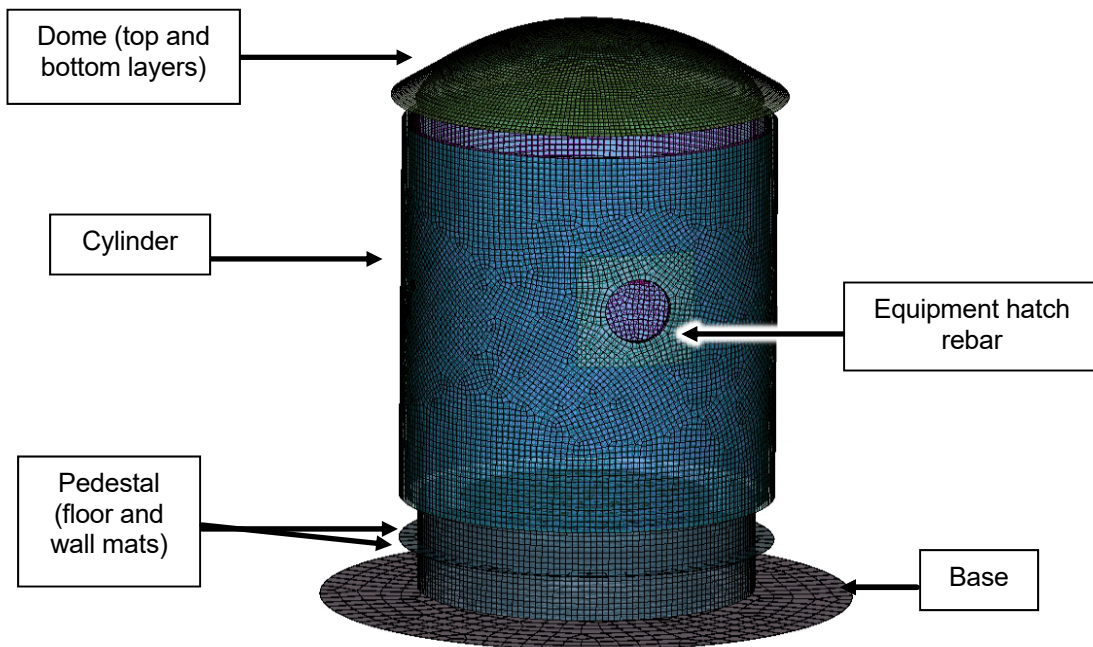
Figure 3-18   Rebar surface layers used in the PCCV.

Steel rebar diameter and spacing were determined upon review of EDF drawings. The vertical rebar in the cylinder used HA8 and HA10 bars (8 mm and 10 mm diameter, respectively) alternating inner and outer faces. The vertical rebar in the cylinder was spaced at 190 mm (inner) and 200 mm (outer). In the simulation, surface rebar layers were included equivalent to one vertical HA9 (9 mm diameter) bar was placed every 97.5 mm.

Horizontal hoop rebar in the cylinder used HA6 and HA8 (6 mm and 8 mm diameter, respectively) bars alternating inner and outer faces spaced at 133 mm. In the simulation, surface rebar layers were included equivalent to one horizontal hoop HA7 (7 mm diameter) bar was placed every 67.5 mm.

Dome rebar used HA8 and HA10 (8 mm and 10 mm diameter, respectively) bars alternating inner and outer faces spaced at 100 mm (lower) and 104 mm (upper) in both directions. In the simulation, surface rebar layers were included equivalent to one HA9 (9 mm diameter) dome rebar was placed every 51 mm in both directions for both upper and lower layers.

The pedestal wall rebar used HA20 (20 mm diameter) bars placed at 200 mm for both vertical bars and horizontal hoop bars. The pedestal horizontal mats, interspersed throughout the pedestal, used either HA12 or HA16 bars spaced at 200 mm in both directions. The basemat rebar used surface rebar layers equivalent to HA20 rebar placed at 200 mm in both directions.

The pedestal floor mat rebar was not constructed in an X-Y grid per EDF drawings. The floor mat rebar was constructed using a combination of concentric rings of rebar with a center X-Y grid as exemplified in Figure 3-19a. The simulation in ABAQUS instead used solely an X-Y grid as shown in Figure 3-19b. The difference in rebar layout in the pedestal did not have any impact

on the behavior of the PCCV. The area of steel per area of concrete in the two rebar layouts remained unchanged.

(a)   (b)
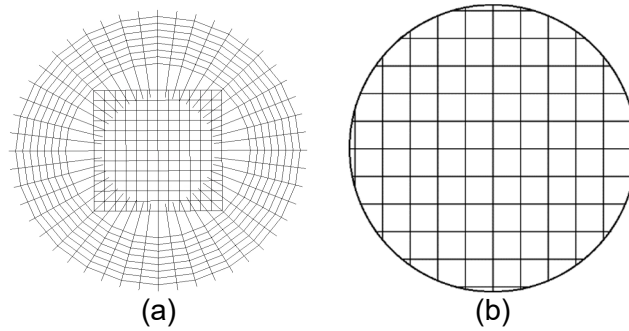
Figure 3-19   (a) Schematic of combined radial/X-Y floor mat rebar grid actually constructed in the CV. (b) Schematic of ABAQUS representation of floor mat rebar grid used in the simulation.

3.2.1.3   Tendons

The PT tendons geometry and mesh is shown in Figure 3-20. The tendons mesh contains 44,466 2-noded beam elements with each element approximately 0.5 m long. The hoop tendons encircle the entire cylinder and are tensioned using protruding elements (not shown). Hoop tendons alternate on which side of the cylinder the strands protrude to evenly distribute PT forces. The vertical tendons and dome tendons in the CV are separated into three different groups: vertical tendons, dome tendons, and combined J tendons. Vertical tendons range from the bottom of the CV to the top of the cylinder. Dome tendons range across the dome and do not extend into the cylinder wall. Combined J tendons as shown in Figure 3-21 range from the base of the cylinder wall up and across the dome.

Figure 3-20   VeRCoRs tendon geometry and mesh.
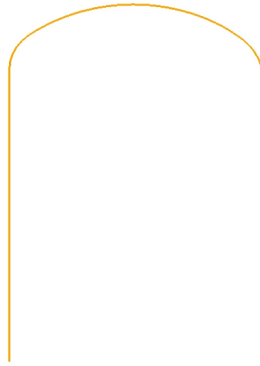
Figure 3-21   Example J-tendon ranging from the pedestal (bottom left) up and around the dome (top right) of the CV.

The PT tendon elements were embedded into the surrounding concrete elements. Embedded elements are a precise representation of the grouted tendons used in the VeRCoRs experiment. Each element in each tendon was applied an initial stress as determined in Section 3.2.2 to apply the PT force to the CV.

3.2.1.4   Boundary Conditions

The displacement boundary conditions in the simulation are shown in Figure 3-22. Only six nodes were fixed against all displacements and rotations (encastre boundary condition). These six nodes were chosen to be the zero-displacement reference point because they are in the center of the base of the CV. Any effects that occur to the CV, including pressurizations, creep effects, drying shrinkage, and potential basemat uplift, will be relative to the fixed location of these six nodes (Figure 3-22a).

The entire geometry was subjected to gravity at sea level: 9.81 m/s^2.

In addition, 1003 nodes in the bottom of the CV were fixed against Z-displacement (Figure 3-22b). ABAQUS had trouble converging with only the six encastre nodes; a larger boundary condition was required to stabilize the simulation. These nodes were not expected to experience displacements in the Z-direction during the simulation. Simulations experimenting with various Z-displacement boundary conditions on the bottom of the CV indicated that, indeed, the number of nodes in the Z-displacement boundary condition had negligible effects on the simulation. No soil mechanics were simulated as the primary purpose of the simulations was to determine strains and stresses in the concrete cylinder and dome. Nodes that are not highlighted in Figure 3-22 were unconstrained to allow for potential basemat uplift (none occurred).
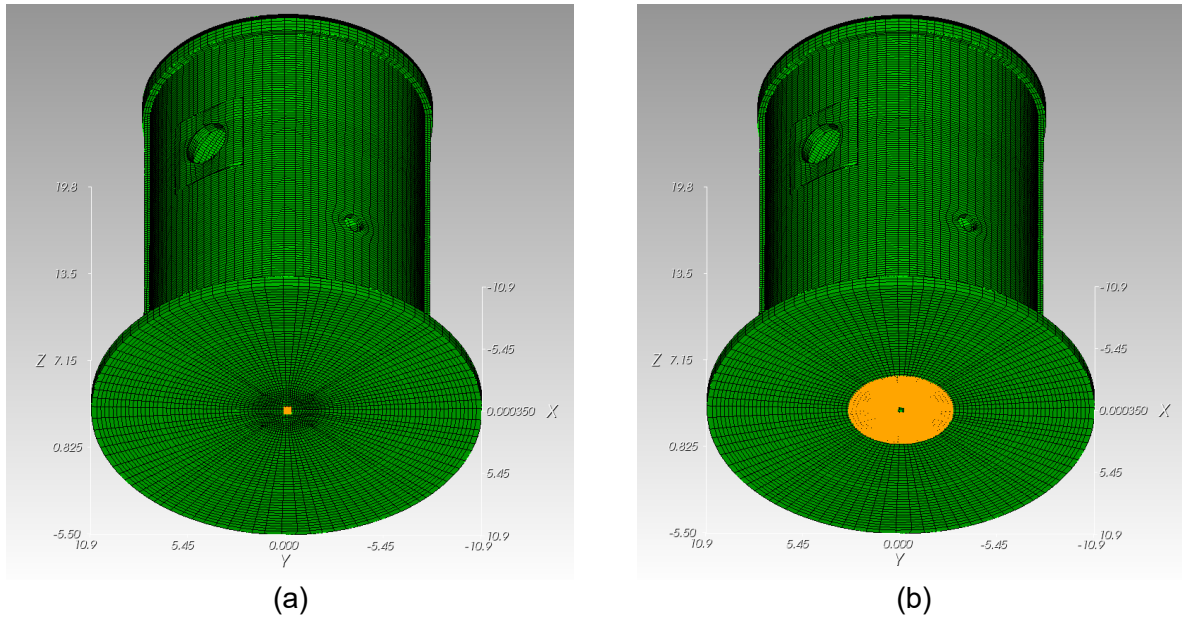
Figure 3-22   (a) 6 encastre (fixed in all directions and rotations) nodes. (b) 1003 nodes fixed against movement in the Z-direction (vertical).

An internal pressurization boundary condition was applied during pressurization steps. All nodes on the surface of the interior of the CV were assigned a uniform pressure according to the "Actual Load" shown in Figure 3-23. The pressure applied at each node was perpendicular to the surface. The theoretical pressurization history is described in Section 3.1 and show in Figure 3-23 as "Theoretical Load"; however, the VeRCoRs organizing committee requested that the pressurization history follow the pressurization history shown as "Actual Load".

To account for the pressure applied to the equipment hatch and other penetrations, a force was applied to a node at the center of each penetration. The geometry of this boundary condition is described in Section 3.2.1.1 . Each node had an applied force during pressurizations in the simulation to account for the pressure that would be applied to the material passing through the penetration. For example, the equipment hatch is sealed with a steel door in the mockup. The steel door in the mockup does not align with the concrete. In this simulation, the steel door is omitted as it would provide negligible structural support to the hatch area. However, during a pressurization test, the equipment hatch door would accumulate a force that would be applied to the edge of the penetration concrete. The force applied to the node was determined by multiplying the applied pressure with the cross-sectional area of the penetration.
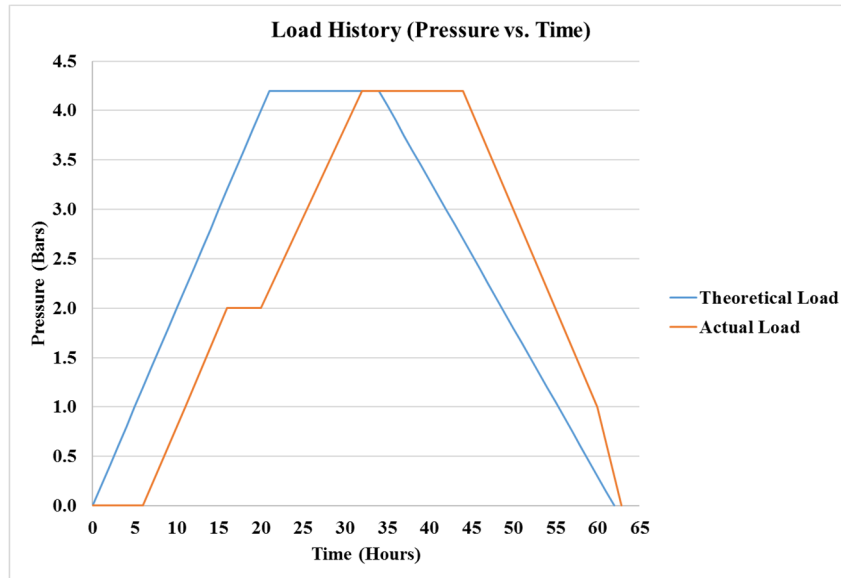
Figure 3-23 **VeRCoRs pressurization curves. The Actual Load has a delayed start, a pressure hold at 2.0 bars relative, and a steeper decline post-4.2 bars relative.**

A RH boundary condition was applied to all of the surface interior and exterior nodes of the CV excluding the nodes on the base of the CV. The nodes on the base of the CV were excluded because these were 100% in contact with the ground and not exposed to the ambient air RH. The experimental RH data is shown in Figure 3-24. RH data points were recorded every 5 minutes. Note that there are gaps in experimental data from January 22, 2016 – March 1, 2016 as well as from May 17, 2016 – June 23, 2016. Also note that the simulation begins August 17, 2015 and ends April 5, 2018. There are significant periods of time before and after RH data was recorded where the simulation does not have experimental data.
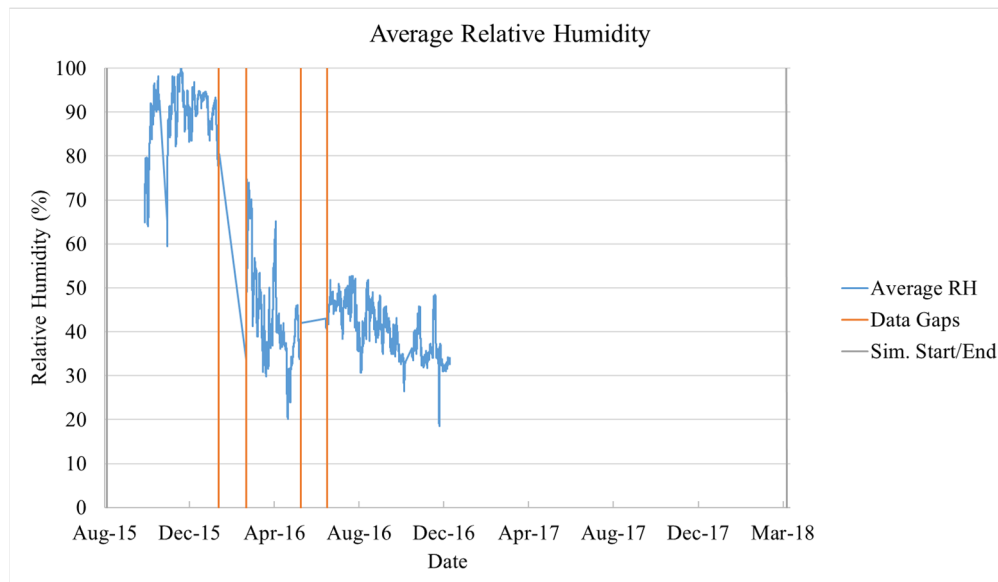
Figure 3-24 **Average relative humidity in contact with the VeRCoRs concrete. Gaps in data are shown between vertical lines. Dates are listed as Month-Year.**

For the simulation, a moving average using data over 3 days was used to smooth the experimental data as shown in Figure 3-25. Smoothing the data over 3 days removed peaks that may or may not be representative of the behavior of the CV over the 3-day period. A data-smoothing function was chosen because of the way that ABAQUS reads input data: when ABAQUS reads input data for a boundary condition, it reads only one data point and carries that data point until it reads another data point. If the raw RH data was used as an ABAQUS input, ABAQUS may by chance read a peak or a relative minimum data point and carry that value for several days of simulation. That peak or relative minimum would not be representative of the RH over the ABAQUS time step. Keep in mind that RH experimental data was recorded *every five minutes*. Using a data-smoothing function reduces the likelihood that ABAQUS reads a non-representative data point. As will be discussed in Section 3.2.4 , ABAQUS time steps were limited to a maximum of ~4.1 days to increase simulation RH fidelity.

Figure 3-25 only indicates a *change from initial* RH rather than absolute RH values as shown in Figure 3-24. This is because ABAQUS assumes all starting values as zero. The simulation is also assumed to be 'zero' starting point when it begins, so only changes in RH need to be used as inputs. The initial RH inside the concrete is assumed to be the first RH measurement data point provided by EDF: 65%.

ABAQUS linearly interpolates between the two bounding data points for time steps during the gaps of RH data. For time steps before and after RH data was available (before October 9, 2015 and after December 14, 2016), ABAQUS assumes the nearest data point value. That is, ABAQUS assumes that the initial change in RH is ~0.09, and it assumes that the final change in RH is ~ -0.3.
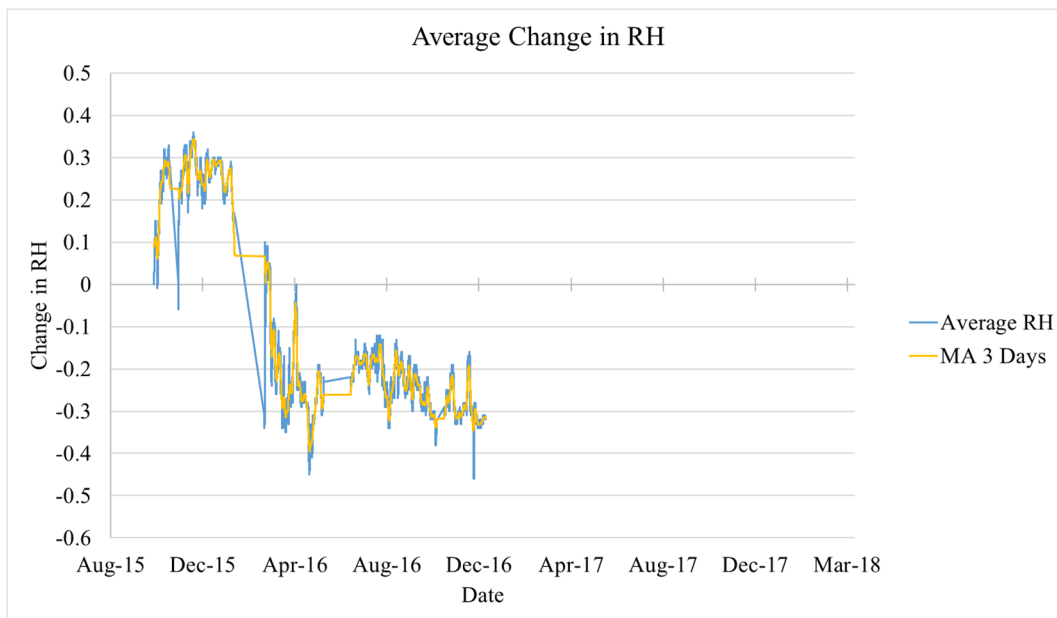
Figure 3-25   Change in relative humidity inputs for ABAQUS. A moving average (MA) of 3 days of data was utilized to smooth the experimental data. Dates are listed as Month-Year.

3.2.2 Tendon Initial Post-Tensioning Stress and Tendon-Pulling Algorithm

The PT tendon material and jacking information was provided by EDF as shown in Table 3-5. While equations exist to estimate the stress along each PT strand based on geometry, tendon material properties, and friction/wobble coefficients, SNL implemented a more accurate method for obtaining the initial stress states along the tendons (Jones, Dameron, & Sircar, 2015). In a separate simulation, the PT tendons were not embedded into the concrete elements, and the displacement of each node along the tendons was restricted to moving only along the tendon profile. A jacking force as dictated by Table 3-5 was applied to each end of each tendon, and the tendons were assigned a friction coefficient between tendon and concrete based on the friction and wobble coefficients provided by EDF. The tendon-jacking simulations were carried out by Moffatt & Nichol of San Diego, CA. The tendon stresses resulting from the tendon jacking and anchor set are shown in Figure 3-26 through Figure 3-33. Tendon stresses after anchor set were included as initial tendon stress conditions in the simulation. As the tendons were grouted in the VeRCoRs experiment, the tendons in the simulation were not allowed to slip in the concrete.

Table 3-5   Post-tensioning data provided by EDF.

Ducts	
Smooth Steel Pipes	
external diameter	50 mm
internal diameter	47 mm
thickness	1,5 mm
Smooth Steel Pipes (for unbonded prestressing)	
external diameter	55 mm
internal diameter	51 mm
thickness	2,0 mm
Steel Strip Sheaths	
internal diameter	45 mm
thickness	0,4 mm
Steel Strip Sheaths (for unbonded prestressing)	
internal diameter	55 mm
thickness	0,5 mm
Prestressing system	
System C (4C15) (Freyssinet) ETA-06/0226	
Bonded prestressing (except 4 vertical tendons and 2 horizontal tendons)	
Pull-In at wedge blocking	8 mm
Strands	
Strand section (T15)	139 mm²
Tensile strength	1860 MPa
Yield strength	1620 MPa
Relaxation losses	$\rho_{1000} = 2.5\%$.
Tendons	
Tendon	4T15
Tendon maximal prestressing stress (at anchor, before wedge blocking)	1488 MPa
Tendon Young modulus	190000 MPa
Friction	
Vertical tendons	
Friction coefficient	f = 0.16
Wobble effect coefficient	ϕ = k.f = 0.0008
Horizontal tendons	
Friction coefficient	f = 0.17
Wobble effect coefficient	ϕ = k.f = 0.0015
Gammas tendons	
(Vertical part) Friction coefficient	f = 0.16
(Vertical part) Wobble effect coefficient	ϕ = k.f = 0.0008
(Dome part) Friction coefficient	f = 0.16
(Dome part) Wobble effect coefficient	ϕ = k.f = 0.0015
Dome tendons	
Friction coefficient	f = 0.16
Wobble effect coefficient	ϕ = k.f = 0.0015
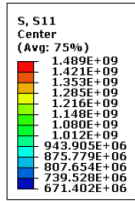
Figure 3-26   Set 1 of 2 hoop tendon stress after jacking.
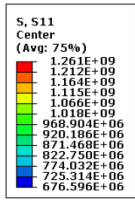
Figure 3-27   Set 1 of 2 hoop tendon stress after anchor set.
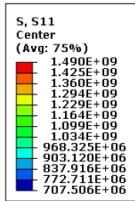
Figure 3-28   Set 2 of 2 hoop tendon stress after jacking.
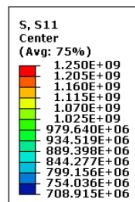
Figure 3-29   Set 2 of 2 hoop tendon stress after anchor set.
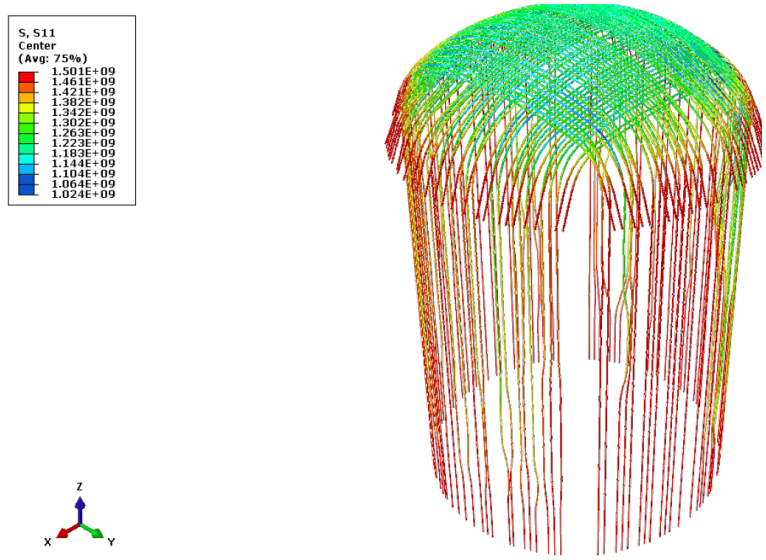
Figure 3-30   J-tendon stress after jacking.
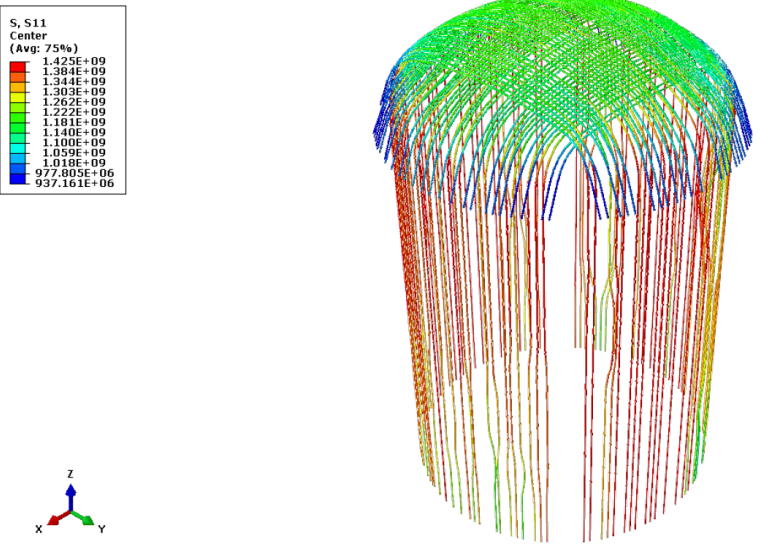
Figure 3-31   J-tendon stress after anchor set.
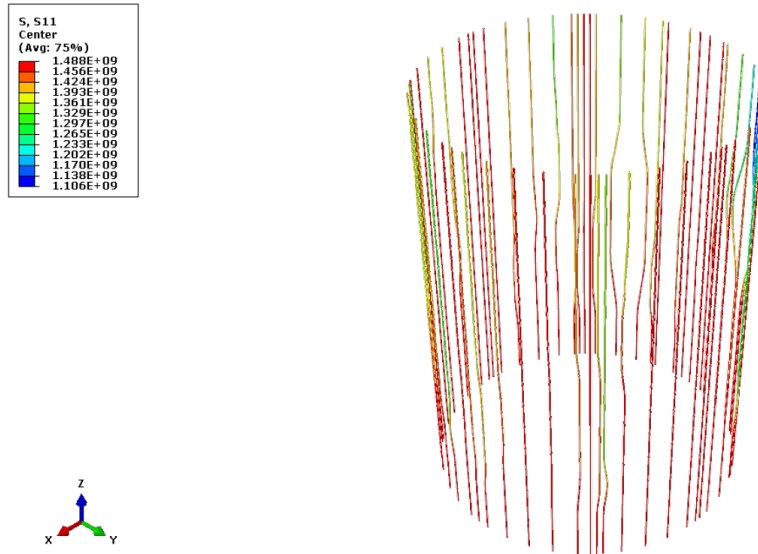
Figure 3-32   Vertical tendon stress after jacking.
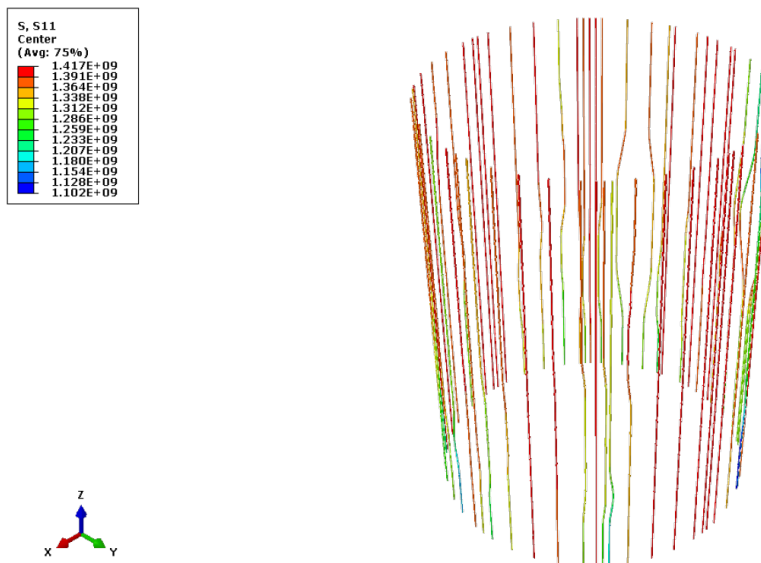
Figure 3-33   Vertical tendon stress after anchor set.

3.2.3   Material Properties

The material properties and constitutive model for each material used in the simulation are described in detail in the following sections.

3.2.3.1   *Rebar Model*

The rebar in the simulation was modeled as linear elastic. Given the conditions of the experiment, the rebar was not expected to approach stresses incurring any material

nonlinearity. The only information provided by EDF about the rebar material properties was the yield strength and Young's modulus. The density and Poisson's ratio were assumed from standard values in engineering practice.

- Density: 7850 kg/m^3
- Young's modulus: 200.0 GPa
- Poisson's ratio: 0.3
- Yield strength: 500 MPa

3.2.3.2   Tendons Model

The tendons in the simulation were modeled as purely elastic. Under the conditions in this simulation, the tendons were not expected to approach stresses incurring any material nonlinearity. Detailed tendon information is presented in Table 3-5. The elastic information is listed here. The density and Poisson's ratio were assumed from standard values in engineering practice.

- Density: 7850 kg/m^3
- Young's modulus: 190.0 GPa
- Poisson's ratio: 0.3

3.2.3.3   Concrete Model

The concrete composition provided by EDF is listed in Table 3-6. "Total water" is what is included into the mixture, but some water adheres to aggregates and to the side of the mixer, so not all of the "total water" can react with the cement. The water-to-cement ratio is calculated using the "Effective water".

Table 3-6   VeRCoRs concrete composition.

Component	Kg/m^3
Cement CEMI 52.5 N CE CP2 NF Gaurain	320
Effective water	167.2
Total water	197.6
Sand 0/4 rec GSM LGP1	830
Aggregate 4/11R GSM LGP1	445
Aggregate 8/16R Balloy	550
Admixture: Sikaplast Techno 80	2.4

The concrete in the simulation was modeled using a combination of three constitutive models: elastic for instantaneous response, viscoelastic for creep effects, and drying shrinkage based on RH.

Two separate simulations were run in parallel to fully capture the concrete behavior. The two simulations were identical in every way (e.g., initial conditions, PT, mesh, geometry, boundary conditions, time steps…) except for the concrete material properties and the internal pressurizations. In one simulation, the concrete was defined with a linear elastic constitutive model combined with a thermal[6] constitutive model and subjected to internal pressurizations as prescribed in the VeRCoRs experiment. In the second simulation, the concrete was defined with a viscoelastic constitutive model and was not subjected to internal pressurizations. Creep is most prominent over long-term loads such as PT and gravity; therefore, excluding internal pressurizations from the viscoelastic simulation has a negligible effect on total results.

Two simulations were used due to the mathematical formulation of the ABAQUS viscoelastic material model. The reader is directed to the ABAQUS user's manual for specific viscoelasticity mathematical formulations (Dassault Systemes, 2013), but a more general description is written here. A viscoelastic constitutive model responds elastically to an initial applied force or stress. The model then continues to accrue time-dependent deformation based on the applied stress (Figure 3-34). Viscoelastic constitutive models are often used in simplistic creep simulations. More complicated simulations with widely varying load scenarios will progress to viscoplastic constitutive models, but those were deemed excessive for the requirements of these simulations. For the majority of time in the simulations representing the VeRCoRs experiment, the primary stress was due to gravity and PT. Therefore, the ABAQUS viscoelastic model was chosen to model the creep behavior of the concrete.
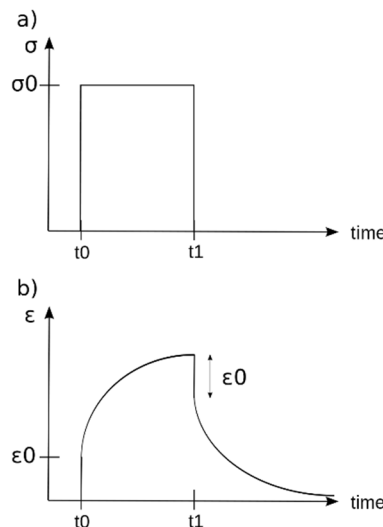
Figure 3-34 (a) Applied stress and (b) induced strain as functions of time over a short period for a viscoelastic material.

The reason that two simulations were required to capture the concrete behavior is that the ABAQUS viscoelastic constitutive model stifled the elastic response of the concrete as time progressed. As discussed in Section 2.3.2.3 , concrete creep is a reactionary effect. Concrete creep, and creep in general, is a response to an application or removal of stress. If a sample of concrete is under stress, and another stress is applied, the elastic response of the material for

---

[6] The ABAQUS thermal equation was used to model the drying shrinkage. See Section 3.2.3.3.2 .

both stresses will follow the same governing equation: simply, $\sigma = E\varepsilon$. However, the ABAQUS viscoelastic constitutive model was not responding elastically to new applied stresses after the beginning of the simulation. Using the ABAQUS viscoelastic constitutive model, the response to the first applied load was elastic as indicated in Figure 3-34. However, if a new load was applied later in the simulation, there was no elastic response, only a viscoelastic (or creep) response to the pressurization stress.

Therefore, two simulations were run:

- One simulation to capture:
    - The elastic response to PT and pressurizations; and
    - The drying shrinkage mechanism.
- One simulation to capture the viscoelastic (creep) response to PT and pressurization stresses.

3.2.3.3.1 Elastic Concrete Model

The elastic material parameters for the concrete were taken from data provided by EDF. The concrete was not allowed to crush or crack in the simulations. Compressive strength, density, and elastic moduli were provided for several batches. As the values were similar, the average was taken for all concrete in the PCCV. No Poisson's ratio information was provided, so it was assumed based on standard values from (Mindess, Young, & Darwin, 2003).

- Density: 2390 kg/m^3
- Young's modulus: 34.26 GPa
- Poisson's ratio: 0.20

3.2.3.3.2 Relative Humidity and Drying Shrinkage Concrete Model

The drying shrinkage mechanism in concrete is based on the inherent capillary porosity within cement, the moisture content inside said porosity, and the effects of capillary action. Cement paste is inherently porous due to the chemical reaction of Portland cement and water. Moisture in these pores creates a capillary effect similar to the schematic shown in Figure 3-35. If the pores in the concrete contain some moisture, but not enough to be fully saturated, the pores will be experiencing capillary suction. The capillary action in the pores creates a suction force that shrinks the concrete. This capillary suction force within the concrete is directly related to the moisture content in the pores as shown in Figure 3-36. Assuming that the reaction of the cement within the concrete is complete, concrete can shrink or swell depending on the difference between the moisture content within the cement pores and the moisture available outside the specimen. If the concrete is losing moisture to the atmosphere (drying), then the capillary suction force within the pores will increase and the specimen will volumetrically shrink. Conversely, if the concrete is absorbing moisture from outside the specimen, then the capillary suction force within the concrete will decrease and the specimen will volumetrically swell. More information on moisture transport and capillary action in concrete is available (Bazant & Jirasek, Moisture Transport in Concrete, 2018).
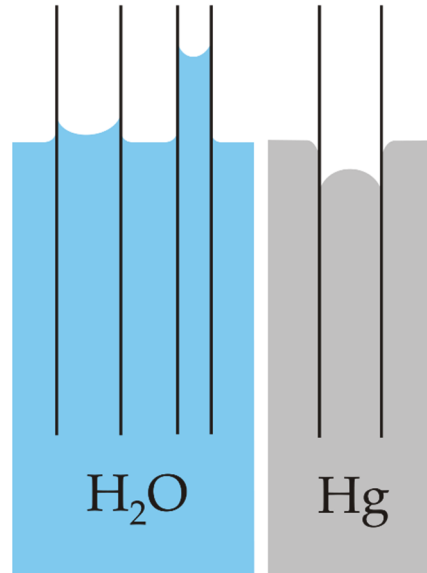
Figure 3-35   Capillary action of (left) water and (right) mercury, in each case with respect to a polar surface such as glass.
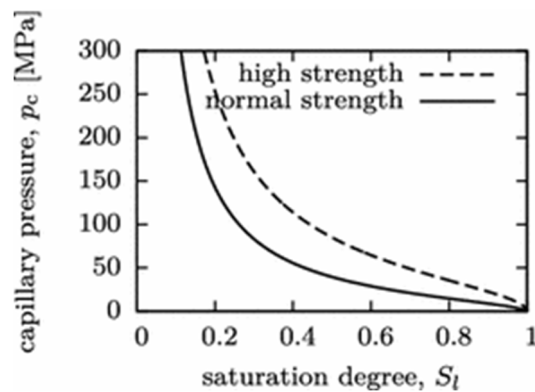
Figure 3-36   Cement pore capillary pressure vs degree of saturation. (Bazant & Jirasek, Moisture Transport in Concrete, 2018)

The most common method of measuring moisture content in cements and concretes is to measure the RH in the sample. Therefore, by utilizing a RH boundary condition, the drying shrinkage or moisture swelling of the concrete can be simulated.

Moisture transport within the concrete was modeled utilizing the following thermal equation in ABAQUS.

$$\frac{\partial u}{\partial t} = \frac{k}{c_p \rho} \nabla^2 u$$

Where

- u is the temperature as a function of space and time;

- $\frac{\partial u}{\partial t}$ is the rate of change of temperature at a point over time;

- $\nabla^2 u$ are the second spatial derivatives of temperature in the *x, y,* and *z* directions;

- k is the thermal conductivity;

- c_p is the specific heat capacity; and

- ρ is the mass density.

A change in temperature alters the volume of the specimen according to

$$\alpha = \frac{1}{V}\left(\frac{\partial V}{\partial T}\right)_p$$

Where *V* is the volume, *T* is the temperature, and α is the coefficient of thermal expansion.

Note that the thermal equation in ABAQUS is exactly the same as Fick's 2nd Law of Diffusion:

$$\frac{\partial C}{\partial t} = \gamma \nabla^2 C$$

Fick's 2nd Law of Diffusion is commonly used to model diffusion of various properties in materials including but not limited to electricity, heat, and moisture. Therefore, the thermal equation in ABAQUS can be used to model moisture transport with the following change of definitions:

- u is the RH as a function of space and time;

- $\frac{\partial u}{\partial t}$ is the rate of change of RH at a point over time;

- $\nabla^2 u$ are the second spatial derivatives of RH in the *x, y,* and *z* directions;

- k is the RH 'conductivity';

- c_p is the 'specific RH capacity'; and

- ρ is the mass density.

- α is the 'coefficient of drying shrinkage expansion'.

A cylinder of concrete was cast, cured for 28 days, and then exposed to a dry environment of 50% RH for 762 days by EDF for the VeRCoRs experiment (Corbin, 2018). See Figure 3-37 and Figure 3-38. The experimental data and the ABAQUS simulation results are presented in Figure 3-39. The ABAQUS simulation geometry and mesh is presented in Figure 3-40. The material properties used in the simulation were as follows:

- Density: $2390 \frac{kg}{m^3}$

- Young's modulus: 34.26 GPa

- Poisson's ratio: 0.20

- RH 'Expansion coefficient': $0.0014 \frac{m^3}{\Delta RH}$

- RH 'Conductivity' (Wang & Xi, 2017): $1.0 \times 10^{-10} \frac{RH}{m \cdot s \cdot \Delta RH}$

- Specific RH capacity': $0.0004 \frac{RH}{kg \cdot \Delta RH}$

While the 'conductivity' term could be found in literature, the specific 'RH' capacity and the 'RH' expansion coefficient were curve-fitted utilizing an iterative approach. Changing the specific RH capacity altered the x-axis stretch of the results while changing the specific RH expansion coefficient altered the y-axis strain of the results. Simply, the RH capacity term governs how much moisture a "block" of concrete can absorb, while the RH expansion term governs how much a "block" of concrete strains for any given absorbed moisture. Figure 3-39 indicates that the simulation is accurate.

Figure 3-37   Drying shrinkage concrete cylinder specimen.
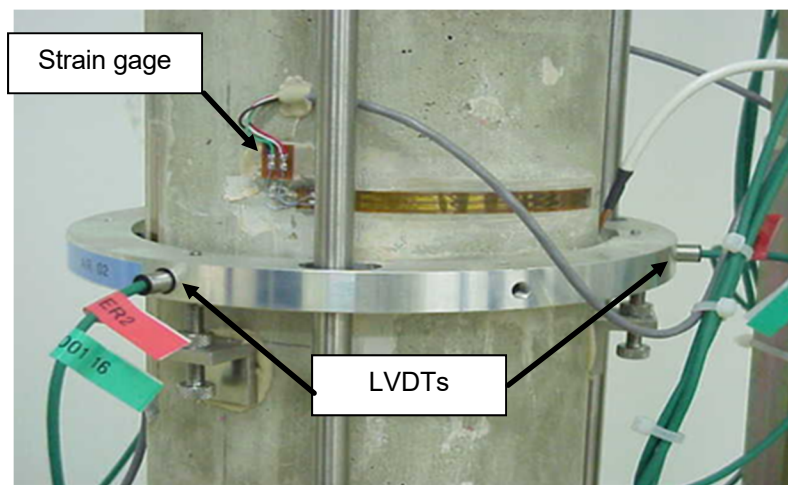
Figure 3-38   Drying shrinkage concrete cylinder specimen strain gages and liner variable differential transformers (LVDTs) for measuring axial strain and radial displacements, respectively.
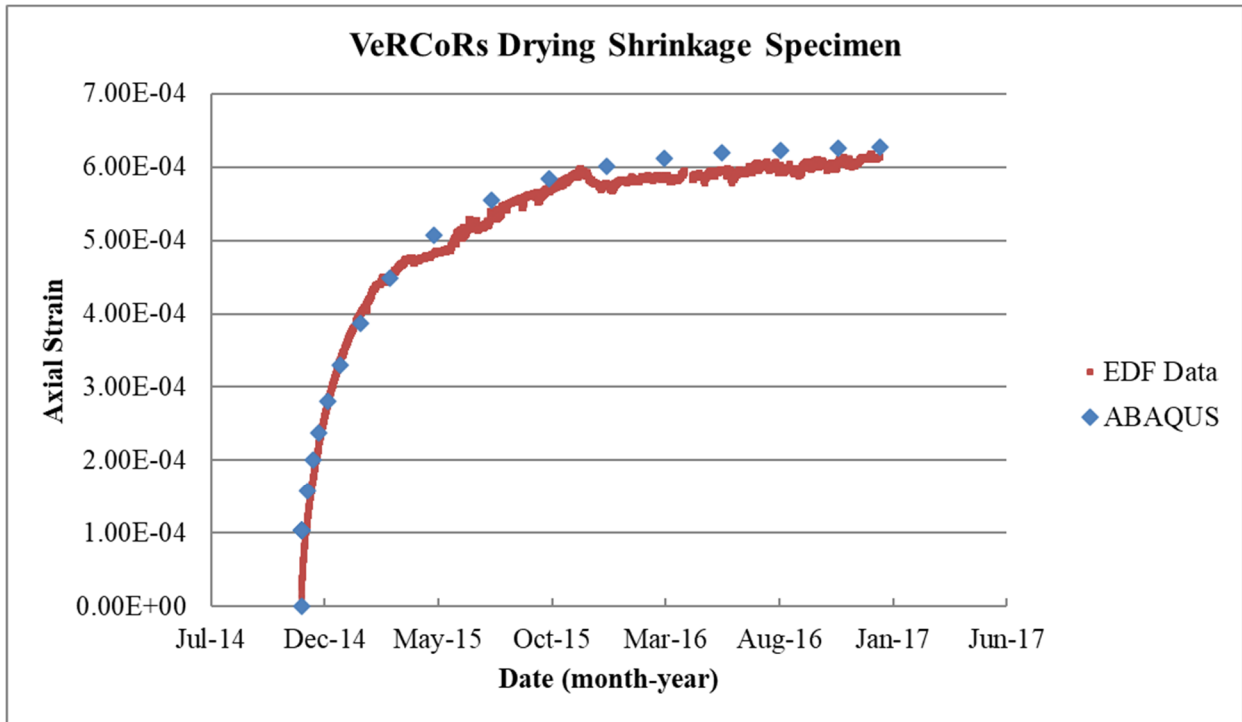
Figure 3-39 **Drying shrinkage concrete cylinder EDF experimental data and ABAQUS simulation results.**
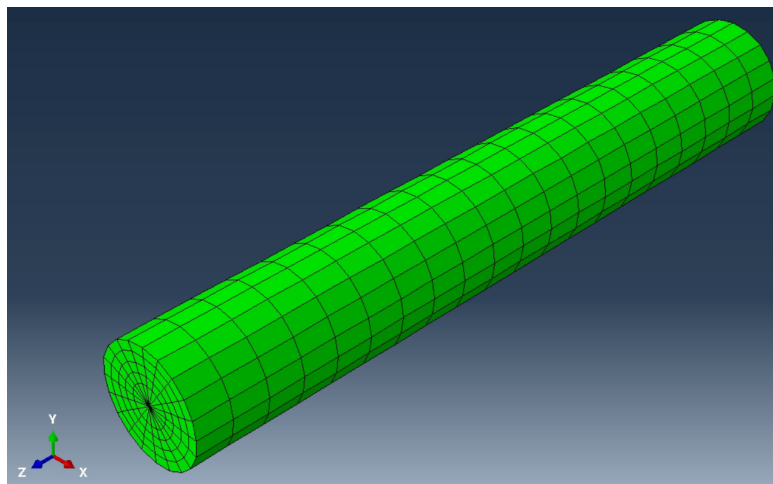
Figure 3-40 **ABAQUS drying shrinkage cylinder geometry and mesh. Specimen is 0.16m diameter and 1.00 m tall.**

3.2.3.3.3   Creep Concrete Model

The creep concrete model used in these simulations is based on the Bazant B3 model (Bazant & Baweja, Creep and Shrinkage Prediction Model for Analysis and Design of Concrete Structures: Model B3, 2000). The B3 model is a predictive model based on many material properties commonly measured in concrete such as the water-to-cement ratio, compressive

strength at 28 days, the aggregate-to-cement ratio, the concrete age at loading during creep tests (if tests are performed), and Young's modulus. The model also uses several fit coefficients that were developed by comparing the predictive capabilities of the model to creep test data from concrete specimens and structures in literature. Most importantly, the B3 model acknowledges that even with extremely detailed information about the mixture proportions and aging characteristics of the concrete, no predictive model will yield data that is better than experimental data. Therefore, the B3 model incorporates a method to improve the model's prediction by updating with creep test data. Essentially, the model uses a material-property-based algorithm in combination with experimental data to more accurately provide an extrapolated creep prediction.

The EDF drying creep test experimental setup is shown in Figure 3-41 and Figure 3-42. The EDF basic creep test experimental setup is identical to the drying creep test except that the basic creep test specimen was sealed to prevent drying. The data for both experiments is presented in Figure 3-43.

Figure 3-41   EDF creep test configuration. Specimen is 0.16 m diameter and 1 m tall.
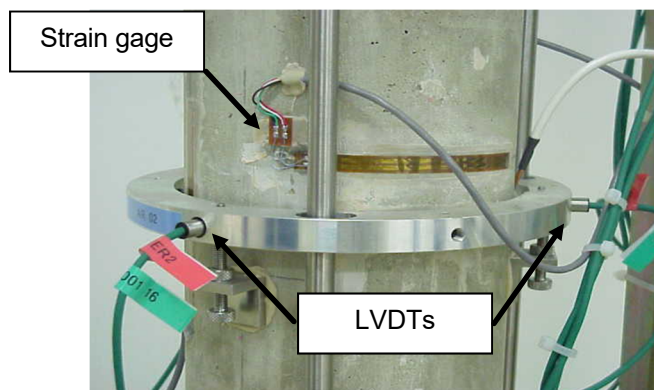
Figure 3-42   EDF creep test strain gages and liner variable differential transformers (LVDTs) for measuring axial strain and radial displacements, respectively.
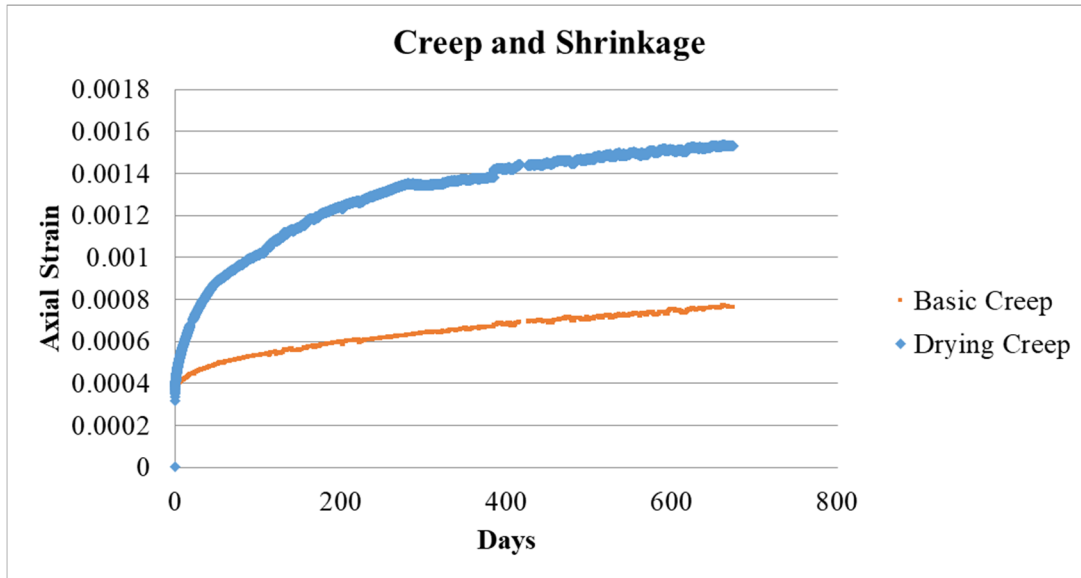
Figure 3-43   EDF creep test experimental data.

As the VeRCoRs CV was exposed to a dry environment on both inner and outer concrete surfaces, the concrete was assumed to undergo drying creep during the experiment. Therefore, the experimental data for drying creep was used to update the B3 model's predictions.

Wolfram Mathematica 12.0 was used to calculate the B3 model predictions. Figure 3-45 shows the B3 drying creep prediction based solely on material inputs compared to the EDF experimental drying creep data. As can be seen, the B3 model does not accurately predict the creep based solely on material inputs[7]. However, as mentioned before, the B3 model includes a correction factor to use experimental data. The B3 model's correction factor is a regression between the model's prediction of a concrete mixture's creep and the experimental creep data for the same concrete mixture, i.e.,

$$Y = AX + B$$

wherein X is the model prediction without correction, A and B are correction constants, and Y is the corrected model prediction. Figure 3-44 shows an example presented in (Bazant & Baweja, Creep and Shrinkage Prediction Model for Analysis and Design of Concrete Structures: Model B3, 2000) for how the use of short-time test data can improve the model's prediction. In this example, a 28-day compressive creep test was performed on an unreinforced concrete cylinder. The concrete mixture was input into the B3 model, but as can be seen the prediction did not accurately represent the experimental results. The regression described above was utilized using only the first five experimental data points, and the improved (corrected) model then accurately predicts the remaining experimental data points. In Figure 3-44, J(t,t') is represented as Y in the above description. The B3 model prediction with the correction factor was used in the analysis of the VeRCoRs mockup.

---

[7] Predicting concrete creep using only material inputs is, under the current state of the art, extremely difficult.
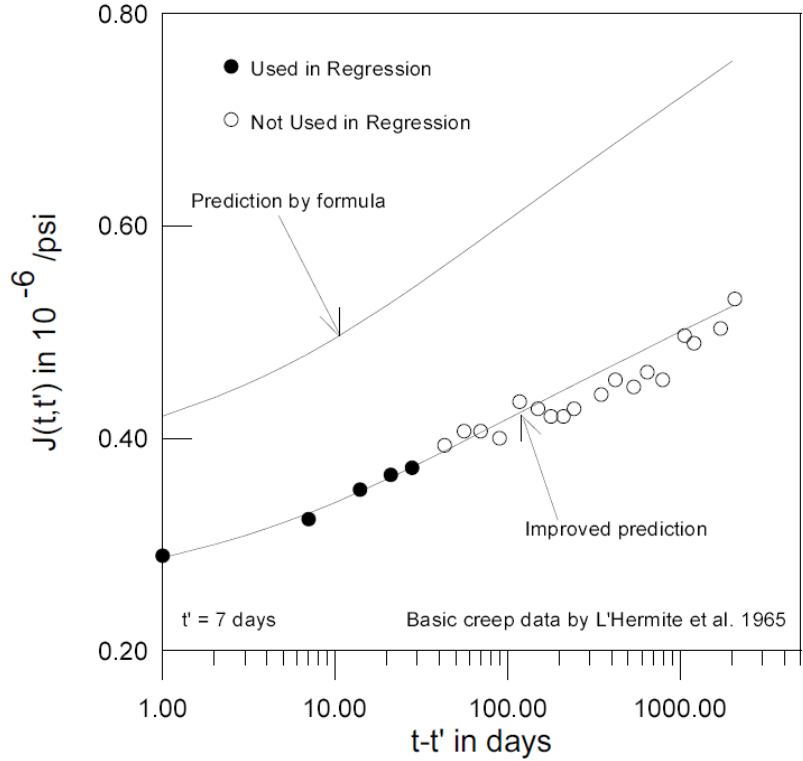
Figure 3-44 Example of improving the prediction of creep by the use of short-time test data. (Bazant & Baweja, Creep and Shrinkage Prediction Model for Analysis and Design of Concrete Structures: Model B3, 2000)

Figure 3-46 shows that, after updating with experimental data, the B3 model accurately matches the EDF drying creep data. After updating with experimental data, Figure 3-47 shows the B3 model's prediction of concrete creep for up to 80 years of sustained load.
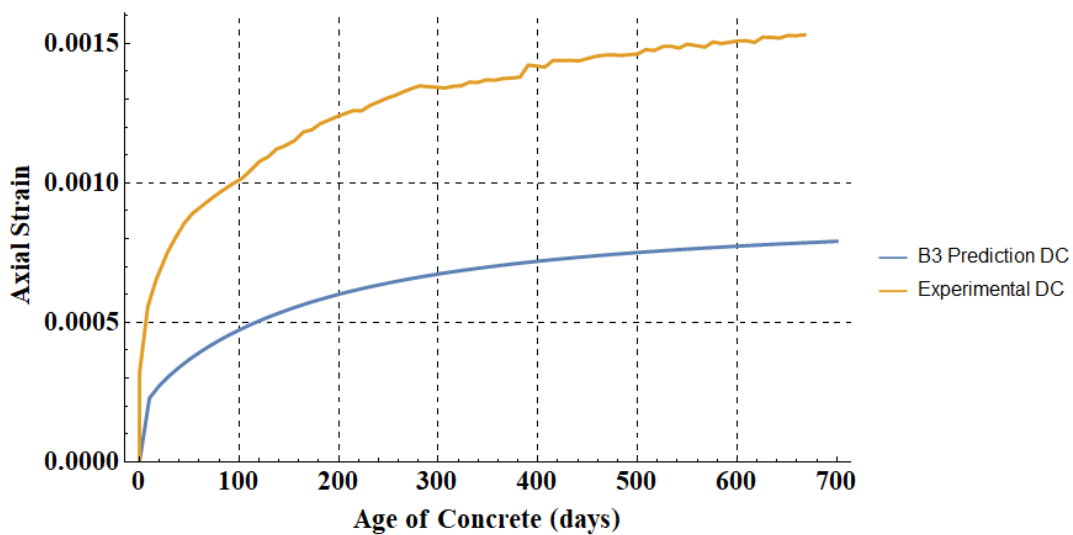
Figure 3-45 Creep strains from (top) the EDF drying creep (DC) experiment and (bottom) the B3 prediction prior to updating with experimental data.
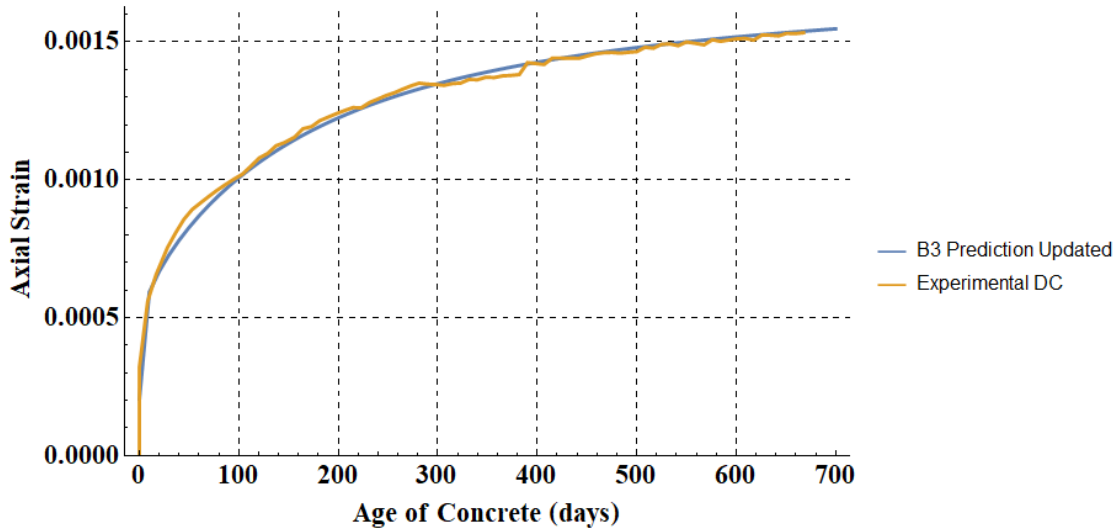
Figure 3-46   Creep strains from the EDF drying creep (DC) experiment and the B3 updated prediction.
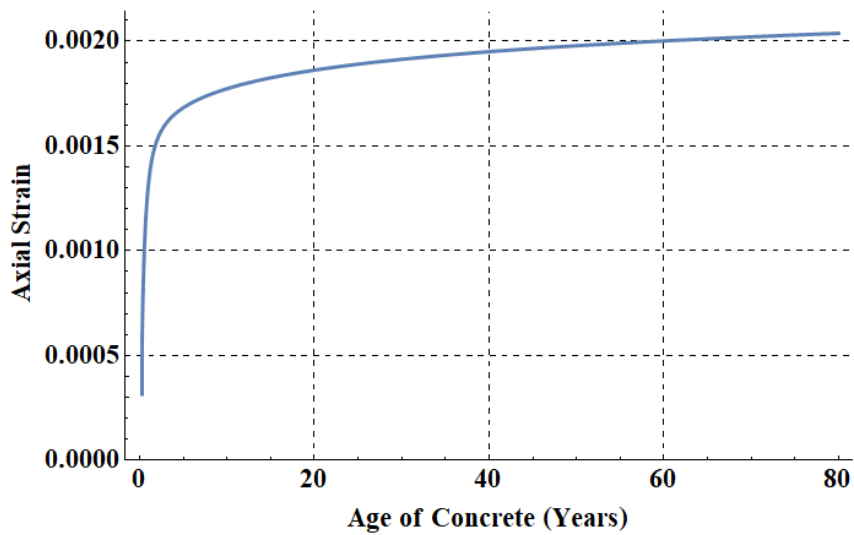
Figure 3-47   Updated B3 creep prediction through 80 years of creep.

Now that the B3 model matches the EDF drying creep experimental data and can predict creep for up to (and over) 80 years, the data must be input into ABAQUS. The B3 model was fitted with a time-domain Prony series for input into ABAQUS. A Prony series is a summation of several exponential terms that can simulate creep data and is implemented into ABAQUS as follows:

$$g_r(t) = 1 - \sum_{i=1}^{N} \bar{g}_i^P \left(1 - e^{\frac{-t}{\tau_i^G}}\right)$$

3-41

Where N, $\bar{g}_i^P$, and τ_i^G are material constants (Dassault Systemes, 2013). The updated B3 model creep data was used to create a "relaxing" shear modulus of elasticity. As the concrete deformed, the elastic modulus could be said to "relax". The "relaxing" elastic modulus was converted to a shear modulus using Poisson's ratio, and the results are shown in Figure 3-48.

Several iterations were run to determine the number of Prony series terms for fitting the B3 model data. 8 Prony series terms were determined to be adequate to match the data as shown in Figure 3-48; the addition of more terms beyond 8 did not significantly decrease the error between the B3 model data and the Prony series. The Prony series terms are listed in Table 3-7.
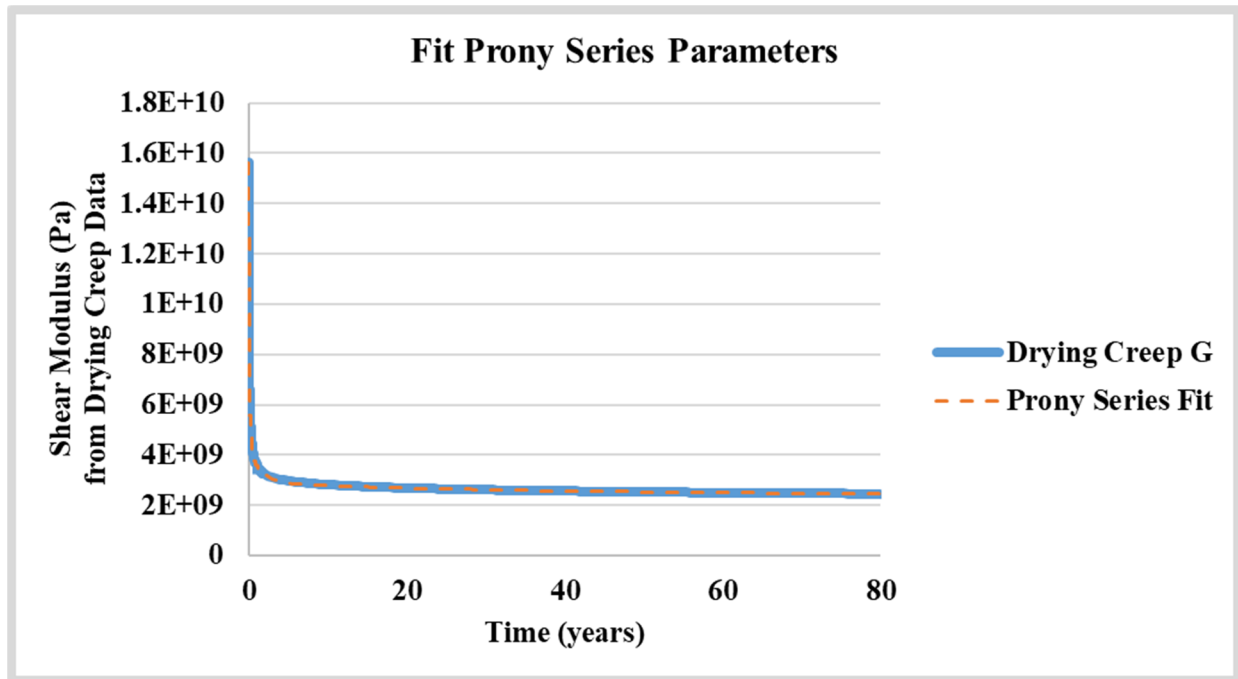
Figure 3-48   EDF drying creep "relaxing" shear modulus G compared to the Prony series fit equation.

Table 3-7   Prony series terms for ABAQUS viscoelastic model.

g_i	τ_i
0.113569	9120.8
0.149441	119170
0.287218	1030100
0.191331	7859700
0.0779597	58408000
0.0454469	3128500000

An ABAQUS simulation of the drying creep test was performed to verify that the Prony series model was matching the experimental data. As the cylinder geometry was the same for the drying shrinkage and creep tests, the ABAQUS geometry and mesh can be seen in Figure 3-40.

As in the EDF experiment, an axial stress of 12 MPa was applied to one end of the cylinder while the other was restrained in the axial direction. The axial strain was output from an element in the same location as the experimental strain gage. The results can be seen in Figure 3-49. The creep data matches well with the ABAQUS simulation results.
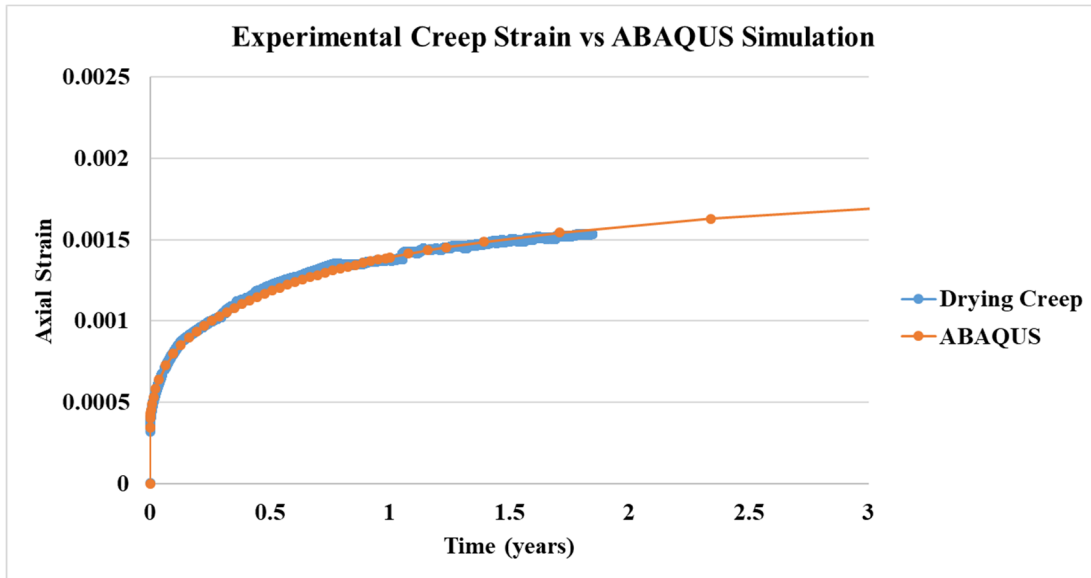
Figure 3-49 ABAQUS simulation results vs EDF experimental data for drying creep.

3.2.4 Simulation Timeline (Start, End, Steps)

The timeline of primary events on the VeRCoRs mockup is presented in Table 3-1. The VeRCoRs simulation step history used in the simulation is presented in Table 3-8. Time between pressurizations is described as 'dormant period'; gravity and post-tensioning are still active in the dormant periods.

Table 3-8 VeRCoRs simulation step history.

Step Title	Date Begin	Date End	Total Time (days)	Description
Initialize	N/A	N/A	10 seconds	Ramp gravity and post-tensioning loads
0	8/17/2015	11/2/2015	77.00	Post-tensioning complete, await first pressurization
1	11/2/2015	11/4/2015	2.253	Strains reference date 11/2/2015
2	11/4/2015	11/6/2015	2.411	Pressurization 'Pre-op'
3	11/6/2015	1/25/2016	80.00	Dormant period
4	1/25/2016	1/28/2016	2.411	Pressurization 'VC1'
5	1/28/2016	3/14/2017	411.2	Dormant period
6	3/14/2017	3/16/2017	2.411	Pressurization 'VD1'
7	3/16/2017	3/21/2017	4.611	Dormant period

8	3/21/2017	3/23/2017	2.411	Pressurization 'VD1 bis'
9	3/23/2017	4/2/2018	374.6	Dormant period
10	4/2/2018	4/4/2018	2.411	Pressurization 'VD2'

3.2.5   Comparison of Experimental Data with Simulation Results

The experimental VeRCoRs strain gage data is compared to the simulation results as exemplified in Figure 3-50. Missing experimental data due to gage malfunction or some other technical issue is shown as a sudden change to zero; two examples are shown in Figure 3-50. Pressurizations are marked by sudden peaks in the data. Not all graphs show pressurization peaks since not all strain gages were significantly impacted by the pressurization (e.g., gage C95R). The date for setting the strain equal to zero is November 2, 2015. Relative humidity data was available for only a portion of the simulation. Two pressurizations were performed in close proximity in March 2017.
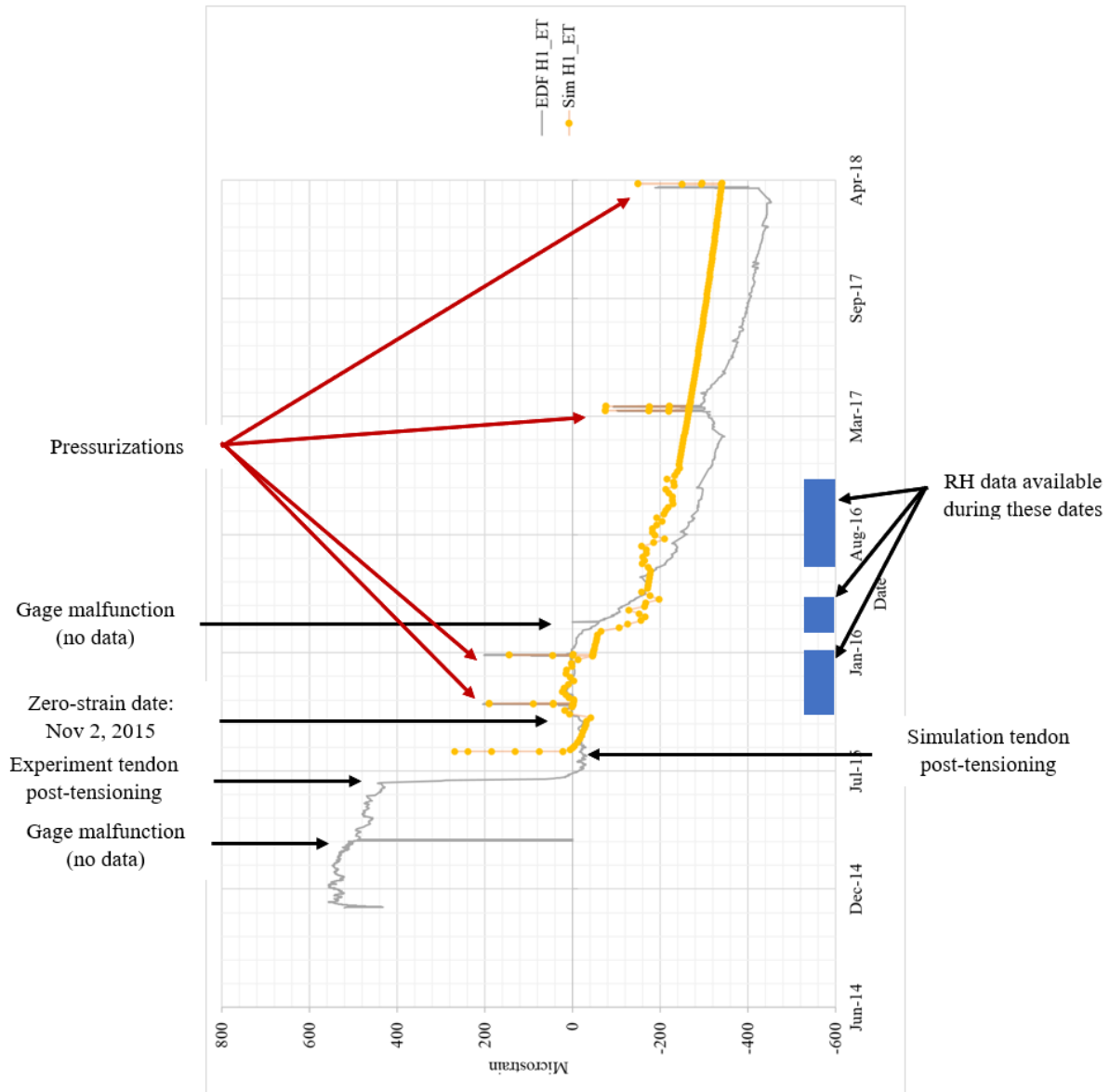
Figure 3-50   VeRCoRs strain gage data comparing experimental data with simulation results.

Moffatt & Nichol performed a brief sanity check on the concrete strain during pressurizations in the PCCV as shown in Figure 3-52. The calculations follow the procedure detailed in (US Nuclear Regulatory Commission, 2003). Assuming elastic behavior during a pressurization, the estimated hoop strain at mid-height in the cylinder wall away from all penetrations and structural changes is 209.6 $\mu\varepsilon$. The strain gage closest to this type of estimate—mid-height in the cylinder away from buttresses and penetrations—is H1ET (location shown in Figure 3-11). The strain of H1ET during the first pressurization 'Pre-Op' in November 2015 is shown in Figure 3-51. The pressurization history is slightly different between the experiment and the simulation. The experiment's exact pressurization history during 'Pre-Op' is unknown as only the pressurization history shown in Figure 3-23 was given to VeRCoRs participants. The experimental change in strain magnitude during pressurization was 205 $\mu\varepsilon$ while the simulation predicted a change of

3-45

191 $\mu\varepsilon$. These changes in strain magnitude during pressurizations are in close agreement with each other and with the calculated value. Therefore, the VeRCoRs PCCV can be assumed to behave elastically during pressurizations, and the elastic response of the simulation closely matches the experiment.
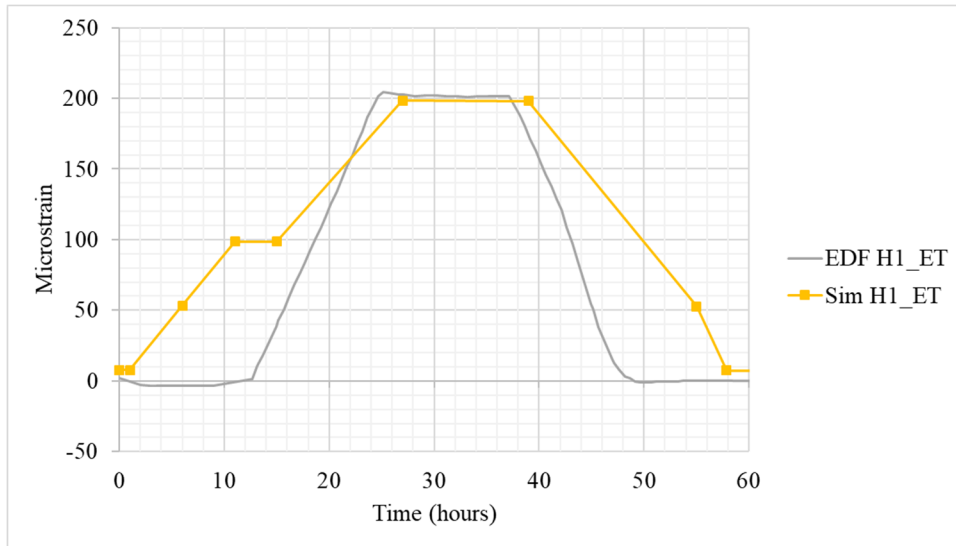
Figure 3-51   Strain gage H1ET strains during the first pressurization 'Pre-Op'.

Calculation for Approximate Hoop Strain in VERCORS PCCV

Material Properties

$$E_s := 200 \cdot 10^6 \, kPa \qquad \text{Reinfocing steel}$$

$$E_c := 34 \cdot 10^6 \, kPa \qquad \text{Concrete}$$

$$E_t := 190 \cdot 10^6 \, kPa \qquad \text{Tendons}$$

Concrete Thickness

$$t_c := 400 mm \qquad \text{thickness}$$

$$R_c := 7.3 m \qquad \text{Radius}$$

Hoop Bars

$$s_h := 133 mm \qquad \text{based on drawings}$$

$$\rho_{hoop.reinf} := \frac{\left(28.27 mm^2 + 50.265 mm^2\right) \cdot 2}{s_h \cdot t_c} = 2.952 \times 10^{-3}$$

Tendons

$$A_s := 139 mm^2$$

$$A_t := 4 \cdot A_s$$

$$s_t := 0.1333 m \qquad \text{approximate spacing}$$

$$\rho_{hoop.tendon} := \frac{A_t}{s_t \cdot t_c} = 0.01 \qquad \text{steel ratio}$$

Loading

$$P_o := 4.2 bar = 420 \, kPa \qquad \text{Applied Pressure}$$

$$t_{eqt} := \left(1 + \frac{E_s}{E_c} \cdot \rho_{hoop.reinf} + \frac{E_t}{E_c} \cdot \rho_{hoop.tendon}\right) \cdot t_c = 0.43 m \qquad \text{Transformed section with rebar and tendons}$$

$$\sigma_c := \frac{P_o \cdot R_c}{t_{eqt}} = 7.126 \times 10^3 \cdot kPa \qquad \text{Concrete Stress}$$

$$\varepsilon_c := \frac{\sigma_c}{E_c} = 209.6 \times 10^{-6} \qquad \text{Concrete Strain}$$

Figure 3-52   Moffatt & Nichol calculations for concrete hoop strain in the VeRCoRs PCCV during a pressurization away from penetrations or buttresses.

The full time history of gage H1ET is shown in Figure 3-53 (gage is located mid-height in the cylinder wall away from structural changes). The EDF experimental data matches well with the simulation results that include both drying and creep effects, particularly when the RH data is provided. The drying shrinkage effects were immediately noticeable upon implementation of the first available RH data in the code in October 2015. Periods of time with missing RH data, such as the times indicated in the figure, made a significant impact on the simulation response. If the RH changed significantly and the data was not available, the simulation results strayed from experimental data.

Also notable in Figure 3-53 is the importance creep in the overall strain magnitude. The line that shows simulation data without creep effects typically does not agree with experimental results.
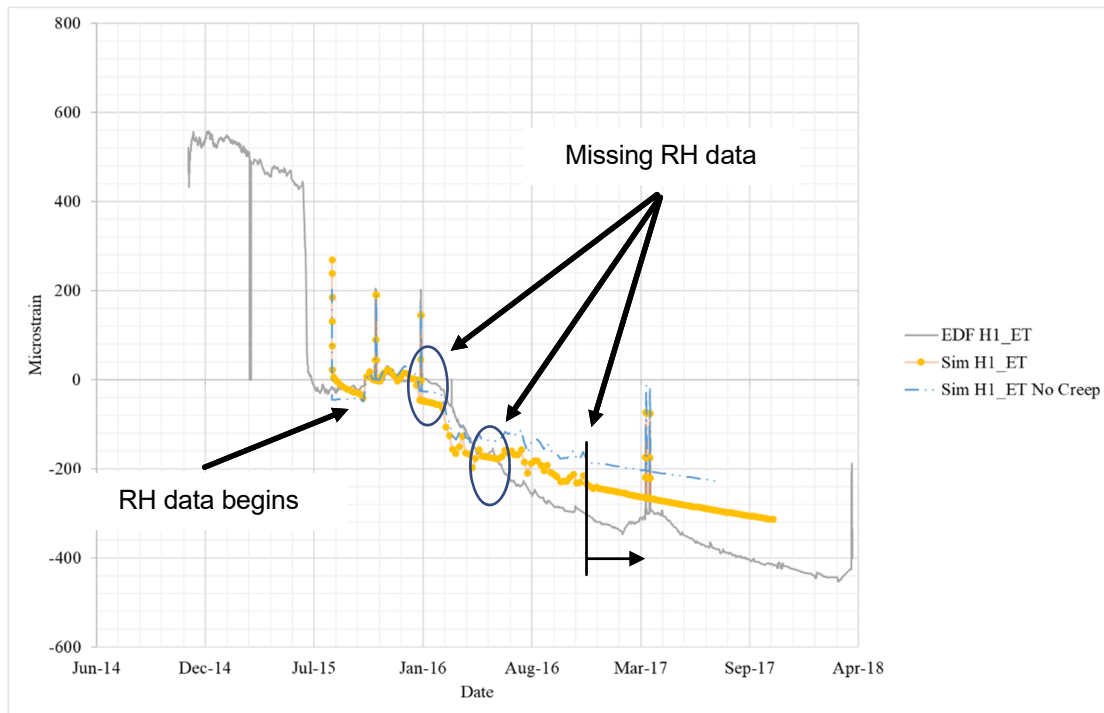
Figure 3-53   Time history of gage H1ET showing EDF experimental data, the simulation results, and the simulation results excluding creep effects.
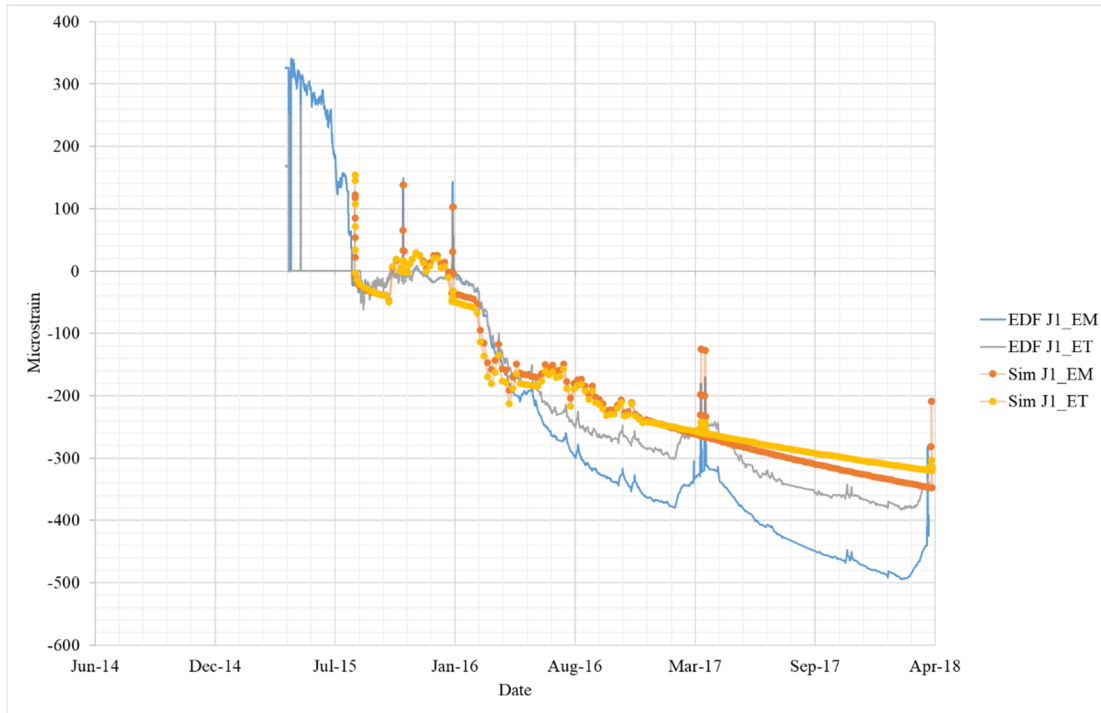
Figure 3-54   Comparison of EDF experimental data and SNL simulation results for strain gages J1EM and J1ET.

3.3   VeRCoRs Analysis by Moffatt & Nichol

Moffatt & Nichol analyzed SNL's simulation results as a third-party reviewer. The full document is presented in APPENDIX D , and select information is presented here.

First, Moffat & Nichol analyzed the strains on the interior and exterior surfaces of the VeRCoRs PCCV. The strains were analyzed at the end of each analysis step. For the pressurization step, an additional time increment at peak pressurization was extracted. On the interior and exterior surfaces, strain concentrations were found adjacent to the equipment penetrations (as seen in other containment vessels and as dictated by linear elasticity). Away from equipment penetrations, strains are fairly uniform. There is evidence of significant vertical bending at the wall-base juncture and adjacent to penetrations, but the strain magnitudes are not large enough to indicate damage. As the priority of this document is not focused on surface cracking, and as the analysis by Moffatt & Nichol indicates that no significant cracking would have occurred from the pressurizations, the reader is directed to APPENDIX D for the detailed cracking analysis.

Some noteworthy tensile strains were also observed in the radial direction of the finite element model. These are of particular interest for investigation of the potential of delamination-type failure. Two plots have been extracted from ABAQUS highlighting the mentioned strains as shown in Figure 3-55. These plots were taken after 575 days of simulation, roughly 60% of the total simulation time. This particular step represents a time after significant shrinkage has occurred, and after two full pressure cycles have taken place, but at the zero pressure unloaded conditions. The plots in Figure 3-55 show a pronounced band of elevated radial tension within the interior of the cylinder wall and within the interior of the tendon anchorage. The magnitude of this tension is in the range of approximately 0.000100 strain. So, although it is significant

3-49

enough to be captured numerically, it is insignificant with respect to cracking or delamination. In earlier time steps of the simulation (not shown here), this interior band of radial strain is not present. Therefore, this observed phenomenon is driven by drying shrinkage and exacerbated by the tendons pressing inward on the interior of the wall and by related Poisson effect. However, the relatively coarse mesh size (5 elements though the wall thickness with only 2 crossing the hoop tendons) may have limitations to capturing the detailed development of radial tensile creep strains. In short, Moffatt & Nichol recommended a finer mesh size for the radial tensile creep strain analysis.
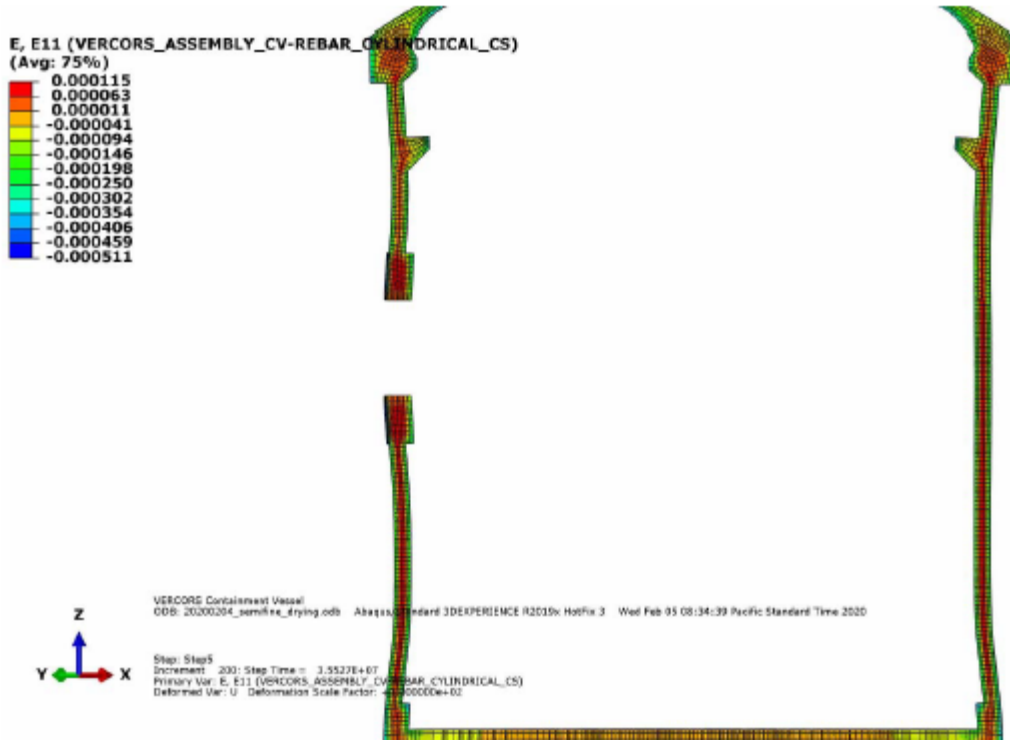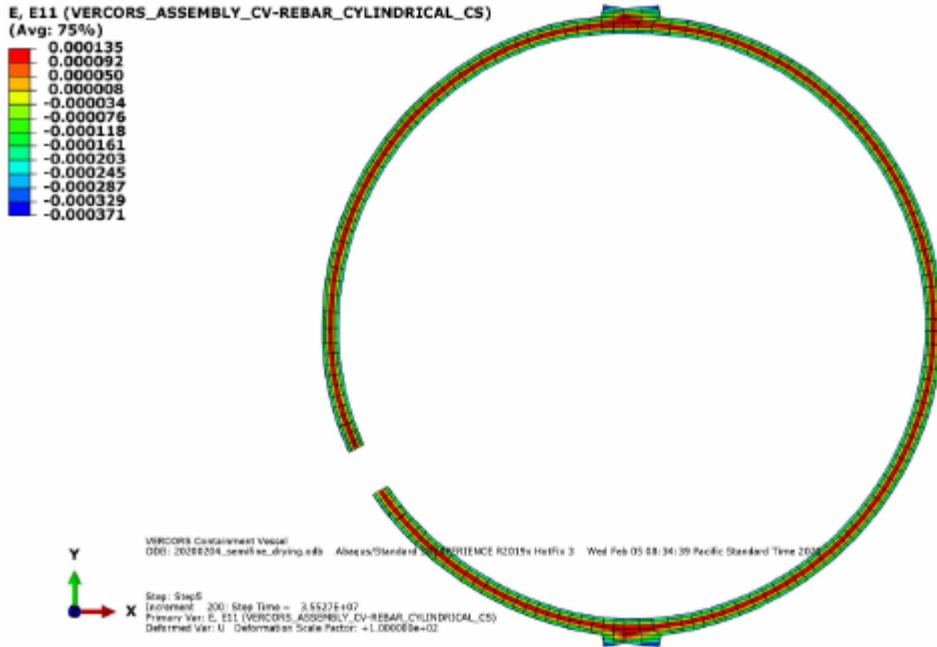
Figure 3-55   Moffat & Nichol ABAQUS plots of tensile "radial" strains in the containment vessel.

3.4   PCCV Thin-Slice Analysis

In response to the recommendation from Moffatt & Nichol for a finer mesh analysis of radial tensile creep strains in the containment, a finite element simulation was developed based on the VeRCoRs mockup that focused specifically on the effect of hoop tendons on tensile strain development in the wall of the containment vessel. The section of the PCCV selected for the analysis is shown in Figure 3-56. This section is away from penetrations but does include the buttresses.
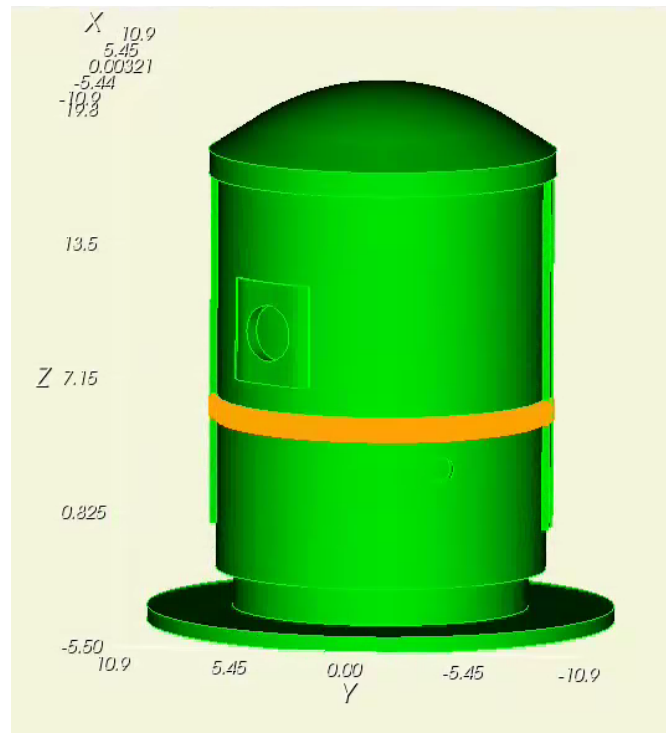
Figure 3-56   Thin-slice section of the VeRCoRs PCCV selected for fine mesh analysis.

3.4.1   Geometry and Mesh

The thin slice was 1.0 m high and shared the same diameter geometry as the VeRCoRs PCCV as shown in Figure 3-57. Two layers of rebar were included in the simulation, one on the interior face and one on the exterior face of the concrete with cover of 0.040 m as shown in Figure 3-58. Eight tendons were included in the simulation as shown in Figure 3-59, four interior tendons and four exterior tendons. As the buttresses and surrounding regions were not priority in this simulation, the tendons were simplified in this simulation as perfect circles rather than protruding from the buttresses. The tendons were vertically spaced at 0.153 m intervals, similar to the VeRCoRs PCCV. A cut view of the geometry including the concrete, rebar, and tendons is shown in Figure 3-60. The concrete mesh is shown in Figure 3-61. The concrete contained 70,752 8-noded hexahedral elements. Each rebar layer contained 1,626 4-noded surface elements. There were 4 layers of rebar: 2 on each face, one hoop and one vertical layer on each face, totaling 6,504 4-noded surface elements. Each tendon contained 287 2-noded beam elements, totaling 2,296 elements for all 8 tendons. The average element edge length for all geometries was 0.140 m. Tendons and rebar were embedded in the concrete with no slip allowed.

No vertical tendons were explicitly modeled in this simulation. A uniform vertical compressive pressure was applied to capture the effect of vertical prestressing in the concrete as described in Section 3.4.2 .
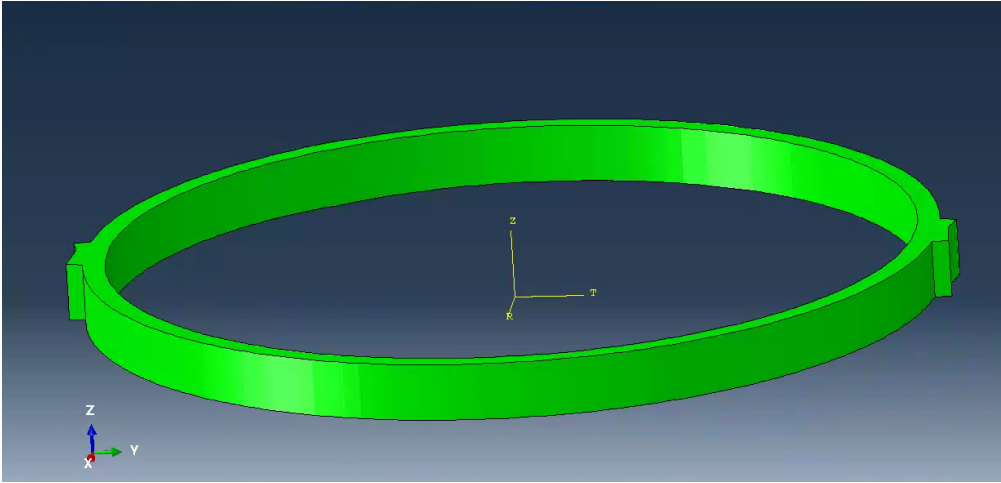
Figure 3-57   Thin slice of the VeRCoRs PCCV concrete geometry.
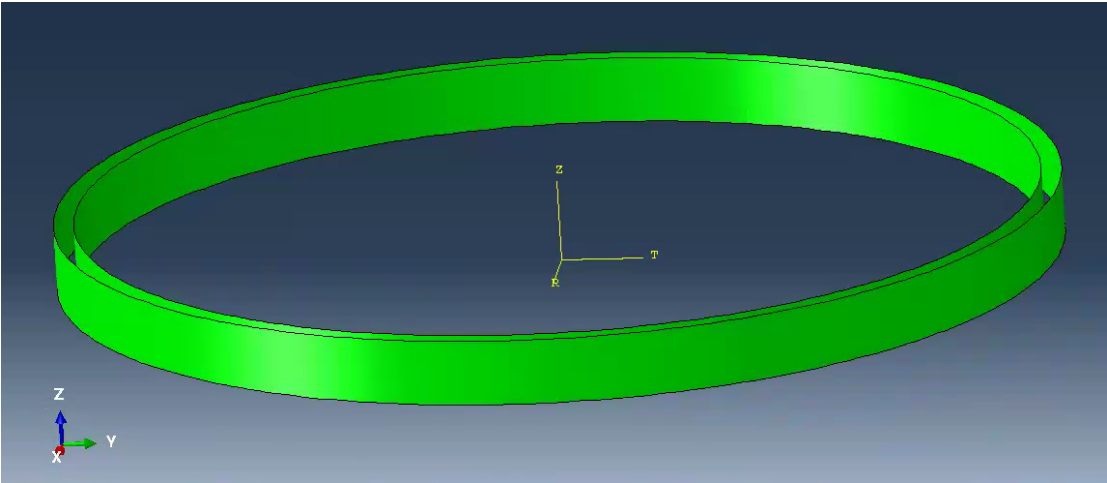
Figure 3-58   Thin slice of the VeRCoRs PCCV rebar geometry.
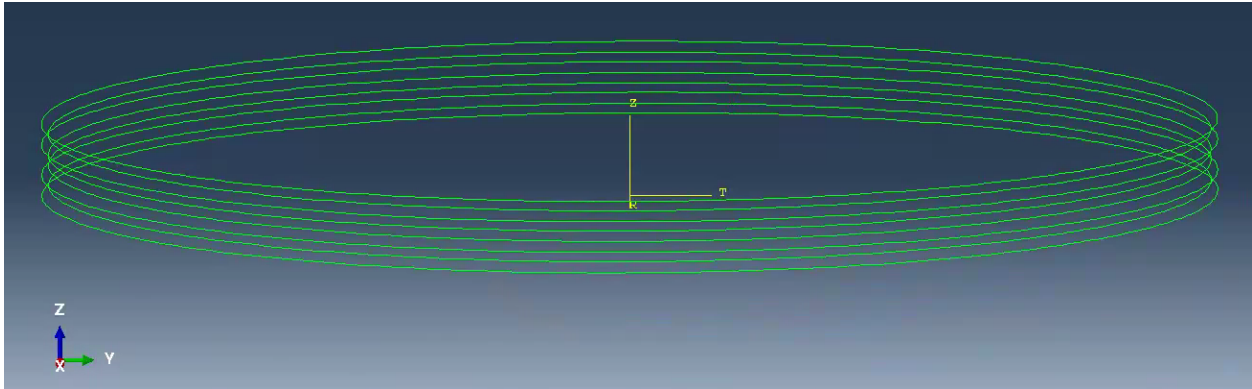
Figure 3-59   Thin slice of the VeRCoRs PCCV tendon geometry.
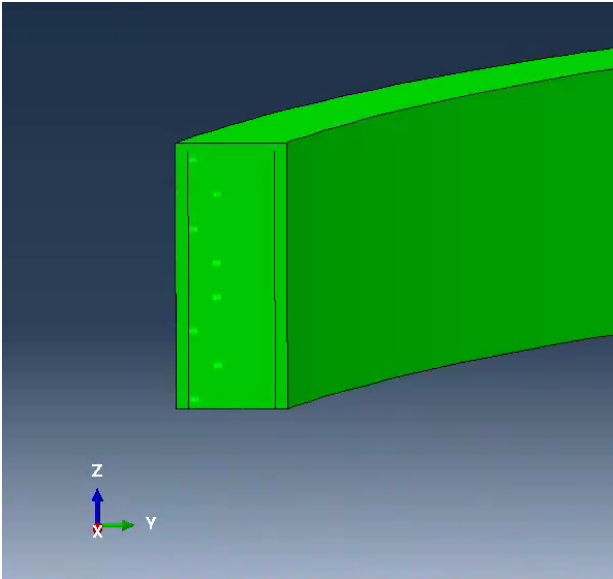
Figure 3-60   Cut view of the thin slice geometry including concrete, rebar, and tendons. The tendons are the small circular highlighted spots. The rebar layers are the black lines 0.040 m away from each concrete face.
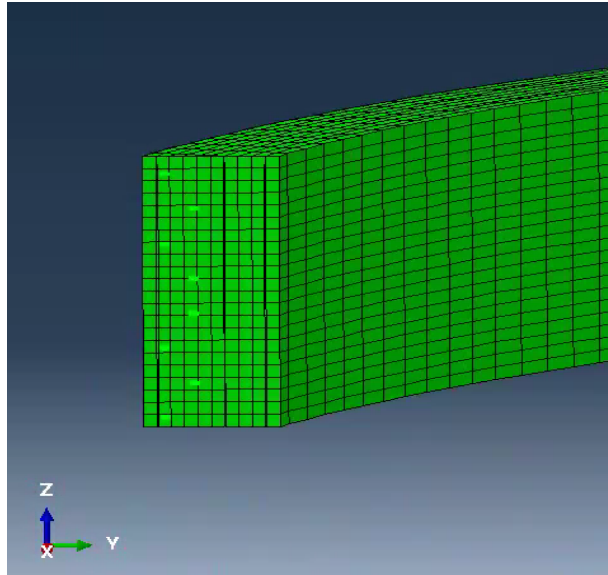
Figure 3-61   Cut view of the thin slice geometry showing concrete mesh. The lighter spots are the tendon locations.

3.4.2   Boundary and Initial Conditions

The entire bottom surface of the geometry was fixed against movement in the Z-direction (vertical). A uniform vertical compressive pressure of 5 MPa was applied across the entire top surface of the geometry to account for the compressive stress from the vertical tendons. The VeRCoRs concrete in this region of the PCCV sustained compressive stresses ranging from 4-8 MPa immediately after loading as shown in Figure 3-62 with the majority of stresses at ~5 MPa, so 5 MPa was used as an average value for this simulation. Since this simplified simulation was proof-of-concept rather than looking for specific numerical values representative of the VeRCoRs mockup, the PT tendons were subjected to an initial stress of 1000 MPa as an averaged value compared to the VeRCoRs mockup tendons. Five nodes on the exterior edge of one buttress were fixed in all directions to ensure numerical stability for this simulation.
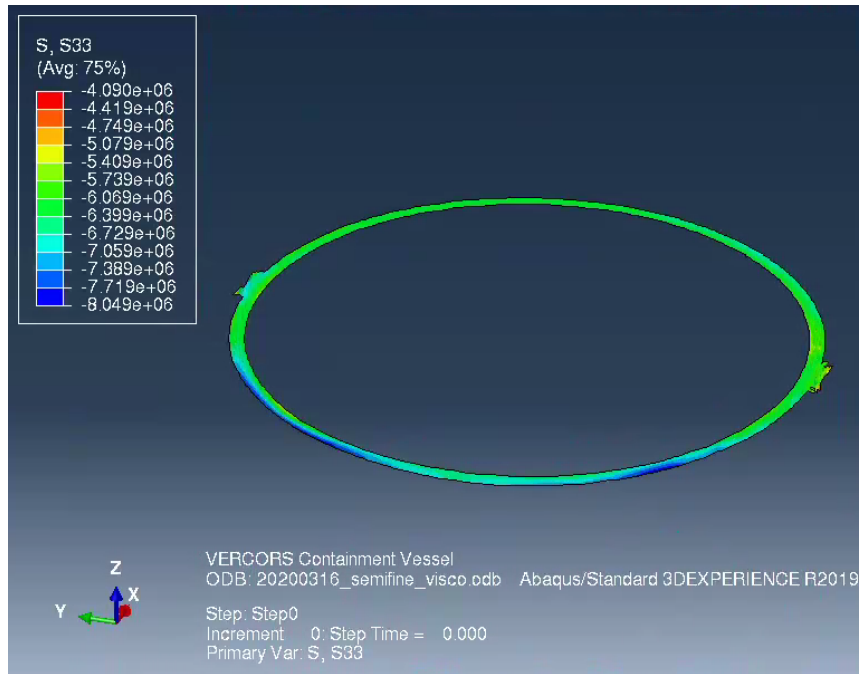
Figure 3-62   Slice of the VeRCoRs PCCV simulation immediately after post-tensioning and gravity showing vertical stresses in the concrete. Vertical compressive stresses in the concrete range from 4 to 8 MPa.

The simulation was allowed to progress for 40 years of simulation time. No pressurizations occurred. The only change over time was concrete creep.

3.4.3   Material properties

The material properties used in this simulation are the same as those used in the VeRCoRs simulation described in Section 3.2.3 .

3.4.4   Results

The radial stresses immediately after loading (including both vertical pressure and tendon prestress loads) are shown in Figure 3-63. In this image, positive values indicate tensile stresses while negative values indicate compressive stresses. Radial stresses range from approximately 273 kPa in tension to 663 kPa in compression. The tendon locations are indicated in Figure 3-63b. As can be seen, the region of tensile stress lies immediately on the outside (radially) of the hoop tendons with higher compressive stress immediately in the inside (radially) of the hoop tendons.

Figure 3-64 shows the radial strains in the thin-slice PCCV simulation immediately after application of loads. These results indicate that all radial strains were positive due to the Poisson effect from the vertical pressure. However, the effect of the hoop tendons on the radial strains is evident as the changes in radial strains follow the same pattern as changes in the radial stress in Figure 3-63.
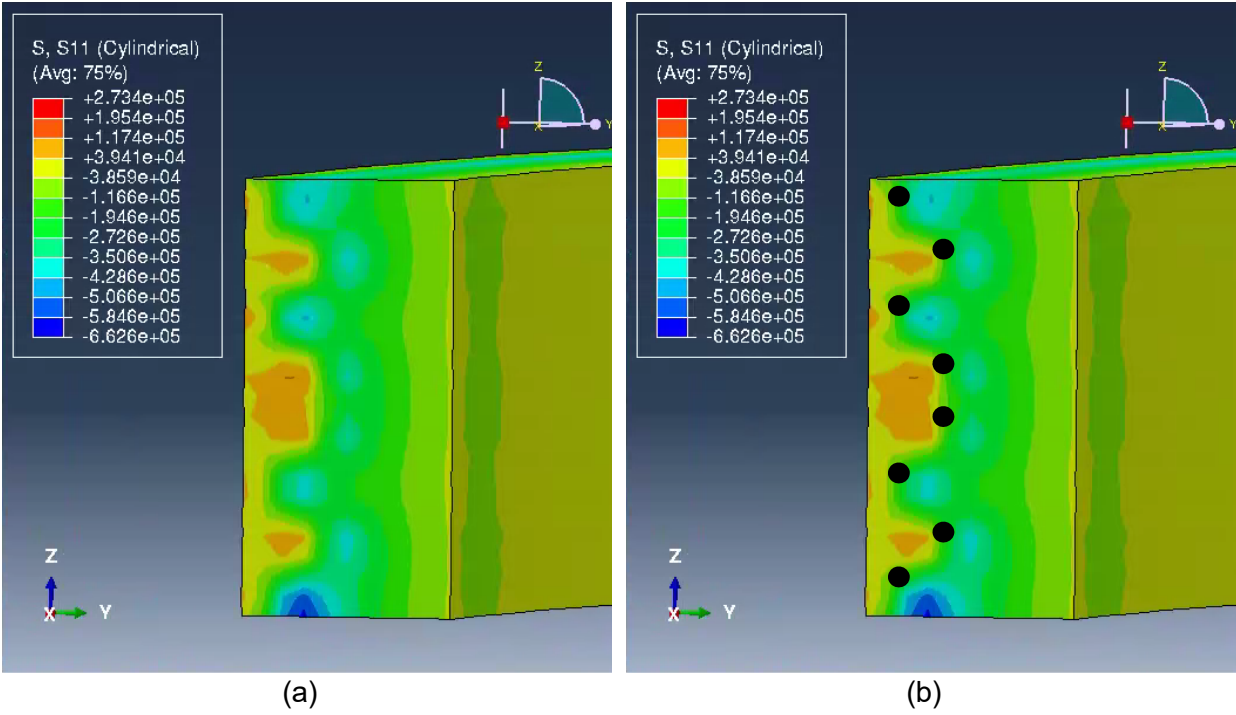
Figure 3-63 **(a) Radial stresses in the thin-slice PCCV simulation after application of loads. (b) Same image as (a) but with the tendon locations indicated.**
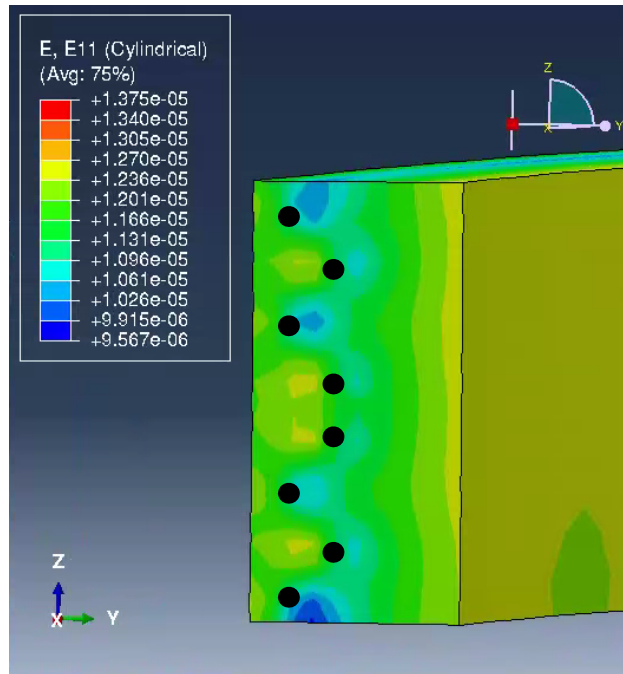
Figure 3-64 **Radial strains in the thin-slice PCCV simulation after application of loads. Tendon locations are indicated.**

Figure 3-65 shows the radial creep strains in the thin-slice PCCV simulation after 40 years of applied load. The creep strains immediately behind the post-tensioning tendons in Figure 3-65 (~6 x 10^{-5}) are on the same order of magnitude as the elastic response strains at the same location in Figure 3-64 (~1.2 x 10^{-5}), but the creep strains are ~5x larger than the elastic strains. The creep strains from post-tensioning being significantly larger than the elastic strains indicate that creep could be an issue in PCCVs that do not have radial reinforcement.

While the Moffatt & Nichol simulations in Figure 3-55 showed radial tensile strains (~1 x 10^{-4}) of similar magnitude to the combined strains from Figure 3-64 and Figure 3-65 (~0.72 x 10^{-4} combined), the strain profiles between the two simulations are different enough to warrant a brief discussion. Moffatt & Nichol summarized that the radial strains present in Figure 3-55 were driven by drying shrinkage. With only 5 elements through the thickness, the inner and outer elements shrank due to drying, pulling the inner elements into a radial tensile strain profile. However, Figure 3-64 and Figure 3-65 clearly show the effects of the post-tensioning tendons on the radial strain profile. The location of each tendon shows a reduced radial tensile strain "inside" the tendon and an increased radial tensile strain "outside" the tendon. While these strains are all likely too small to cause delamination failure without exacerbation, they do provide a layer of increased tensile strain that could be a weakness in the structure.
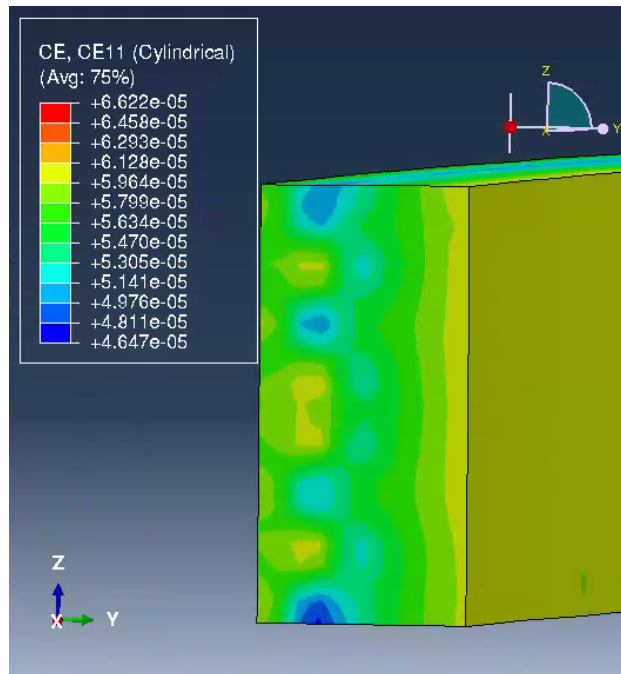
Figure 3-65   Radial creep strains in the thin-slice PCCV simulation after 40 years of applied loads.

Figure 3-66 shows the effect of the applied vertical load on radial stresses in the thin slice PCCV. Bear in mind that the applied compressive vertical stresses in this thin-slice simulation ranged from 0-5 MPa, values which are representative of the compression applied from PT tendons but also considerably lower than the uniaxial compressive strength of the concrete. With a vertical load of 5 MPa, the maximum radial tensile stress is 264 kPa. With a vertical load of 2.5 MPa, the maximum radial tensile stress is 261 kPa. With no vertical load, the maximum radial tensile stress is 259 kPa. The change in compressive vertical stress on the thin PCCV slice has little effect on the radial tensile stresses, likely due to the relatively low applied vertical stresses.

(a)	(b)	(c)
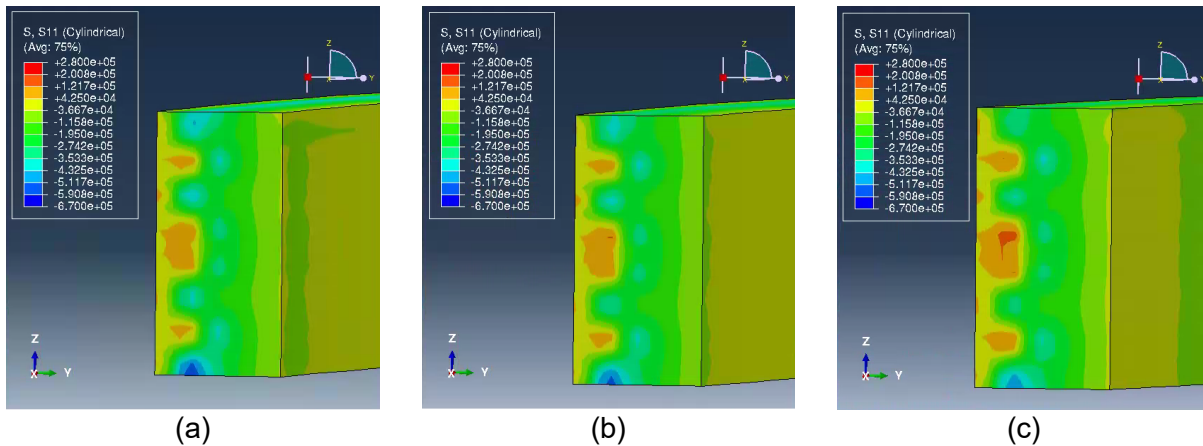
Figure 3-66   Radial stresses in the thin-slice PCCV simulation with varying vertical compressive loads: (a) 5 MPa, (b) 2.5 MPa, and (c) no vertical compressive load.

3.5   Limited Scope Study of Long-Term Effects of Creep on Post-tensioned Containments

Creep and creep rupture of concrete were identified in the EMDA report, NUREG\CR-7153, Vol. 4, as an area of low-knowledge and potential high significance (US Nuclear Regulatory Commission, 2014). A limited scope study on the effects of delayed creep in post-tensioned concrete containment vessels has been performed in collaboration with SIA and SSC. Jointly SSC with SIA have specialized experience of analyzing complicated concrete structural damage and material topics and specifically they have specialized knowledge of the CR3 PCCV delamination events. The SSC owner, Mr. Randy James, has some experience with the CR3 event as well as intimate knowledge of the ANACAP model and its use in the analysis of NPP structures, which were useful to define the models and scope of the analyses for the limited scope study. The effort consisted of simulations of various scenarios including possible existing defects, variations of facture properties and creep compliance, and/or detensioning sequence of groups of tendons (Table 3-9) into a PCCV structure in order to understand the sensitivity of each scenario on the creep response of the PCCV under those conditions. SIA has a proprietary concrete model called ANACAP that includes creep effects, nonlinear compressive stress-strain behavior of concrete, modeling of concrete cracking and shear degradation due to cracking, and interaction between concrete and reinforcement. A summary is presented here. See Appendix C for the full report.

Per the SIA/SSC report's Background section:

> The effects of creep on the long-term integrity of PCCVs is complicated and not intricately analyzed by structural engineers. While creep is included in the design basis for pre-stress loss in PCCVs, the long-term effects on the structural integrity have not been critically studied. The general sense has been that creep is mostly a shorter-term effect, and the effects of creep should decrease over time as the structure ages and the rate of creep dissipates. However, the delamination cracking that developed in the containment at Crystal River during a construction modification (see Figure 2-28) raised concerns about the possible longer-term effects of creep, especially when there

are changes in the loading. Research is needed to further investigate the effects of creep and identify situations where the integrity and pressure capacity of PCCVs may or may not be of some concern in the longer term.

This study is a limited scope to examine the issue of creep in concrete containment vessels and identify any need for further research. This effort is not an attempt to reconstruct all the circumstances that occurred in the Crystal River delamination problem as a kind of "root cause" analysis. Rather, the intent is to consider representative conditions for a situation where a known problem develops in order to show that the modeling employed can provide an indication of potential problems.

Table 3-9   Summary of Analyses (copy of SIA/SSC report Table 4-1)

Case	Section
Case A1 – Baseline Case, No Creep	4.1
Case A2 – Baseline Case, With Creep	4.2
Case B1 – Delamination During Initial Tensioning	4.3
Case B2 – Investigating Potential Delamination After Initial Tensioning	4.4
Case B3 – Intentional Delamination After Initial Tensioning	4.5
Case B4 – Intentional Delamination After 6.5 Years	4.6
Case B5 – Intentional Delamination Prior to Detensioning	4.7
Case B6 – Intentional Delamination After Detensioning	4.8
Case C1 – Differential Creep Compliance (0.5x & 1.0x)	4.9
Case C2 – Differential Creep Compliance (1.0x & 2.0x)	4.10
Case C3 – Differential Creep Compliance (1.0x & 0.5X)	4.11
Case C4 – Not Used	4.12
Case C5 – Differential Creep Compliance (0.5x & 3x)	4.13
Case D1 – Not Used	4.14
Case D2 – Not Used	4.15
Case D3 – Time Dependent Material	4.16
Case D4 – Time Dependent Material, Differential Creep Compliance (0.5x & 1.0x)	4.17
Case D5 – Time Dependent Material, Differential Creep Compliance (1.0x & 2.0x)	4.18
Case Fb2 – Variation of Case B2	4.19
Case Fc1 – Variation of Case C1	4.20
Case Fc2 – Variation of Case C2	4.21
Case Fd3w – Variation of Case D3	4.22
Case Fd4w – Variation of Case D4	4.23
Case Fd5w – Variation of Case D5	4.24

3.5.1   Single-Element Test Simulations

SIA/SSC begins their efforts by performing single-element test simulations to demonstrate the ANACAP concrete creep model capabilities. Simulations showed ANACAP's capability to

include concrete material properties that evolve over time. In practice, concrete material properties change over time. Excluding degradation, concrete increases in strength and elastic modulus as it ages. Although commonly designs are based on the 28-day material properties of concrete; SIA/SSC included in the study the effects of time-dependent material properties in an aging PCCV.

Single-element test simulations were performed to validate the capability of ANACAP for simulating time-dependent creep properties. Increasing the elastic modulus as the concrete ages alters the concrete's response to physical stimuli. The example scenario used by SIA/SSC subjects the element to an arbitrary compressive load, holds the load constant for 30 years, and then release the load. The load initially displaces the element by an axial strain of 500 $\mu\epsilon$. Unloading the element after 30 years, including an aging elastic modulus, returns the element to an axial strain of 95 $\mu\epsilon$. Because the elastic modulus has increased with age, the concrete element does not return to zero strain upon unloading. Similarly, the creep modulus of concrete decreases as concrete ages; young concrete subjected to a given load will creep more over time than old concrete subjected to the same given load. The single-element simulations also exemplify the effect of a time-dependent creep modulus, indicating that aging concrete will creep less than young concrete.

The single-element test simulations also illustrate that cracking damage in ANACAP is based on mechanical strains (total strains minus creep strain) where the crack initiation criteria are not dependent on creep response. That is, ANACAP captures cracking damage when mechanical strains are induced or affected by creep response, but it does not alter the input crack initiation criterion because of creep. Current literature on concrete creep does not provide a definitive conclusion about the effect of concrete creep strains on specimen fracture strain. In other words, research is unclear about the question, "If a concrete specimen is allowed to creep under a constant but relatively low stress, would the creep strain that accumulates cause the specimen to fail at lower ultimate stress relative to a specimen subjected to the same loads but without time to creep?" Therefore, the fact that ANACAP does not correlate or adjust tensile capacity with creep strains is important to note and is not in disagreement with current theory. Tensile cracking in ANACAP is governed by the magnitude of the load in the directions of principal mechanical strain. Cracks are assumed to form perpendicular to the directions of the largest tensile strains. Multiple cracks are allowed to form at each material point, but they are constrained to be mutually orthogonal. If cracking occurs, the normal stress across the crack is reduced to zero and the distribution of stresses around the crack is recalculated through equilibrium iterations. This allows stress redistribution and load transfer to reinforcement or other load paths in the structure. Once a crack forms, the direction of the crack remains fixed and can never change or heal. However, a crack can close, resisting compression and shear, and re-open under load reversals.

3.5.2   Model of Containment Structure

A representative containment structure was used in this study. Elements of the model are described below. Figures depicting the model are shown in Figure 3-67, Figure 3-68, and Figure 3-69.

- Buttresses: The model assumes six vertical buttresses equally spaced along the circumference. The buttresses are 6 ft wide and 5 ft 10 in thick. The buttresses are modeled as elastic with a Young's Modulus of $4 \cdot 10^6$ psi.

- Ring Girder: The model includes a 6 ft tall, 5 ft 10 in thick girder at the top of the panel to represent the ring girder (or the stiffened equipment hatch in the quarter-symmetric model). The girder is modeled as elastic with a Young's Modulus of $8 \cdot 10^6$ psi. This modulus is a factor of 2 greater than the other concrete components to account for additional stiffness provided by the adjacent concrete elements not explicitly modeled.

- Steel Liner: A 3/8 in steel liner (modeled as a membrane) is bonded to the inner diameter of the structure. The liner is modeled as elastic-plastic ($f_y = 50$ ksi, $f_u = 75$ ksi at 20% strain) with a Young's Modulus of $30 \cdot 10^6$ psi.

- Containment Wall: The containment wall is modeled as 3.5 ft thick and is modeled with the ANACAP concrete constitutive model. Unless otherwise stated, the concrete is assumed to have a 5 ksi strength, $4 \cdot 10^6$ psi Young's Modulus, and a Poisson's Ratio of 0.2. The containment wall is modeled with quadratic solid elements.

- Containment Wall Reinforcement: The containment wall includes vertical and horizontal reinforcement. The reinforcement is modeled as elastic- plastic ($f_y = 60$ ksi, $f_u = 75$ ksi at 10% strain) with a Young's Modulus of 29·106 psi. The horizontal rebar is modeled as #9 @ 12 in on each face. The vertical rebar is modeled as #9 @ 10 in on each face. Rebar is modeled as linear truss elements. Tie bars (stirrups) are not included in the model. The reinforcement is embedded in the concrete through an embedment constraint providing strain compatibility between the concrete and rebar.

- Containment Wall Tendons: The containment wall includes vertical and horizontal tendons. The tendons are modeled as elastic-plastic ($f_y = 200$ ksi, $f_u = 235$ ksi at 10% strain) with a Young's Modulus of $28 \cdot 10^6$ psi. Both horizontal and vertical tendons have a cross-sectional area of 10.9 in^2. Vertical tendons are spaced radially every 2.5°, which roughly equates to a 35.2 in circumferential spacing. Horizontal tendons are located in alternating layers spaced at 12.75 in and 25.5 in respectively. The vertical and horizontal tendons are located 15.2 in and 10 in from the containment wall outer radius, respectively. The tendon prestress is applied through an imposed temperature change of 810°F, which for a $6.5 \cdot 10^{-6}$ in/in/°F expansion coefficient, equates to $5.27 \cdot 10^{-3}$ in/in or 147 ksi or 1600 kip per tendon. This roughly equates to 1 ksi and 2 ksi compression in the vertical and horizontal directions, respectively. The tendon force is not altered to account for friction, wobble, steel relaxation, etc. The tendons are embedded in the concrete through an embedment constraint and are modeled as linear truss elements. No reduction in concrete area (accounting for tendon ducts) is included.
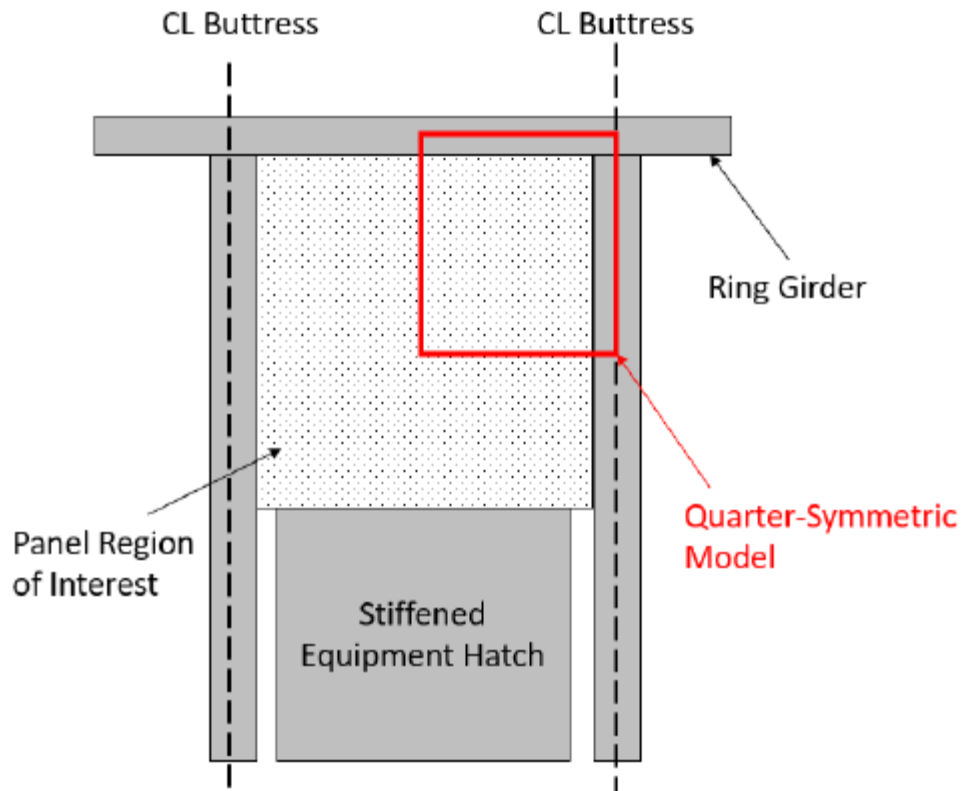
Figure 3-67   Schematic of modeled region.
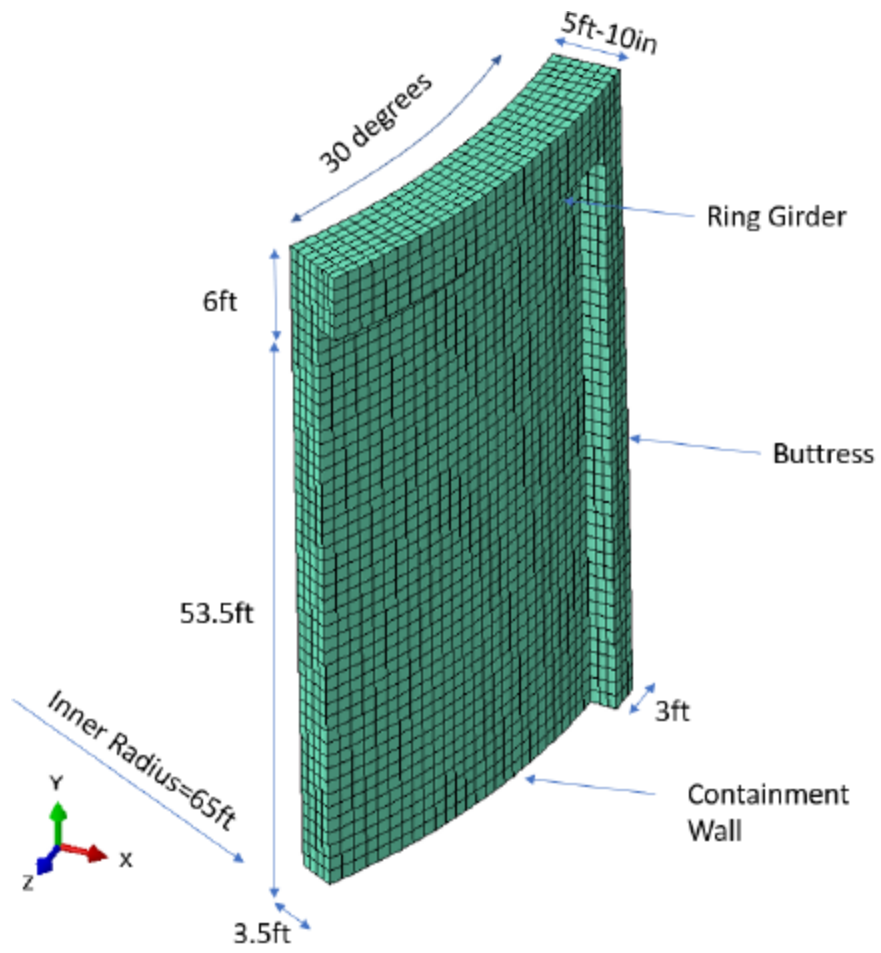
Figure 3-68   FEM - Concrete geometry.
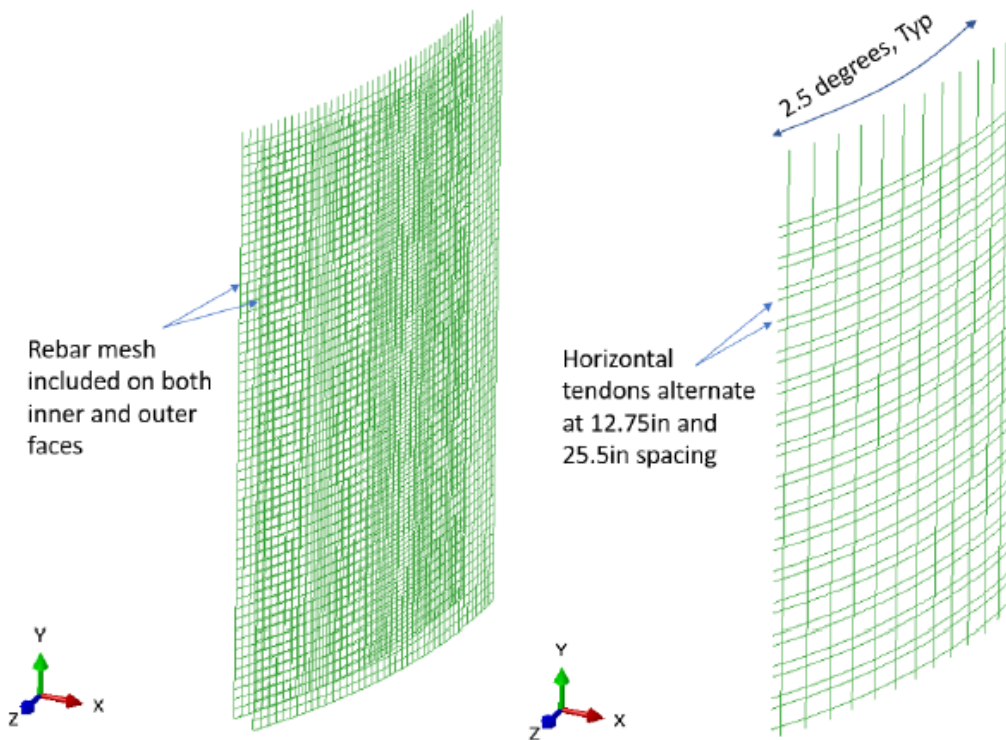
Figure 3-69   FEM - Vertical and horizontal rebar (left) and tendons (right).

The structure is modeled with quarter symmetry. A vertical boundary is included at the base of the model ($\Delta y = 0$). A circumferential boundary is included at the buttress and containment wall ($\Delta\theta = 0$). These boundary surfaces are highlighted in Figure 3-70.
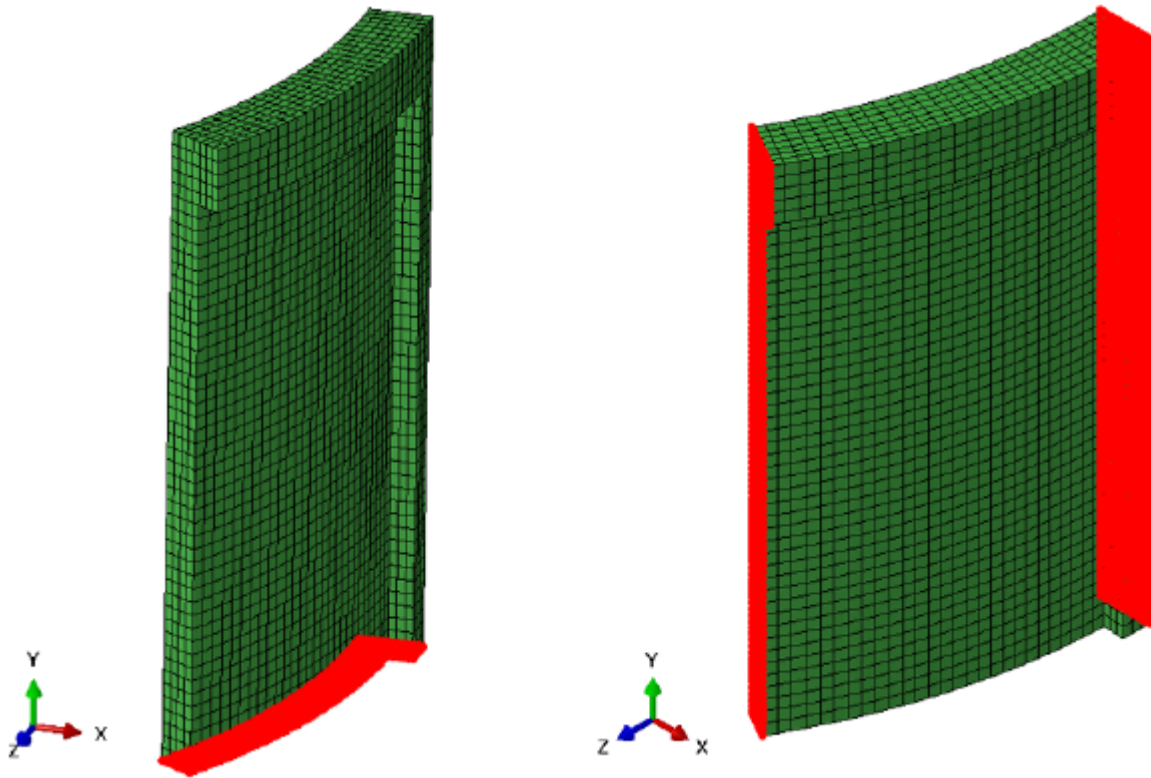
Figure 3-70   FEM - Vertical (left) and circumferential (right) boundary conditions.

Unless otherwise stated, the creep compliance used in the assessments is that indicated in Figure 3-71 (e.g., creep compliance = (total strain – initial strain) / initial strain). The creep model includes both primary and secondary creep and treats both as fully recoverable with a viscoelastic formulation.
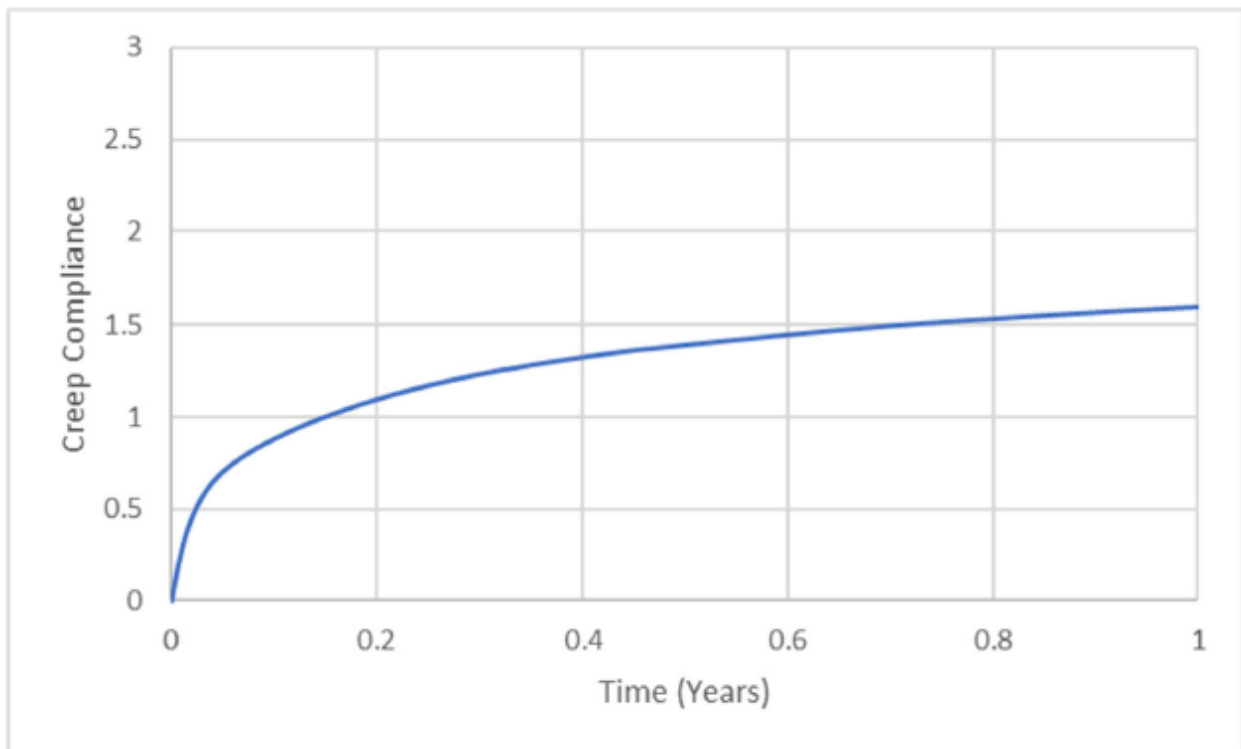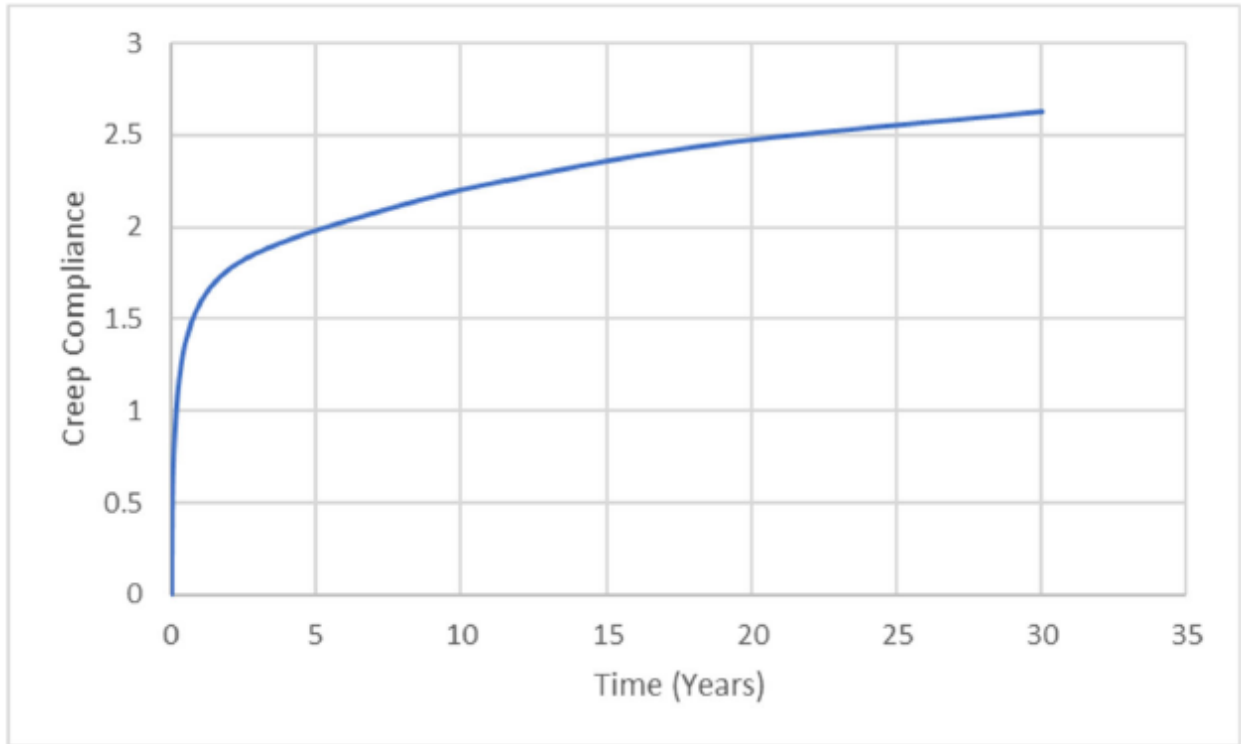
Figure 3-71   FEM—Creep compliance (Top = 30 year, Bottom = 1 year).

Each analysis is segregated into multiple analysis steps. The first steps apply gravity and the tendon tensioning force. The analyses are then permitted to run through the creep steps that span ~30 years. At the end of ~30 years several tendons (both horizontal and vertical) are removed to represent de-tensioning that would occur before an equipment opening would be cut into the containment wall. The tendons that are de-tensioned are shown in Figure 3-72 with the approximate location of the proposed equipment opening also highlighted. These analyses do not include effects of cutting the opening. The tendons are both tensioned and de-tensioned by applying a temperature load to the tendon elements.
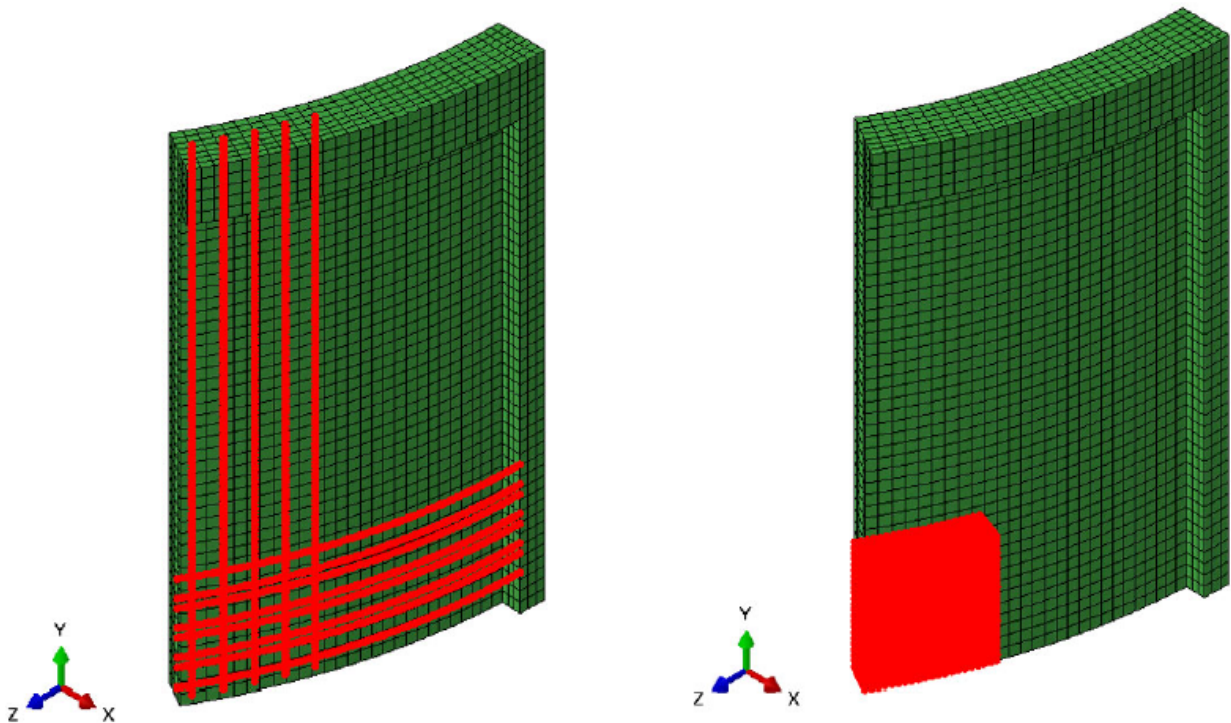
Figure 3-72   FEM—De-tensioned tendons (left) and future concrete opening (right).

3.5.3   Summary of Assessments and Findings

Twenty-one analysis variations (Table 3-9) were considered in this study. Variables considered included concrete fracture strain, creep compliance factors, differential creep, time dependent concrete material properties, and tendon removal sequence. Results were obtained from the ABAQUS ODB file (i.e., strain magnitudes and contours) and the ABAQUS MSG file (number of concrete cracks). Investigation of the MSG file was required as the ODB file does not present mechanical strain, which causes crack formation, but total strain. The MSG file reports the number of cracks opened (and closed) from the ANACAP concrete model for the three directions allowed in the model. The references in the SIA/SCC report for 1, 2, and 3 cracks refer to cracks in the three principal strain directions where crack 1 is in the maximum principal strain direction for the uncracked system, crack 2 is then relative to that rotated system, and crack 3 would be perpendicular to both direction 1 and 2. By comparing the opening and closing of these cracks with the calculated strain directions, the type of induced cracking (bending or radial/delamination) can be determined. It is also noted that some plots in the SIA/SSC report show radial strains much higher than the cracking strains but without cracks reported. This

3-68

again is due to the plots only showing total strains and not just the mechanical strains that induce cracking. In addition, some references are made to radial mechanical strains higher than the fracture strain, but no cracking is initiated. This is due to the crack initiation criteria where split cracking can initiate near a free surface where there is little tensile stress but requires sufficient tensile strain that is about twice the fracture strain to initiate split cracking. This is illustrated in Figure 3-4 of the SAI/SSC report in Appendix C. Select SIA/SSC conclusions are as follows.

- The radial strain profile after detensioning is significantly different if creep is included in the analysis (Case A1 vs A2, Figure 3-73 and Figure 3-74 respectively), and the profile with creep better resembles the hourglass shape found in the delamination cracking pattern at Crystal River (see Figure 2-28 for the hourglass delamination shape).
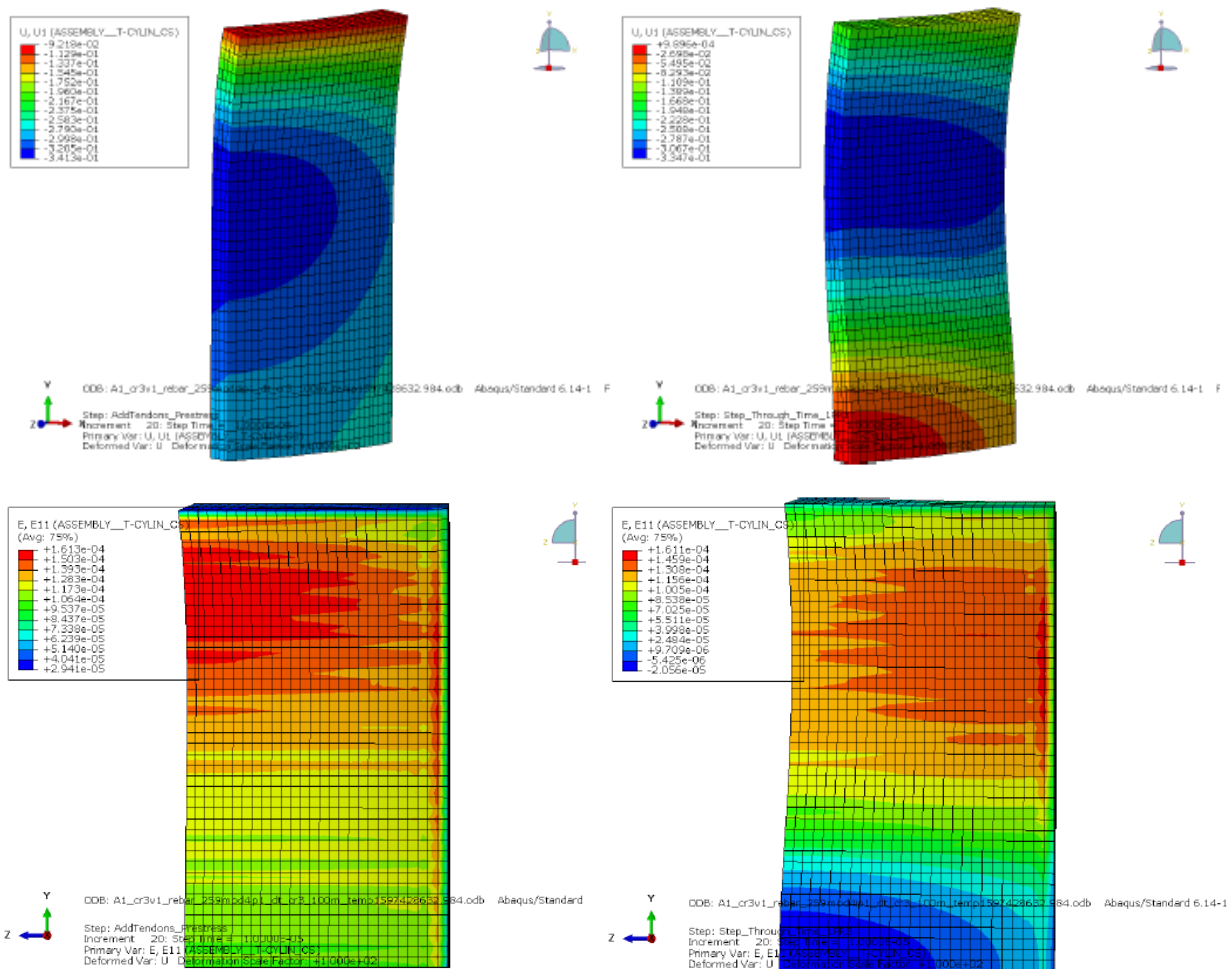
Figure 3-73   Case A1—Radial displacement after initial stressing (top left) and after detensioning (top right); radial strain after initial stressing (bottom left) and after detensioning (bottom right).
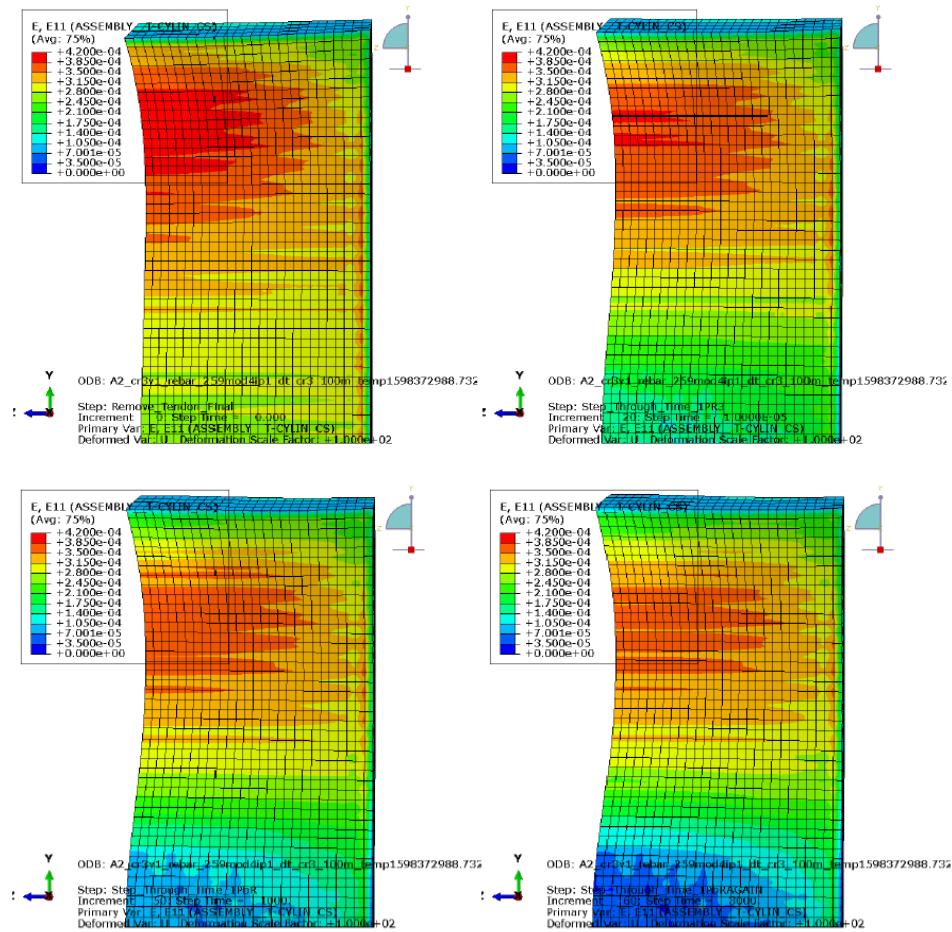
Figure 3-74   Case A2 – Radial strain before (top left) and after (top right) detensioning; radial strain after 1250 hours (bottom left) and 5250 hours (bottom right) of creep recovery. Note that the strain profile now resembles the hourglass shape seen at Crystal River.

- A sufficiently large concrete fracture strain capacity is required during initial tendon stressing or delamination may occur (Case B1, Figure 3-75) due to radial tensile strains that develop on the outer side of hoop tendons. Delamination, when it occurs, appears to follow the radial strain contour which is observed in actual delamination failures.

3-70
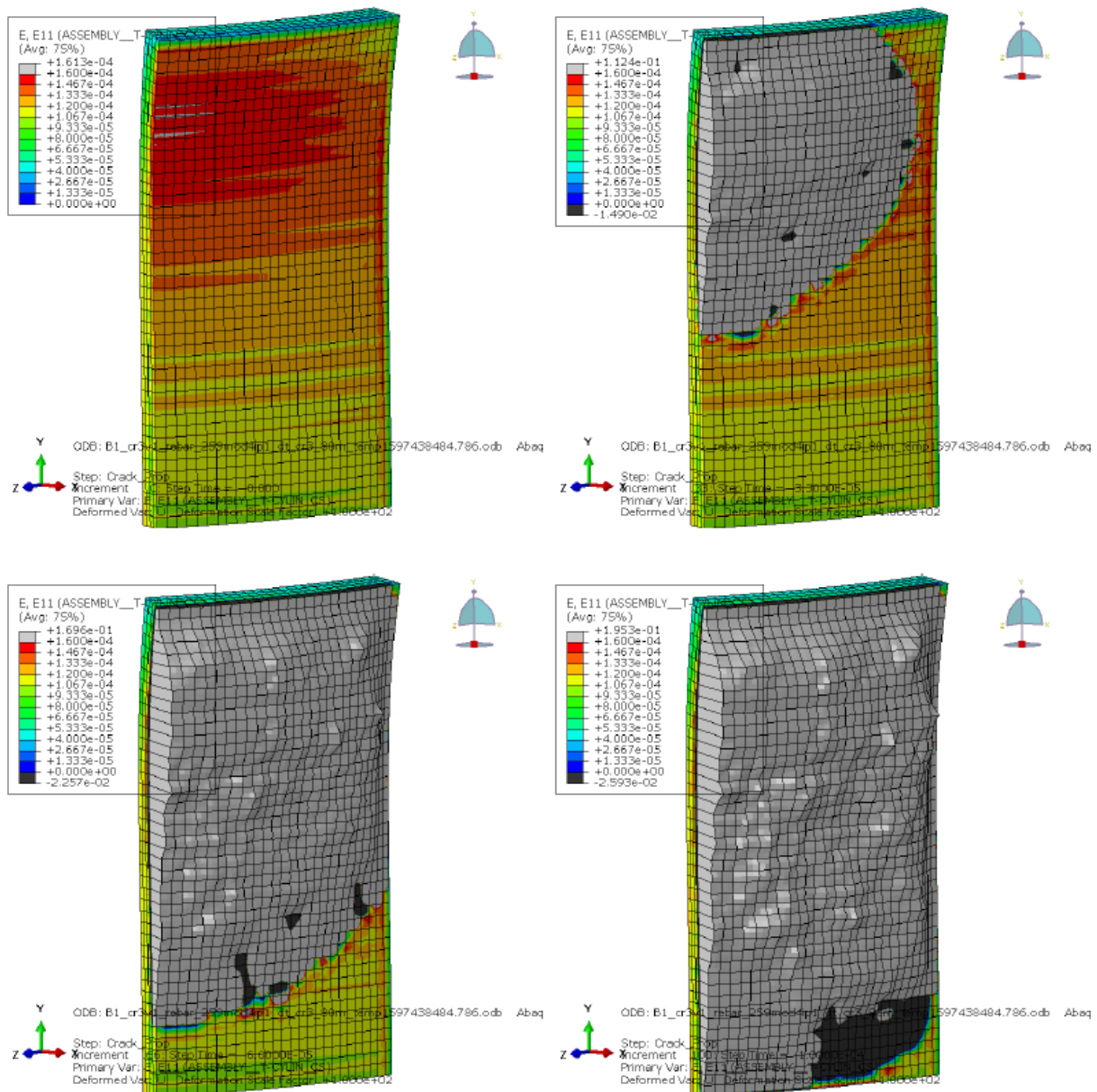
Figure 3-75   Case B1—Crack propagation (radial strain) at end of initial stressing. In this analysis tensile strain was iteratively reduced to allow a crack to form at 0 years, and then an assessment was performed to observe how the crack in the containment wall might propagate due to creep.

- After initial stressing, creep appears to reduce the radial mechanical strain, resulting in a lower likelihood of delamination (Case B2, Figure 3-76). However, if a local defect is introduced just after initial tensioning (i.e., early in the creep analysis), there may still be sufficient mechanical strain demand to cause widespread delamination (Case B3, Figure 3-77).
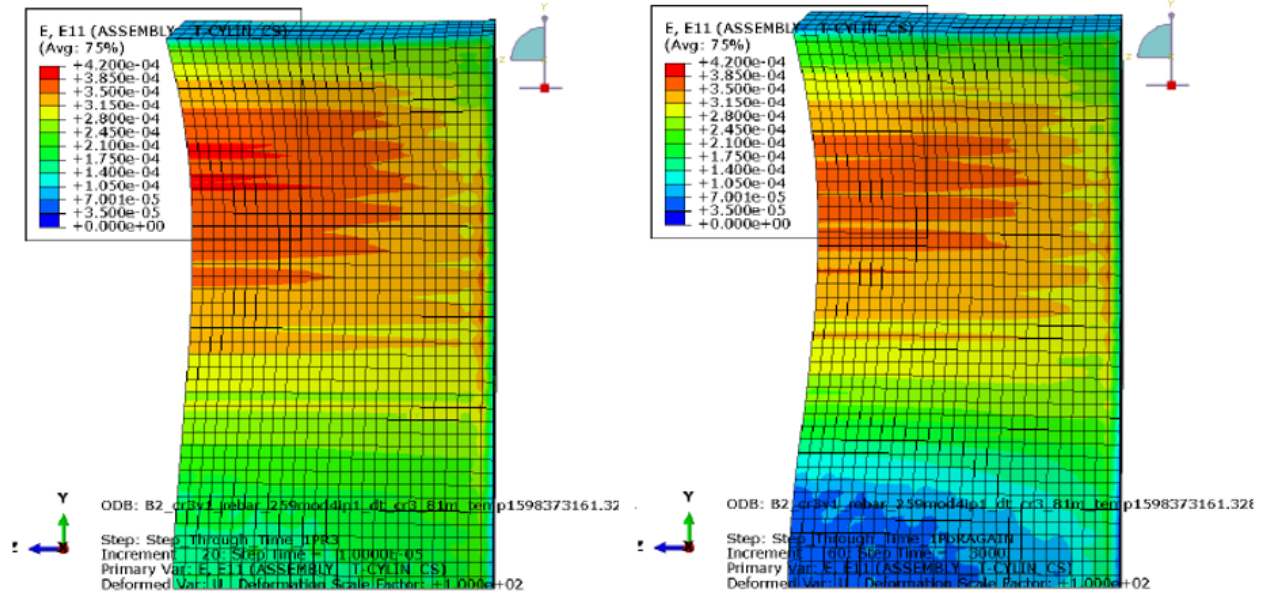
Figure 3-76   Case B2—Radial strain after detensioning (left) and after 5250 hours of creep recovery (right).
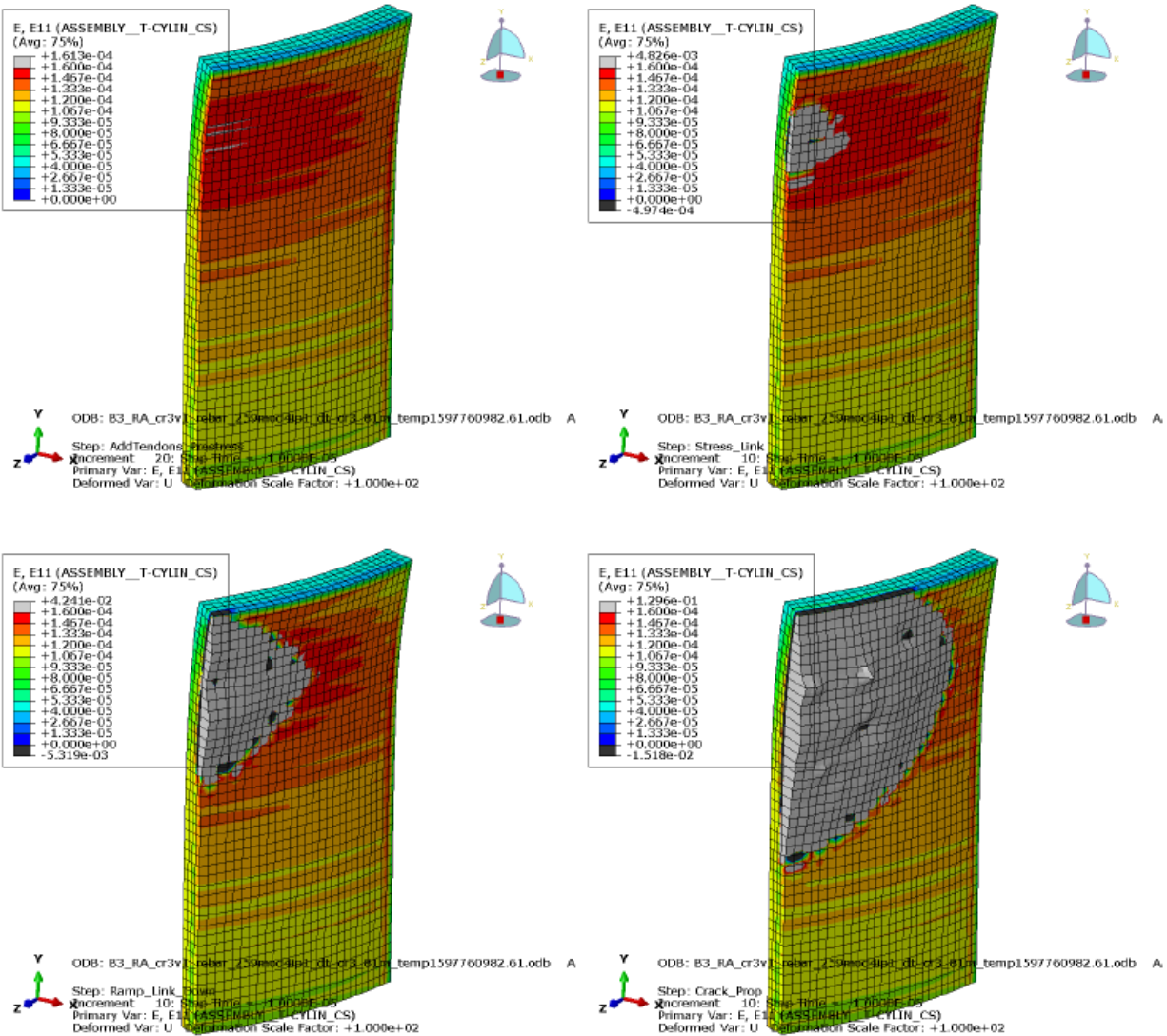
Figure 3-77   Case B3—Crack propagation (radial strain) at end of initial stressing (top left) and start of creep strain (bottom right).

- If a local defect is introduced in a manner similar to Case B3 but significantly after initial tensioning (6.5 years after initial tensioning (Case B4), just prior to detensioning (Case B5), or immediately after detensioning (Case B6)), a cascading delamination event was not observed. See Figure 3-78.
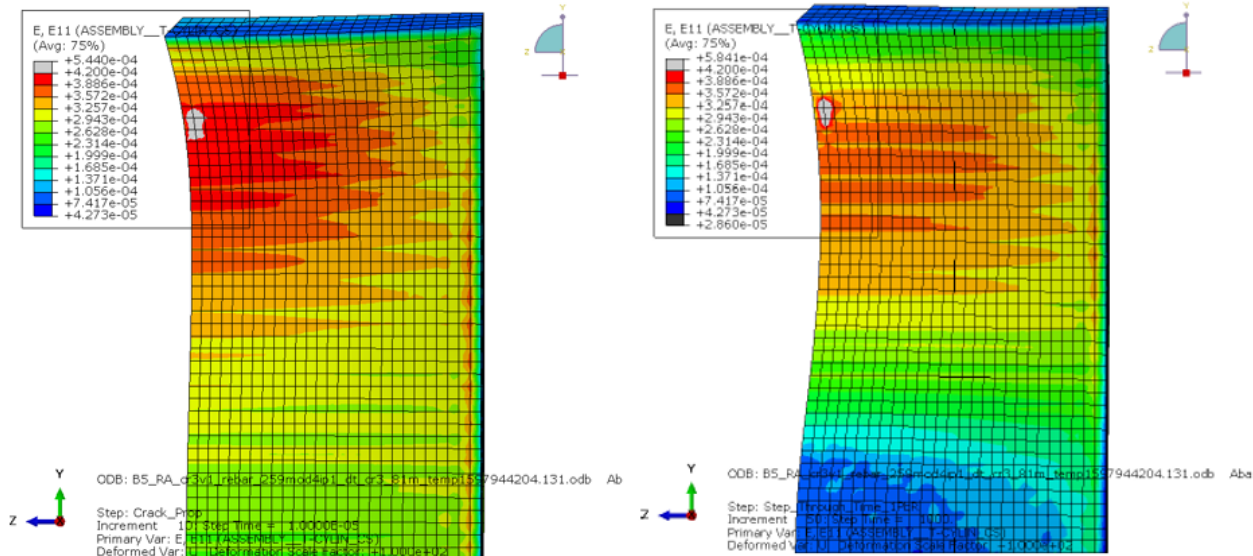
Figure 3-78   Case B5—Radial strain after introduction of local defect (left) and 1250 hrs after detensioning (right).

- Removing the horizontal tendons while leaving the vertical tendons in place shows an increase in mechanical radial strain after detensioning and an increase in total radial strain during the creep recovery steps. The effects of creep coupled with the sequence and timing of tendon detensioning may play a role in exacerbating delamination cracking.

- Differential creep analyses, wherein a lower creep factor was assigned to the outer concrete elements, caused a delamination failure to occur during the creep steps. The outer diameter concrete elements appear to act as a displacement restraint, leading to the development of mechanical strain as the interior concrete elements creep inwards.

3.6   Simulation Conclusions

- When RH data was available, the VeRCoRs simulation results aligned well with experimental data. Missing RH data skewed the simulation results away from the experimental data.

- The implementation of the Bažant B3 concrete creep model (with its correction factor) into the simulation via a Prony series was successful in modeling the creep response of the PCCV. Figure 3-53 indicates that incorporating the creep response was necessary to match experimental data.

- The implementation of concrete drying shrinkage strains using Fick's 2nd Law of diffusion via the ABAQUS thermal equation was successful in modeling the concrete drying shrinkage response of the PCCV. Figure 3-53 indicates that incorporating drying shrinkage was necessary to match experimental data.

- The mechanical response of the PCCV to the internal pressurizations in the simulation matched the experimental response as shown in Figure 3-51 and the calculations performed by Moffatt & Nichol as shown in Figure 3-52.

- The Moffatt & Nichol analysis indicates that the PCCV strains are likely within design limits during pressurizations at design pressure of 4.2 bar, and no significant cracking is expected.

- The PCCV thin-slice analysis, which is representative of the VeRCoRs PCCV, clearly indicates the development of tensile stress and tensile creep strain zones in the radial direction in the PCCV wall.

- The SIA/SSC analyses indicate that cascading delamination events can occur under certain circumstances. However, not all structural defects in the delamination plane are guaranteed to lead to cascading delamination events such as seen at Crystal River. If a local defect is introduced into the structure just after initial tensioning, a cascade delamination may occur. However, if a local defect is introduced into the structure significantly after initial tensioning, a cascading delamination event may not occur.

- The SIA/SSC differential creep analyses, wherein a lower creep factor was assigned to the outer concrete elements, caused a delamination failure to occur during the creep steps. This material scenario could potentially exist if a large thermal or humidity gradient exists radially across the PCCV concrete. A large humidity gradient is not expected due to the extremely low transport properties in mass concrete, but a thermal gradient scenario may warrant further investigation.

- Additional research can better determine the conditions in which these radial strains and creep effects could lead to initiation of delamination.

4 NONDESTRUCTIVE EVALUATION AND MONITORING TECHNIQUES

Since the degradation mechanisms for concrete tend to be variable in distribution and severity, monitoring and evaluation of containment structural health provides updated and complimentary information of predictive structural modeling. In this section, state of the art monitoring and inspection techniques are presented including both NDE techniques and long term continued sensing technologies. Particularly, the techniques used in the VeRCoRs experiment are described and evaluated.

4.1 Brief Summary of Current Techniques in Practice

Current NDE and monitoring techniques in NPPs have the capacity to utilize a wide array of technologies. Concrete inspections in NPPs are most often strictly visual, and any visible anomalies will require further NDE inspection. Visual cues of concrete degradation include spalling, efflorescence, surface staining, and cracking. Existing concrete NDE techniques such as impulse response, half-cell potential, cover meter, and hammer sounding have been used in NPPs. Hammer sounding is very easy to perform and is typically done by plant personnel. However, more advanced NDE techniques require a higher level of experience with and knowledge about equipment than does a routine hammer sounding inspection (Electric Power Research Institute, 2015).

Tendon inspections are performed by tendon lift-off tests, and tendons with low stress levels or obvious signs of corrosion at the tendon jacking location (such as free water or rust) indicate further inspection is necessary. Steel liner inspections are performed visually and any visual indication of corrosion or structural changes (such as liner bulge) warrant further inspections. Monitoring techniques of PCCVs range from routine visual inspections, strain gages on tendons and embedded in concrete, temperature sensors, humidity sensors, etc. However, monitoring equipment in NPPs are susceptible to damage, degradation, and failure (Electric Power Research Institute, 2014).

A thorough presentation of NPP aging management plans (AMPs), which includes monitoring and inspection techniques, can be found in:

- American Society of Mechanical Engineers (ASME) code Section XI IWE (steel) and IWL (concrete) (ASME, Boiler Pressure Vessel Code Section XI, 2011)

- Standard Review Plan for Review of License Renewal Applications for Nuclear Power Plants NUREG 1800 Rev 2 (US Nuclear Regulatory Commission, 2010)

- Generic Aging Lessons Learned (GALL) Report NUREG 1801 Rev 2 (US Nuclear Regulatory Commission, 2010)

- Generic Aging Lessons Learned for Subsequent License Renewal (GALL-SLR) Report NUREG 2191 Volume 1 and 2 (US Nuclear Regulatory Commission, 2017) (US Nuclear Regulatory Commission, 2017)

- Standard Review Plan for Review of Subsequent License Renewal Applications for Nuclear Power Plants NUREG 2192 (US Nuclear Regulatory Commission, 2017)

- Non-destructive Testing of Nuclear Power Plant Concrete Structures State of the Art Report (Wiggenhauser, et al., 2013)

Information on current concrete NDE and monitoring techniques are available in literature such as provide by the American Concrete Institute, the American Society for Nondestructive Testing, the Federal Highway Administration, and (Maierhofer, Reinhardt, & Dobmann, 2010). Some examples of non-destructive testing and evaluation in NPPs include:

- Locating steel reinforcement and identification of its cover and depth.

- Locating tendon ducts, both metal and plastic, and (if tendons are grouted) identification of the condition of the grout materials.

- Detection of cracking, voids, delamination, and honeycombing in concrete structures.

- Detection of inclusions of different materials or voids adjacent to the concrete side of the containment liner.

- Identification of corrosion occurrence on the concrete side of the containment liner.

4.2   Select Proposed and Experimental Techniques

This section summarizes proposed and experimental NDE and monitoring techniques. Emphasis in this section is on information from the VeRCoRs project and a parallel project by EDF titled the Non-Destructive Evaluation of Containment Nuclear Plant Structures (ENDE) project aimed at developing NDE for containment enclosure applications.

4.2.1 Electric Power Research Institute

EPRI is researching nondestructive evaluation techniques for concrete and large concrete structures. EPRI is also conducting research on the efficacy of current NDE practices.

In an extensive review of automated and remote inspection techniques, EPRI has reviewed over a dozen proposed, prototype, and commercial systems for inspecting large concrete structures (Electric Power Research Institute, 2013) (Electric Power Research Institute, 2014). These systems are designed to reduce time and costs as well as inspect the structures without putting personnel at risk (i.e., no scaffolding is required). The reports reviewed tethered and untethered robotic crawlers with various adhesion mechanisms, helicopters and multi-rotors/quadcopters, and cable-guided systems. Each system was assessed for accuracy, ease of implementation, cost, time requirement, and NDE capabilities (e.g., weight capacities and concrete contact). The reports also reviewed various location tracking systems and their capacity to be integrated with the inspection systems. Location tracking systems included satellite GPS, wired and non-wired total stations, and stationary and/or mobile multi-camera systems. The report describes an integrated remote inspection system capable of traversing large curved concrete structures.

Another EPRI report reviews concrete NDE techniques for their accuracy in various concrete mockups with cracks, voids, delamination, and honeycomb defects (Electric Power Reseach Institute, 2015). Evaluated NDE techniques included sounding, impulse response, impact echo, ultrasonic shear wave, ground-penetrating radar, and ultrasonic pulse velocity. Each technique was tested on various concrete mockups constructed with defects. The mockup defects included delamination, horizontal or vertical cracks, voids of various sizes, and honeycomb

defects (a void in concrete that is filled with a loose or solid material but is distinctly separated from the surrounding concrete). While the reviewed NDE techniques performed with varying accuracy and precision, the concept of concrete mockups specifically designed with included defects is a valuable method to verify and validate NDE techniques prior to performing inspections in NPPs.

4.2.2 VeRCoRs and ENDE

The information and images in this section are summarized from (Corbin, 2018) (Garnier, et al., 2018) (Henault, et al., 2018).

4.2.2.1 VeRCoRs Monitoring

The complete monitoring system in the VeRCoRs mockup is as follows:

- 1 meteorological station
- For the ambient air measure: 10 thermometers, 10 RH sensors, 1 atmospheric pressure gage, and 1 flow meter
- 12 pendulums (4 plumb lines, each with 3 tables at different heights)
- 4 vertical Invar wires (Figure 4-1)
- 336 embedded GEO INSTRUMENTATION SG1 strain gages—the distance between the external wall and strain gages is 7.6 cm while the distance between the internal wall and strain gages is 7.3 cm
- 221 PT100 thermometers
- 2 km of optic fiber
- 31 time domain reflectometry sensors
- 30 pulse sensors for permeability measures
- 6 dynamometers for instrumented tendons
- 160 strain gages on rebar

The location of the primary sensors in the mockup are detailed in Section 3.1 . The strain gages in both the concrete and on the rebar are used to measure mechanical strains in response to internal pressurization tests and to material mechanical property phenomena (e.g., concrete creep and drying shrinkage). The Invar wires run from the bottom to the top of the containment and measure the change in containment height; Invar is used because its coefficient of thermal expansion is small, and the material does not significantly expand/contract with changes in temperature. The pendulums are used to measure horizontal displacements at various heights of the containment. Similar to the Invar wire shown in Figure 4-1, the pendulums were suspended from the top of the containment. The horizontal distance between the pendulum wire and the containment wall measured horizontal displacements of the containment wall.

Invar wire

Data measurement and acquisition hardware
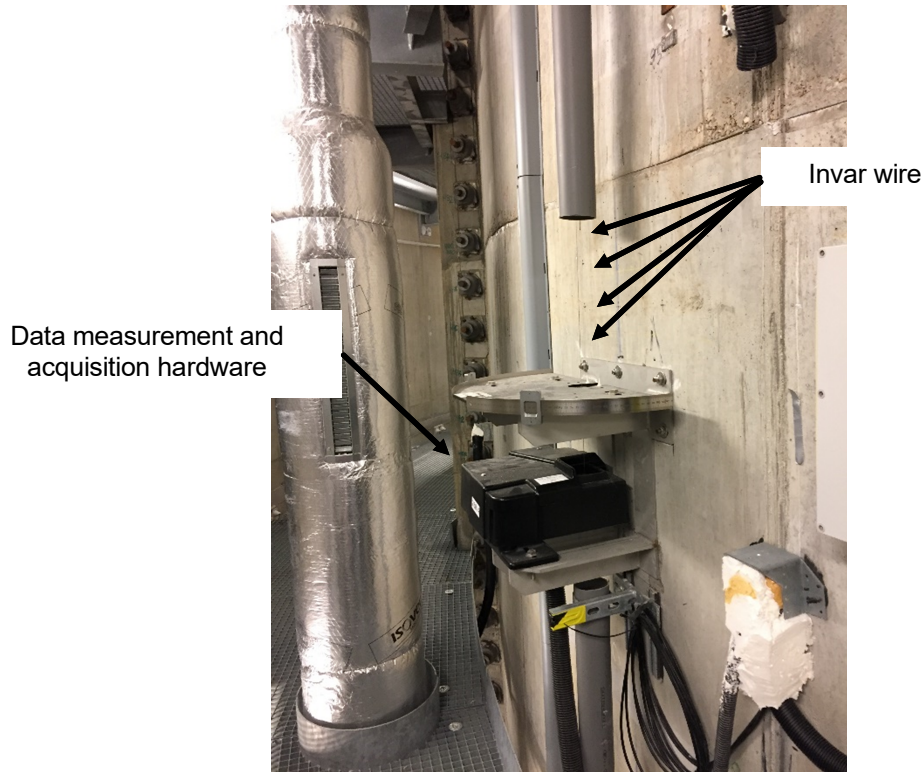
Figure 4-1   End of vertical Invar wire for measuring containment vertical change in height.

4.2.2.2   Evaluation of Non-Destructive Examinations (ENDE)

In parallel with the VeRCoRs mockup, EDF sponsored the ENDE project aimed at developing NDE for containment enclosure applications. ENDE consisted of testing concrete specimens under various conditions and transferring the techniques to the VeRCoRs mockup.

Ten NDE techniques were implemented by ENDE: transmitted ultrasonic waves, surface waves, impact echo and diffuse waves, time reversal TREND, nonlinear acoustics Coda Wave Interferometry, acoustic emission, ground penetrating radar, resistivity, and Torrent permeability. The most promising method that was applied to the VeRCoRs containment was acoustic monitoring and surface wave measurements. Stress was evaluated using a combination of three pieces of equipment that measured the velocity of ultrasonic pressure waves, the velocity of ultrasonic surface waves, and the capacitive permittivity (Figure 4-2). Figure 4-3a shows the evolution of the surface wave velocity with the stress for different damage levels on the tested pieces. The acoustoelasticity that results in the increase of the velocity of the waves with the stress indicates concrete damage. Figure 4-3b shows the evolution of the diffusivity with increasing stress. In both cases, the sensitivity to damage is greater than that to stress.
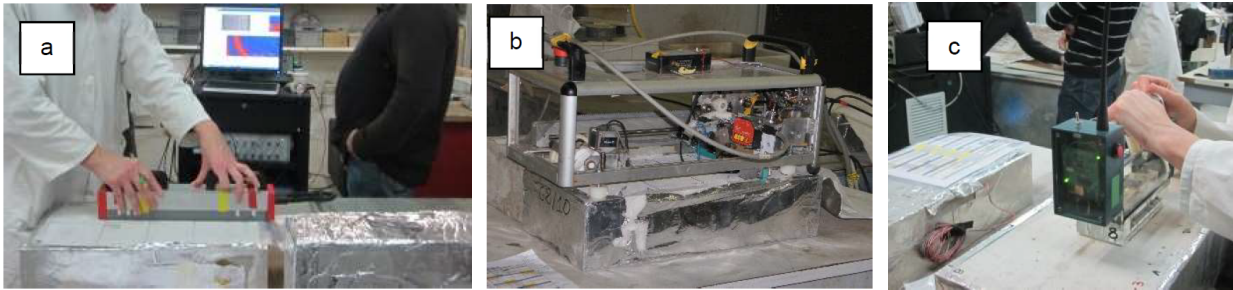
Figure 4-2 **(a) and (b) Ultrasonic surface wave measurements, and (c) capacitive measurement. (Garnier, et al., 2018)**
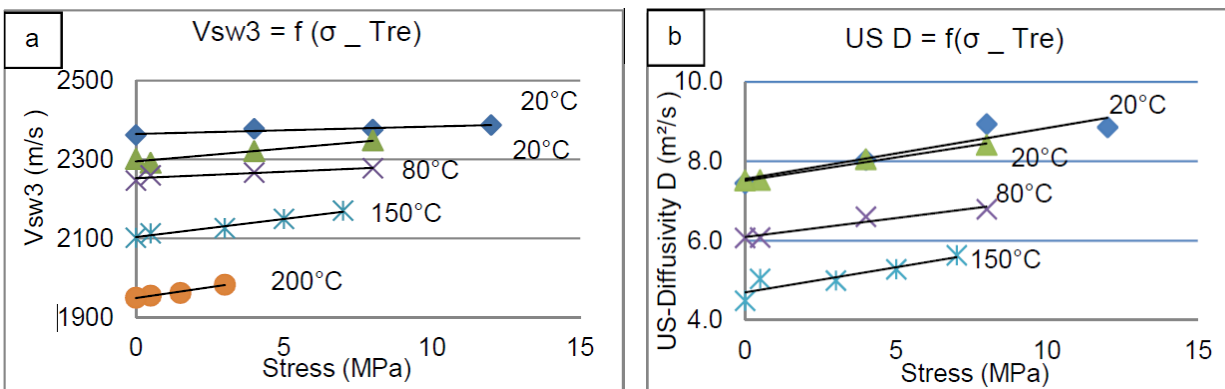
Figure 4-3 **(a) Ultrasonic surface waves and (b) ultrasonic diffusivity D versus the stress and the concrete damage. (Garnier, et al., 2018)**

Three-point bend tests were monitored using acoustic emission as shown in Figure 4-4. Each incident was recorded, and the data was combined into a crack location image as shown in Figure 4-5. Acoustic emission techniques were found to be useful for estimating position and dimension of a crack so long as the monitoring system was active prior to acoustic energy release.

Figure 4-4 **3-point bending test of concrete specimen monitored with acoustic emission. (Garnier, et al., 2018)**
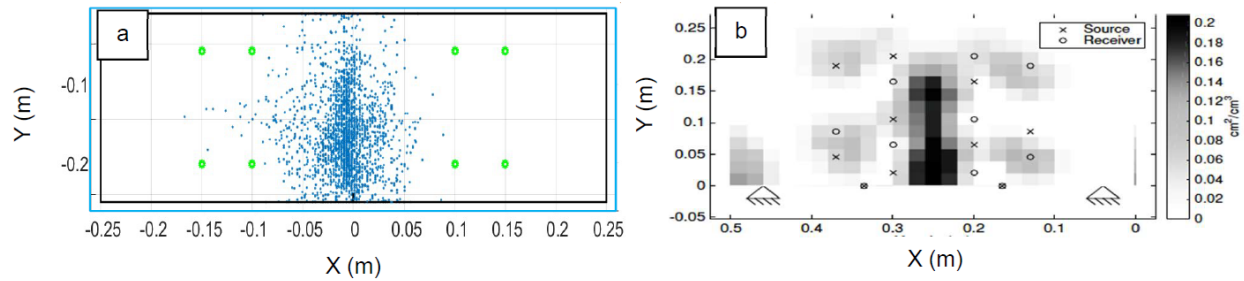
Figure 4-5 **(a) Cumulated events and (b) decorrelation of waves during a 3-point bending test. (Garnier, et al., 2018)**

Surface wave propagation can also be used to estimate crack location as shown in Figure 4-6. The surface wave weakens (attenuates) when the receiver is too far from the source emitter.
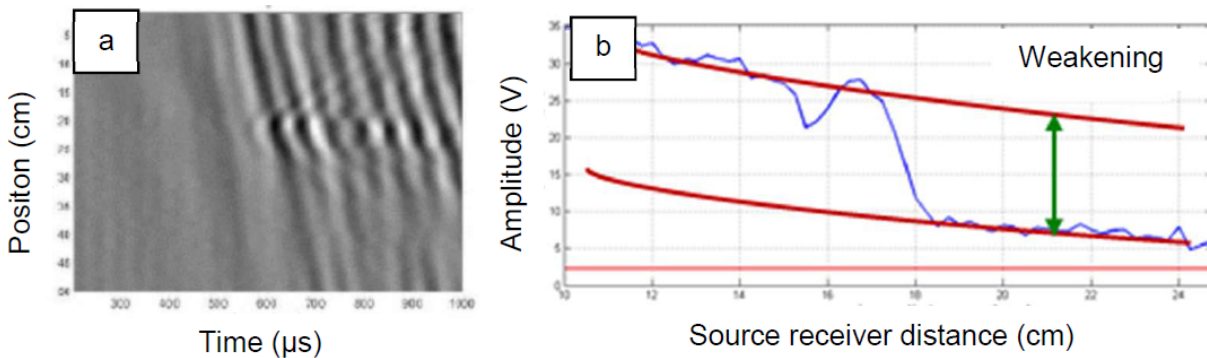
Figure 4-6 **(a) Seismograms of a crack and (b) definition of the signal weakening vs source/receiver distance. (Garnier, et al., 2018)**

The surface wave stress evaluation technique was applied to the VeRCoRs mockup at two points A1 and C3 (not defined). The results are shown in Figure 4-7. Surface wave measurements were conducted on the PCCV wall before, during, and after a pressurization test. In Figure 4-7a, the surface wave speed reduced between June 2016 and March 2017, correlating to a decrease in the water saturation of the concrete. During the pressurization test to 4.2 bar in March 2017, the stress decreased at maximum pressure. The stress is initially between 8 and 12 MPa compressive, and the stress theoretically reduces to 0 at maximum pressure. Therefore, the lower surface wave velocity at maximum pressure follows the trend presented in Figure 4-3: lower stress correlates to lower surface wave velocity. Figure 4-7b shows the surface wave velocity as a function of pressure, also implying that lower surface wave velocity indicates lower stress.
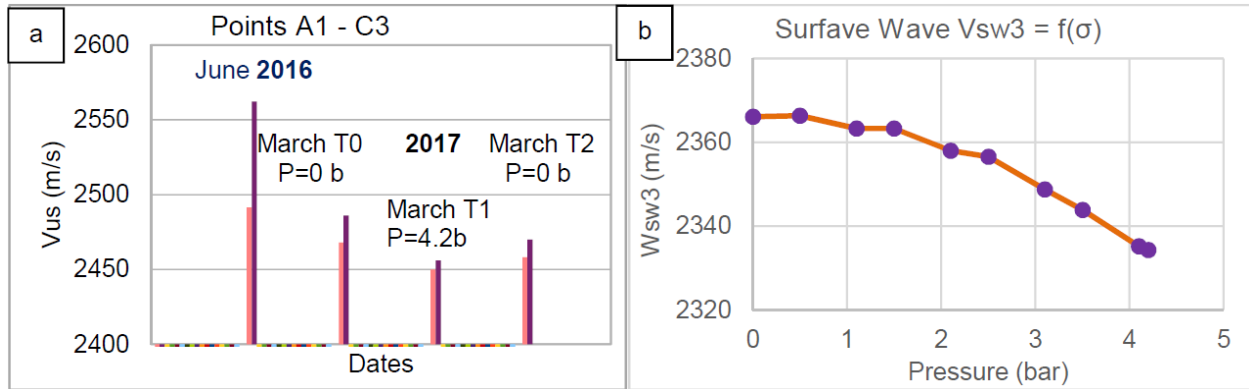
Figure 4-7 **(a) Surface wave evolution with the dates of measurement for points A1 and C3. (b) Surface wave evolution for one point obtained by monitoring the concrete during a pressurization test. (Garnier, et al., 2018)**

Cracks in the PCCV wall during pressurization were also evaluated utilizing surface wave attenuation measurements. Figure 4-8 shows the change in surface wave velocity during a pressurization test for a small portion of the PCCV wall. The bottom of the figure (0 bar) has relatively few changes in surface wave velocity, indicating sound concrete. The top of the figure (4.2 bar) has many changes in surface wave velocity, indicating that the concrete is becoming damaged or is being subjected to local stress variations (which also indicates damage).
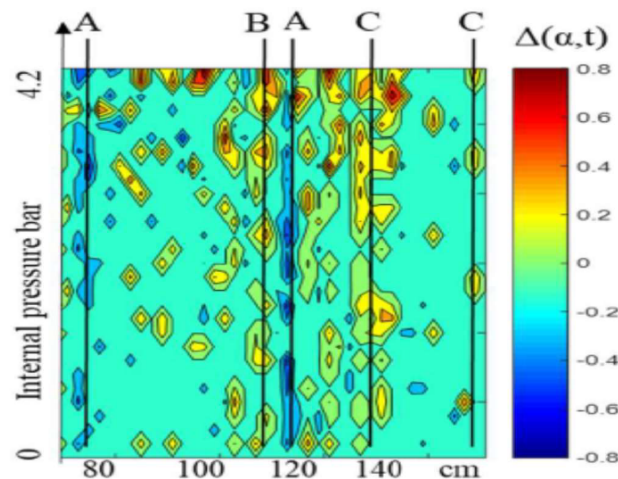
Figure 4-8 **Evolution of the surface wave attenuation variations measured along the horizontal profile as an increasing pressure function. (Garnier, et al., 2018)**

4.2.2.3 *VeRCoRs Integrated Leak Rate Testing*

One of the aims of the VeRCoRs project is the assessment of the leakage rate over time. Once per year, and integrated leak rate test (ILRT) was performed on the VeRCoRs mockup, pressurizing it to 4.2 bar relative (5.2 bar absolute). The ILRT test is equivalent to the Type A test defined in appendix J of (US Nuclear Regulatory Commission, 2019) and in French codes RCC-G, ETC-C, and RCC-CW. EDF was focused on new methods to assess the leakage rate

during ILRTs. Figure 4-9 shows the pressure cycle for the VeRCoRs pressurization test VC1. During the ILRT, the pressure was gradually increased. Once the maximum pressure was reached, the pressurized air entrance valve was shut down. A stabilization period was necessary for the temperature and humidity to reach a steady state in the containment volume. The global leak rate is measured by the so-called "absolute pressure decay method" which consists of measuring pressure decrease of the dry air containment in the PCCV and correcting them based on mean temperature and hygrometry variations. The uncertainty of the global leakage rate is ~1%.
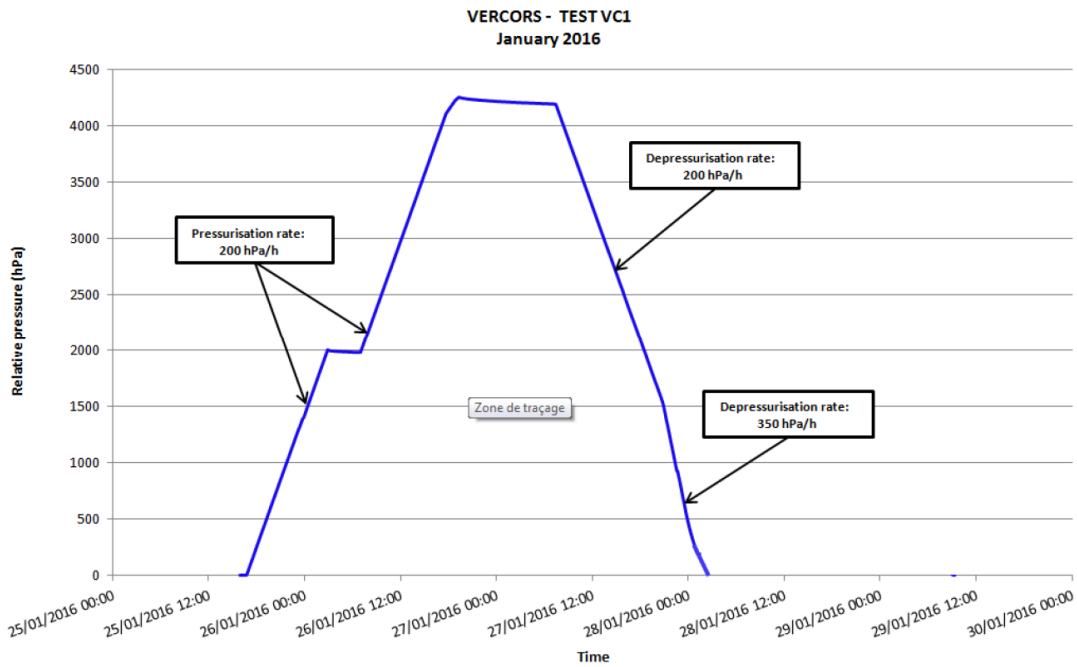
Figure 4-9   **Pressure cycle for VeRCoRs pressurization test VC1. (Henault, et al., 2018)**

Another measurement system, called SUGTEN, allowed EDF to collect the air flow going from the pressurized PCCV to the annular space between the inner and outer walls of the mockup. In steady state conditions and considering a constant permeability, the measured flow rate plots as a straight line against the difference between the squares of pressure as shown in Figure 4-10. Given that the leak rates during the pressurizations were observed to be linear in Figure 4-10, no significant damage was assumed to have occurred during the tests. However, the curves differ from each other, suggesting that the air flow permeability of the structure increased with time. ILRTs VC1, VD1, and VD1bis occurred in January 2016, mid-March 2017, and late-March 2017, respectively.
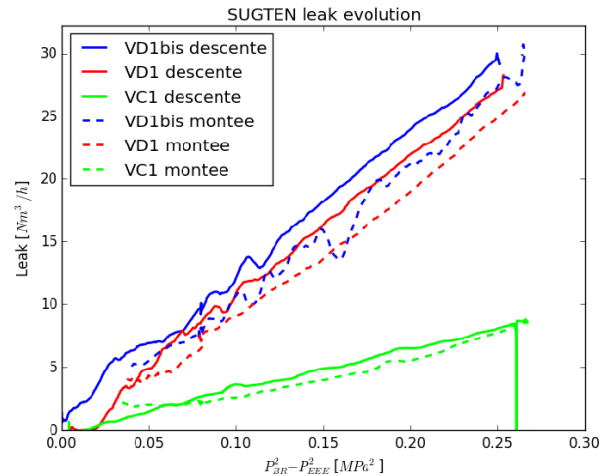
Figure 4-10   SUGTEN measurements during VeRCoRs ILRTs for both ascending (montee) and descending (descente) pressures. (Henault, et al., 2018)

In addition to measuring the flow rate from the PCCV as a whole, EDF implemented a method to detect and measure the flow rate from individual cracks as shown in Figure 4-11. A soap-water mixture was sprayed on the exterior surface of the PCCV during the ILRTs, and air leaks were revealed by soap bubbling. A collection box was then attached to the surface of the PCCV around the leak, and a flowmeter measured the air flow from the leak flowing through a flow pipe from the collection box.

(a)

(b)

Figure 4-11   (a) Leaking zones revealed by soap bubbling. (b) Flow rate measurement with collecting box and flowmeter. (Henault, et al., 2018)

New techniques implemented in the VeRCoRs mockup for crack detection included a combination of fiber optic and acoustic sensors. The acoustic emission technique is a passive method used for many applications, one of which is detecting local cracks in concrete or in prestressed cables in large scale civil structures. Several high-sensitivity accelerometers were fixed to the external concrete wall to measure vibrations induced by the release of acoustic energy. Measurements were analyzed during the pressure steps at 2 and 4.2 bars when ambient noise level was lower since the pressurizer was not operating. An example of the acoustic data is presented in Figure 4-12. Acoustic emission data in a zone without leaks is mostly constant, but acoustic emission data in a zone with high leakage has significant changes between applied pressure magnitudes.
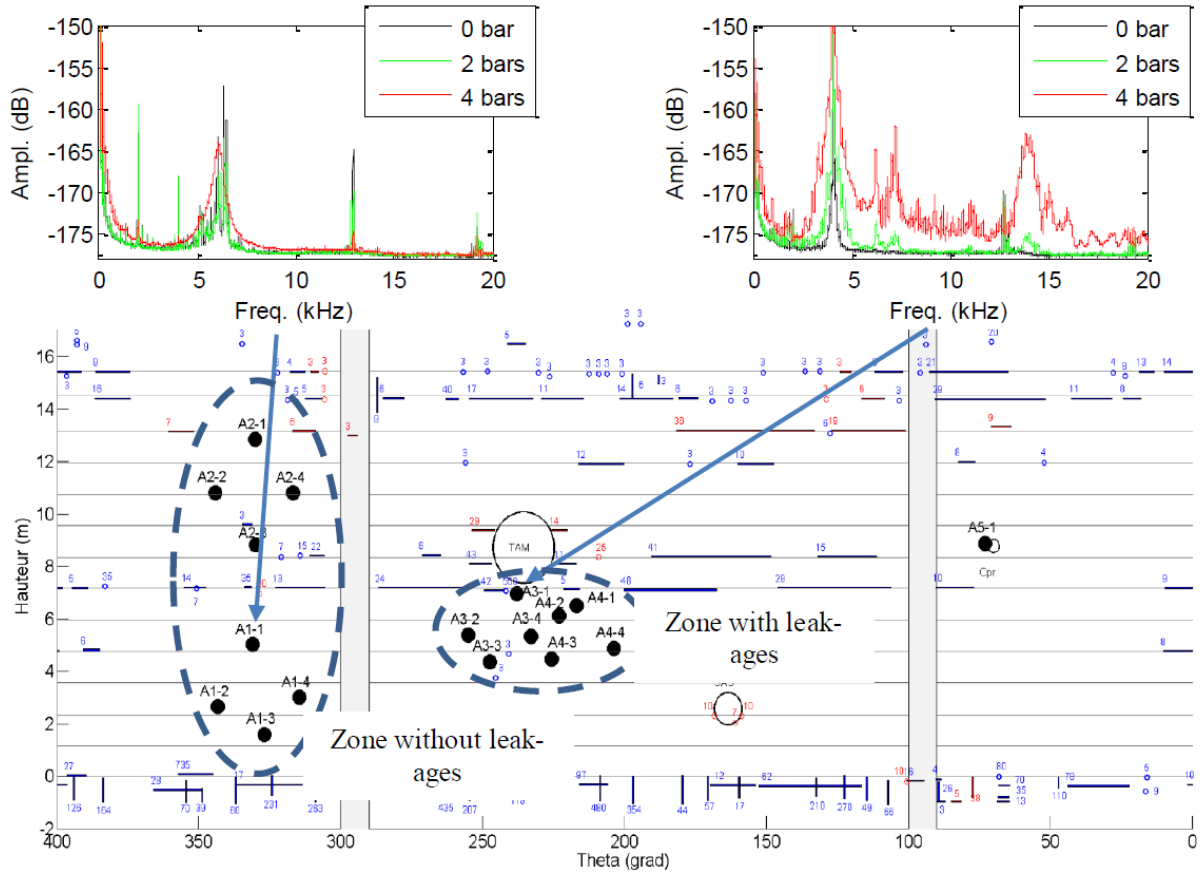
Figure 4-12   Evolution of the amplitude spectrum for two sensors located in two different areas (with and without leakage). Measurements were obtained during an IRLT conducted on the VeRCoRs mockup in 2017. (Henault, et al., 2018)

Vertical cracking was observed by visual inspection on the concrete surface in the gusset zone in the structures' early age; the cracks were a result of the geometric discontinuity between the raft and the cylinder wall, leading to stress concentrations and localized material failure. Air leakage through these cracks increased during each subsequent ILRT. EDF decided to use Rayleigh measurements through fiber optic cables embedded throughout the structure to determine vertical crack paths.

Fiber optic cables were embedded throughout the PCCV and connected to data acquisition units (DAQs) as shown in Figure 4-13. All fiber optic cables were monitored for temperature and strain profiles in the structure, and the gusset fiber optic cable was also used for Rayleigh measurements. The Rayleigh measurement DAQ was able to monitor the strain in the fiber optic cables. As the cables were embedded in the concrete, strains in the cables measured cracks in the concrete including detection, localization, and opening quantification.
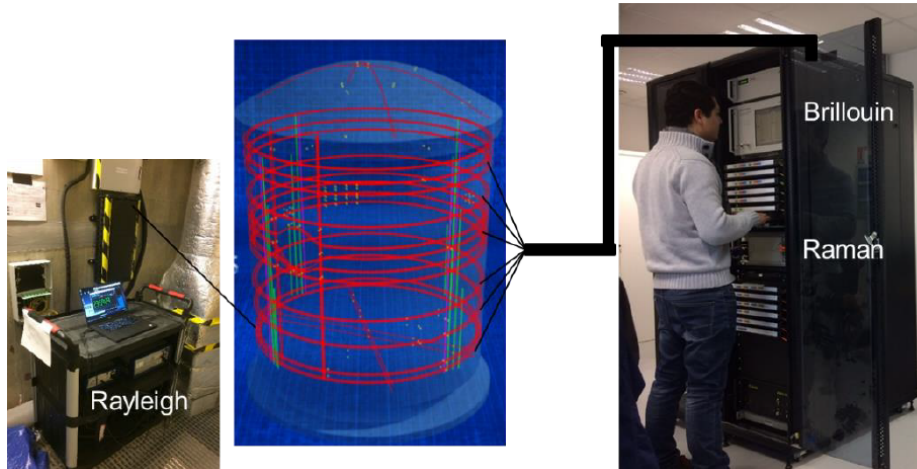
Figure 4-13   (Left) Rayleigh measurement DAQ. (Center) Fiber optic installations in VeRCoRs. (Right) Temperature and strain DAQs. (Henault, et al., 2018)

Using various data processing techniques, the Rayleigh measurement DAQ was able to determine crack widths along the entire length of the fiber optic cables. Figure 4-14a shows the location of the fiber optic cables in the gusset. Figure 4-14b and Figure 4-15 show the cracks measured with the Rayleigh DAQ. In Figure 4-15, cracks that appear in all three fiber optic cables indicate through cracks.
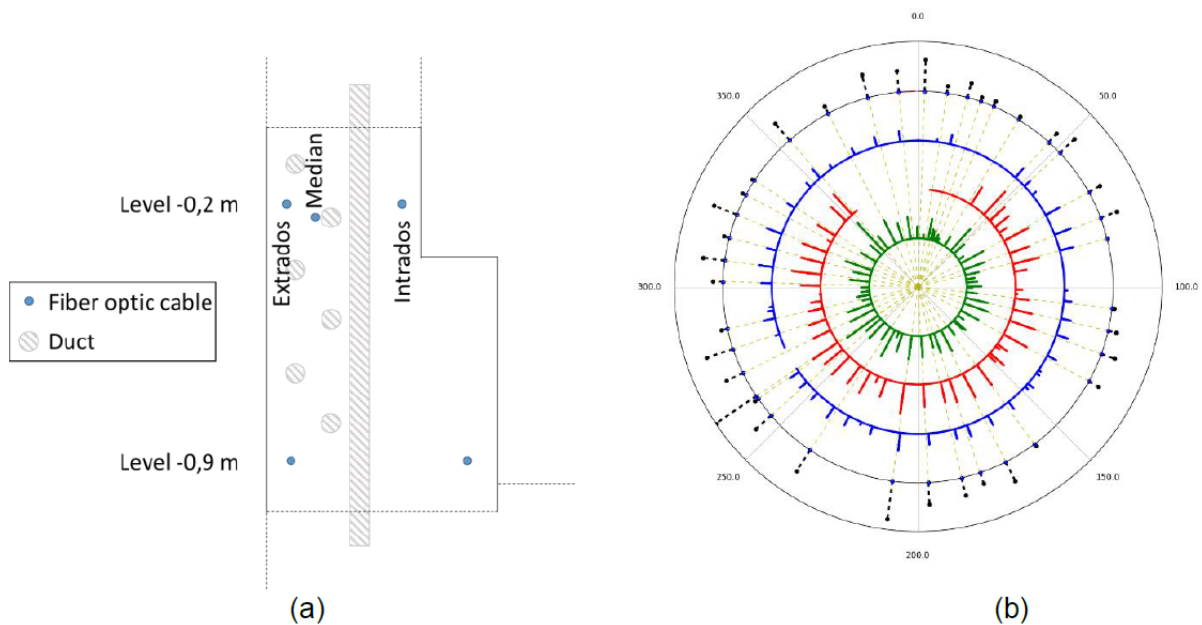
Figure 4-14   (a) Localization of the outer (extrados), middle (median), and inner (intrados) fiber optic cables in the gusset zone as presented by EDF. (b) Radial map of cracks obtained with Rayleigh measurements at level -0.2m at 3 different depths. (Henault, et al., 2018)
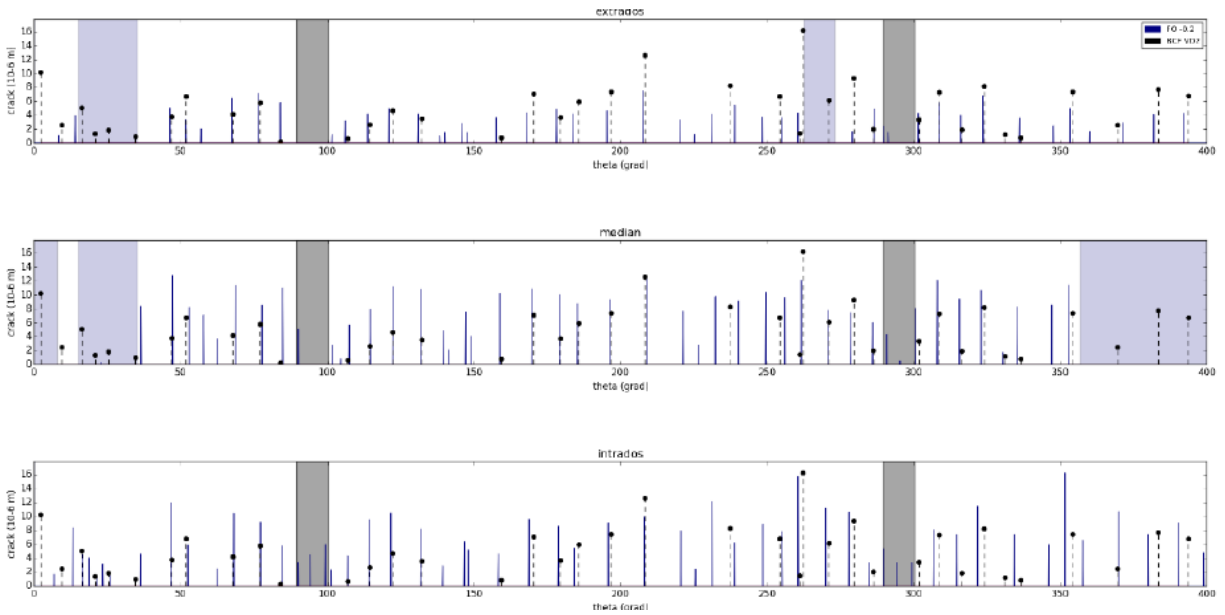
Figure 4-15 **Map of cracks obtained with Rayleigh measurements at level -0.2m at 3 different depths (straight lines) compared with local flow rate measurements (dotted lines). Blue zones correspond to zones with questionable data for Rayleigh measurements due to noise or fiber cut, grey zones correspond to the two buttresses. (Henault, et al., 2018)**

The air leak flow rates in select vertical cracks in the gusset were measured using the device shown in Figure 4-16a. The air leak flow rate and the crack opening width are shown in Figure 4-16b as functions of the pressure during the VeRCoRs VD2 ILRT.

(a)   (b)
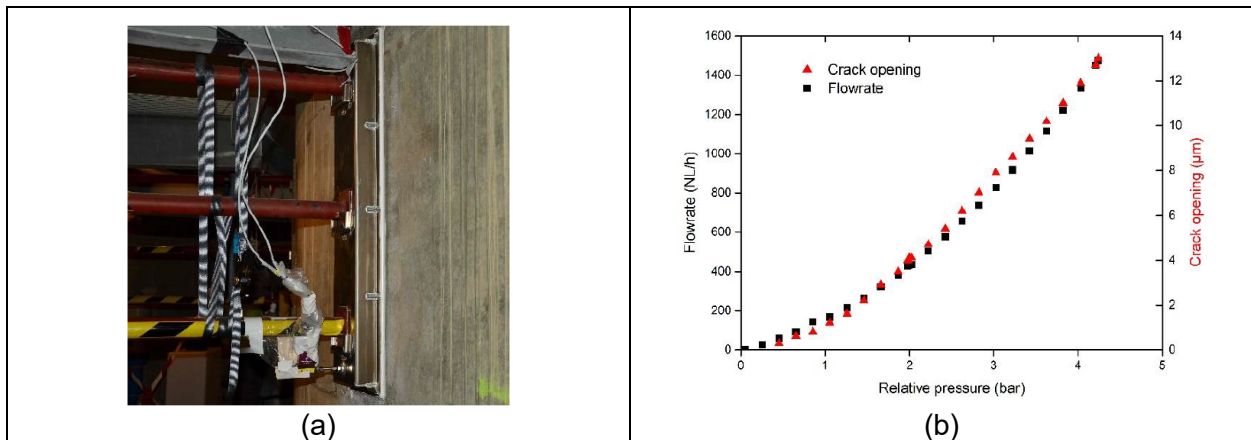
Figure 4-16 **(a) Flowrate monitoring installation of a vertical leaking crack in the gusset. (b) Flowrate and crack opening as functions of relative pressure during the VD2 ILRT. (Henault, et al., 2018)**

5 OTHER RECENT OR ONGOING RESEARCH INDPENDENT OF NRC

This section lists selected recently completed research conducted by other research organizations and not sponsored by the NRC, which is pertinent to PCCVs including effects of creep. The following is provided not as a comprehensive discussion of all related research efforts, but to highlight other experimental research projects potentially beneficial for the design and maintenance of PCCVs with respect to delamination and concrete creep.

5.1 Experiment on Post-Tensioned Wall at University of Texas at Austin

Research was conducted at the University of Texas at Austin (UT Austin) on the behavior of curved post-tensioned concrete structures without through-thickness reinforcement (Choi, Woods, Hrynyk, & Bayrak, 2017) (Ebrahimkhanlou, Choi, Hrynyk, Salamone, & Bayrak, 2019) (Woods, 2016). In the experiment, two curved post-tensioned concrete wall assemblies were constructed and tested to delamination failure under monotonically increasing prestressing loads as represented in Figure 5-1. The second specimen was twice the size of the first to study size effect—reinforcement ratios were held constant. Acoustic emission sensors were included to monitor the onset of delamination in PCCVs. No vertical PT was used in the experiment. The research focused on:

- Investigating the structural behavior of curved post-tensioned concrete structures and the radial stress distribution owing to the prestressing tendons by:
  - Providing experimental data on curved post-tensioned concrete structures without radial reinforcement;
  - Evaluating patterns of crack propagation due to the development of localized tensile stresses;
  - Investigating the relationship between the tensile strength of concrete and the delamination failure load of curved post-tensioned structures.
- Classifying and interpreting acoustic emission data in post-tensioned concrete containment structures.
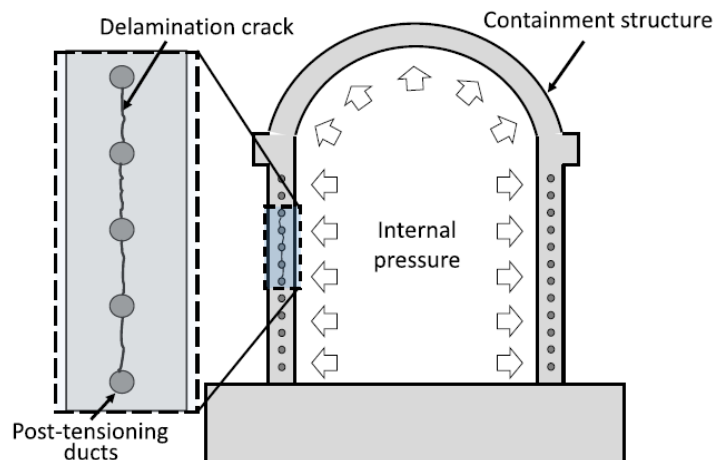
Figure 5-1   **Schematic of delamination cracking in a post-tensioned concrete containment structure. (Ebrahimkhanlou, Choi, Hrynyk, Salamone, & Bayrak, 2019)**

Plans of the two curved post-tensioned walls constructed at UT Austin are shown in Figure 5-2. The instrumentation plans for the walls are shown in Figure 5-3.
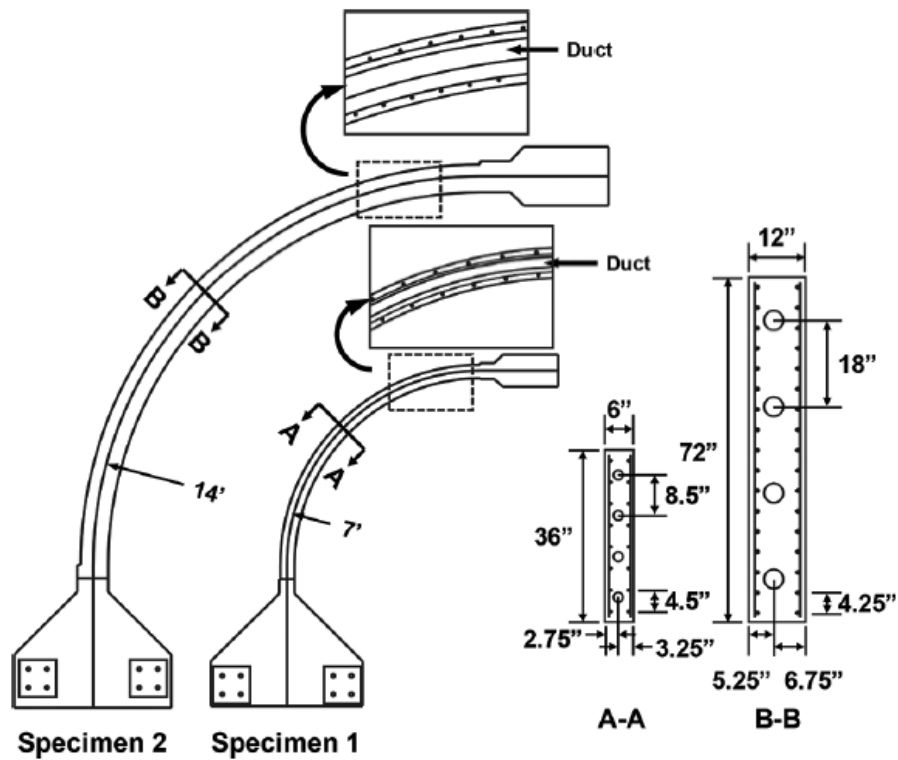
Figure 5-2 Summary of dimensions and reinforcement details. Duct numbering starts from the top duct (e.g., Duct 1 is the top duct). (Choi, Woods, Hrynyk, & Bayrak, 2017)
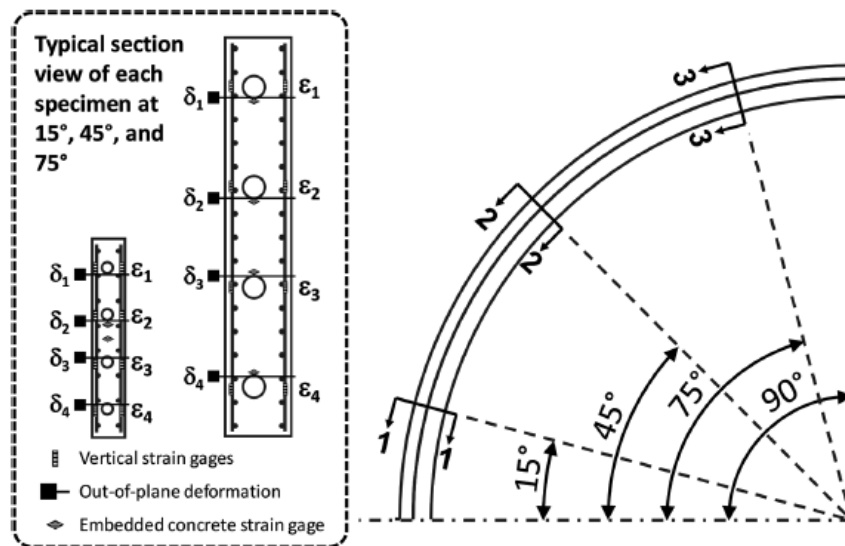
Figure 5-3 Summary of mechanical instrumentation plan including strain gages on the vertical reinforcement, out-of-plane deformation sensors, and embedded concrete strain gages. (Choi, Woods, Hrynyk, & Bayrak, 2017)

The PT loads measured from both ends of the structures revealed a 46.8% friction loss for Specimen 1 and a 45.2% friction loss for Specimen 2; these friction losses were greater than estimated using design codes. The delamination failures of the walls (shown in Figure 5-4 and Figure 5-5) occurred abruptly and were violent/explosive in nature. The delamination failure of both specimens initiated approximately at the 15° location of the wall section. The delamination crack initiated at the top duct first and propagated toward the bottom duct, possibly due to the different boundary conditions at the top and bottom of the wall. The sustained concrete tensile stress/tensile capacity ratio for Specimen 1 (smaller) and Specimen 2 (larger) were 0.69 and 0.55, respectively, indicating a size effect that is seen in most other concrete specimens: larger specimens fail at lower normalized stresses than smaller specimens.
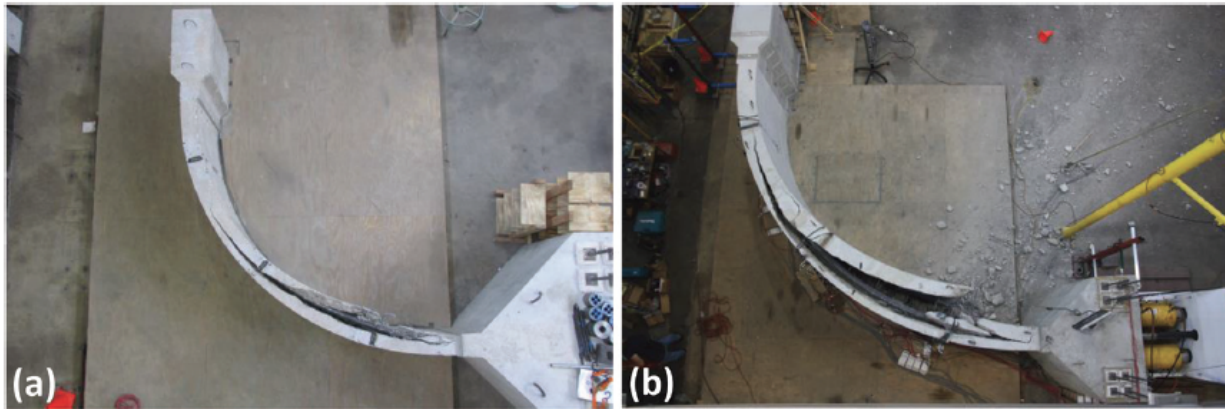
Figure 5-4   Specimens after delamination failure: (a) Specimen 1—delamination crack formed from 0° to 68°; (b) Specimen 2—delamination crack formed from 0° to 78°. (Choi, Woods, Hrynyk, & Bayrak, 2017)
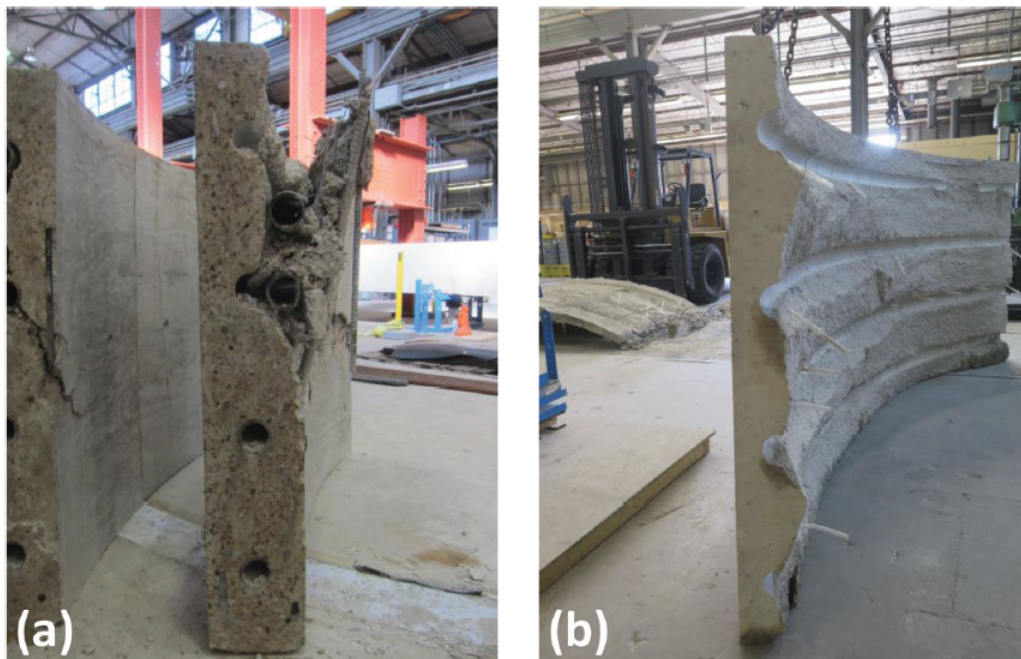
Figure 5-5   Typical sectional crack pattern: (a) Specimen 1 at 15° location; and (b) Specimen 2 at 8° location. (Choi, Woods, Hrynyk, & Bayrak, 2017)

The vertical strains at the duct locations were monitored to estimate when the internally developed bending moments and shear forces led to concrete cracking. The vertical reinforcement strain measurements produced near-linear load-strain responses prior to the development of longitudinal cracking of the wall at the duct locations as shown in Figure 5-6. The normalized tensile stress-vertical strain responses initially showed near-linear trends and then the slopes gradually changed. This response is likely indicative of delamination crack initiation in the vicinity of the duct. It is assumed that the formation of the first horizontal crack approximately coincided with the slope change observed from the tensile stress-vertical strain response. The first horizontal crack was estimated to form at approximately 32% of the failure load for Specimen 1 and at 50% of the failure load for Specimen 2. Until 87% load for both specimens, the slope continued to change due to further cracking. Above ~85% of ultimate failure load, the walls quickly delaminated.
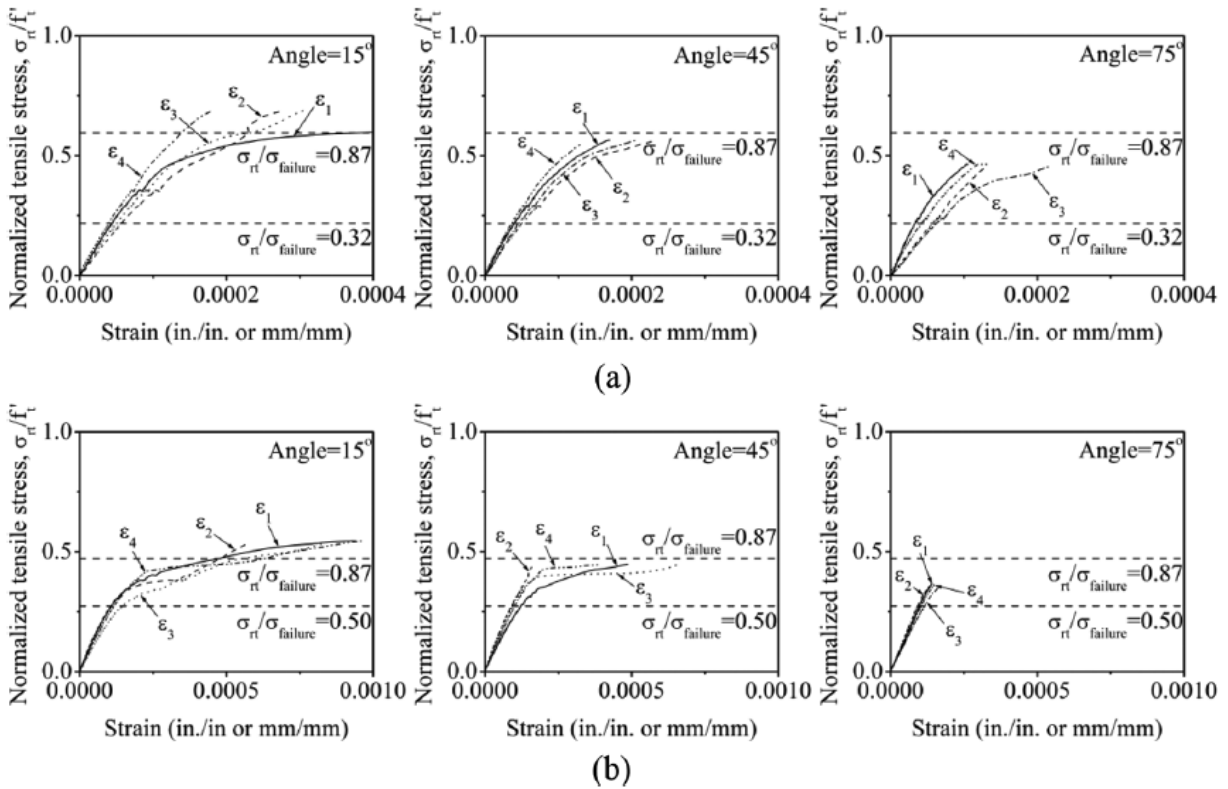
Figure 5-6   Measured vertical strains versus normalized tensile stresses: (a) Specimen 1 and (b) Specimen 2. (Choi, Woods, Hrynyk, & Bayrak, 2017)

The tensile strength normalized delamination failure load was shown to decrease as the specimen size increased. Through-thickness expansions, radial strains, and vertical reinforcement strain measurements were found to be good indicators of delamination crack initiation and growth. Wall delamination cracks initiated at compressive stress levels between 0.13 and $0.23f'_c$, which is significantly less than the $0.35f'_c$ limit provided by ACI 359-15. (ACI-ASME Joint Committee 359, 2015).

Eight (8) acoustic emission sensors were installed on Specimen 2 as shown in Figure 5-7. After significant post-processing of the test data, not discussed here, the authors were able to

distinguish between shear and tensile microcracking. The crack detection information is shown in Figure 5-8. The sensors were also able to detect the formation of macro cracks as shown in Figure 5-9. According to the work completed at UT Austin, acoustic emission monitoring could be used in PCCVs during repair or routine maintenance operations involving tendon detensioning, tendon retensioning, or internal pressurizations to detect potential delamination cracks.
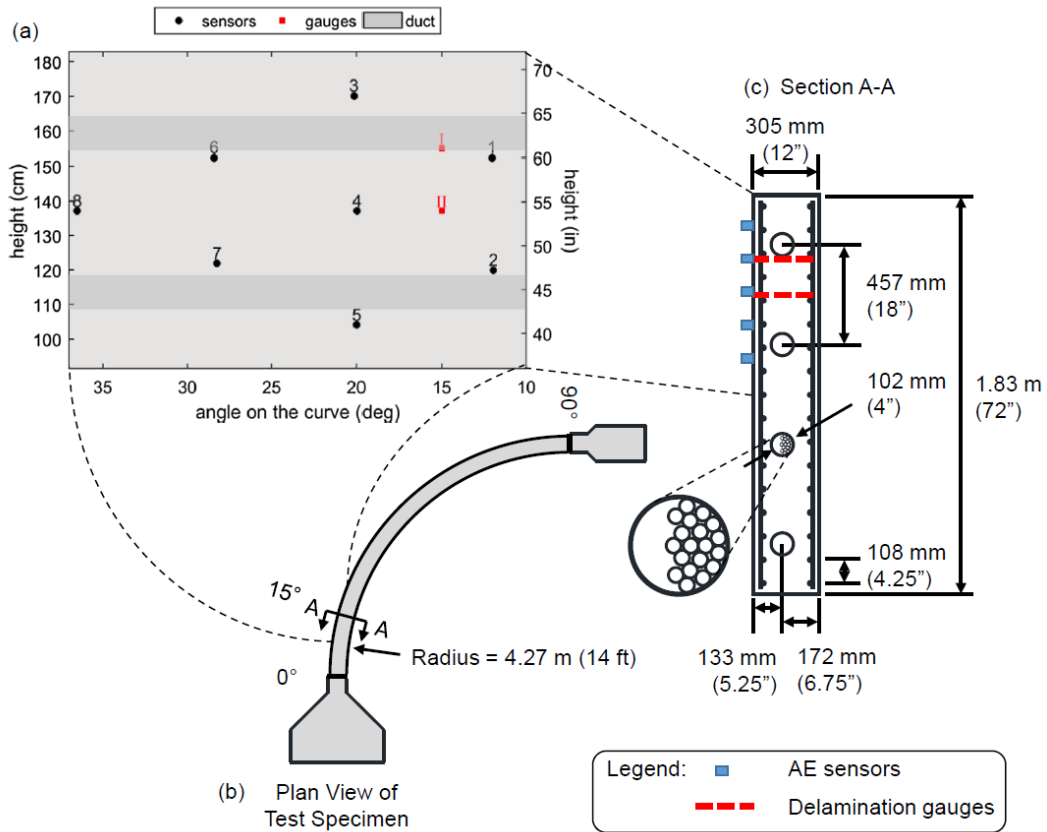
Figure 5-7   **Acoustic monitoring plan and section view of Specimen 2. (Ebrahimkhanlou, Choi, Hrynyk, Salamone, & Bayrak, 2019)**
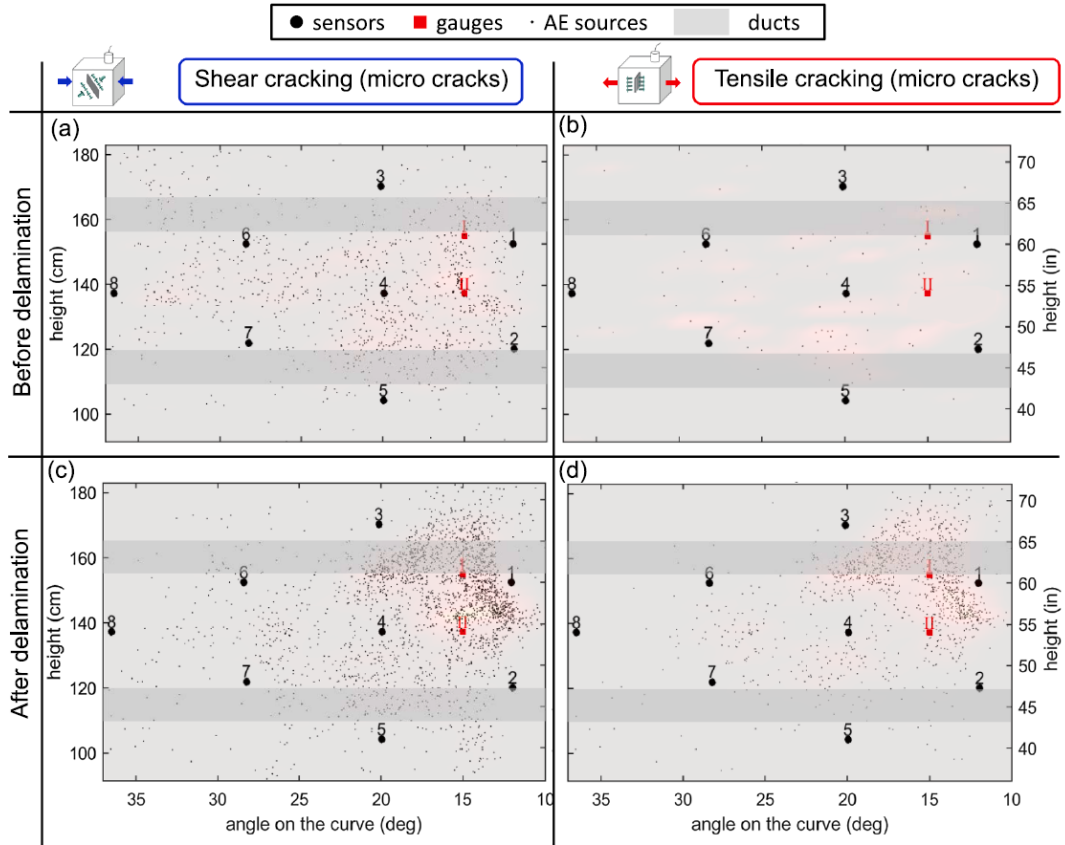
Figure 5-8   Location of acoustic emission data clusters: (a) cluster 1, before delamination; (b) cluster 2, before delamination; (c) cluster 1, after delamination; and (d) cluster 2, after delamination. The color map indicates the density of clusters. (Ebrahimkhanlou, Choi, Hrynyk, Salamone, & Bayrak, 2019)
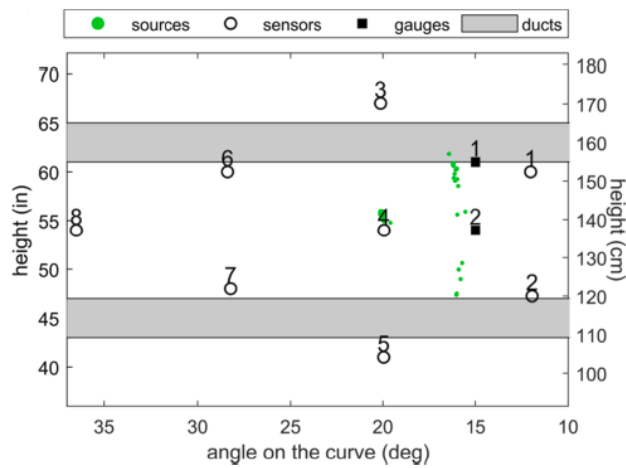
Figure 5-9   Location of acoustic emission data cluster 3 (macro cracking). (Ebrahimkhanlou, Choi, Hrynyk, Salamone, & Bayrak, 2019)

5.2   Experiments at Texas A&M University

5.2.1   Post-Tensioned Slab Experiments

Texas A&M University, in collaboration with SNL and Idaho National Labs, conducted a study focused on observing the effects of concrete creep with three large-scale reinforced concrete wall sections (Kelley, 2018). Concrete strain, temperature, and RH values through the thickness, as well as the strain in select PT bars, were measured once per hour. The specimens are shown in Figure 5-10 through Figure 5-14. The design of Specimen 1 was based on SNL's 1:4 experimental specimen (US Nuclear Regulatory Commission, 2003), both with wall thicknesses of 33 cm (13 in). Specimen 1 used the same reinforcement ratio as in SNL's 1:4 experimental specimen. Specimen 2 was designed with 3x the thickness and 1/3 of the steel reinforcement ratios of Specimen 1 to capture the effects of changing geometry and reinforcement ratios. The level of applied stress to Specimen 1 and Specimen 2 was effectively equivalent. Specimen 3 was constructed to serve as a control specimen, containing no reinforcing steel and no PT bars, to determine how the concrete behaves independent of applied loads (including post-tensioning loads) and reinforcement. One side of each of the three wall specimens was sealed with water-resistant wrapping to mimic 1-dimensional drying in typical US PCCVs due to the internal steel liner. The specimens were located outside without cover in College Station, TX, USA. The concrete mixture for all specimens was based on the VeRCoRs concrete mixture.
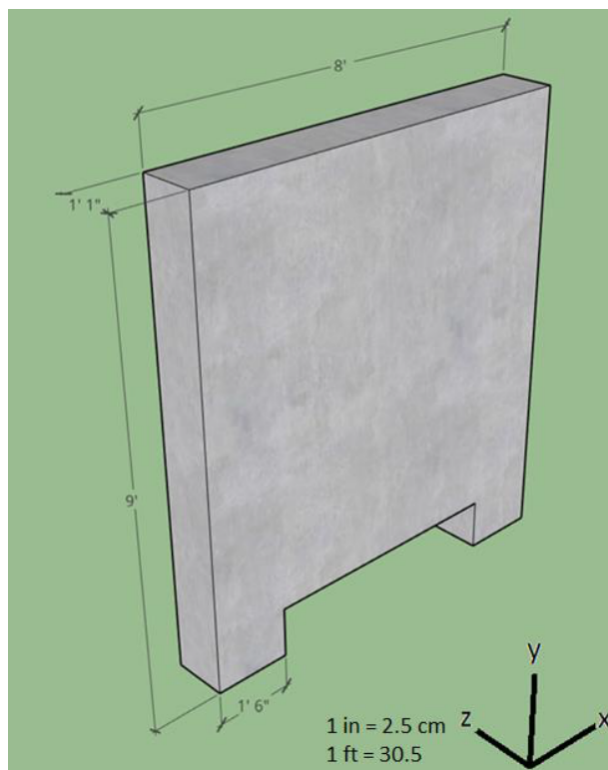
Figure 5-10   Texas A&M Specimen 1 dimensions. (Kelley, 2018)
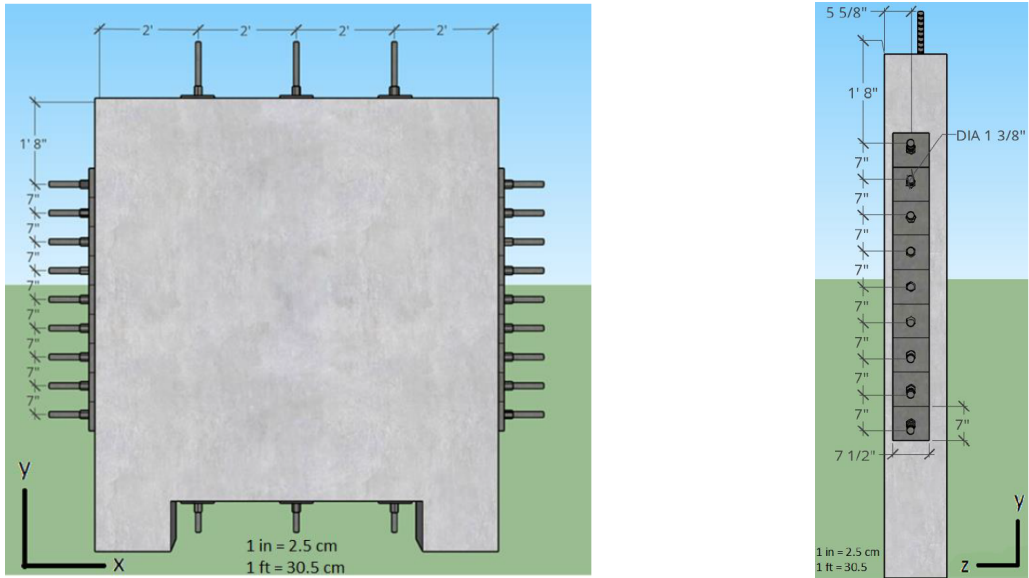
Figure 5-11   Texas A&M Specimen 1 post-tensioning bar layout. (Kelley, 2018)
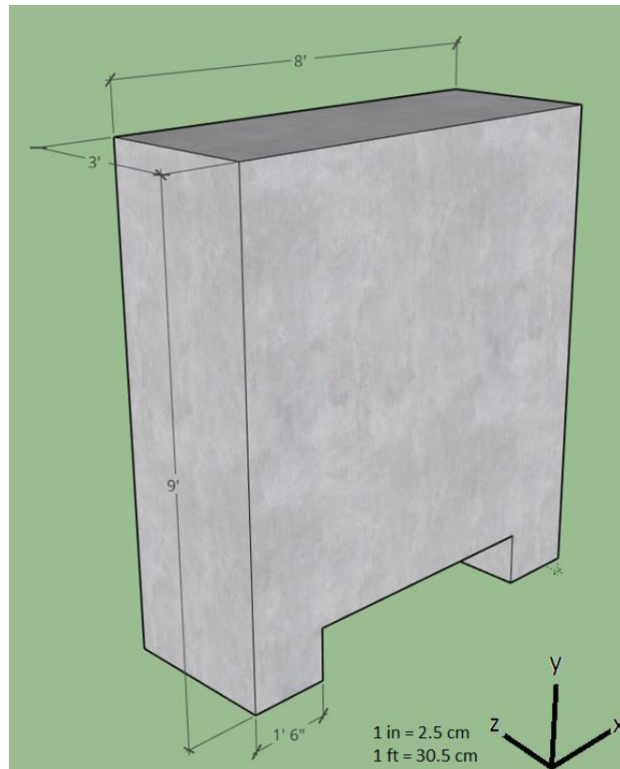
Figure 5-12   Texas A&M Specimen 2 dimensions. (Kelley, 2018)
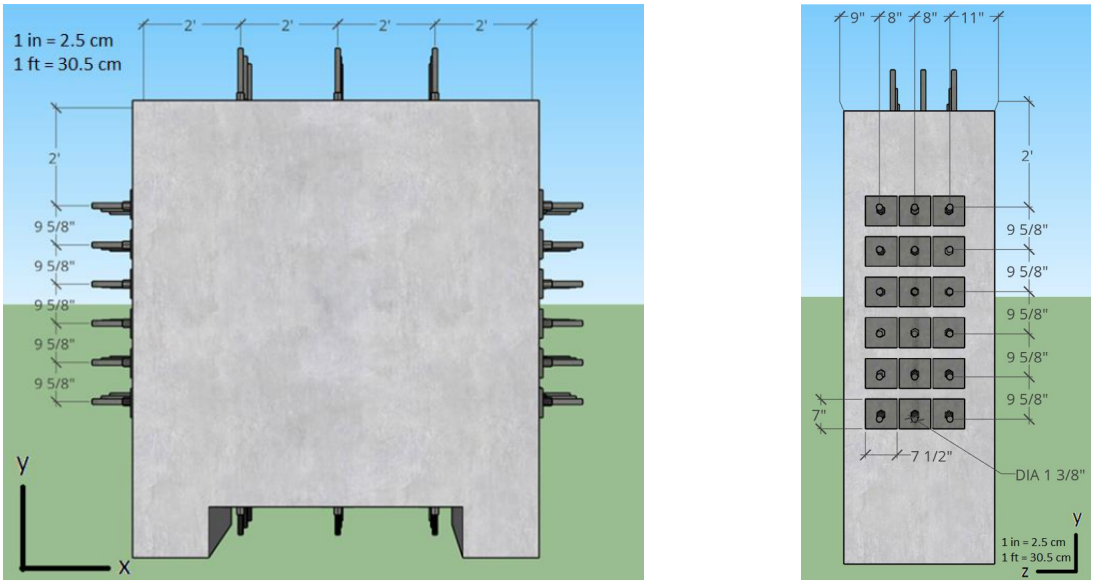
Figure 5-13   Texas A&M Specimen 2 post-tensioning bar layout. (Kelley, 2018)
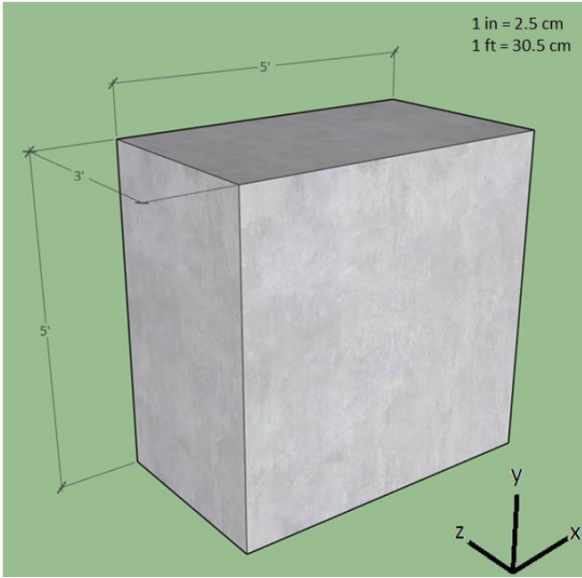
Figure 5-14   Texas A&M Specimen 3 dimensions (Control Specimen). (Kelley, 2018)

Data from all operating gages was collected from the day concrete was poured on July 7, 2017 through September 2019; as of this publication, data was being recorded for the foreseeable future. The DAQ system is solar powered with a stand-alone battery and stand-alone recording system. All concrete gages experienced a sharp increase in strain (tensile and compressive) as a result of the concrete pour. Over the month of curing, the gages stabilized, reflecting strains induced from the temperature changes internally. During PT, the x-direction concrete gages generally measured compressive strains, whereas the y-direction and z-direction gages varied in compression and tension and had much smaller strain magnitudes. There

were significant changes in the strain readings during PT steel seating and also some changes due to probable early age creep of the concrete. The data (if available) from the concrete strain gages at the geometric center of each specimen is shown in Figure 5-15 through Figure 5-20. Compressive strains are negative. Daily and seasonal changes in temperature are apparent in the data as sinusoids. Seasonal changes are seen as low-frequency sinusoids with one period per year; daily changes in temperature are seen as high-frequency sinusoids with one period per day. Each gage's data shows a slow drift between September 2017 and September 2019. Some drifts are tensile, and some are compressive. The drift in data is due to two factors: concrete drying shrinkage and concrete creep. Specimen 1, the thinnest specimen, is more susceptible to drying shrinkage that Specimen 2 and Specimen 3. The X-direction drift strains in Specimen 1 and Specimen 2 are compressive, indicating that the combination of both drying shrinkage and creep strain caused compressive strains. However, the Z-direction drift strains in Specimen 1 and Specimen 2 are opposite: compressive in Specimen 1 and tensile in Specimen 2. Theoretically, the drying shrinkage strains in the specimens are compressive while the Z-direction strains are tensile due to the Poisson effect from PT. The compressive Z-direction drift strains in Specimen 1 (Figure 5-16) indicate that drying shrinkage is more prominent than the Poisson tensile creep strains. The tensile Z-direction drift strains in Specimen 2 (Figure 5-18) indicate that, in the larger specimen, the Poisson tensile creep strains are more prominent than the drying shrinkage strains. The difference in reinforcement ratios between Specimen 1 and Specimen 2 reduce the PT magnitude of the strains but not the drift direction. Specimen 3, which has no reinforcement or, is more susceptible to temperature fluctuations. Specimen 3's drift strains are due to drying shrinkage as no PT forces were present to cause significant creep strains.
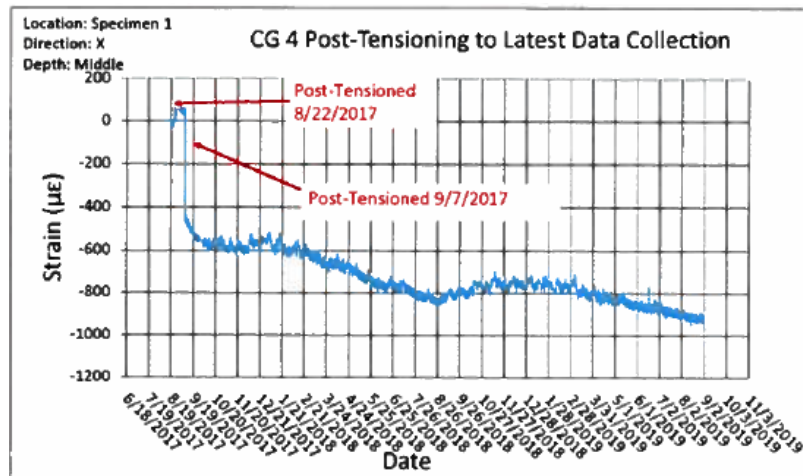
Figure 5-15   Specimen 1 X-direction (horizontal) concrete strain data. Dates are shown as Month/Day/Year. Figure courtesy of Dr. Joseph Bracci, Texas A&M University.
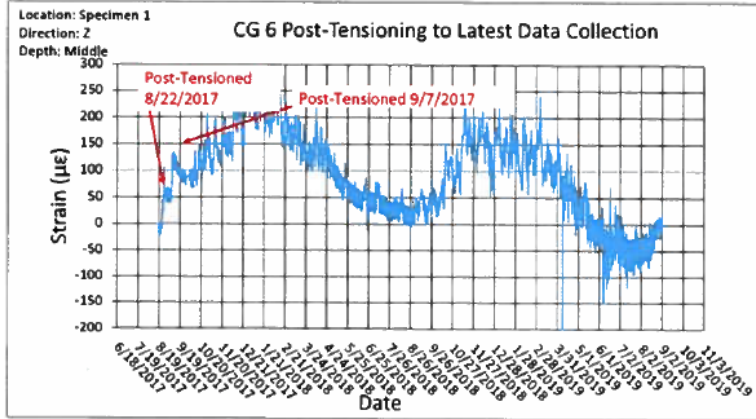
Figure 5-16 Specimen 1 Z-direction (Poisson direction) concrete strain data. Dates are shown as Month/Day/Year. Figure courtesy of Dr. Joseph Bracci, Texas A&M University.
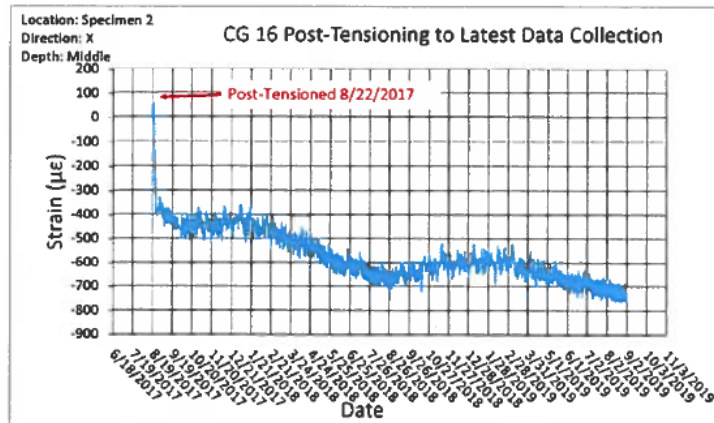
Figure 5-17 Specimen 2 X-direction (horizontal) concrete strain data. Dates are shown as Month/Day/Year. Figure courtesy of Dr. Joseph Bracci, Texas A&M University.
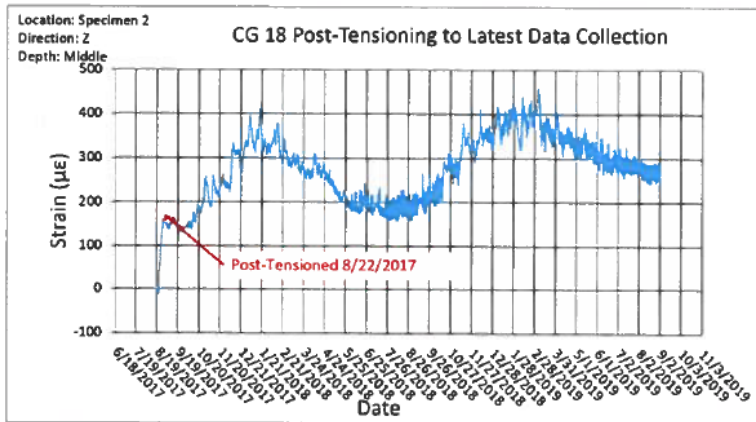
Figure 5-18 Specimen 2 Z-direction (Poisson direction) concrete strain data. Dates are shown as Month/Day/Year. Figure courtesy of Dr. Joseph Bracci, Texas A&M University.
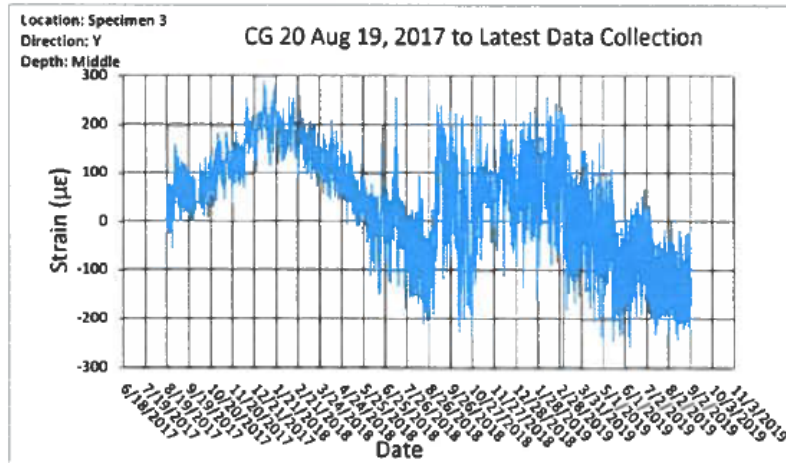
Figure 5-19 Specimen 3 Y-direction (vertical) concrete strain data. Dates are shown as Month/Day/Year. Figure courtesy of Dr. Joseph Bracci, Texas A&M University.
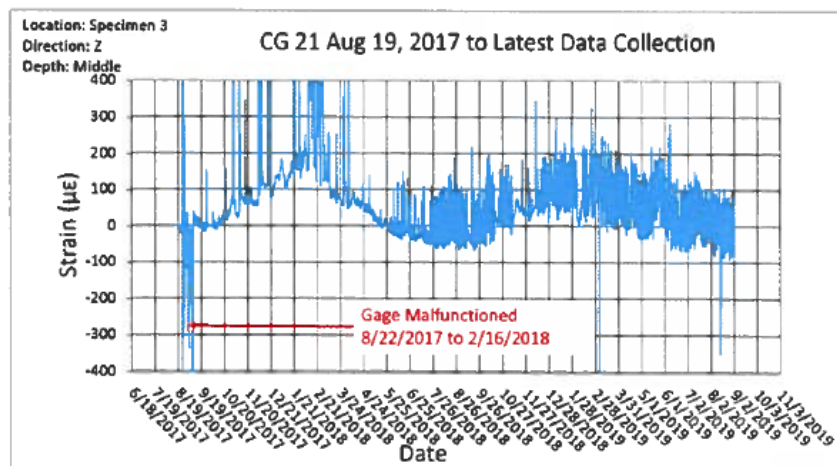
Figure 5-20 Specimen 3 Z-direction (Poisson direction) concrete strain data. Dates are shown as Month/Day/Year. Figure courtesy of Dr. Joseph Bracci, Texas A&M University.

5.2.2 Creep Prediction Experiments

In addition to performing post-tensioned concrete slab experiments, Texas A&M University performed cementitious material experiments to improve long-term creep predictions. The information presented in this section is summarized from (Baranikumar, Torrence, & Grasley, Using Time-Temperature Superposition to Predict Long-Term Creep of Nuclear Concrete, 2019) (Baranikumar, Torrence, & Grasley, 3D Creep Response of Nuclear Concrete, 2019).

As mentioned in Section 2.3.2 , concrete creep is difficult to predict even with accurate concrete mixture proportions and known environmental conditions, not to mention the sensitivity of concrete creep to temperature. Several publications summarized in (Baranikumar, Torrence, &

Grasley, Using Time-Temperature Superposition to Predict Long-Term Creep of Nuclear Concrete, 2019) indicate that concrete behaves as a thermo-rheologically simple material: during similar deformation processes at different temperatures, the same sequence of molecular events occur with different speed and can be correlated using temperature dependent shift factors. The shift factor is not necessarily a linear function of temperature (i.e., the rate at which events occur between 20°C and 40°C need not be the same as the rate between 40°C and 60°C). In concrete, the slope of creep strain against temperature is not linear between 27°C and 100°C because the rate of increase of creep accelerates as the temperature increases.

The temperature properties of thermo-rheologically simple materials can be used to describe the material behavior at various time or temperature scales using the time-temperature superposition principle (TTS). TTS is used to determine temperature-dependent mechanical properties for various thermo-rheologically simple materials from known properties at a reference temperature. In essence, the creep behavior of concrete at 80°C in a short-term test can be used to predict the behavior of the same concrete at 20°C for long-term applications. Creep tests can be performed on a specific concrete mixture at various temperatures, and the data from all tests can be post-processed into a single master curve for a given temperature.

The creep experimental work at Texas A&M University described in this section used mortar specimens with mixture proportions designed based on the VeRCoRs mockup. Mortar cylinder specimens were subjected to uniaxial creep tests at various temperatures: 20°C, 60°C, and 80°C. The average creep strain data at different temperatures is presented in Figure 5-21. Creep compliance curves were generated from the data, and the fitted creep compliance curves obtained at 60°C and 80°C were shifted along the logarithmic time axis to obtain a master curve at 20°C as shown in Figure 5-22.
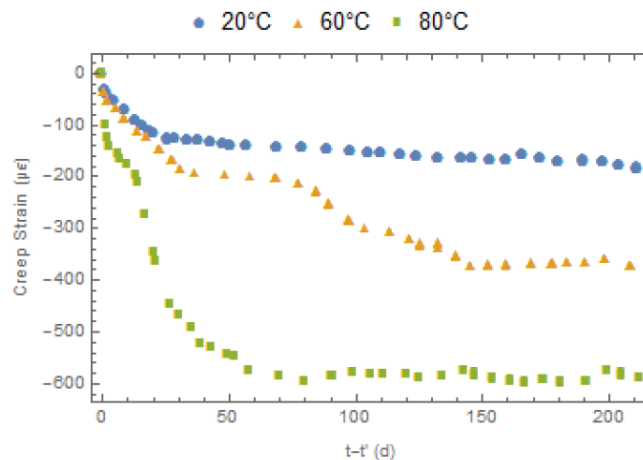
Figure 5-21   Average creep strain data at different temperatures. Figure courtesy of IASMiRT. (Baranikumar, Torrence, & Grasley, Using Time-Temperature Superposition to Predict Long-Term Creep of Nuclear Concrete, 2019)
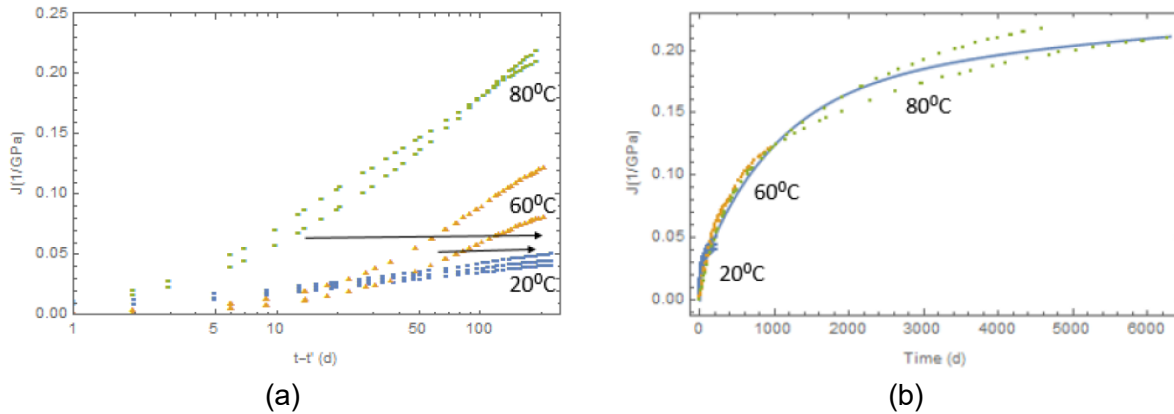
Figure 5-22 **(a) Creep compliance functions shifted along the logarithmic time axis; (b) Master curve of creep compliance using TTS. Figures couresty of IASMiRT. (Baranikumar, Torrence, & Grasley, Using Time-Temperature Superposition to Predict Long-Term Creep of Nuclear Concrete, 2019)**

Using the TTS technique, the creep compliance of mortar specimens measured at temperatures up to 80°C for a period of 200 days were used to obtain a master curve to predict long-term creep compliance corresponding to 6000+ days at 20°C.

5.3   Other Research Conclusions

- There are several PCCV monitoring and NDE techniques that have been successfully implemented in experiments and/or are in development. Many of these techniques can be used on or added to existing PCCVs.

- EPRI has constructed various concrete mockups constructed with defects. The mockup defects included delamination, horizontal or vertical cracks, voids of various sizes, and honeycomb defects (a void in concrete that is filled with a loose or solid material but is distinctly separated from the surrounding concrete). While the reviewed NDE techniques performed with varying accuracy and precision, the concept of concrete mockups specifically designed with included defects is a valuable method to verify and validate NDE techniques prior to performing inspections in NPPs.

- UT Austin has performed experiments on curved post-tensioned walls and has shown that wall delamination cracks initiated at compressive stress levels between 0.13 and $0.23f'_c$, which is significantly less than allowable $0.35f'_c$ limit at initial prestress (before losses) provided in the ASME BPVC, Section III, Division 2, Part CC-3431.

- According to the work completed at UT Austin, acoustic emission monitoring could be used in PCCVs during repair or routine maintenance operations involving tendon detensioning, tendon retensioning, or internal pressurizations to detect potential delamination cracks

- Texas A&M University is performing experiments to study concrete creep effects in post-tensioned concrete slabs. Thin slabs are more impacted by drying shrinkage than by concrete creep, while thick slabs are more impacted by concrete creep than by drying shrinkage.

- Texas A&M University has shown that creep tests can be performed on a specific concrete mixture at various temperatures, and the data from all tests can be post-processed into a single master curve for a given temperature. This allows concrete creep data gathered over a limited amount of time to be accurately extrapolated over a significantly longer amount of time.

6   CONCLUSIONS

The U.S. NPP fleet is experiencing aging and degradation. NPPs undergo inspections to determine adequate intended performance and to search for potential degradation. While most degradation events are routine and can be corrected with relatively less effort, degradation of prestressing system, if it were to occur, could require more rigorous corrective actions.

6.1   Literature Review Conclusions

- The effects of concrete creep and particularly concrete creep rupture on aging PCCVs have been little studied before this report. This report presents a thorough review of concrete creep, concrete creep rupture, and case summaries of post-tensioned concrete structures that have suffered from concrete creep effects.

- Post-tensioned concrete structures are susceptible to creep effects that may not have been adequately predicted during design.

- Design practices attempt to limit the stresses in concrete to stresses below what required for the occurrence of concrete rupture. Tertiary creep and creep rupture will not occur if the concrete stress remains below a specific threshold. However, if continuing concrete creep causes excessive deformations, the threshold stress in either compression or tension may be exceeded. Concrete creep rupture is more probable at 70%, and significantly more probable at stresses above 75% of ultimate uniaxial capacity in either compression or tension.

- As of this publication, there is little research or literature on temperature effects on concrete creep rupture.

- The ASME BPVC Section III Division 2 (ASME, Boiler Pressure Vessel Code Section III, 2019) prohibits the reliance on concrete tensile strength to resist the external loads and moments or the forces and moments resulting from internal self-constraint. However, no radial reinforcement was required in the PCCV wall prior to 2019, leaving the concrete unreinforced in an area subject to tensile stresses.

- PCCVs are subject to many degradation mechanisms ranging from individual material phenomena to system-wide issues. Every instance of a potential issue in a PCCV should be analyzed by an expert to determine the severity of the situation.

6.2   Simulation Conclusions

- When RH data was available, the VeRCoRs simulation results aligned well with experimental data. Missing RH data skewed the simulation results away from the experimental data.

- The implementation of the Bažant B3 concrete creep model (with its correction factor) into the simulation via a Prony series was successful in modeling the creep response of the PCCV. It should be noted that calibration of the B3 concrete creep model was required, and the calibration technique is included in the B3 model publication. Figure 3-53 indicates that the creep response was required to match experimental data.

- The implementation of concrete drying shrinkage strains using Fick's 2nd Law of diffusion via the ABAQUS thermal equation was successful in modeling the concrete drying shrinkage response of the PCCV. Figure 3-53 indicates that drying shrinkage was required to match experimental data.

- The mechanical response of the PCCV to the internal pressurizations in the simulation matched the experimental response as shown in Figure 3-51 and the calculations performed by Moffatt & Nichol as shown in Figure 3-52.

- The Moffatt & Nichol analysis indicates that the PCCV strains are likely within design limits during pressurizations at design pressure, and no significant cracking is expected. However, their analysis was limited to a minimally discretized global response, and they anticipated the need for enhanced discretization to capture radial creep strains.

- The PCCV thin-slice analysis, which is representative of the VeRCoRs PCCV with finer discretization, clearly indicates the tensile stress and tensile creep strain zones in the radial direction in the PCCV wall.

- In the PCCV thin-slice analysis, the creep strains immediately behind the post-tensioning tendons are on the same order of magnitude as the elastic response strains at the same location, but the creep strains are ~5x larger than the elastic strains. The creep strains from post-tensioning being significantly larger than the elastic strains indicate that creep could be an issue in PCCVs that do not have radial reinforcement. While these strains are all likely too small to cause delamination failure without exacerbation, they do provide a layer of increased tensile strain that could be a weakness in the structure.

- The limited scope SIA/SSC analyses indicate that cascading delamination events can occur under certain circumstances when a local defect is introduced. However, not all structural defects in the delamination plane may lead to cascading delamination events such as seen at Crystal River. If a local defect is introduced into the structure just after initial tensioning, a cascade delamination may occur. If a local defect is introduced into the structure significantly after initial tensioning, a cascading delamination event may not occur.

- The SIA/SSC differential creep analyses, wherein a lower creep factor was assigned to the outer concrete elements, caused a delamination failure to occur during the creep steps. This material scenario could potentially exist if a large thermal or humidity gradient exists radially across the PCCV concrete. A large humidity gradient is not expected due to the extremely low transport properties in mass concrete, but a thermal gradient scenario may warrant further investigation.

- Additional research can better determine the conditions in which these radial strains and creep effects could lead to initiation of delamination.

6.3   Nondestructive Evaluation, Monitoring, and Other Research Conclusions

- There are several PCCV monitoring and NDE techniques that have been successfully implemented in experiments and/or are in development. Many of these techniques can be used on or added to existing PCCVs.

- EPRI has constructed various concrete mockups with defects. The mockup defects included delamination, horizontal or vertical cracks, voids of various sizes, and honeycomb

defects (a void in concrete that is filled with a loose or solid material but is distinctly separated from the surrounding concrete). While the reviewed NDE techniques performed with varying accuracy and precision, the concept of concrete mockups specifically designed with included defects is a valuable method to verify and validate NDE techniques prior to performing inspections in NPPs.

- UT Austin has performed experiments on curved post-tensioned walls and has shown that wall delamination cracks initiated at compressive stress levels between 0.13 and 0.23f'_c, which is significantly less than allowable 0.35f'_c limit at initial prestress (before losses) provided in the ASME BPVC, Section III, Division 2, Part CC-3431.

- According to the work completed at UT Austin, acoustic emission monitoring could be used in PCCVs during repair or routine maintenance operations involving tendon detensioning, tendon retensioning, or internal pressurizations to detect potential delamination cracks

- Texas A&M University is performing experiments to study concrete creep effects in post-tensioned concrete slabs. Thin slabs are more impacted by drying shrinkage than by concrete creep, while thick slabs are more impacted by concrete creep than by drying shrinkage.

- Texas A&M University has shown that creep tests can be performed on a specific concrete mixture at various temperatures, and the data from all tests can be post-processed into a single master curve for a given temperature. This allows concrete creep data gathered over a limited amount of time to be accurately extrapolated over a significantly longer period of time.

7   REFERENCES

ACI-ASME Joint Committee 359. (2015). Code for Concrete Containments (ACI 359-15). *Part of ASME Boiler and Pressure Vessel Code, Section III*.

American Association of State Highway and Transportation Officials. (September 2017). *AASHTO LRFD Bridge Design Specifications, 8th Edition.*

American Concrete Institute. (2001). *ACI 222.2R-01: Corrosion of Prestressing Steels.* ACI Committee 222.

American Concrete Institute. (2005). *209.1R Report on Factors Affecting Shrinkage and Creep of Hardened Concrete.* ACI Committee 209.

American Concrete Institute. (2008). *209.2R Guide for Modeling and Calculating Shrinakge and Creep in Hardened Concrete.* ACI Committee 209.

American Concrete Institute. (2013). *349-13 Code Requirements for Nuclear Safety-Related Concrete Structures and Commentary.* ACI Committee 349.

American Concrete Institute. (2014). *318-14 Building Code Requirements for Structural Concrete and Commentary.* ACI Committee 318.

American Concrete Institute. (2015). Code for Concrete Reactor Vessels and Containments. *ACI 359-15*.

American Concrete Institute. (2018). *349.3R-18: Report on Evaluation and Repair of Existing Nuclear Safety-Related Concrete Structures.*

ASME. (2011). Boiler Pressure Vessel Code Section XI.

ASME. (2019). Boiler Pressure Vessel Code Section III.

ASTM. (n.d.). Standard E 139, "Standard Practice for Conducting Creep, Creep-Rupture, and Stress-Rupture Tests of Metallic Materials".

Baltimore Gas and Electric Company. (1997). *Calvert Cliff Unit No. 1 20-Year Containment Tendon Surveillance Engineering Evaluation (ML060340143).*

Baranikumar, A., Torrence, C., & Grasley, Z. (2019, August). 3D Creep Response of Nuclear Concrete. *American Nuclear Society 19th International Conference on Envrionmental Degradation of Materials in Nuclear Power Systems - Water Reactors*.

Baranikumar, A., Torrence, C., & Grasley, Z. (2019, August 4-9). Using Time-Temperature Superposition to Predict Long-Term Creep of Nuclear Concrete. *Transactions*. Charlotte, NC, USA: SMiRT-25.

Bažant, Z. P. (1974). *Creep and Shrinkage Effects in Nuclear Reactor Containment Shells.* Chicago, Ill.: Sargent and Lundy Engineers.

Bažant, Z. P. (1975). Creep and Shrinkage of Concrete. *Mechanics Today, 2*, 1-93.

Bazant, Z. P. (1975). Theory of Creep and Shrinkage in Concrete Structures: A Precis of Recent Developments. *Mecahnics Today, 2*, 1-93.

Bazant, Z. P., & Baweja, S. (2000). Creep and Shrinkage Prediction Model for Analysis and Design of Concrete Structures: Model B3. *SP-194*.

Bazant, Z. P., & Jirasek, M. (2018). Moisture Transport in Concrete. In *Creep and Hygrothermal Effects in Concrete Structures* (pp. 271-408). Springer, Dordrecht.

Bažant, Z. P., & Planas, J. (1997). *Fracture and Size Effect in Concrete and Other Quasibrittle Materials.* Boca Raton, FL: CRC Press.

Bažant, Z. P., Carreira, D., & Walser, A. (1975). Creep and Shrinkage in Reactor Containment Shells. *Journal of the Structural Division, ST10*, 2117-1232.

Bazant, Z. P., Cusatis, G., & Cedolin, L. (June 2004). Temperature Effect of Concrete Creep Modeled by Microprestress-Solidification Theory. *Journal of Engineering Mechanics, 130*(6).

Bažant, Z., Hubler, M., & Yu, Q. (2011). Excessive Creep Deflections: An Awakening. *Concrete International, 33*(8), 44-46.

Bažant, Z., Hubler, M., & Yu, Q. (2011). Pervasiveness of Excessive Segmental Bridge Deflections: Wake-Up Call for Creep. *Concrete International Structural Journal, 108*(6), 766-774.

Bažant, Z., Qiang, Y., & Guang-Hua, L. (2011). Excessive Long-Time Deflections of Prestressed Box Girders. I: Record-Span Bridge in Palau and Other Paradigms. *Journal of Structural Engineering, 1*(38), 676-686.

Benboudjema, F., & Torrenti, J. M. (2008). Early-age behaviour of concrete nuclear containments. *Nuclear Engineering and Design, 238*, 2495-2506.

Benjamin (Senior Editor), D. (1980). *Metals Handbook: Properties and Selection: Stainless Steels, Tool Materials, and Special-Purpose Materials, Vol. 3, 9th Edition.* American Society for Metals.

Boresi, A. P., & Schmidt, R. J. (2003). *Advanced Mechanics of Materials, 6th Ed.* Hoboken, NJ: John Wiley & Sons, Inc.

BridgeHunter.com. (2017, November 1). Retrieved January 15, 2020, from http://bridgehunter.com/va/richmond-city/bh63745/

California Department of Transportation (CalTrans). (2000). *Design Criteria for the San Francisco - Oakland Bay Bridge New East Spans.*

Carpinteri, A., Valente, S., & Zhou, F. P. (1995). Crack Propagation in Concrete Specimens Subjected ot Stustained Loads. *Fracture Mechanics in Concrete Structures, Proceedings FRAMCOS-2*, 1315-1328.

Carpinteri, A., Valente, S., Zhou, F. P., Ferrara, G., & Melchiorri, G. (1997). Tensile and flexural creep rupture tests on partially damaged concrete specimens. *Materials and Structures, 30*, 269-176.

Chen, D., Yang, Y., & Liu, P. (2015). Analysis of Deflection Problems of Large-Span Continuous Rigid Frame Bridge and Prevention Measures. *MATEC Web of Conferences, 22*.

Choi, J., Woods, C., Hrynyk, T., & Bayrak, O. (2017). Behavior of Curved Post-Tensioned Concrete Structures without Through-Thickness Reinforcement. *ACI Structural Journal, 114*(4).

Corbin, M. (2018). *VeRCoRs 2018 International Benchmark: Overview, Synthesis, and Lessons Learnt.* Paris-Saclay, France: EDF.

Daou, H., Salha, W. A., Raphael, W., & Chateauneuf, A. (2019). Explanation of the collapse of Terminal 2E at Roissy-CDG Airport by nonlinear deterministic and reliability analyses. *Journal of Case Studies in Constructuion Materials, 10*, 1-12.

Dassault Systemes. (2013). ABAQUS Analysis User's Guide 6.13. *DS Simulia*.

Dunn, D. S., Pulvirenti, A. L., & Hiser, M. A. (2011). *Containment Liner Corrosion Operating Experience Summary, Techincal Letter Report - Revision 1.* Washington, DC: U.S. Nuclear Regulatory Commission Office of Nuclear Regulatory Research.

Ebrahimkhanlou, A., Choi, J., Hrynyk, T., Salamone, S., & Bayrak, O. (2019, November 30). Acoustic Emission Monitoring of Containment Structures during Post-Tensioning. *Engineering Structures*.

El Kamari, Y., Raphael, W., & Chateauneuf, A. (2015). Relaibility study and simulation of the progressive collapse of Roissy Charles de Gaulle Airport. *Journal of Case Studies in Engineering Failure Analysis, 3*, 88-95.

Electric Power Reseach Institute. (2015). *Nondestructive Evaluation of Concrete Delaminations, Voids, and Cracks Perpendcular to the Surface.* Technical Report.

Electric Power Research Institute. (2013). *Augmented Containment Inspection and Monitoring Report.* Technical Report.

Electric Power Research Institute. (2013). *Remotely Controlled Vehicle for Nondestructive Examination Inspection of Large Vertical Concrete Structures.* Technical Report.

Electric Power Research Institute. (2014). *Nondestructive Evaluation: Automated Inspection of Concrete Structures: Concrete Crawler - Integration of Three Technologies.* Technical Report.

Electric Power Research Institute. (2014). *Supplemental Report on Containment Tendon Monitoring and on Containment Internal Temperature Monitoring at the R. E. Ginna Nuclear Power Plant.* Technical Report.

Electric Power Research Institute. (2015). *Program on Technology Innovation: Concrete Repairs in the Power Generation Industry.* Technical Report.

Electric Power Research Institute. (2015). *Strain Development in Posttensioned Containment Concrete.* Technical Report.

Électricité de France. (2018). VeRCoRs Mock-up Basic Monitoring System Layout. *H-44200971-2014-002919*.

Exelon Generation. (2016). *Safety Evaluation Report Related to the License Renewal of LaSalle County Station, Unit 1 and 2 (ML16126A503).*

Garnier, V., Henault, J., Piwakowski, B., Payan, C., Abraham, O., Chaix, J., . . . Drelich, R. (2018). *Non Destructive Evaluation for Containment Monitoring.* Paris-Saclay, France: TINCE 2018: Technological Innovations in Nuclear Civil Engineering.

Goodyear, D., & Smith, M. (1988, May-June). A Practial Look at Creep & Shrinkage in Bridge Deck Design. *PCI Journal*.

Gross, H. (1975). High-Temperature Creep of Concrete. *Nuclear Engineering and Design, 32*, 129-147.

Helmerich, D. -I., Krause, D. M., Mielentz, D. F., Niederleithinger, D. E., Taffe, D. A., & Wilsch, D. -P. (2013). *Non-destructive Testing of Nuclear Power Plant Structures State of the Art Report.* Berlin, Germany: Bundesanstalt für Materlalforschung und -prüfung.

Henault, J., Laviron, P., Desforges, S., Vautrin, D., Courtois, A., Martin, B., & Legrix, A. (2018). *How to Characterize the Airtightness of Containment Structures: Overview of Monitoring Techniques Tested on VeRCoRs Mock Up.* Paris-Saclay, France: TINCE 2018: Technological Innovations in Nuclear Civil Engineering.

HighestBridges.com. (2009, December 10). Retrieved January 15, 2020, from http://www.highestbridges.com/wiki/index.php?title=Parrotts_Ferry_Bridge

Hogancamp, J., Flores, G., James, R., Dameron, R., & Jones, C. (2019). *Review of Failure Modes Applicable to Prestressed Concrete Containments.* Albuquerque, NM: Sandia National Laboratories.

Hu, H.-T., & Lin, J.-X. (2016). Ultimate analysis of PWR prestressed concrete containment under long-term prestressing loss. *Annals of NUclear Energy, 87*, 500-510.

Illston, J. (1965, June). The creep of concrte under uniaxial tension. *Magazine of Concrete Research, 17*(51), 77-84.

Installations, N. E. (1999). *NPP Containment Prestress Loss Summary Statement.* Organization for Economic Co-operation and Development.

Installations, N. E. (2015). *Bonded or Unbonded Technologies for Nuclear Reactor Prestressed Concrete Containments.* Organization for Economic Co-operation and Development.

International Federation for Structural Concrete. (October 2013). *Model Code for Concrete Structures 2010.*

Javanmardi, P. (2020). Experimental Study of Triaxial Behavior of Concrete under Lateral Confining Stress . *The Open Civil Engineering Journal, 14*.

Jinke Li, K. L. (2017, April). Nuclear Power Plant Prestressed Concrete Containment Vessel Structure Monitoring During Integrated Leakage Rate Testing using Fiber Bragg Grating Sensors. *Applied Sciences, 7*(4), 419.

Jones, C. A., Dameron, R., & Sircar, M. (2015, December 15). Improving the state of the art in FEM analysis of PCCVs with bonded and unbonded prestress tendons. *Nuclear Engineering and Design, 295*, 782-788.

Kelley, L. (2018, May). Large Scale Specimen Design and Creep Analysis for Nuclear Conainment Concrete Walls. *Master's Thesis*. Texas A&M University.

KEPRI. (2000). *Concrete Long-Term Test for Young-Kwang Power Plant unit 5 & 6.* Korea Electric Power Research Institute.

Kim, S.-G., Park, Y.-S., & Lee, Y.-H. (2019, October). Comparison of Concrete Creep in Compression, Tension, and Bending under Drying Condition. *Materials (Basel), 12*(20), 3357.

Kodur, V. (2014). Propteries of Concrete at Elevated Temperatures. *Hindawi Publishing Corporation, 2014*, 15.

Lee, S.-K., Song, Y.-C., & Han, S.-H. (2004). Biaxial behavior of plain concrete of nuclear containment building. *Nuclear Engineering and Design, 227*, 143-153.

Lee, Y., Kim, G., Gucunski, N., Choe, G., & Yoon, M. (2015). Thermal Strain Behavior and Strength Degradation of Ultra-High-Strength-Concrete. *Materials and Structures, 49*, 3411-3421.

Lundqvist, P., & Nilsson, L.-O. (2011). Evaluation of prestress losses in nuclear reactor containments. *Nuclear Engineering and Design, 241*, 168-176.

Maierhofer, C., Reinhardt, H.-W., & Dobmann, G. (2010). *Non-Destructive Evaluation of Reinforced Concrete Structures, Volume 2.* Woodhead Publishing Limited.

Manjoine, M. J. (1982, February). Creep-Rupture Behavior of Weldments. *Welding Research Supplement*.

Mazzotti, C., & Savoia, M. (2002). Nonlinear Creep, Poisson's Ratio, and Creep-Damage Interaction of Concrete in Compression. *ACI Materials Journal, September-October*, 450-457.

Mazzotti, C., & Savoia, M. (2003). Nonlinear Creep Damage Model for Concrete under Uniaxial Compression. *Journal of Engineering Mechanics, 129*(9), 1065-1075.

McCormac, J. C., & Brown, R. H. (2009). *Design of Reinforced Concrete, 8th Edition.* Danvers, MA: John Wiley & Sons, Inc.

Medeiros-Junior, R. A., de Lima, M. G., & de Medeiros, M. H. (2015). Service life of concrete structures considering the effects of temperature and relative humidity on chloride transport. *Environment, Development and Sustainability, 17*(5), 1103-1119.

Mhamankar, S., & Jones, C. (2019, August 4-9). Stress-State and Time-Dependent Deformation Characteristics for Cementitious Materials. *Transactions*. Charlottte, NC: SMiRT-25.

Mindess, S., Young, J. F., & Darwin, D. (2003). *Concrete, 2nd Edition.* Upper Saddle River, NJ: Pearson Education, Inc.

Naguib, W., & Mirmiran, A. (2003). Creep modeling for concrete-filled tubes. *Journal of Construction Steel Research, 59*, 1327-1344.

Nasser, K. W., & Neville, A. M. (1966). Creep of Concrete at Elevated Temperatures. *American Concrete Institute, 62*(12), 1567-1580.

National Institute of Standards and Technology (NIST). (2020).

Nilson, A. H. (1987). *Design of Prestressed Concrete, 2nd Ed.* New York, NY: John Wiley & Sons.

Oak Ridge National Laboratory. (1986). *Concrete Component Aging and its Significance Relative to Life Extension of Nuclear Power Plant (NUREG/CR 4652. ML040230118).*

Pandey, M. D. (1997). Relaibility-based assessment of integrity of bonded prestressed concrete containment structures. *Nuclear Engineering and Design, 176*, 247-260.

Pavement Tools Cosortium. (n.d.). *Pavement Interactive*. Retrieved 09 09, 2019, from https://www.pavementinteractive.org

Pensado, O., Shukla, P., Das, K., Mintz, T., Pabalan, R., Stothoff, S., & Sagues, A. (2013). *Containment Building Liner Corrosion - Corrosion and Leak Rate Models.* Washington, DC: US Nuclear Regulatory Commission.

Petti, J. P., Naus, D., Sagues, A., Weyers, R. E., Erler, B. A., & Berke, N. S. (2011). *Nuclear Containment Steel Liner Corrosion Workshop: Final Summaryand Recommendation Report SAND2010-8718.* Albuquerque, NM: Sanida National Laboratories.

Pipilikaki, P., & Beazi-Katsoiti, M. (May 2009). The Assessment of Porosity and Pore Size Distribution of Limestone Portland Cement Pastes. *23*(5).

Port of Long Beach. (2010). *Design Criteria for the Gerald Desmond Bridge Replacement.*

Raphael, W., Faddoul, R., Feghaly, R., & Chateauneuf, A. (2012). Analysis of Roissy Airport Terminal 2E collapse using deterministic and reliability assessments. *Journal of Engineering Failure Analysis, 20*, 1-8.

Raphael, W., Zgheib, E., & Chateauneauf, A. (2018). Experimental investigations and sensitivity analysis to explain the large creep of concrete deformations in the bridge of Cheviré. *Journal of Case Studies in Construction Materials, 9*, 1-8.

Sandia National Laboratories. (2018). *Nuclear Containment Steel Liner Corrosion Workshop: Final Summary and Recommendation Report (SAND2010-8718).*

Sellin, J.-P., Barthélémy, J.-F., Bondonet, G., & Cauvin, B. (2015). Delayed deformations of concrete structures: the Savines bridge and the Cheviré bridge. *Multispan large bridges.* Porto.

Song, H.-W., Kim, S.-H., Byun, K.-J., & Song, Y.-C. (2002). Creep prediction f concrete for reactor containment structures. *Nuclear Engineering and Design, 217*, 225-236.

South Texas Projct Nuclear Operating Company. (2013). *Safety Evaluation Report with Open Items Related to the License Renewal of South Texas Project, Units 1 and 2 (ML13045A356).*

Takacs, P. (2002). Deformations in Concrete Cantilever Bridges: Observations and Theoretical Modeling. Trondheim, Norway: Dept. of Structural Engineering - Norwegian University of Science and Technology, Doctoral Thesis.

Tang, M.-C. (2014). *The Story of the Koror Bridge.* Zurich, Switzerland: International Association for Bridge and Structural Engineers.

Terrey, P., Bradford, M., & Gilbert, R. (1994). Creep and shrinkage in concrete-filled steel tubes. In *Tubuluar Structures VI* (pp. 293-298). Rotterdam, Netherlands: Balkema.

The International Union of Laboratories and Experts in Construction Materials, Systems and Structures (RILEM). (June 1998). RILEM TC 129-MHT: Test Methods for Mechanical Properties of Concrete at High Temperatures. *Materials and Structures, 31*, 290-295.

Theryo, T. (2011). Long-Term Effect of Creep & Shrinkage on Segmental Concrete Bridges. *Virginia Concrete Conference.* Richmond, VA.

Trent, W. D. (2018, August). Effects of Alkali-Silica Reaction on the Fracture Behavior of Concrete. *Master's Thesis*. Knoxville, TN: University of Tennessee Knoxville.

US Nuclear Regulatory Commission. (1999). *Information Notice No. 99-10, Revision 1: Degradation of Prestressing Tendon Systems in Prestressed Concrete Containments.* Washington, DC: US Nuclear Regulatory Commission Office of Nuclear Reactor Regulation.

US Nuclear Regulatory Commission. (1999). *Information Notice No. 99-10: Degradation of Prestressing Tendon Systems in Prestressed Concrete Containments.* Washington, DC.

US Nuclear Regulatory Commission. (2000). *Safety Evaluation Report Related to License Renewal of Oconee Nuclear Station Units 1, 2, and 3 (NUREG-1723, ML003695154).*

US Nuclear Regulatory Commission. (2003). *Overpressurization Test of a 1:4-Scale Prestressed Concrete Containment Vessel Model (NUREG/CR-6810, SAND2003-0840P).*

US Nuclear Regulatory Commission. (2006). NUREG/CR 6906 Containment Integrity Research at Sandia National Laboratories. *SAND2006-2274P.*

US Nuclear Regulatory Commission. (2010). *Crystal River Unit 3 NRC Special Inspection Report 05000302/2009007.*

US Nuclear Regulatory Commission. (2010). Generic Aging Lessons Learned (GALL) Report. *NUREG 1801, Rev 2*.

US Nuclear Regulatory Commission. (2010). Standard Review Plan for Review of License Renewal Applications for Nuclear Power Plants. *NUREG 1800, Rev 2*.

US Nuclear Regulatory Commission. (2011). *Resolution of Generic Safety Issues: Issue 118: Tendon Anchor Head Failure (Rev. 1) NUREG-0933.* Washington, DC: US Nuclear Regulatory Commission.

US Nuclear Regulatory Commission. (2012). *Regulatory Guide 1.90: In-Service Inspection of Pre-stressed Concrete Containment Structures with Grouted Tendons, Rev. 2.* Washington, DC.

US Nuclear Regulatory Commission. (2013). *Regulatory Guide 1.35.1: Determining Pre-stressing Forces for Inspection of Pre-stressed Concrete Containments.* Washington, DC.

US Nuclear Regulatory Commission. (2014). NUREG/CR 7153 Expanded Material Degradation Assessment Report. *Aging of Concrete and CIvil Structures NUREG/CR-7153 Vol. 4*.

US Nuclear Regulatory Commission. (2015). *NUREG/CR 7208 Study on Post Tensioning Methods.*

US Nuclear Regulatory Commission. (2017). Generic Aging Lessons Learned for Subsequent License Renewal (GALL-SLR) Report. *NUREG 2191 Vol 1*.

US Nuclear Regulatory Commission. (2017). Generic Aging Lessons Learned for Subsequent License Renewal (GALL-SLR) Report. *NUREG 2191 Vol 2*.

US Nuclear Regulatory Commission. (2017). Standard Review Plan for Review of Subsequent License Renewal Applications for Nuclear Power Plants. *NUREG 2192*.

US Nuclear Regulatory Commission. (2019). *10 CFR 50: Domestic Licensing of Production and Utilization Facilities.* Regulatory Document.

Wang, S., & Munshi, J. (2013, February). Design of radial reinforcement for prestressed concrete containments. *Nuclear Engineering and Design, 255*, 153-161.

Wang, Y., & Xi, Y. (2017). The Effect of Temperature on Moisture Transport in Concrete. *10*(8).

William D. Callister, J. (2007). *Materials Science and Engineering, An Introduction, 7th Edition.* York, PA: John Wiley & Sons, Inc.

Williams, S. J., Bache, M. R., & Wilshire, B. (2010). 25 Years Perspective Recent Developments in Analysis of High Temperature Creep and Creep Fracture Behavior. *Materials Science and Technology, 26*(11), 1332-1337.

Woods, C. R. (2016, December). Experimental Investigation of the Delamination Behavior of Curved Post-Tensioned Concrete Structures without Through-Thickness Reinforcement. *Master's Thesis*. University of Texas at Austin.

Yoon, M., Kim, G., Kim, Y., Lee, T., Choe, G., Hwang, E., & Nam, J. (2017). Creep Behavior of High-Strength Concrete Subjected to Elevated Temperatures. *Materials, 10*(7), 781.

Zhou, F. P. (1992). Time-Dependent Crack Growth and Fracture in Concrete. Lund, Sweden: Doctoral Dissertation, Lund University.

Zhou, F. P., & Hillerborg, A. (1992). Time Dependent Fracture of Concrete: Testing and Modeling. *Proceedings of the First International Conference on Fracture Mechanics in Concrete Structures*, 906-911.

APPENDIX A

This appendix presents the strain gage data given by EDF for the VeRCoRs mockup as well as comparisons between the EDF data and simulation results. Strain gage experimental data was not provided for H2IT, M3EV/ET, M4IV/IT, M7EV/ET, or M8IV/IT.

A.1   EDF Strain Gage Data

This section presents the raw VeRCoRs EDF strain gage data.
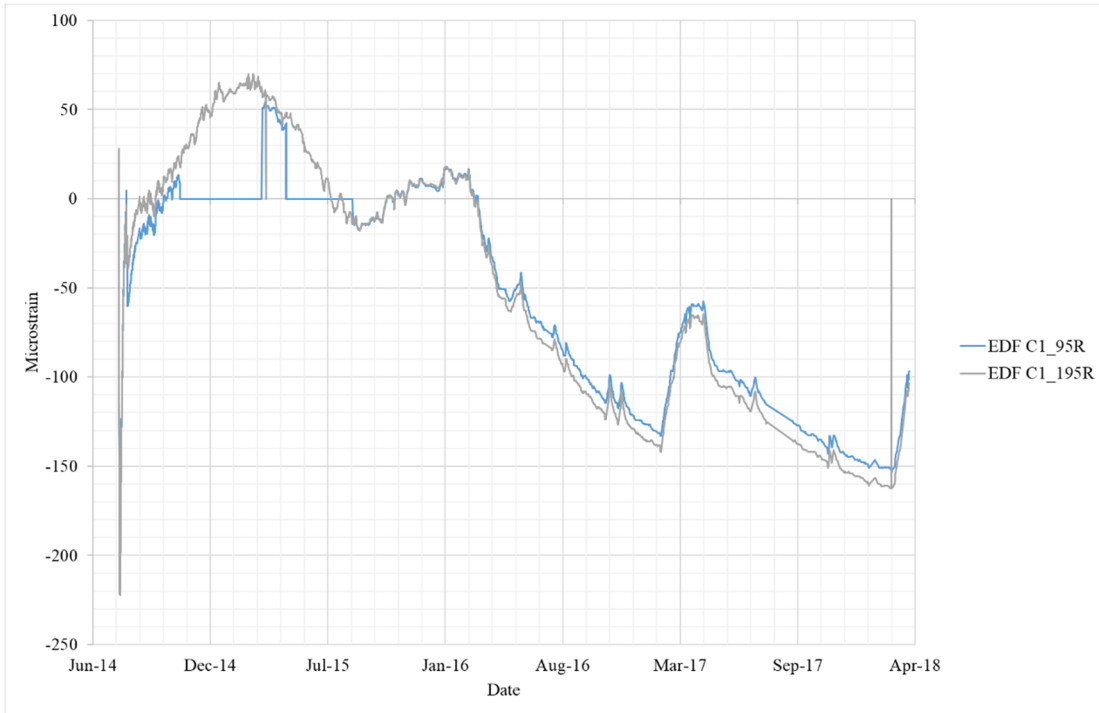
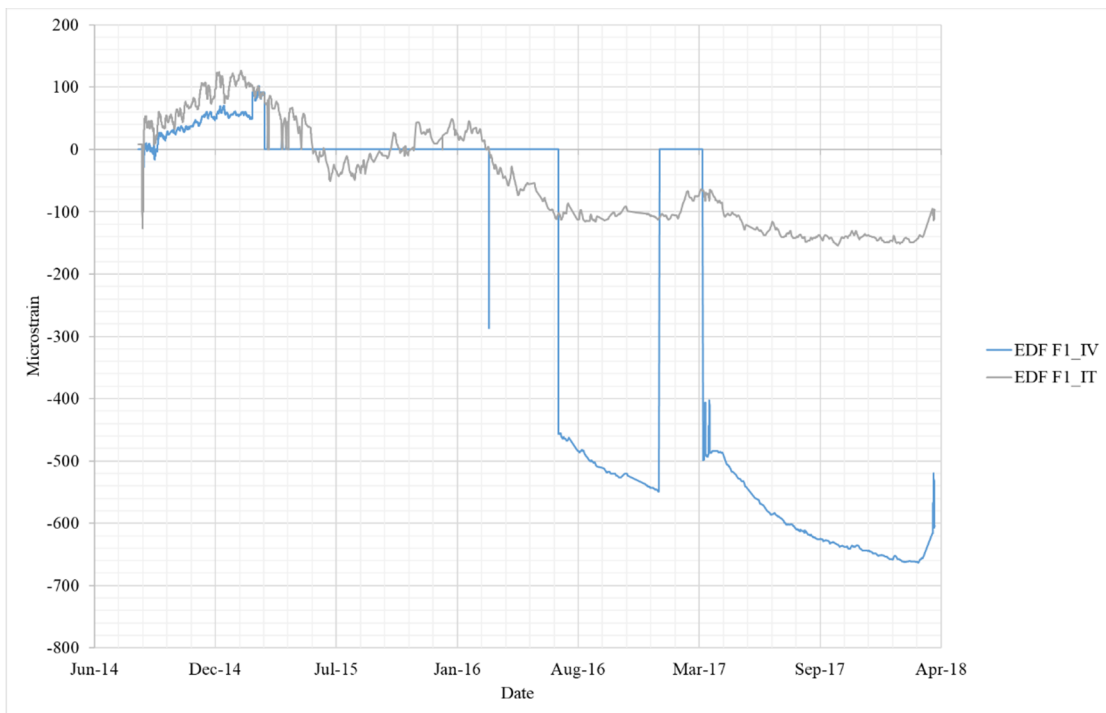**Figure A-1**   **EDF strain gage data for C95R and C195R.**

Figure A-2   EDF strain gage data for E95R and E195R.
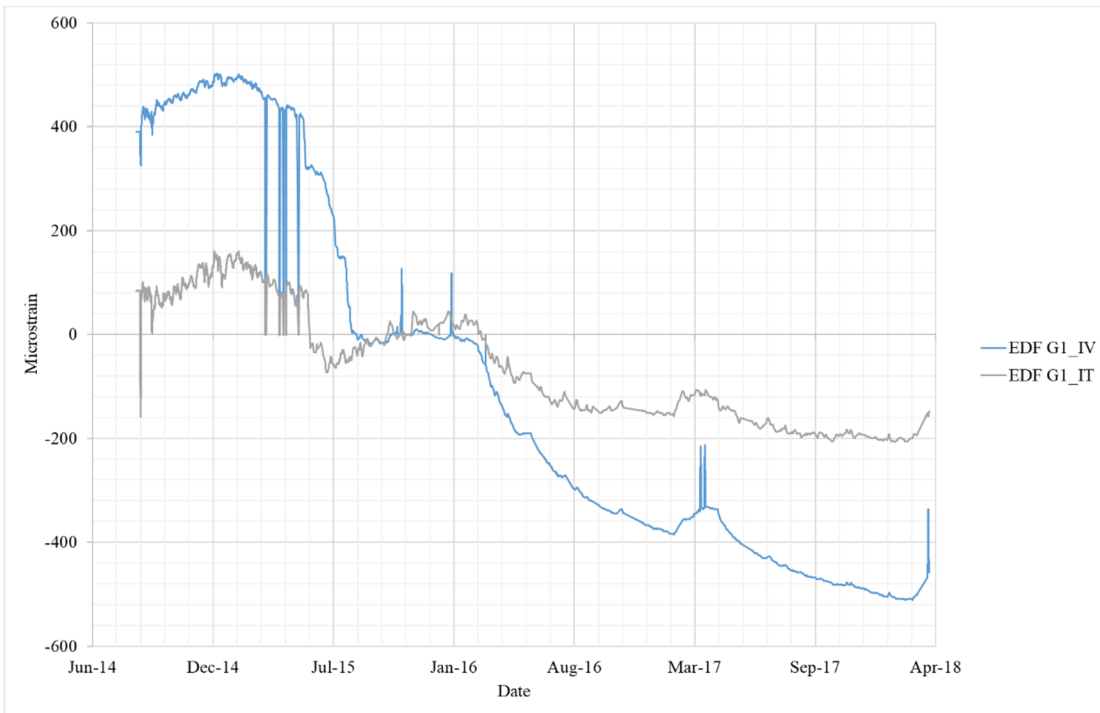
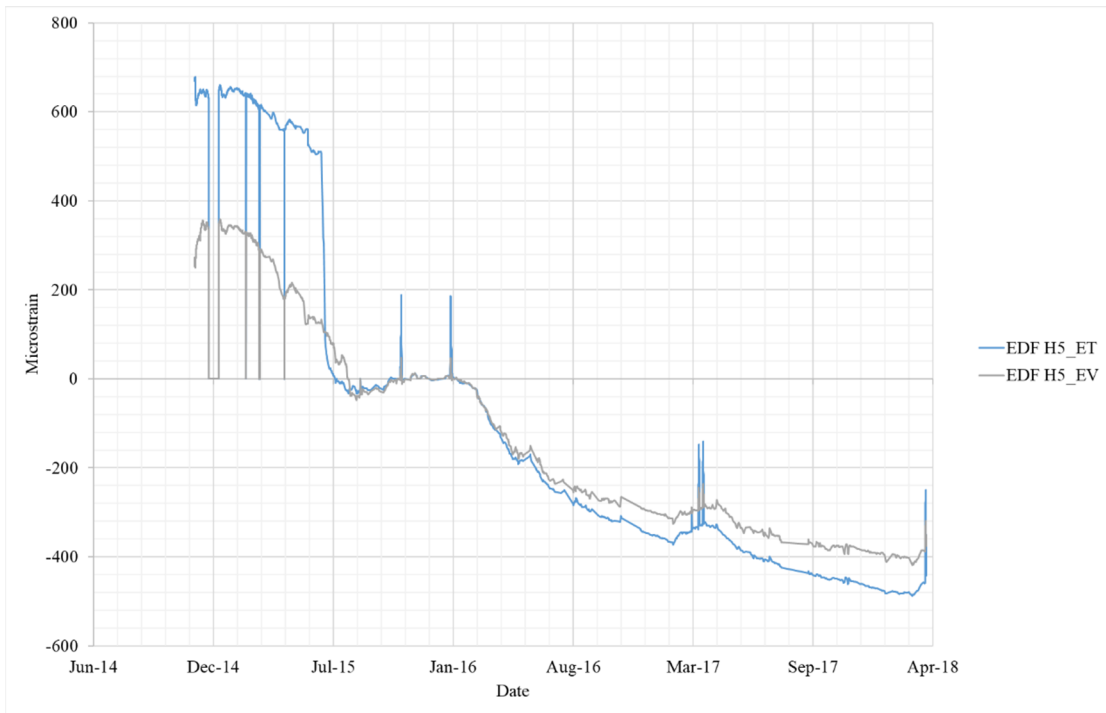**Figure A-3   EDF strain gage data for G1IV and G1IT.**
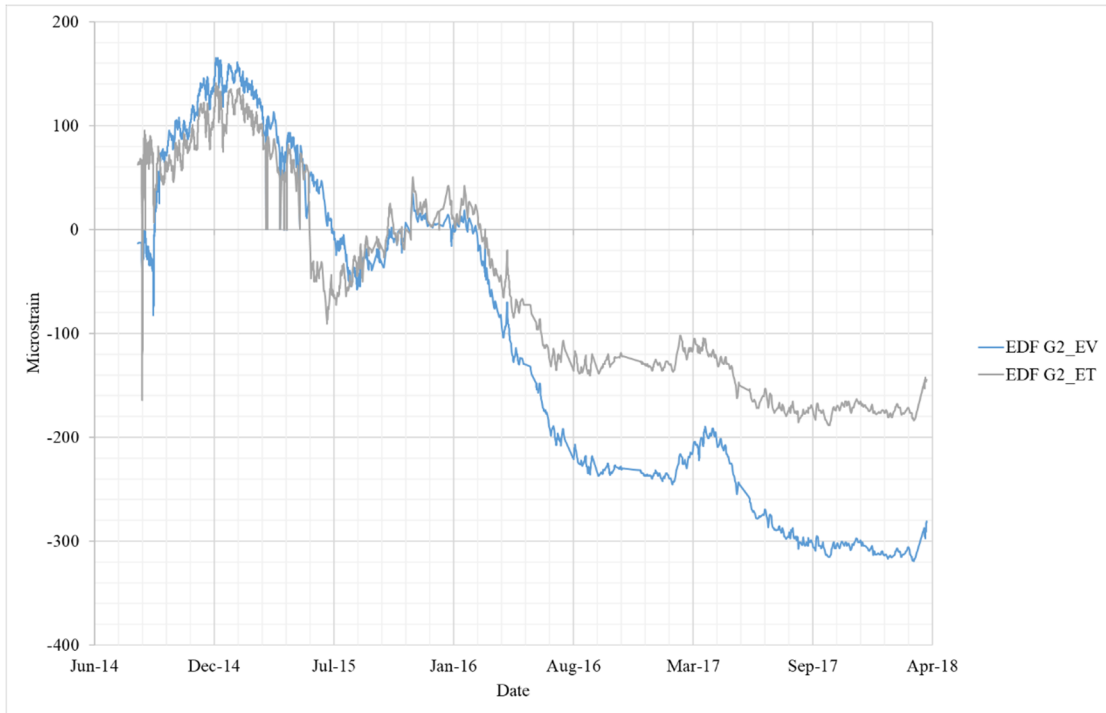
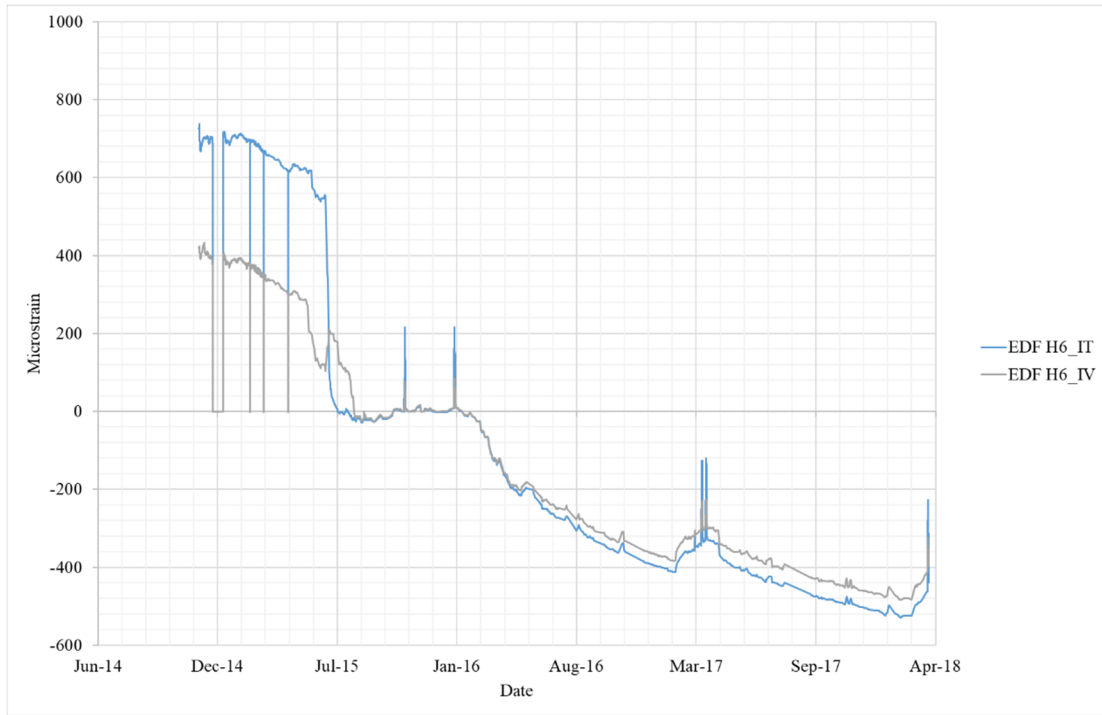**Figure A-4   EDF strain gage data for G2EV and G2ET.**

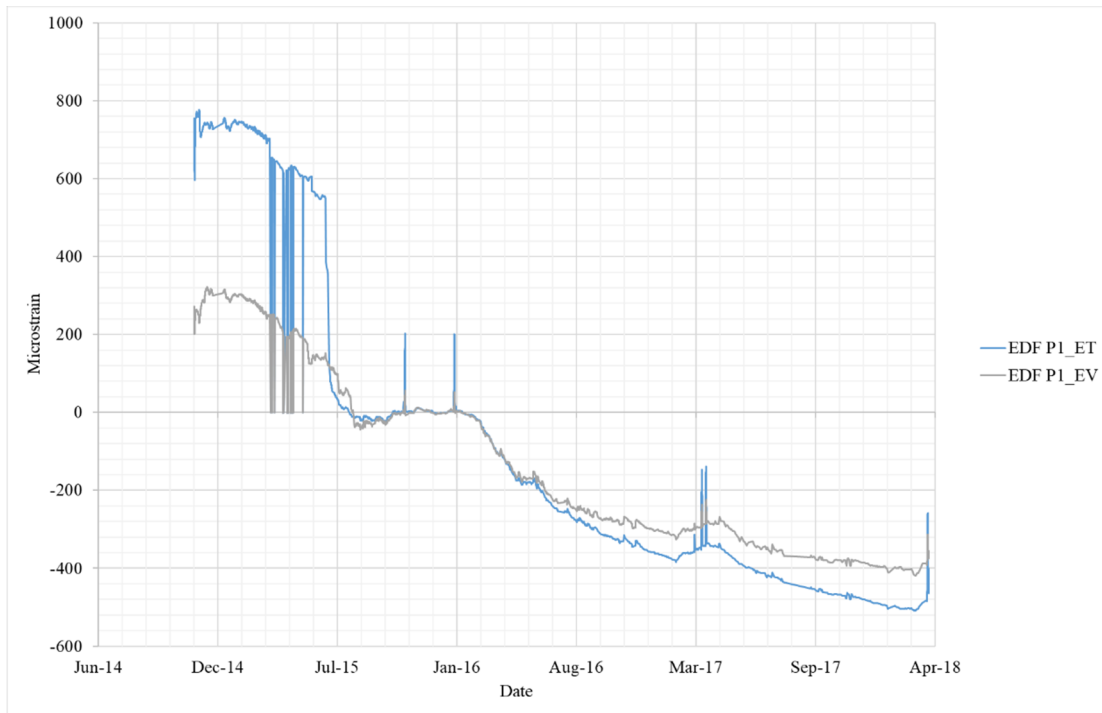**Figure A-5   EDF strain gage data for F1IV and F1IT.**

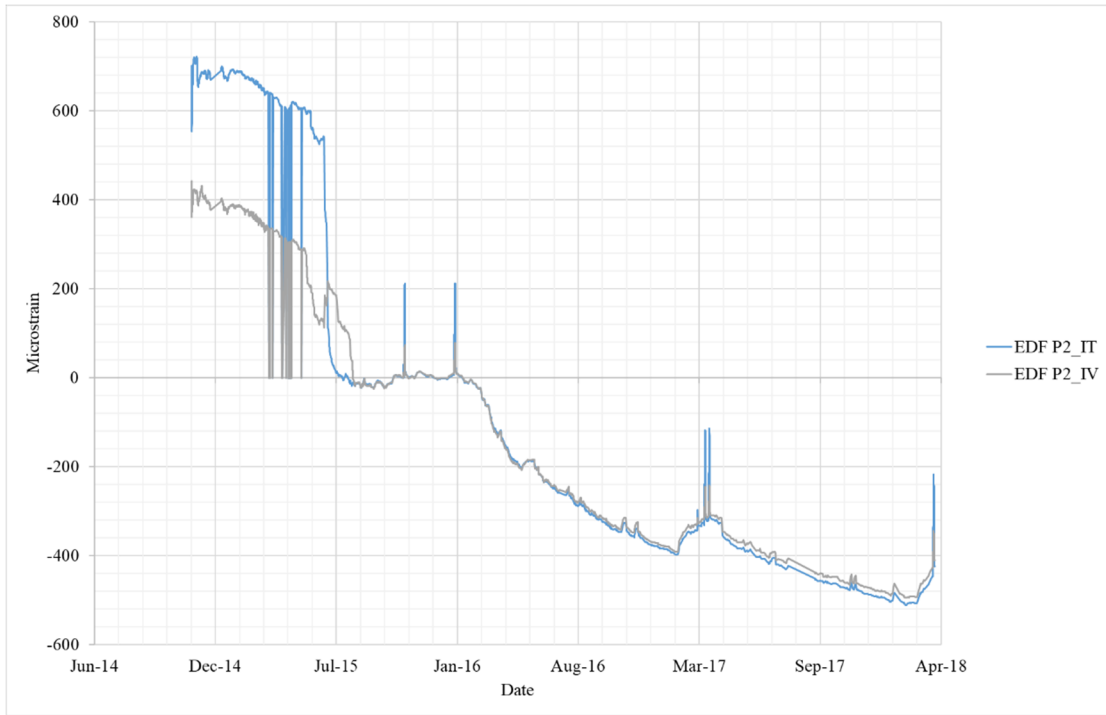**Figure A-6   EDF strain gage data for F2EV and F2ET.**

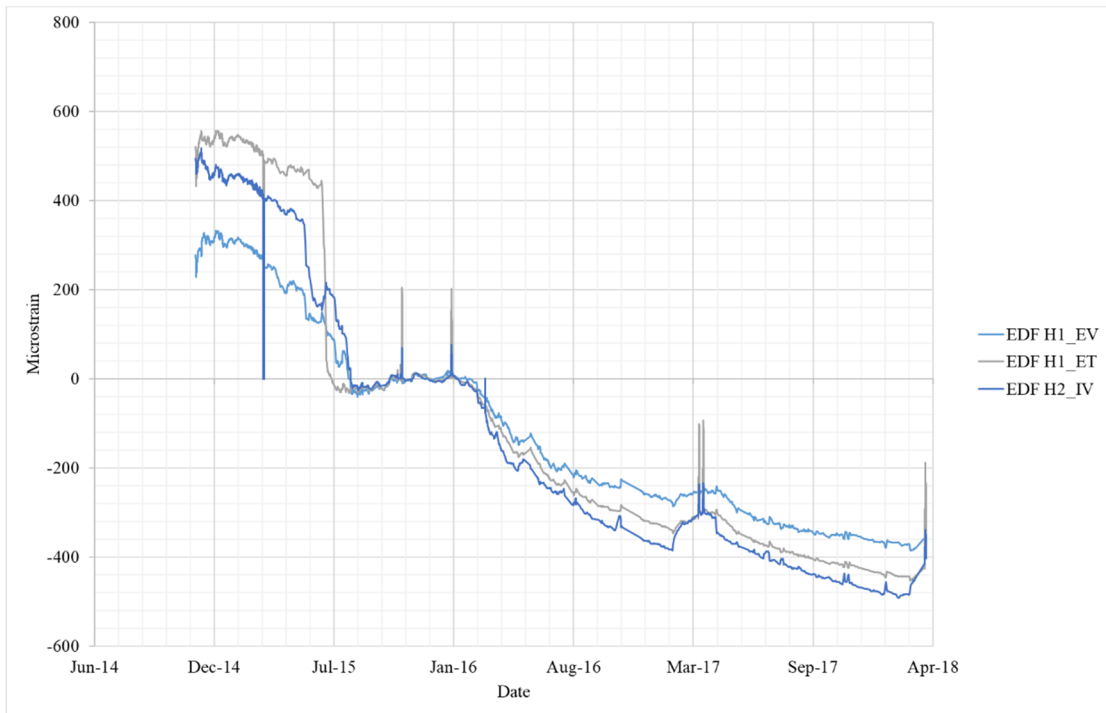**Figure A-7   EDF strain gage data for H5EV and H5ET.**

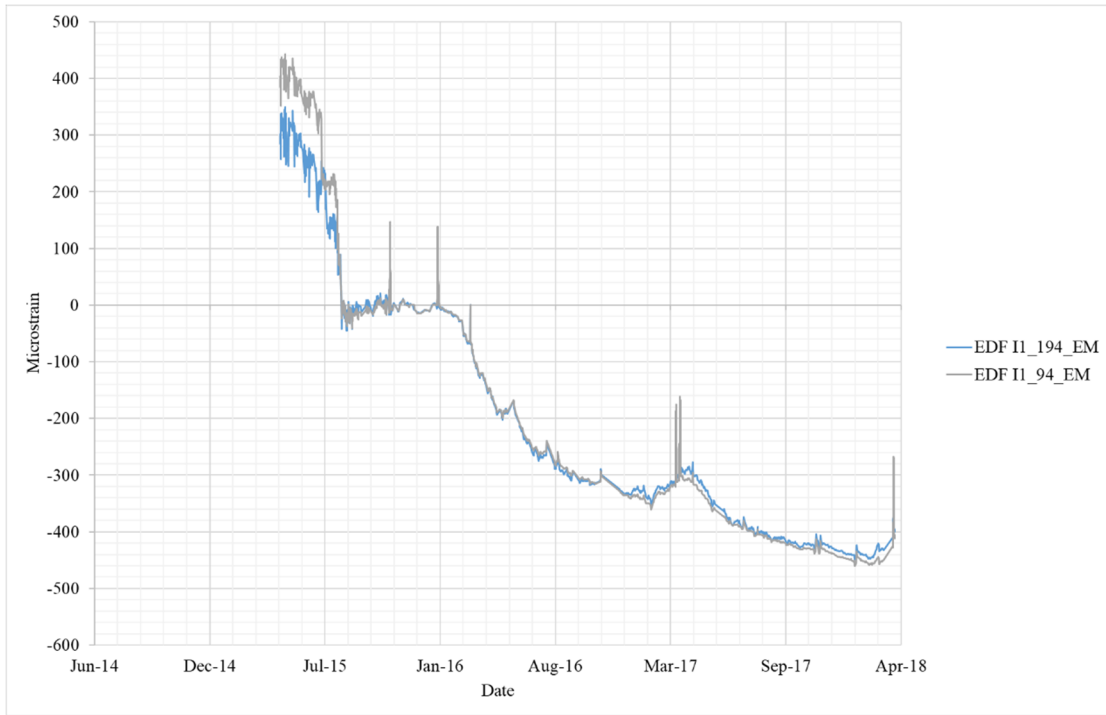**Figure A-8   EDF strain gage data for H6IV and H6IT.**

Figure A-9   EDF strain gage data for P1ET and P1EV.
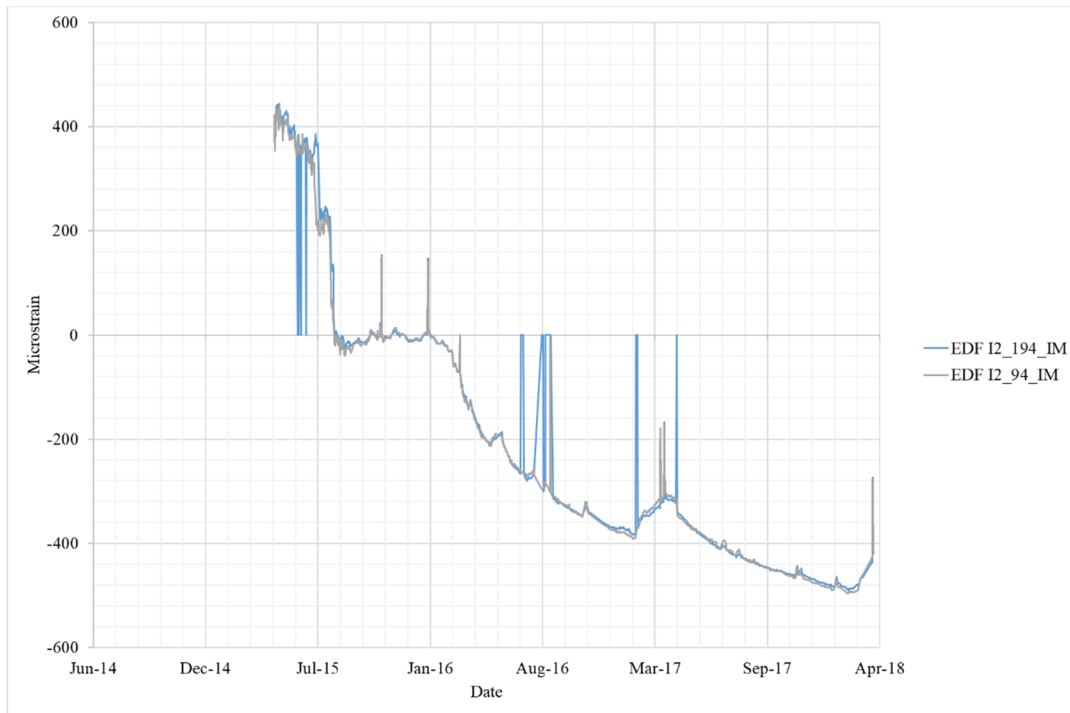
Figure A-10   EDF strain gage data for P2IV and P2IT.
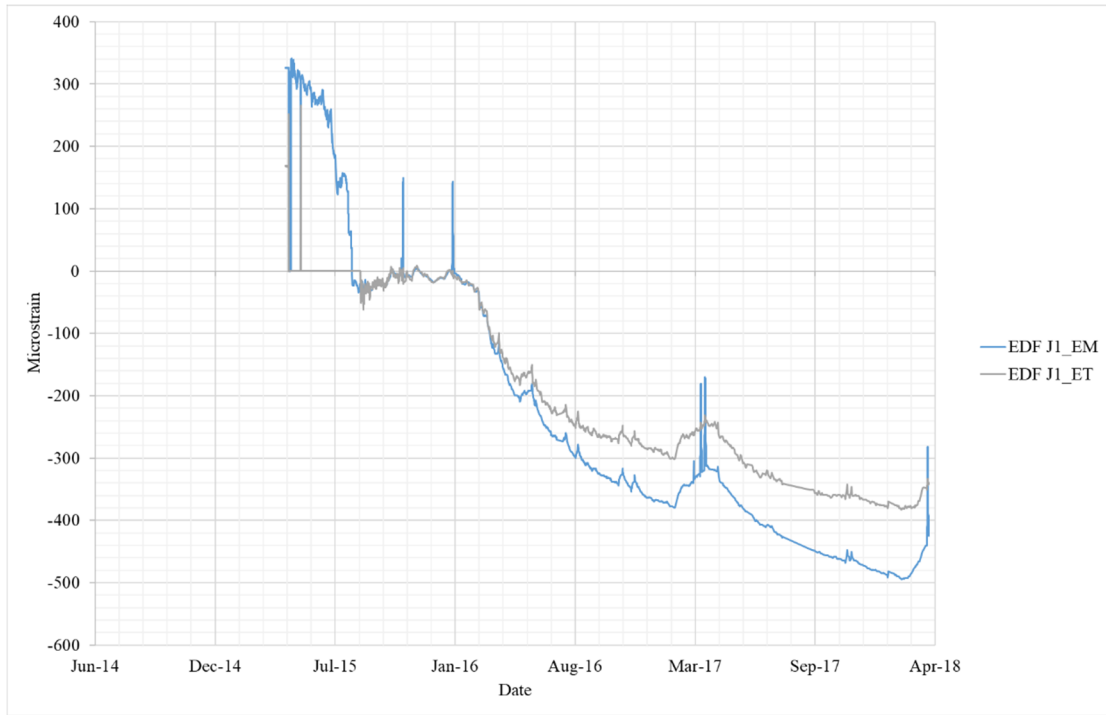

Figure A-11   EDF strain gage data for H1EV, H1ET, and H2IV.

Figure A-12   EDF strain gage data for I94EM and I194EM.

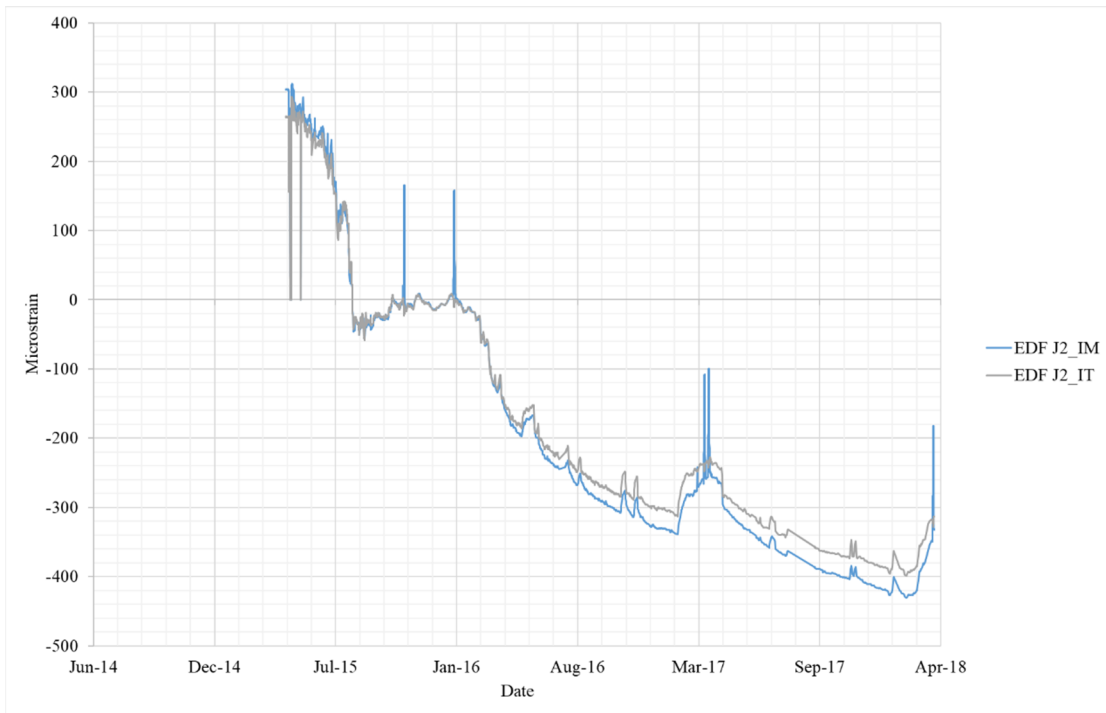**Figure A-13   EDF strain gage data for I94IM and I194IM.**

Figure A-14   EDF strain gage data for J1EM and J1ET.

Figure A-15   EDF strain gage data for J2IM and J2IT.

A.2   EDF Strain Gage Data Compared to Simulation Results

This section presents the raw VeRCoRs EDF strain gage data compared to the simulation results.

Figure A-16   Comparison strain gage data for C95 and C195R.

Figure A-17   Comparison strain gage data for E95R and E195R.
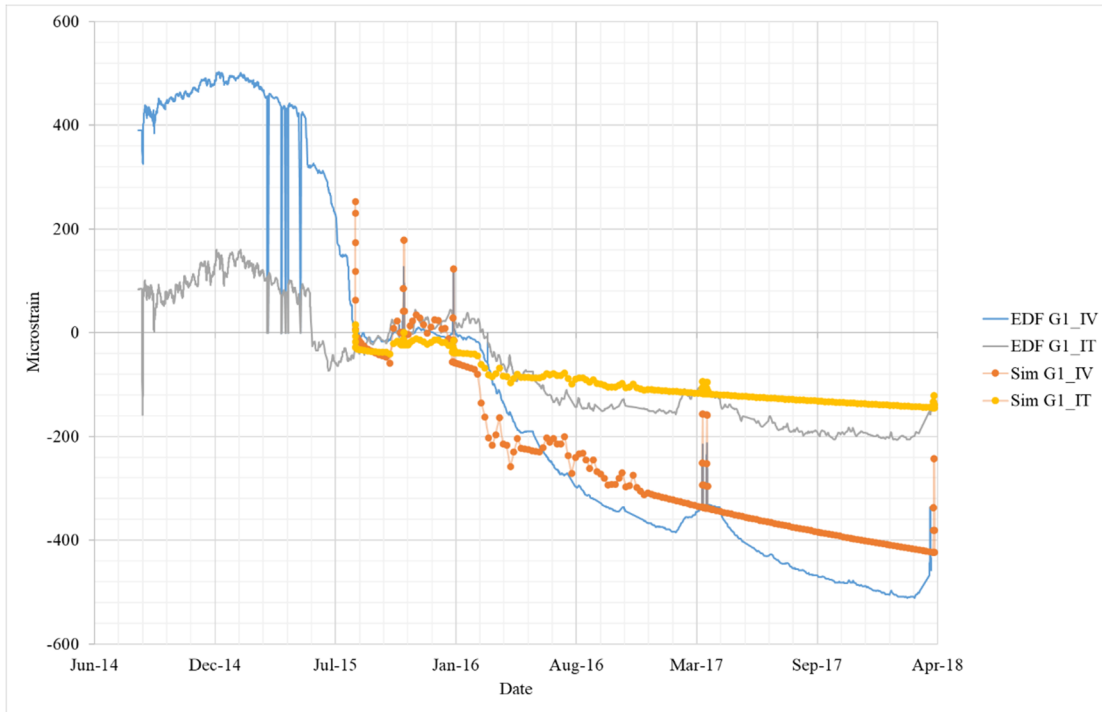
Figure A-18   Comparison strain gage data for G1IV and G1IT.

Figure A-19   Comparison strain gage data for G2EV and G2ET.
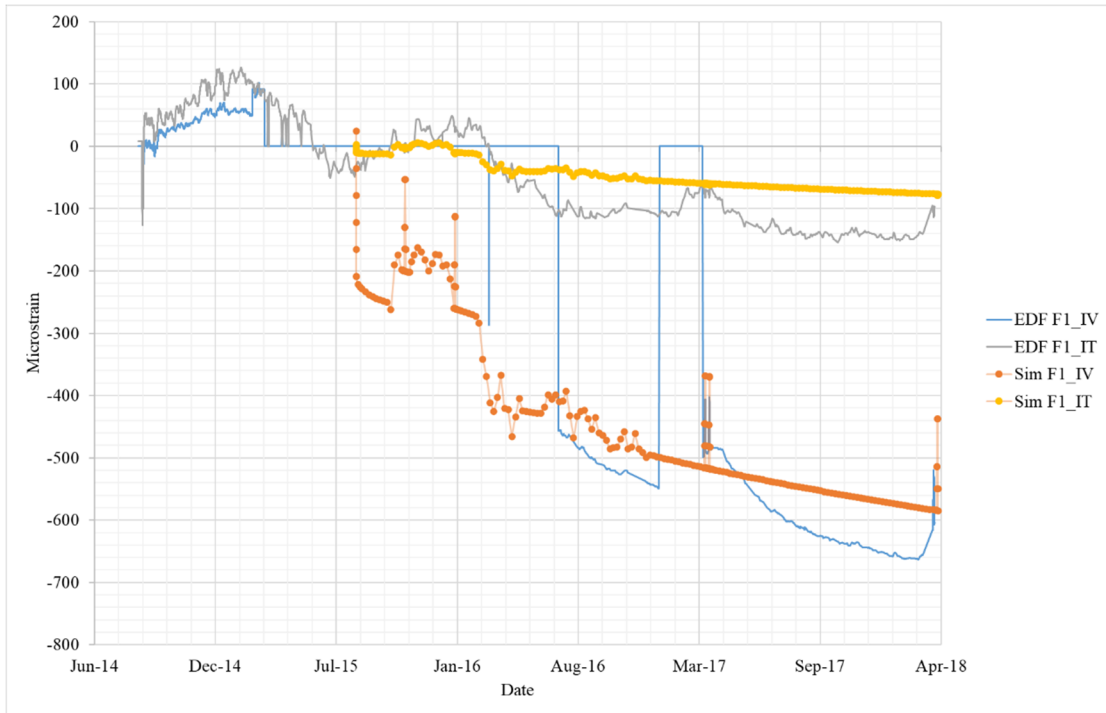
Figure A-20   Comparison strain gage data for F1IV and F1IT.

Figure A-21   Comparison strain gage data for F2EV and F2ET.
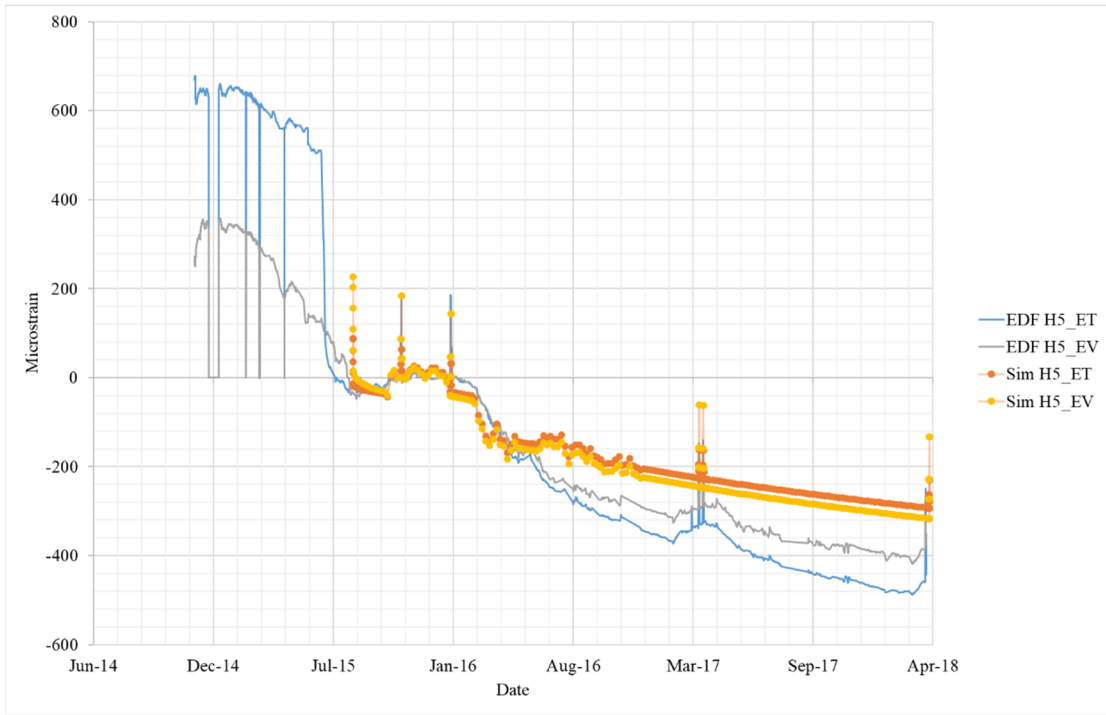
Figure A-22   Comparison strain gage data for H5EV and H5ET.
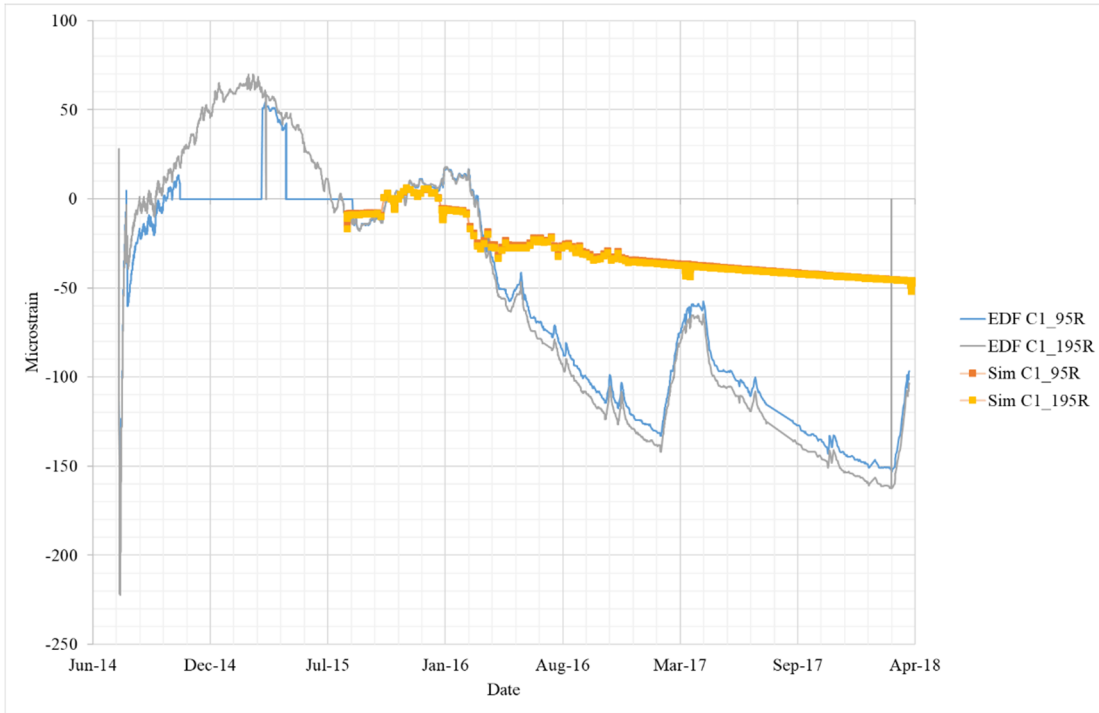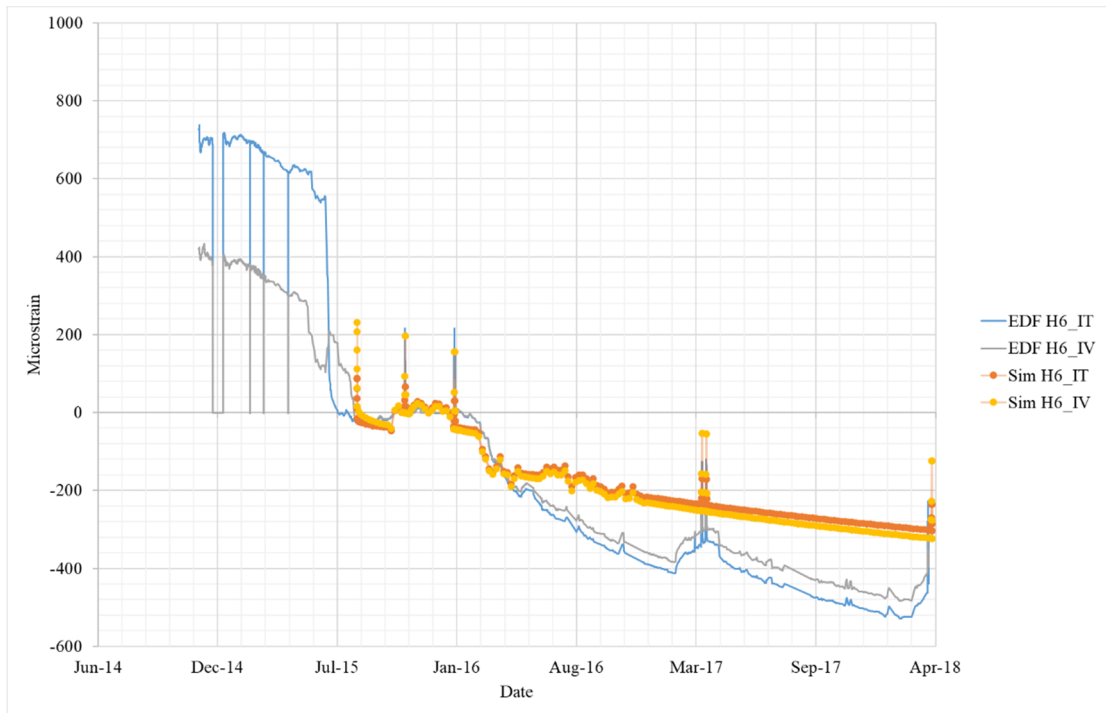

Figure A-23   Comparison strain gage data for H6IV and H6IT.
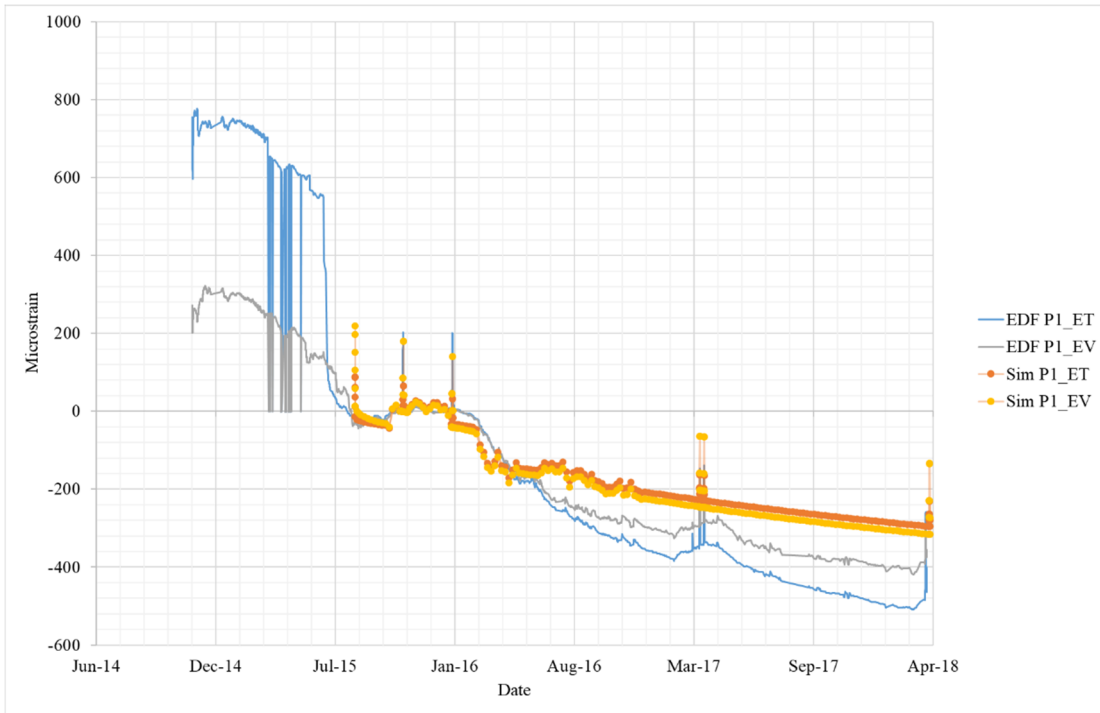
Figure A-24   Comparison strain gage data for P1EV and P1ET.
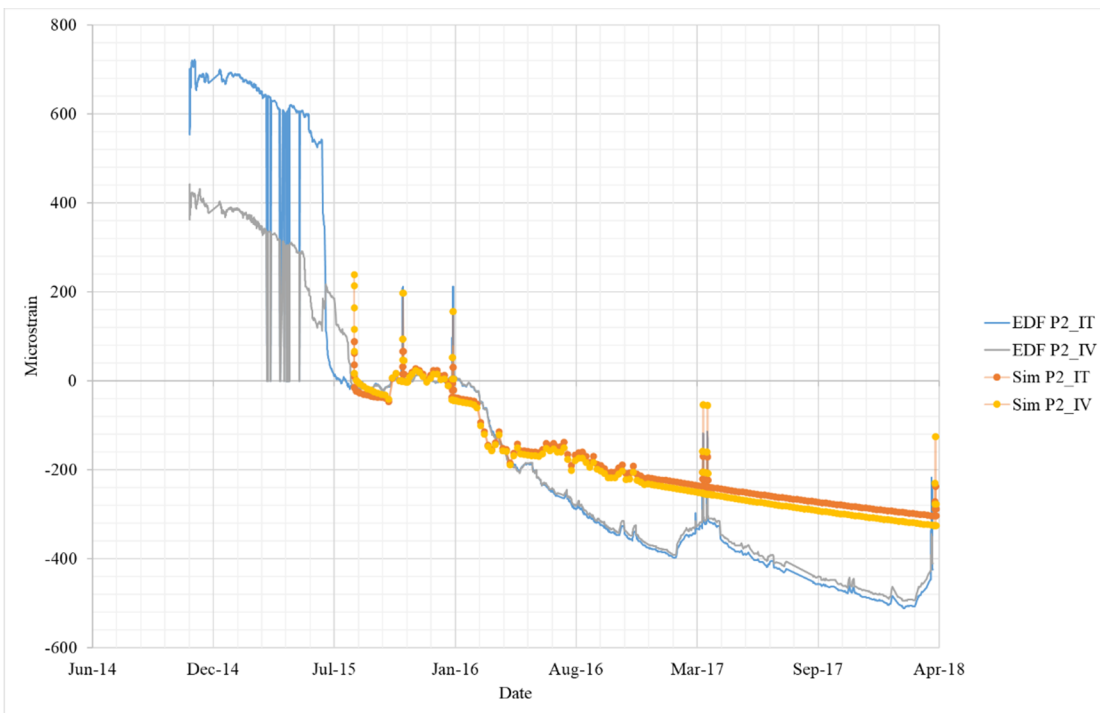
Figure A-25   Comparison strain gage data for P2IV and P2IT.
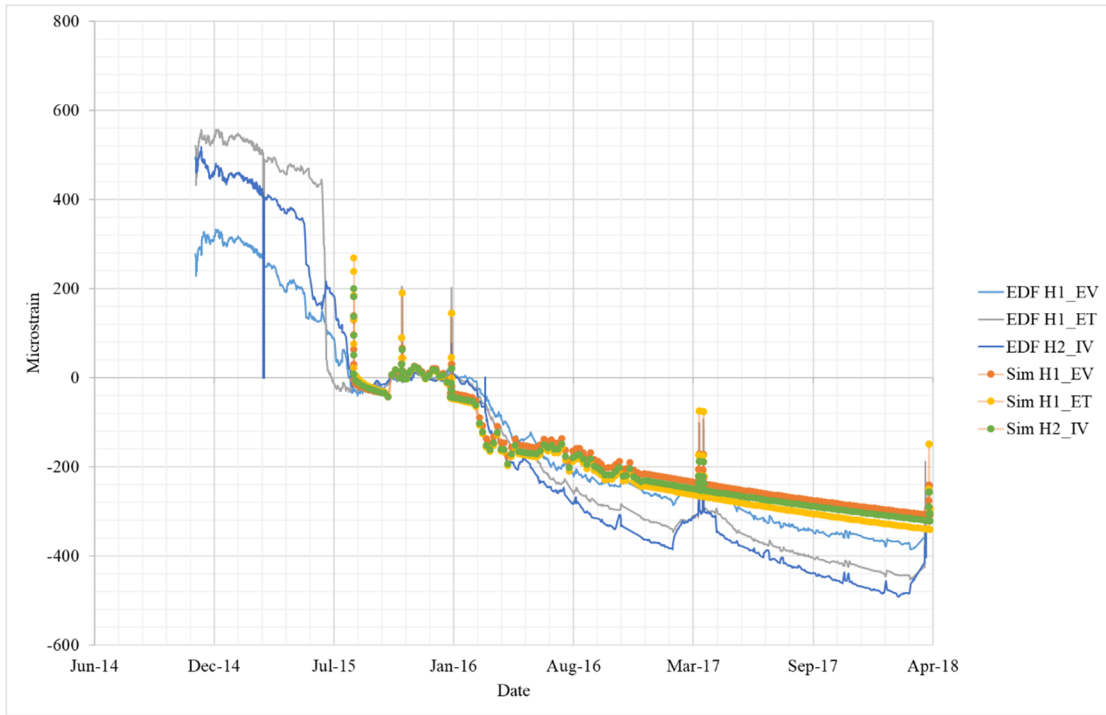
Figure A-26   Comparison strain gage data for H1EV, H1ET, and H2IV.
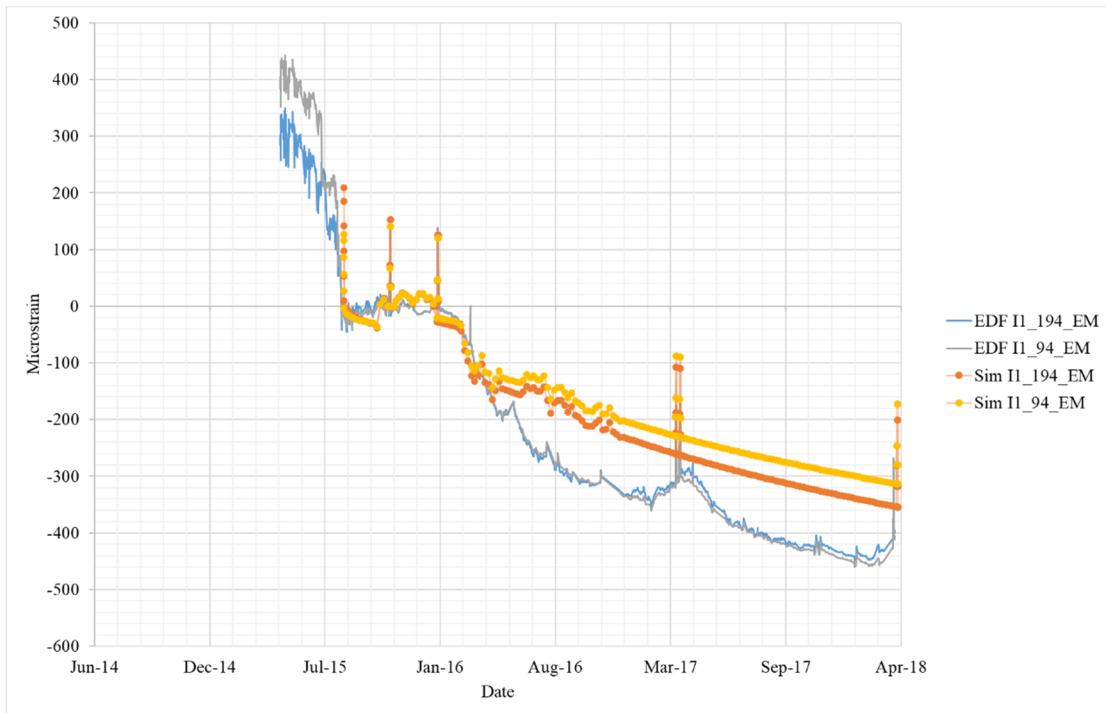
Figure A-27   Comparison strain gage data for I1_94EM and I1_I194EM.

Figure A-28   Comparison strain gage data for I2_94IM and I2_I194IM.
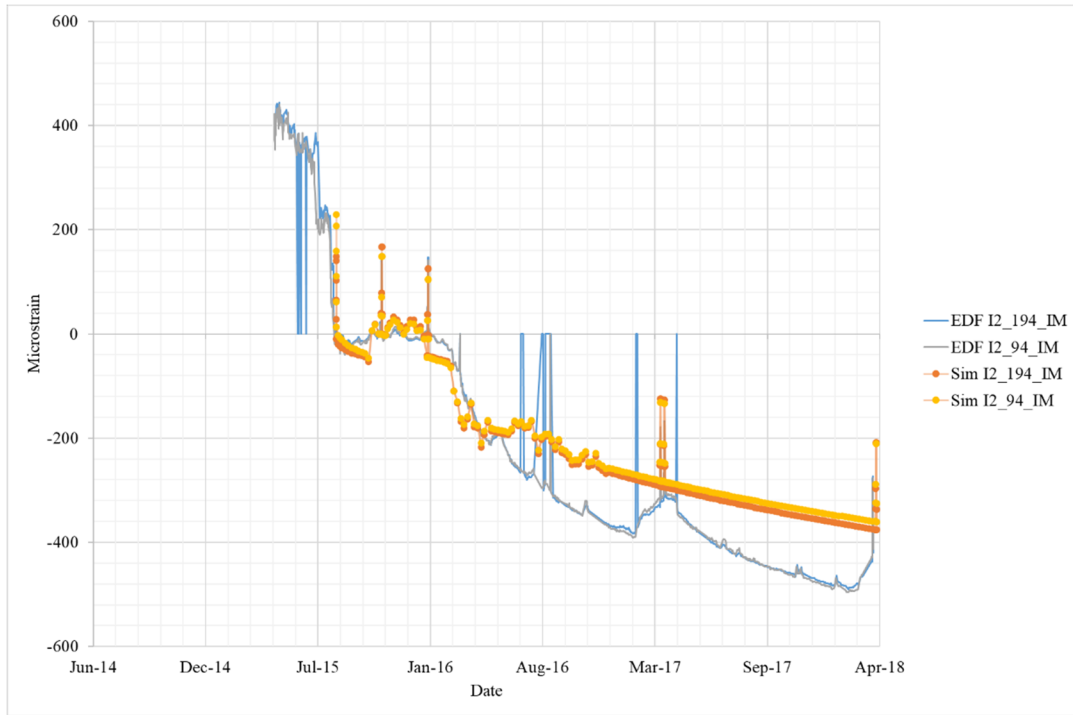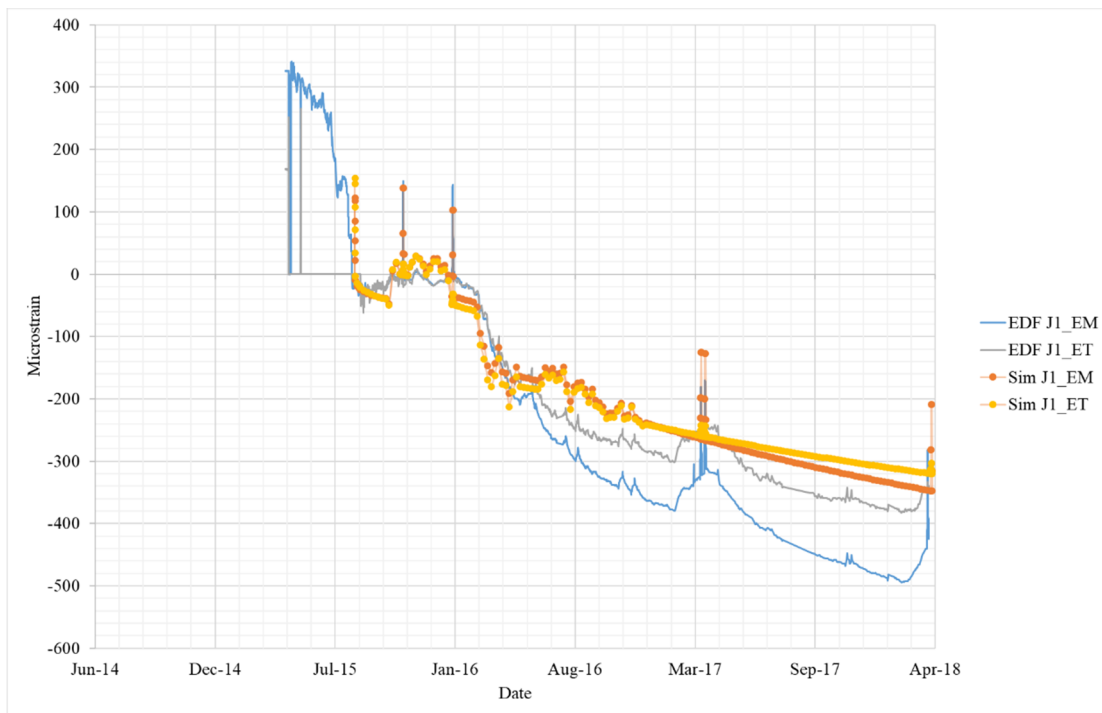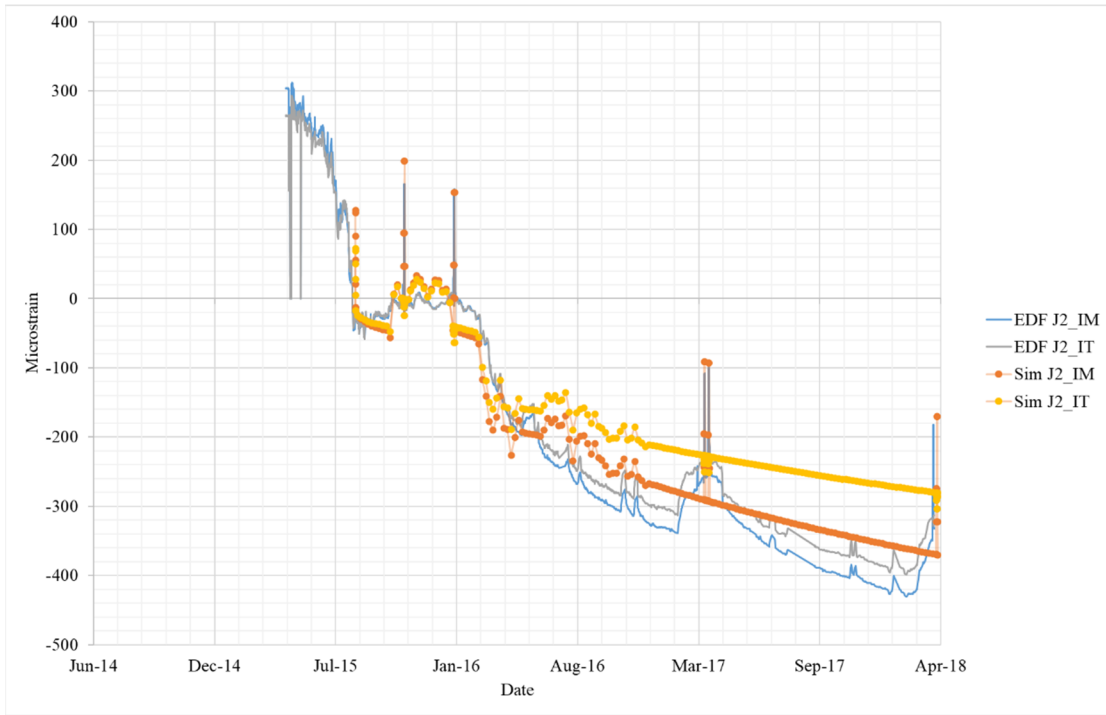

Figure A-29   Comparison strain gage date for J1ET and J1EM.

Figure A-30   Comparison strain gage data for J2IM and J2IT.

APPENDIX B

Operational Plants with Post-Tensioned Concrete Cylinder Vessel (PCCV)

Number	Reactor Name	Status	Primary Containment	Construction Type
1	Arkansas Nuclear 1	Operational	Large Dry	Post-Tensioned Concrete
2	Arkansas Nuclear 2	Operational	Large Dry	Post-Tensioned Concrete
3	Braidwood 1	Operational	Large Dry	Post-Tensioned Concrete
4	Braidwood 2	Operational	Large Dry	Post-Tensioned Concrete
5	Byron 1	Operational	Large Dry	Post-Tensioned Concrete
6	Byron 2	Operational	Large Dry	Post-Tensioned Concrete
7	Callaway	Operational	Large Dry	Post-Tensioned Concrete
8	Calvert Cliffs 1	Operational	Large Dry	Post-Tensioned Concrete
9	Calvert Cliffs 2	Operational	Large Dry	Post-Tensioned Concrete
10	Farley 1	Operational	Large Dry	Post-Tensioned Concrete
11	Farley 2	Operational	Large Dry	Post-Tensioned Concrete
12	Fort Calhoun	Operational	Large Dry	Post-Tensioned Concrete
13	Ginna	Operational	Large Dry	Post-Tensioned Concrete
14	H.B. Robinson 2	Operational	Large Dry	Post-Tensioned Concrete
15	Joseph M Farley 1	Operational	Large Dry	Post-Tensioned Concrete
16	Joseph M Farley 2	Operational	Large Dry	Post-Tensioned Concrete
17	La Salle 1	Operational	Large Dry	Post-Tensioned Concrete
18	La Salle 2	Operational	Large Dry	Post-Tensioned Concrete
19	Millstone 2	Operational	Large Dry	Post-Tensioned Concrete
20	Ocnee 1	Operational	Large Dry	Post-Tensioned Concrete
21	Ocnee 2	Operational	Large Dry	Post-Tensioned Concrete
22	Ocnee 3	Operational	Large Dry	Post-Tensioned Concrete
23	Palisades	Operational	Large Dry	Post-Tensioned Concrete
24	Palo Verde 1	Operational	Large Dry	Post-Tensioned Concrete
25	Palo Verde 2	Operational	Large Dry	Post-Tensioned Concrete
26	Palo Verde 3	Operational	Large Dry	Post-Tensioned Concrete
27	Point Beach 1	Operational	Large Dry	Post-Tensioned Concrete
28	Point Beach 2	Operational	Large Dry	Post-Tensioned Concrete
29	South Texas Project	Operational	Large Dry	Post-Tensioned Concrete
30	South Texas Project	Operational	Large Dry	Post-Tensioned Concrete
31	Summer 1	Operational	Large Dry	Post-Tensioned Concrete
32	Three Mile Island 1	Operational	Large Dry	Post-Tensioned Concrete
33	Turkey Point 3	Operational	Large Dry	Post-Tensioned Concrete

34	Turkey Point 4	Operational	Large Dry	Post-Tensioned Concrete
35	Vogtle 1	Operational	Large Dry	Post-Tensioned Concrete
36	Vogtle 2	Operational	Large Dry	Post-Tensioned Concrete
37	Wolf Creek	Operational	Large Dry	Post-Tensioned Concrete

APPENDIX C

This appendix includes a list of reactors and concrete component degradation occurrences as listed in NUREG/CR 4652 (Oak Ridge National Laboratory, 1986).

Reactor Plant	Docket No.	Year of commercial operation	Year of occurrence	Summary description
Yankee Rowe	50-29	1961	1967	A 15 ft. shrinkage crack, covered with fiberglass and recoated
San Onofre 1	50-206	1968	1976	Voids at 14 locations in diesel generation building center wall; areas from $1ft^2$ with 3-4 in penetration to several square feet with full penetration; repaired with dry pack, grout, or concrete
Ginna	50-244	1970	1981	Excessive loss of pre-stressing, tendons re-tensioned with no recurrence noted in subsequent inspections
Indian Point 2	50-247	1974	1974	Concrete temperature local to hot penetration > 150 °F but < 200 °F, no safety problem due to relatively low periods of exposure
Turkey Point 3	50-250	1972	1968	Voids below containment wall and near reactor pit, repaired with high-strength grout, guniting, or dry packing
			1970	Dome delamination; delaminated concrete removed, additional rebars provided, concrete replaced
			1974	Grease leakage from 110 of 832 tendons at casing, tendon casings repaired and refilled
			1975	Concrete spalling at horizontal joint at containment ring girder with cavities 1 to 2 in wide by 3 to 4 deep, no threat to structural integrity, repaired by dry packing
			1982	Small void under equipment hatch barrel, no threat to structural integrity, repaired by grouting
Turkey Point 4	50-251	1973	1981	Approximately 0.4 ft^2 of concrete with inadequate fines, area removed and refilled with concrete
Palisades	20-255	1971	1975	63 of 3780 buttonheads inspected found split, no threat to structural integrity
Fort St. Vrain	50-267	1979	1984	Tendon wire failures noted because of tendon corrosion caused by microbiological attack of corrosion inhibitor, analysis revealed sufficient tendons intact to provide structural integrity, and surveillance increased, and tendons inserted by nitrogen blanket

Oconee 2/3	50-270/278	1974	1982	During final reactor building interior inspection, 2 vertical tendons in secondary shield wall of unit 2 were found failed and some tendons in units 2 and 3 were exhibiting corrosion near stressing washers; tendons are not required to meet shield wall functions but were replaced and bottom grease caps redesigned to permit water drainage; surveillance was increased
			1983	4 tendons in reactor building found ungreased, tendons inspected, and grease applied
Peach Bottom 2/3	50-277/278	1974	1969	Aluminum pipe used to place concrete caused concrete strength reduction up to 50%, low-strength concrete in biological shield wall and floor slab of turbine building replaced
Surry 1	50-280	1972	1979	Cracking in concrete supports for 2 heat exchangers caused by thermal expansion of heat exchanger shells, cracks repaired and supports modified
Three Mile Island 1	50-289	1974	1975	2 of 6 concrete footings for rigid pipe supports cracked due to design deficiency, footings were replaced using a new design
			1974	Cracking < 0.010 in. wide in containment building ring girder and around tendon bearing plates, cracks repaired and monitored during subsequent surveillance
Zion 1	50-295	1973	1972	Excessive pitting observed in some tendon wires of unit 2 during installation, cause was outdoor storage in conjunction with high precipitation and inadequate protection, defective tendons replaced
Crystal River 3	50-302	1978	1974	28 day concrete strength was low due to failure of cement to meet specifications; design review revealed strength attained to be adequate; cement inspection increased
			1976	Dome delaminated over 105 ft. area due to low concrete properties, radial tension due to pre-stressing, and biaxial failure criterion; upper delaminated section removed, additional rebars provided, concrete replaced, dome re-tensioned, and structural integrity test conducted
Salem 2	50-311	1981	1974	Incomplete concrete pour near equipment hatch due to use of wrong concrete mix, voids repaired with high-strength non-shrink grout
Rancho Seco	50-312	1975	1974	Concrete surface temperature >150 °F during initial power escalation

Cook 1/2	50-315/316	1975/1978	1974	Cracking in spent fuel pit wall and slabs framing into pit walls, cause was thermal expansion and hydrostatic pressure, no threat to structural integrity
Calvert Cliffs 1/2	50-317/318	1975/1977	1971/1972	11 of top bearing plates of units 1 and 2 depressed into concrete because of voids; 190 plates of each containment exhibited voids upon inspection; tendons de-tensioned, plates grouted and tendons re-tensioned
Three Mile Island 2	50-320	1978	1974	4 of 6 sets of compression cylinders had low f'c because of mishandling and inventory control at cement silo, 90-d strengths were acceptable and concrete in-place determined to have adequate strength; cement storage and sampling techniques improved
			1975	Void 3in. high x 6 ft. wide x (3 to 5 ft.) deep occurred in south exterior wall of fuel-handling building, cause was improper placement, void determined not to be a threat to structural or shielding effectiveness; void refilled
			1976	Void 3 to 4 ft. into concrete 1.5 ft. high by 6 to 8 ft. wide in north exterior wall of fuel transfer canal, void repaired, no structural or shielding effectiveness threat
Hatch 1	50-321	1975	1981	Cracks in concrete wall around base plate
			1981	Concrete in pedestal for several recirculation line snubbers exhibited spalling and cracking due to design deviation, 1 in. plates with 4 wedge anchors installed on top of existing plates
Shureham	50-322	UC	1974	Unconsolidated and honeycombed areas in first lift of reactor support pedestal, voids repaired after determining that they were not a threat to structural integrity, placement procedures improved
Brunswick 1/2	50-324/325	1977/1975	1974	Voids occurred behind liner during construction of suppression chamber, grout injected into voids through holes drilled in liner, some grout in unit 1 did not harden but was left in place to provide limited resistance
Sequoyah 2	50-328	1982	1978	Concrete in outer 1 to 2 in. of unit 2 shield building was understrength because of exposure to freezing temperatures at early concrete age, determined not to affect shield building capability
Midland 2	50-330	Cd	1975	Rebar spacing deficiencies in reactor containment building, determined error not significant enough to affect safety

Duane Arnold	50-331	1974	1974	Hairline cracks in floor under torus, cracks permitted to self-heal
Fitzpatrick	50-333	1975	1973	Horizontal crack from hairline to 3/8 in. wide in reactor pedestal extending into concrete 9 to 30 in., cause believed to be welding procedure causing tension; structural integrity of pedestal not impaired, crack sealed by epoxy injection
Beaver Valley 1	50-334	1977	1982	Void 37 in. long x 3 ft. deep in outer containment wall in concrete ring around equipment hatch, no threat to structural integrity, void repaired
St. Lucie 1	50-335	1976	1974	Concrete spalled because of scaffolding fire in annulus between containment vessel and shield building, area affected ~ 11ft. X 2 ft. x 1in., temperature reached 300 to 350 °F inflicting only superficial damage, spalled are replaced
			1978	Hairline crack ~ 1/24 in. wide by 39 in. long in east wall of reactor containment refueling canal near embedded steel plate, crack repaired by grouting and column added to support platform girder
North Anna 2	50-339	1980	1974	Cracks > 1/16 in. in containment floor slab occurred around neutron shield tank anchor bolts, following pressure testing of seal chambers, cause was inadvertent pressurization, cores showed cracks extended into concrete vertically, cracks no structural threat, routed and sealed to prevent fluid penetration
Ferni 2	50-341/342	1985	1972	Cracks < 1/32 in. wide in basement floor slab permitted groundwater to seep into building, cracks caused by shrinkage, cracks repaired by pressure grouting after determining that they were no threat to structural integrity
			1984	Voids detected around one of auxiliary building watertight doors, defective concrete removed by chipping and area grouted, other doors inspected
Davis Besse 1	50-346	1977	1982	2 concrete expansion anchors and upper part of base plate pulled from wall ~ 3/8 in. because of improper installation, anchors replaced and torque checked
Farley 1	50-348	1977	1985	Cracks detected in 6 containment tendon anchors during refueling outage
			1980	Portions of unit 1 walls had areas where vertical reinforcing and grout were missing, corrective action taken

San Onofre 3	50-362	1984	1983	Tendon liftoff force in excess of maximum value listed in technical specifications, cause was lower relaxation rate than expected, no threat to structural integrity
Farley 2	50-364	1981	1985	3 anchors heads on bottom ends of vertical tendons failed and 18 cracked with several tendon wires fractured, occurred about 8 years after tensioning, cause attributed to hydrogen stress cracking, all tendons and anchors heads from same heat inspected with no further problems noted, 20 tendons replaced
Hatch 2	50-366	1979	1979	Approximately 10% of failures occurred during testing of 183 anchor bolts because of improper installation, failed bolts replaced with wedge anchors
			1982	Main steam pipe hangers had significant concrete spalling around embedded plate with concrete missing 2in. adjacent to plate, cause was defective concrete material or faulty placement, plate redesigned
McGuire 1	50-369	1981	1976	2 buttonheads failed during stressing of CRDM missile shield tendons at underside of bottom plate and 2 wires failed in another tendon near base anchor, additional failed wires found during checking, cause was excessive corrosion, design modified to replace tendons with 1 3/8 in. threaded rods that were grouted into place
La Salle 1/2	50-373/374	1982/1984	1976	Low concrete strength at 90 d, in-place strength determined acceptable from cores and cement contents for future pours increased, strength low in only small percent of pours so did not threaten structural integrity
Waterford 3	50-382	1984	1976	Improper concrete placing sequences used in foundation met forming a cold joint and not achieving stepped bedding planes, core drilling revealed fine cracks and honeycombed areas, defective concrete removed and replaced, supervision and inspection increased
			1976	Improper placement of concrete in reactor auxiliary building interior wall resulted in honeycombed areas, voids, and cold joints; unsound concrete removed and repaired
			1977	Crane boom fell during construction on common foundation structure wall causing concrete cracking and spalling over area 12

				in. x 4 in. x 1 in., rebars and concrete removed and replaced over entire height of damaged area for a length of 31 ft.
			1977	Low concrete compressive strength in 5.5 yd3 of concrete in wall contiguous with portion of condensate storage pool wall and wall of refueling water pool
			1977	Low concrete strength in reactor auxiliary building slab, cores yielded satisfactory strength, amount of sand in future mixes increased as well as mixing requirements
			1984	Spalled concrete observed in corbel exposing and displacing rebars and cracking in plane of anchor bolts, no loss of structural support, area repaired
Susquehanna 1/2	50-387/388	1983/1984	1976	Coarse aggregate with excessive fines used because of quality control deficiency, concrete strength exceeded requirements so structural integrity not affected, aggregate material for future batches replaced
Summer 1	50-395	1984	1976	Voids located behind liner plate of reactor containment building wall, windows cut in liner revealed voids up to 8.5 in. deep, cause was use of low slump concrete with insufficient compaction, voids chipped and cleaned to sound concrete, filled with non-shrink grout and liner repaired with all welds leak tested
			1977	Excessive heat from welding caused liner attached to concrete on inside face of concrete primary shield wall cavity to buckle and fail stud anchors and crack concrete, liner and concrete to depth of 6 in. removed, new liner plate welded in place and space filled with high-strength grout
Hanford 2	50-397	1966	1973	Deficiency in vertical cad weld splice sleeves in reactor building mat
Catawa 2	50-414	UC	1976	Cement used in reactor building base slab had been contaminated by fertilizer, 7 d strengths exceeded 28-d design values, cement feed transferred to another silo
Grand Gulf 1/2	50-416/417	1984/UC	1975	7 of 19 cylinders for control building base slab concrete did not meet 28-d design strength, 90-d values were acceptable
			1976	Voids found beneath drywell wall embed and shear key because of too stiff concrete mix; holes drilled through embed and used to fill voids with high strength grout; voids below shear key repaired

				by removing central portion of plate, chipping to good concrete, adding rebars, replacing concrete and liner, and leak testing liner
Bellefonte 1/2	50-438/439	UC	1984	Expansion shell anchor failures occurred in control building concrete because of low surface concrete strength, anchors replaced by more deeply embedded bolts or grouted anchors
			1976	8 rock anchor heads failed during construction because of possible stress corrosion cracking, anchor heads replaced with cleaner steel
Seabrook 1/2	50-443/444	UC/C	1983	Cracking occurred in walls at end of stiffening slabs separating pump cells in category 1 service water and circulating water pumphouse, cause was shrinkage and temperature variations, stiffening slabs were modified
Commanche Peak 1/2	50-445/446	UC	1975	Cold joint formed in reactor mat, concrete removed, rebars exposed and new joint poured
			1976	Voids 3/8 to 5/8 in. found under sump plates in concrete base mat, voids filled with neat cement grout using holes drilled through plates
			1976	Concrete not properly compacted around one of valve isolation embeds forming a void, faulty material removed by chipping and replaced by mortar or concrete
			1976	Inadequate concrete compaction under containment wall for 190 ft. at 6 to 7 ft. below the top of the mat, 12 by 20 ft area south of reactor pit, 6 by 12 area south of north sump and 4 by 6 ft. area north of north sump; core holes drilled for inspection in conjunction with analytical evaluations revealed base mat was adequate for all loading conditions; cores filled with mortar and interconnecting voids grouted
			1976	Excessive mortar used in concrete placement in preparing joint at reactor cavity wall, not determined to be structurally detrimental
			1976	Fresh concrete placed in area of standing water, because concrete forced water ahead of placement, it was not considered detrimental, excess water removed
			1976	Hardened concrete observed splattered on rebars, extent of occurrence considered minor with bond reduction insignificant

Byron 1	50-454	1984	1979	4 anchor head failures occurred in first year after stressing, cause was use of vanadium grain refinement process in conjunction with temperatures not high enough
Clinton	50-461	UC	1984	Embed plate on outside of drywell wall pulled from concrete because a failure of several Nelson studs occurring as result of weld shrinkage, concrete excavated along plate edges, embed plate redesigned and grout placed into area where concrete was removed
Wolf Creek	50-482	1985	1978	Low concrete strength in reactor building base mat with some 90-d values below 28-d values, in-situ strength tests indicate concrete exceeded design values and low 90-d strengths were due to testing conditions
			1978	Voids up to 6 ft. wide and through-wall thickness occurred under equipment and personnel hatches in reactor containment building, voids repaired, and quality assurance program updated
Callaway 1	50-483	1985	1977	19 randomly located areas of honeycombing extending to bottom layers of rebar in reactor building base mat in annular area of tendon access area, cause was use of low slump concrete in congested area, defective material removed from 33 of 172 tendons and voids repaired
South Texas 1/2	50-498/499	UC	1977	Crack in fuel handling building wall due to shrinkage, no structural significance
			1977	Rebars improperly located in buttress region of unit 1 containment, detailed analysis of as-built condition determined that no safety hazard to public occurred
			1978	Unconsolidated areas occurred in bottom surface of concrete slab in south unit 1 fuel-handling building; material removed by chipping to expose rebars, surface was epoxy-sealed followed by epoxy injection and a combination of dry packing and epoxy injection
			1978	Voids occurred behind liner plate of unit 1 reactor containment building exterior wall because of planning deficiencies, long pour time and several pump breakdowns; sounding and fiberoptic exam through holes drilled in liner plate were used to determine extent, areas were repaired by grout injection

			1979	Voids were detected in 12 areas behind liner plate of reactor containment building exterior wall with cause being attributed to temporary weldments, normal concrete settlement/shrinkage, and liner movement; construction and quality control procedures strengthened
			1983	Rust and pitting were observed on tendons for units 1 and 2 while in storage at fabricating plant, cause was delayed and improper corrosion inhibitor application and storage in a facility without temperature and humidity control; detailed exam of 14 tendons revealed pitting up to > 0.4 mm but strength and ductility exceeded limits; damage tendons were replaced and controlled storage conditions utilized with properly applied corrosion inhibitor
Palo Verde 2/3	50-529/530	UC	1984	Honeycombing around vertical tendon sheath block outs with most voids at buttress/ shell interface above last dome hoop tendon, condition was localized so area repaired
Marble Hill	50-546	C[d]	1979	High concrete pour rate may have bowed liner
			1979	A 12in. void extending 20 x 4.5 ft. in axial direction in base slab for auxiliary building, void repaired by shotcrete injection
			1979	Numerous surface defects (~4000) and inadequate patching resulting from poor concrete compaction and improperly prepared construction joints; breakdown in quality control and construction management attributes as cause; internal concrete inspection revealed it to be of high quality with higher than required strength; patches removed and replaced using good construction practices; providing good workmanship is used in repair and procedures followed, consultants determined structural integrity and shielding requirements should be met.

moffatt & nichol
1660 Hotel Circle North – Suite 500
San Diego, CA 92108
Phone (619) 220-6050 ❖ Fax (619) 220-6055

VERCORS Simulation Post Processing
TECH MEMO

To:	Dr. Josh Hogancamp, Sandia National Laboratories
From:	Robert Dameron and Patrick Chang
Date:	03/04/2020; Radial Strains and Cracking discussion added 03/12/2020

INTRODUCTION

Two ABAQUS analyses for the VERCORS simulation were provided by Josh Hogancamp for which Moffatt & Nichol has been assigned to develop and implement a post-processing procedure. This memo provides a description and guidance on the post processing procedure and how to use the data contained in the results spreadsheets. Since these structures are complex, concrete containment analysis requires specialized ways of extracting results data and viewing the results in order to understand how the structure is responding to loads and time-varying material effects, and to draw conclusions about that response. The biggest challenge is to develop a way to extract and plot strains for the entire pressure-vessel wall, both inside and outside, and also have this data in a form that can be further broken down and, possibly, combined – for example, combining the creep response with the pressure response, or separating the shrinkage response from the pressure + shrinkage response, etc. Another useful measure is to estimate (and separate) bending response from membrane response of the vessel wall. None of these data manipulations are possible with the standard "GUI"-driven post-processing tools resident in ABAQUS.

Both of the Sandia Analyses start with dead load and prestressing forces in all of the tendons (forces generated by M&N in a previous task). One model, named *VERCORS_sim_semifine_visco _20200204*, is analyzed with induced strains to simulate shrinkage; the strains are applied by way of temperature boundary conditions in a coupled thermal-stress analysis. Along with the shrinkage, Internal pressurization is applied then released four times; however, results of the last pressurization step were not available. The second model, named *VERCORS_sim_semifine_elastic_drying_20200204*, used

moffatt & nichol

viscoelastic properties in the concrete to simulate creep. No pressurization occurs in this model, but the analysis is set up to follow the timing sequence of the first model.

The analysis steps were broken out into the following time frames, set up by Sandia;
- Step Initialize: 10 seconds to initiate gravity and prestressing
- Step 0: Aug 17 - Nov 2, 2015 (77.00 days); tendons fully tensioned on Aug 17, 2015
- Step 1: Nov 2 - Nov 4, 2015 (2.253 days); reference date for zero-strain is November 2, 2015
- Step 2: 1st pressurization 'Pre-op', Nov 4 - Nov 6, 2015 (2.411 days)
- Step 3: Dormancy Nov 6, 2015 - Jan 25, 2016 (80.003 days)
- Step 4: 2nd pressurization 'VC1', Jan 25 - Jan 28, 2016 (2.411 days)
- Step 5: Dormancy Jan 28, 2016 - Mar 14, 2017 (411.196 days)
- Step 6: 3rd pressurization 'VD1', Mar 14 - Mar 16, 2017 (2.411 days)
- Step 7: Dormancy Mar 16, 2017 - Mar 21, 2017 (4.611 days)
- Step 8: 4th pressurization 'VD1 bis', Mar 21 - Mar 23, 2017 (2.411 days)
- Step 9: Dormancy Mar 23, 2017 - Apr 2, 2018 (374.585 days)
- Step 10: 5th pressurization 'VD2', Apr 2- Apr 4, 2018 (2.411 days) (not completed in "elastic_drying" analysis)

POST-PROCESSING PROCEDURE

Circumferential and vertical strains were extracted out of the result .odb files using scripts developed by M&N. The two excel files corresponding to the two analyses are named "Concrete strain-drying plus pressure" and "Concrete strain visco". The strains are taken from the outside and inside faces of the vessel walls. Figure 1 and Figure 2 partially show the nodal locations from where data was extracted. The strain values at the nodes were extracted, which ABAQUS interpolates from the element integration points that are closest to the nodes, then averaged. Even though strains are "element-quantities", in ABAQUS parlance, establishing values from nodes is needed to obtain the strains at a coordinate in space. The data was printed to text files then imported into Excel, in a worksheet tab called "abaqus".

2
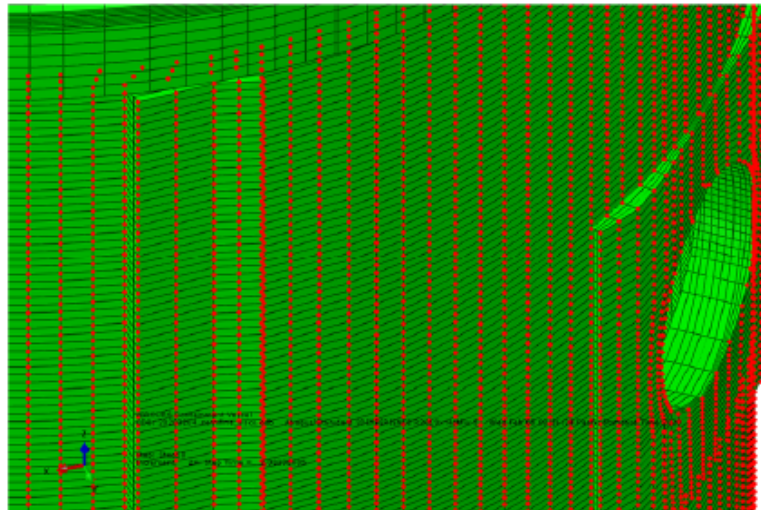
Figure 1. Nodes on Outside Surface
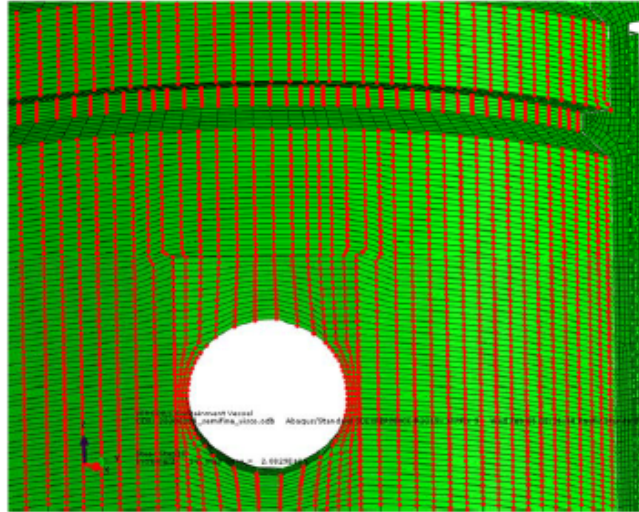
Figure 2. Nodes on Inside Surface

Within Excel, a script using Visual Basic was written to organize the data into a readable layout, based on nodal location and analysis step. The node locations are listed in the tab "nodes", which finds the nodal coordinates from the ABAQUS input file, and converts the x and y coordinate to an azimuth, roughly based on the drawings. It should be noted the azimuths are 4 degrees off from the drawings; the plans show the buttresses at 94° and 274°, while the analysis model has them at 90° and 270°. (If this is problematic for Sandia's use and ultimate data presentation, the M&N scripts could be modified.) The location of the nodes are visualized in Figure 3 and Figure 4, which shows their heights and azimuths. To easily visualize the data, the data from the wall of the vessel is "unwrapped" and laid out based on height and azimuth. We tried to do this in accordance with how 'unwrapped' slices of the vessel are shown on the design drawings.

To reduce the number of data points down to a manageable size, the nodal results were grouped together in "bins" based on location. These bins have a height of 0.345m and an angle of 4.8 degrees. All strains associated with nodes that fall within a bin are averaged. Figure 3 and Figure 4 show the boundaries of the bins and how the nodes lie within them.

3

Figure 3. Node Location on Outside Face
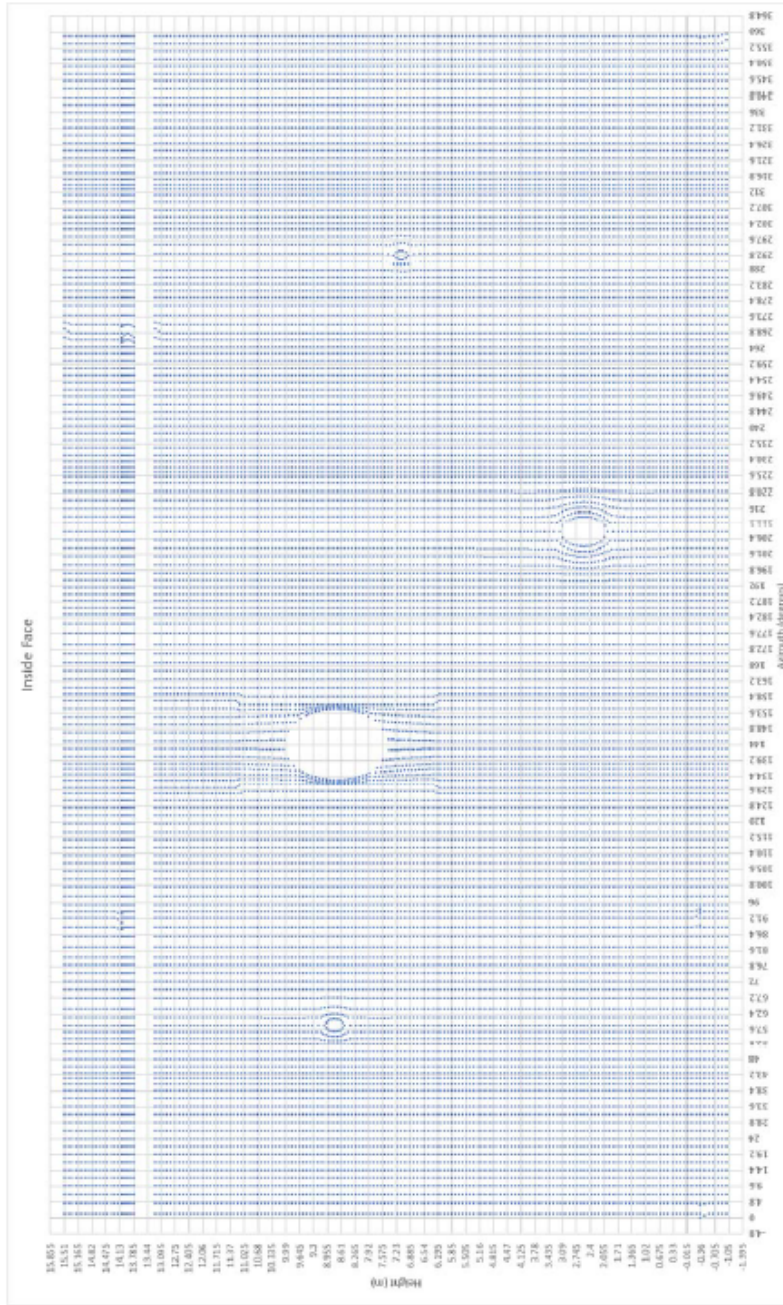
Figure 4. Node Location on Inside Face

For each analysis time step where data was extracted, a separate tab is created in the spreadsheet. Results were taken from the end of each analysis step. For the pressurization steps, an additional time increment at peak pressurization was extracted, shown in Figure 5. In each tab, the strains are presented for both the outside and inside faces, as well as for circumferential and vertical strains. Each cell with results is assigned a color gradient, based on limits set in the top left corner. Values less than the minimum value are green and values larger than the maximum are red, with the values in-between having a color gradient passing through yellow. Figure 6 can be used as a reference for navigating the spreadsheet.
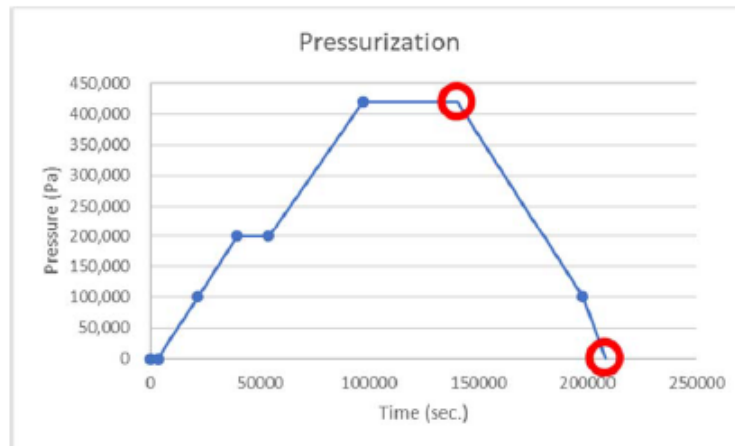
Figure 5. Pressure Time-History (Red Circle Indicates Data Extraction Increment)

The data extraction points are listed here. The intermediate steps between pressure steps represent time passage as the model ages over many months.

1. Initialize
2. Step 0
3. Step 1
4. Step 2 – Peak Pressure
5. Step 2 – Unloaded (final)
6. Step 3
7. Step 4 – Peak Pressure
8. Step 4 – Unloaded
9. Step 5
10. Step 6 – Peak Pressure
11. Step 6 – Unloaded
12. Step 7
13. Step 8 – Peak Pressure
14. Step 8 – Unloaded
15. Step 9

6

moffatt & nichol
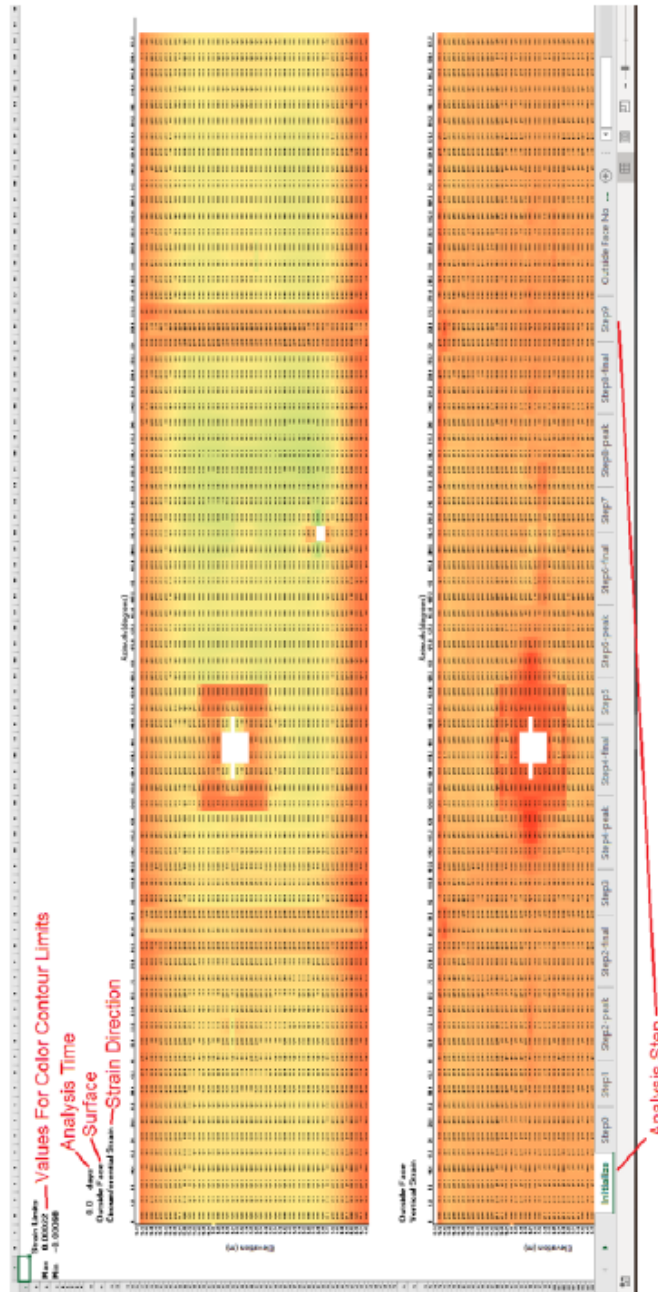
Figure 6. Spreadsheet Guide

7

OBSERVATIONS & CONCLUSIONS

- With the developed post-processing tools in place, the strain data can be mined, dissected, and further combined. Doing this exhaustively is beyond the scope of M&N's assignment, but a few observations can still be made based on a brief review of the spreadsheets.

- Presenting and studying the strain response information in this global way (the 'stretchout plots') has also served as a good sanity check on the overall FEA model, i.e., the results make physical sense and do not show evidence of FE mesh anomalies.

Shrinkage Plus Pressure Case

- There are noticeable strain concentrations adjacent to the equipment penetrations (as we have seen with other Containment Vessel tests);

- But elsewhere, the strains are fairly uniform.

- There is evidence of significant vertical bending at the wall-base juncture and adjacent to penetrations; less so in hoop strain bending near the penetrations.

- When observing/comparing strains from peak-to-peak-to-peak, the maximum strains occur at Step2-peak, and then decrease at later peaks. In the absence of shrinkage, this would likely NOT be the case. So we suggest that shrinkage strains be isolated (subtracted?) somehow from the total strains in order to examine isolated pressure response.

- Bending can be assessed by "differencing" the inside and outside strain worksheets, and we recommend that Sandia look into this.

Visco (Creep Response)

- All strains are more uniform throughout the vessel than they were for the pressure response.

- Strains start out near zero, and grow increasingly negative over time, as expected.

8

Discussion of Through-Wall Strains, and Potential for Cracking and Delamination

In addition to the general review of results described above, the spreadsheeted and additional strain plots were studied with focus on Through-Wall Strains, and on the potential for cracking.

For making these further observations, additional strain plots (using ABAQUS post-processor) were pulled from the two analyses at all 15 analysis time steps for which the spreadsheeted strains were extracted. Pdf files of these are included with this Memo submittal. The ABAQUS plots are taken from section cuts identified below.

9
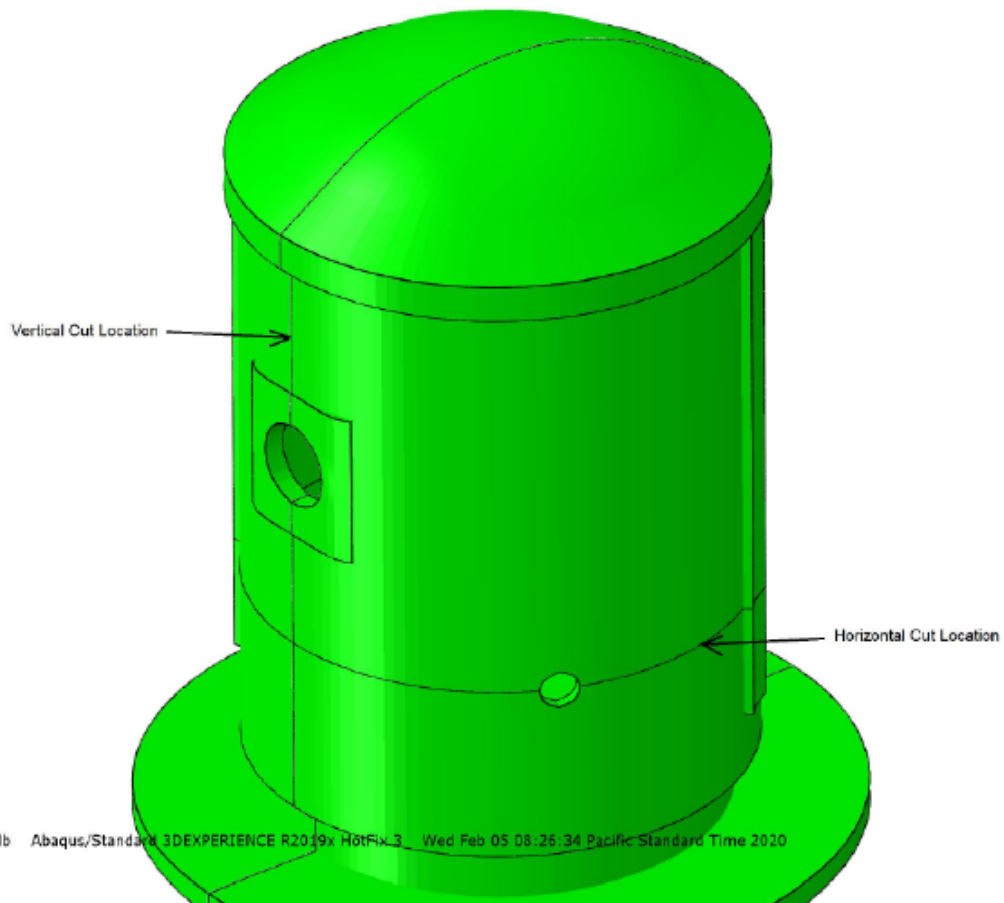
Another useful reference for this discussion is the typical mesh through the wall, that shows the mesh refinement, and the rows of nodes to which the tendon elements are attached with their friction/slider connections.
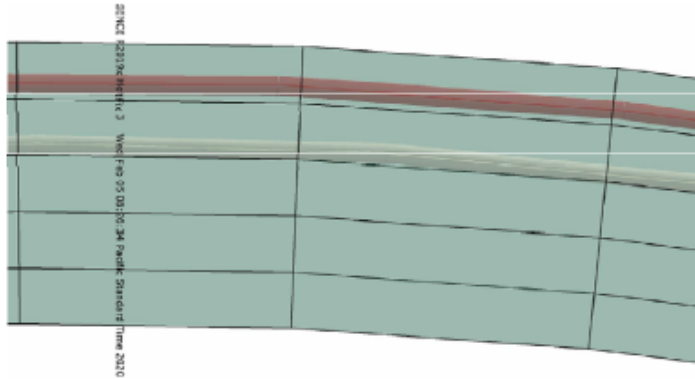
Although the FEA of the VERCORS Model has utilized elastic simulation, the strain results can be used as an indicator of 'hot-spots', potential 'near cracking', and if large enough – actual cracking.

From the VERCORS information package, the measured cracking strength and Youngs Modulus are,

f_{cr} = 5.0 MPa   E = 34,000 MPa

While a concrete tensile test stress-strain curve would be useful, from this limited data, it is typical to assume that the strain for first onset of microcracking can be approximately defined by

$\varepsilon_{cr} = f_{cr}$ / E = 147 microstrain   OR   0.000147

Based on extensive experience and anecdotal evidence for crack prediction using FEA techniques, the strain to cause visible cracks is somewhat larger than this, and sometimes as much as 2X as large. Concrete crack formation is a complex process that depends on many variables, for example whether the stress-strain state is uniaxial or has some biaxiality, and also depending on the chemistry and aggregate content of the concrete mix. But a good rule of thumb has been that ε_{cr} represents the beginning of formation of the microcracking "process zone", and once the strain reaches about 2X this value, cracks are fully formed and visible. It also has been observed that if the tensile loading is cyclical, then fully formed cracks will coalesce upon a few cycles of reaching the lower bound value of ε_{cr}.

The FEA predicted strains have been viewed carefully with this in mind. For the inside and outside surfaces, the spreadsheet information reveals the following:

- There are some noteworthy 'hot spots' in the FEA model that is only subjected to Dead Load, Prestressing, and initial shrinkage, i.e., "Step 1".

10

- o Vertical strains on Outside Face near Wall-Base Juncture of 0.000220 (These occur only at the Buttresses, and are much lower for the rest of the cylinder.) This could be considered large enough for a horizontal-oriented crack to be forming, though it would be a very 'tight' crack difficult to see.
  - o Vertical strains on Inside Face near Springline of 0.000173 (These occur all the way around the vessel.) These are probably not yet visible.

- There is no cracking at all based solely on the creep response of the vessel (i.e., review of the "Concrete strain visco" worksheets).

- For the shrinkage plus pressure response, there are circumferential strains approaching, but not quite reaching the cracking threshold.
  - o Adjacent to the Equipment Hatch (3 o'clock and 9 o'clock position) of about 0.000126 outside face and 0.000113 inside face
  - o Across one of the buttresses near the springline of about 0.000149 on inside face (with much less on the outside face – clearly a circumferential flexure response across the buttress).
- It should be noted that the maxima for these strains occurs at the "Step 2 Peak Pressure" time-step, and these strain peaks then diminish at subsequent pressurizations due to the ongoing shrinkage.

Some noteworthy tensile strains were also observed in the through-thickness "radial" direction of the FE Model. These are of particular interest for investigation of the potential of delamination-type failure of the sort observed for the Crystal River NPP Containment. From the ABAQUS plots prepared and accompanying this memo, two plots have been extracted and placed here for consideration.

11

moffatt & nichol

E, E11 (VERCORS_ASSEMBLY_CV-REBAR_CYLINDRICAL_CS)
(Avg: 75%)

```
 0.000135
 0.000092
 0.000050
 0.000008
-0.000034
-0.000076
-0.000118
-0.000161
-0.000203
-0.000245
-0.000287
-0.000329
-0.000371
```

VERCORS Containment Vessel
ODB: 20200204_semifine_drying.odb   Abaqus/Standard 3DEXPERIENCE R2019x HotFix 3   Wed Feb 05 08:34:39 Pacific Standard Time 2020

Step: Step5
Increment   200: Step Time =   3.5527E+07
Primary Var: E, E11 (VERCORS_ASSEMBLY_CV-REBAR_CYLINDRICAL_CS)
Deformed Var: U   Deformation Scale Factor: +1.000000e+02

E, E11 (VERCORS_ASSEMBLY_CV-REBAR_CYLINDRICAL_CS)
(Avg: 75%)

```
 0.000115
 0.000063
 0.000011
-0.000041
-0.000094
-0.000146
-0.000198
-0.000250
-0.000302
-0.000354
-0.000406
-0.000459
-0.000511
```

VERCORS Containment Vessel
ODB: 20200204_semifine_drying.odb   Abaqus/Standard 3DEXPERIENCE R2019x HotFix 3   Wed Feb 05 08:34:39 Pacific Standard Time 2020

Step: Step5
Increment   200: Step Time =   3.5527E+07
Primary Var: E, E11 (VERCORS_ASSEMBLY_CV-REBAR_CYLINDRICAL_CS)
Deformed Var: U   Deformation Scale Factor: +1.000000e+02

12

D-12

The two figures included show radial strain at horizontal and vertical slices, occurring at the end of Load Step 5. That Load Step represents a time after significant shrinkage has occurred, and after two full pressure cycles have taken place, but at the zero pressure unloaded condition. A few observations and conclusions from studying the radial strain data are as follows:

- The included plots show a pronounced band of elevated radial tension within the interior of the cylinder wall (and also within the interior of the springline tendon anchorage);
  - The magnitude of this tension is in the range of approximately 0.000100, so though significant, does not rise to a level where cracking or delamination would be expected.
  - In the early time regime for the VERCORS Model (not shown here, but included in the attachments) this interior band of radial strain is NOT present (and instead there are some elevated radial strains within the surface elements), so this observed phenomenon appears to be driven by shrinkage, and no doubt exacerbated by the tendons pressing inward on the interior of the wall and by related Poisson Effect.

- There were no tensile strains observed for the creep response analysis that were near cracking. There is an important caveat to these observations – namely, that in our opinion the mesh size – 5 elements through the thickness, with only 2 crossing the hoop tendons - is NOT refined enough to make absolute conclusions from the analysis; instead, these observations should be considered 'trends'. For example, approximately double this mesh size refinement would be considered to be a minimum acceptable, and even more may be needed – the answer to finalizing the mesh would come from performing a mesh size sensitivity study. It may well be that doubling the mesh could possibly double the peak strain in the interior of the wall, in which case the prediction of delamination becomes a possibility. In our experience, a strain peak being compared to a strain failure criteria, that only exists within a single row of elements is highly suspect for drawing definitive conclusions.

13

APPENDIX E

Structural Integrity Associates, Inc.

ekjolsing@structint.com
9710 Scranton Road, Suite 300 San Diego, CA 92121 | 619-354-5658

Creep Effects in PCCVs

Prepared For:

Sandia National Laboratory
Albuquerque, NM

PO 2124868

Prepared By:

Structural Integrity Associates, Inc.
Irvine, CA

Prepared by:	Eric Kjolsing _(Digitally signed by Eric Kjolsing Date: 2020.11.24 15:04:30 -08'00')_	Date:	11/24/2020
	Eric Kjolsing, Sr. Consultant		
Reviewed by:	_Matt N__ — Matthew Naugle, PE mnaugle@structint.com 2020.11.24 15:08:37-08'00'_	Date:	11/24/2020
	Matt Naugle, Engineer		
Reviewed by:	_Randy James (signature)_	Date:	11/24/2020
	Randy James, Structural Solutions Consulting		
Approved by:	Eric Kjolsing _(Digitally signed by Eric Kjolsing Date: 2020.11.24 15:14:03 -08'00')_	Date:	11/24/2020
	Eric Kjolsing, Sr. Consultant		

info.structint.com ✉ 1-877-4SI-POWER ☎ structint.com 🌐

REVISION CONTROL SHEET				
Report Number: 1901160.401				
Title: Creep Effects in PCCVs				
Client: Sandia National Laboratory				
SI Project Number: 1901160.00			**Quality Program:** ☐ Nuclear ☒ Commercial	
SECTION	PAGES	REVISION	DATE	COMMENTS
All	All	A	8/28/2020	Initial DRAFT for Client Comments
3 4 All		0	11/20/2020	Incorporate Client Comments: • Clarification of ANACAP Tensile Strain • Include Table w/Summary of Cases Update Figure & Table Numbering and Table of Contents

Structural Integrity
Associates, Inc.

info.structint.com   1-877-4SI-POWER   structint.com

TABLE OF CONTENTS

Structural Integrity
Associates, Inc.

info@structint.com ✉   1-877-4SI-POWER ☎   structint.com 🌐

7-5

LIST OF FIGURES

LIST OF TABLES

1 BACKGROUND

The effects of creep on the long-term integrity of Pre-stressed Concrete Containment Vessels (PCCVs) is complicated and not intricately analyzed by structural engineers. While creep is included in the design basis for pre-stress loss in PCCVs, the long-term effects on the structural integrity have not been critically studied. The general sense has been that creep is mostly a shorter-term effect, and the effects of creep should decrease over time as the structure ages and the rate of creep dissipates. However, the delamination cracking that developed in the containment at Crystal River during a construction modification (see Figure 1-1) raised concerns about the possible longer-term effects of creep, especially when there are changes in the loading. Research is needed to further investigate the effects of creep and identify situations where the integrity and pressure capacity of PCCVs may or may not be of some concern in the longer term.

This study is a limited scope to examine the issue of creep in concrete containment vessels and identify any need for further research. This effort is not an attempt to reconstruct all the circumstances that occurred in the Crystal River delamination problem as a kind of "root cause" analysis. Rather, the intent is to consider representative conditions for a situation where a known problem develops in order to show that the modeling employed can provide an indication of potential problems.

Structural Integrity
Associates, Inc.

info@structint.com   1-877-4SI-POWER   structint.com

Figure 1-1. Crystal River Structure (Top) and Extent of Delamination (Bottom)

7-10

2 SINGLE ELEMENT TESTS

Single element test problems are analyzed to demonstrate the concrete creep model.

2.1 ANAMAT 259

Four single element tests are performed using realistic, but arbitrary, material properties. The element is 1in x 1in x 1in and modeled with a single C3D20R finite element. The coordinate system for the single element tests are shown in Figure 2-1. Various boundary conditions are imposed:

1. *Unconfined*: Zero displacement on -X, -Z, and -Y faces. Pressure (2ksi compression) imposed on +Y face.
2. *Partially Confined*: Zero displacement on -X, +X, -Z, and -Y faces. Pressure (2ksi compression) imposed on +Y face.
3. *Confined*: Zero displacement on -X, +X, -Z, +Z, and -Y faces. Pressure (2ksi compression) imposed on +Y face.
4. *Unconfined with Imposed Displacement*: Zero displacement on -X, -Z, and -Y faces. Impose 5e-4in displacement (equivalent to 2ksi compression) on +Y face.
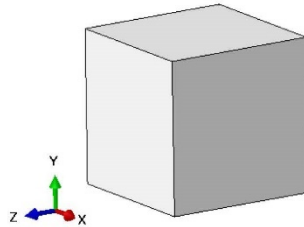
Figure 2-1. Single Element Test Coordinate System

In each of the three pressure tests (1-3) the pressure is applied, the analysis steps through time (creep), the pressure is removed, and the element strains are allowed to recover (creep recovery). In the imposed displacement test (4) the imposed displacement is applied, the analysis steps through time (creep), the imposed displacement is removed (i.e. an imposed displacement of 0in is forcibly applied), and the element strains are allowed to recover (creep recovery).

The three pressure tests show no element cracking and strains (both axial and transverse) that align with theoretical estimates. This illustrates and confirms that "unrestrained" creep and

creep recovery as a visco-elastic process, do not generate mechanical or cracking strains, that is, if the imposed mechanical stress/strain do not induce cracking, then visco-elastic formulated creep affects the total strain but not the mechanical strain. When the material is allowed to unload back along the same path or same conditions as when loaded, then no cracking develops due purely to creep strain. Creep strain can affect the mechanical strain when this unloading path or stress conditions have changed during the creep accumulation. The imposed displacement test illustrates this point. Here, the results also align with theory but show cracking when the imposed displacement is removed. This result is expected; imposing zero total strain requires a tensile mechanical strain to develop to balance the compressive creep strain. Results from these tests are presented in Appendix A.

2.2 ANAMAT 259, IPRUM 7

Commonly, the continuing hydration of concrete over time results in time dependent concrete mechanical properties, and thus time dependent concrete material properties are used in a handful of cases to help assess this synergism with creep. Although the same ANAMAT user material model is called (ANAMAT 259), the time-dependent material subroutine is invoked for these runs. The unconfined single element test described above is used to demonstrate the performance for the time dependent material properties.

Figure 2-2 shows the axial strain (negative = compression) when a pressure is applied at time zero and then removed after 30 years (note that creep is turned off in this test case). Because the modulus has increased over time the element does not return to a zero-strain state upon unloading.

In another case, both time dependent modulus and creep are included in the sample problem. The results are presented in Figure 2-3. Note that when time dependent modulus is included in the assessment there is less strain recovered during the creep recovery phase. This result is in-line with that shown in Figure 2-2.

In a third case, a pressure load is applied periodically in time (i.e. a load is applied instantaneously then removed). The resulting axial strain is shown in Figure 2-4 and is seen to decrease in time (as the modulus increases with time); the results match those calculated from theory.
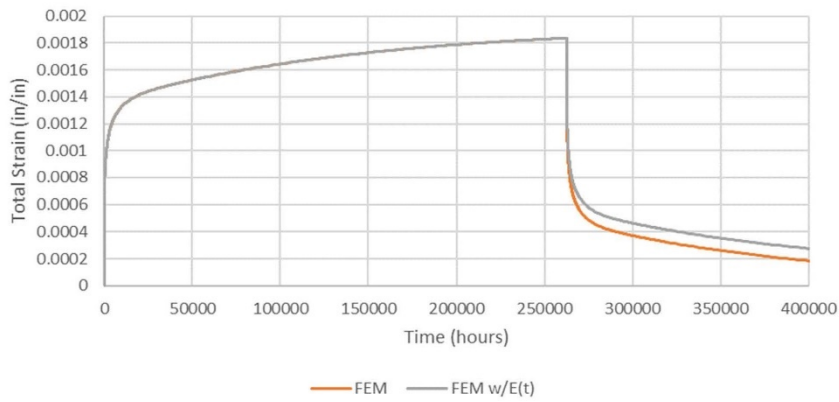
Figure 2-2. Non-Recoverable Displacement

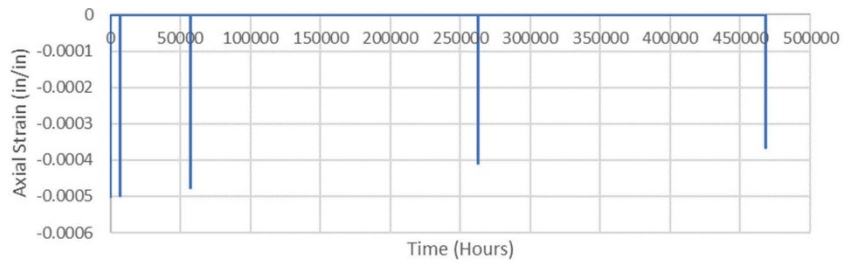Figure 2-3. Creep with Time Dependent Modulus

Figure 2-4. Periodic Loading with Time Dependent Modulus

info@structint.com   1-877-4SI-POWER   structint.com

3 MODEL OF CONTAINMENT STRUCTURE

A representative containment structure is used for this study. A general schematic of the panel of interest is shown in Figure 3-1. Elements of the model are described below. Figures depicting the model are shown in Figure 3-2 and Figure 3-3.

1. **Buttresses:** The model assumes six vertical buttresses equally spaced along the circumference. The buttresses are 6ft ft wide and 5ft-10in thick. The buttresses are modeled as elastic with a Young's Modulus of 4e6psi (the ANACAP material model is not applied to the buttress).

2. **Ring Girder:** The model includes a 6ft tall, 5ft-10in thick girder at the top of the panel to represent the ring girder (or the stiffened equipment hatch in the quarter-symmetric model). The girder is modeled as elastic with a Young's Modulus of 8e6psi (the ANACAP material model is not applied to the ring girder). Note that this Modulus is a factor of 2 greater than the other concrete components to account for additional stiffness provided by the adjacent concrete elements not explicitly modeled.

3. **Steel Liner:** A 3/8in steel liner (modeled as a membrane) is bonded to the inner diameter of the structure. The liner is modeled as elastic plastic (f.y=50ksi, f.u=75ksi at 20% strain) with a Young's Modulus of 30e6psi.

4. **Containment Wall:** The containment wall is modeled as 3.5ft thick and is modeled with the ANACAP concrete constitutive model. Unless otherwise stated, the concrete is assumed to have a 5ksi strength, 4e6psi Youngs Modulus, and 0.2 Poisson's ratio. The containment wall is modeled with quadratic solid elements (C3D20R).

5. **Containment Wall Reinforcement:** The containment wall includes vertical and horizontal reinforcement. The reinforcement is modeled as elastic plastic (f.y=60ksi, f.u=70ksi at 10% strain) with a Young's Modulus of 29e6psi. The horizontal rebar is modeled as #9@12in each face. The vertical rebar is modeled as #9@10in each face. Rebar is modeled as linear truss elements (T3D2). Tie bars (stirrups) are not included in the model. The reinforcement is embedded in the concrete through an embedment constraint providing strain compatibility between the concrete and rebar.

6. **Containment Wall Tendons:** The containment wall includes vertical and horizontal tendons. The tendons are modeled as elastic plastic (f.y=200ksi, f.u=235ksi at 10% strain) with a Young's Modulus of 28e6psi. Both horizontal and vertical tendons have a cross sectional area of 10.9in^2. Vertical tendons are spaced radially every 2.5degrees, which roughly equates to a 35.2in circumferential spacing. Horizontal tendons are located in alternating layers spaced at 12.75in and 25.5in respectively. The vertical and horizontal tendons are located 15.2in and 10in from the containment wall outer radius, respectively. The tendon prestress is applied through an imposed temperature change of 810°F, which for a 6.5e-6 in/in/degF expansion coefficient, equates to 5.27e-3 in/in or 147ksi or 1600 kip per tendon. This roughly equates to 1ksi and 2ksi compression in the vertical and horizontal directions, respectively. The tendon force is not altered to account for friction, wobble, steel relaxation, etc. The tendons are embedded in the concrete through an embedment constraint and are modeled as linear truss elements (T3D2). No reduction in concrete area (accounting for tendon ducts) is included.
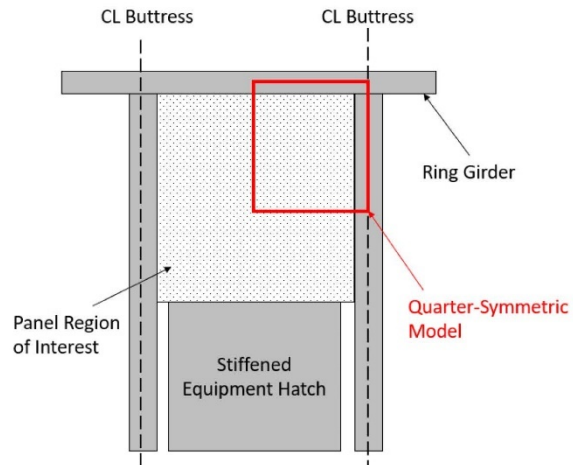
Figure 3-1. Schematic of Modeled Region.
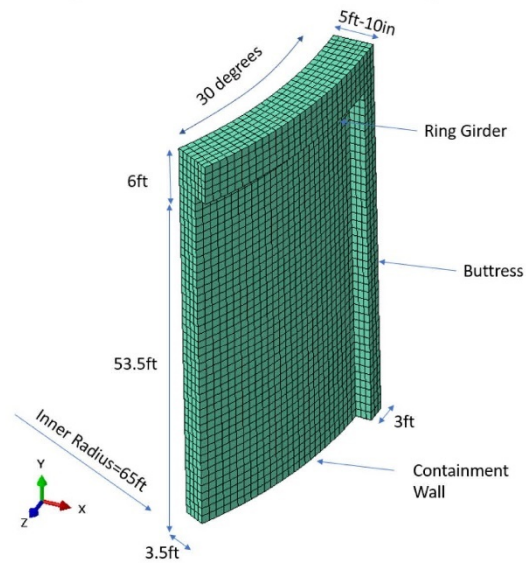
Figure 3-2. FEM – Concrete Geometry
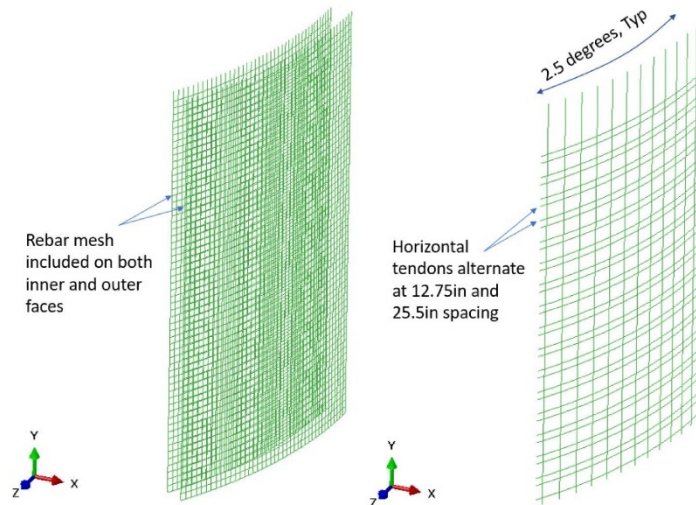
Figure 3-3. FEM – Vertical and Horizontal Rebar (Left) and Tendons (Right)

The analyses utilize ANACAP, SI's proprietary concrete model. A thorough description of ANACAP's features can be found in other references, but a brief discussion of tensile cracking is warranted. Tensile cracking in ANACAP is governed by the magnitude of the load in the directions of principal strain. Cracks are assumed to form perpendicular to the directions of largest tensile strains. Multiple cracks are allowed to form at each material point, but they are constrained to be mutually orthogonal. If cracking occurs, the normal stress across the crack is reduced to zero and the distribution of stresses around the crack is recalculated through equilibrium iterations. This allows stress redistribution and load transfer to reinforcement or other load paths in the structure. Once a crack forms, the direction of the crack remains fixed and can never change or heal. However, a crack can close, resist compression and shear, and re-open under load reversals. The cracking criterion is based on an interaction of both stress and strain as illustrated in Figure 3-4. The model predicts cracking when the generalized (principal) stress and strain state exceeds the limit state shown. Thus, biaxial and triaxial stress states are treated consistently with uniaxial conditions, but the associated cracking will now occur at a slightly higher stress and slightly lower strain. Split cracking, for example near a free edge under high compressive stress, occurs at near zero stress and a tensile strain approximately twice that of uniaxial tensile cracking.
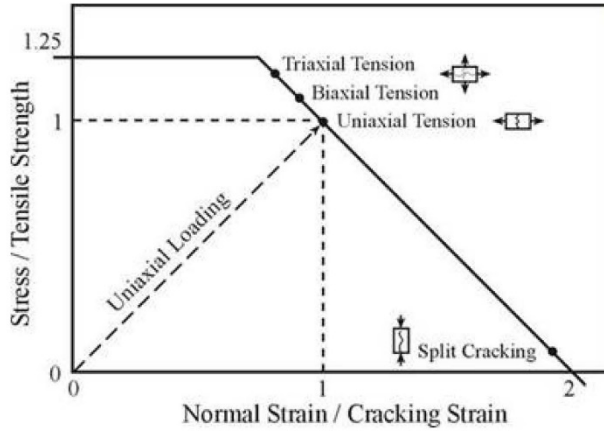
Figure 3-4. Crack Initiation Criteria Curve

The structure is modeled with quarter symmetry. A vertical boundary (Δ_y=0) is included at the base of the model while a circumferential boundary (θ=0in) is included at the buttress and containment wall. These boundary surfaces are illustrated in Figure 3-5.
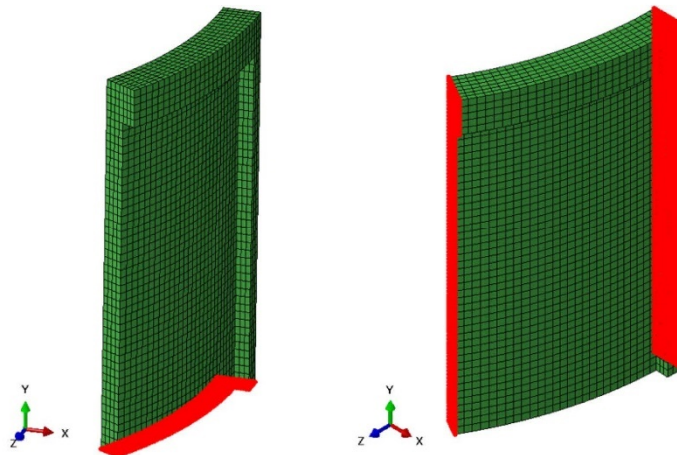
Figure 3-5. FEM – Vertical (Left) and Circumferential (Right) Boundary Conditions

Unless otherwise stated, the creep compliance used in the assessments is that indicated in Figure 3-6 (e.g. creep compliance = (total strain - initial strain) / initial strain). The creep model includes both primary and secondary creep and treats both as fully recoverable. Note that an arbitrary value is chosen with some conservative bias.
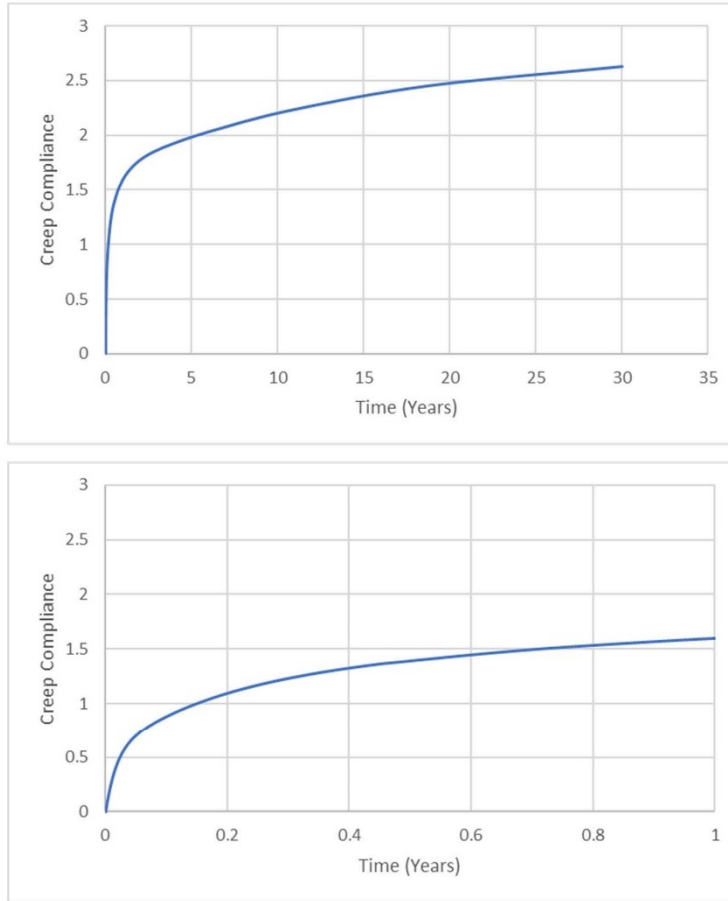
Figure 3-6. FEM – Creep Compliance (Top=30yr, Bottom=1yr)

Each analysis is segregated into multiple analysis steps. The first steps apply gravity and the tendon tensioning force. The analyses are then permitted to run through the creep steps that span ~30 years. At the end of ~30 years several tendons (both horizontal and vertical) are

info@structint.com   1-877-4SI-POWER   structint.com

Structural Integrity
Associates, Inc.

removed to represent the de-tensioning that would occur before an equipment opening would be cut into the containment wall. The tendons that are de-tensioned are shown in Figure 3-7 with the approximate location of the proposed equipment opening also highlighted. These analyses do not include effects of cutting the opening. The tendons are both tensioned and de-tensioned by applying a temperature load to the tendon elements.
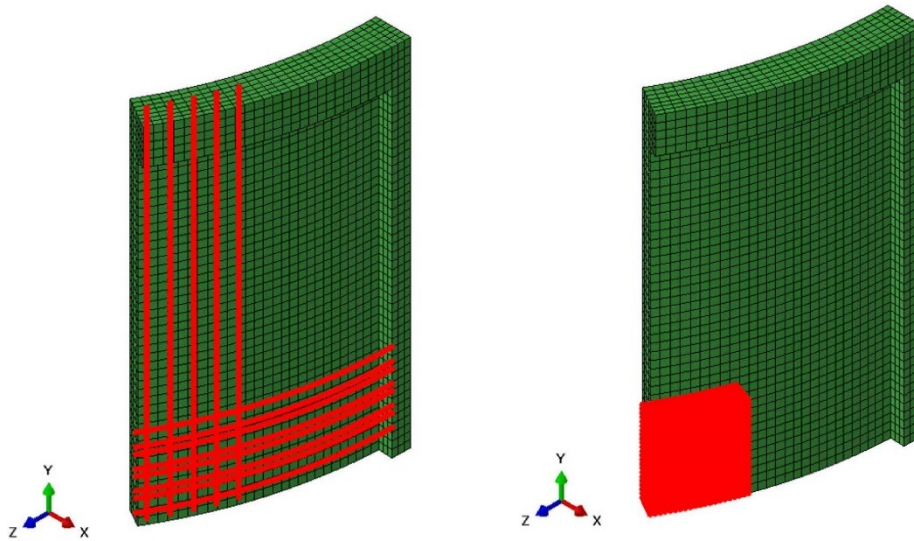
Figure 3-7. FEM – De-tensioned Tendons (Left) and Future Concrete Opening (Right)

Several cases (the C cases) assign different creep factors to different concrete element sets. Two different element sets are identified in Figure 3-8 and are referenced in the discussion of the C cases.
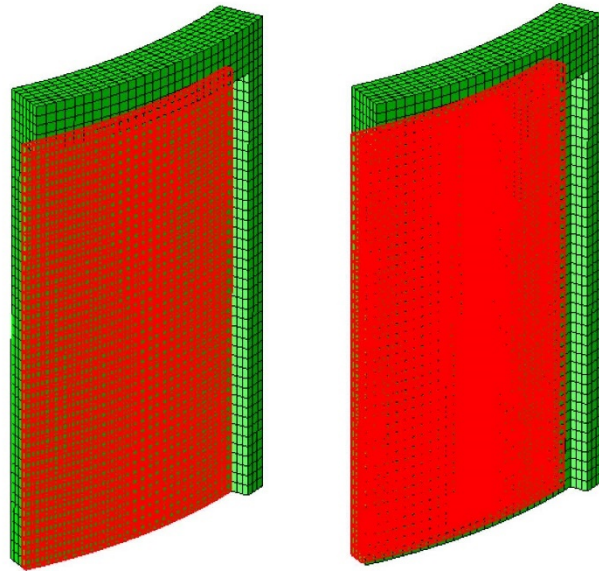
Figure 3-8 Outer (Left) and Inner (Right) Layer Elements

7-20

4 ASSESSMENTS AND FINDINGS

A variety of analyses are performed to investigate the model's behavior (see Table 4-1). Both the analyses and results are described in the sections that follow. For clarity, the ring girder and buttress are not shown in the results figures.

Table 4-1. Summary of Analyses

Case	Section
Case A1 - Baseline Case, No Creep	4.1
Case A2 - Baseline Case, With Creep	4.2
Case B1 - Delamination During Initial Tensioning	4.3
Case B2 - Investigating Potential Delamination After Initial Tensioning	4.4
Case B3 - Intentional Delamination After Initial Tensioning	4.5
Case B4 - Intentional Delamination After 6.5 Years	4.6
Case B5 - Intentional Delamination Prior to Detensioning	4.7
Case B6 - Intentional Delamination After Detensioning	4.8
Case C1 - Differential Creep Compliance (0.5x & 1.0x)	4.9
Case C2 - Differential Creep Compliance (1.0x & 2.0x)	4.10
Case C3 - Differential Creep Compliance (1.0x & 0.5x)	4.11
Case C4 - Not Used	4.12
Case C5 - Differential Creep Compliance (0.5x & 3x)	4.13
Case D1 - Not Used	4.14
Case D2 - Not Used	4.15
Case D3 - Time Dependent Material	4.16
Case D4 - Time Dependent Material, Differential Creep Compliance (0.5x & 1x)	4.17
Case D5 - Time Dependent Material, Differential Creep Compliance (1x & 2x)	4.18
Case Fb2 - Variation of Case B2	4.19
Case Fc1 - Variation of Case C1	4.20
Case Fc2 - Variation of Case C2	4.21
Case Fd3w - Variation of Case D3	4.22
Case Fd4w - Variation of Case D4	4.23
Case Fd5w - Variation of Case D5	4.24

4.1 Case A1 - Baseline Case, No Creep

4.1.1 Description

The baseline configuration is assessed with the creep factor set to zero (no creep). The concrete fracture strain is set to 100e-6 in/in, calculated as tensile strength divided by elastic modulus with nominal value of 400 psi tensile strength for 5 ksi concrete. The results from this baseline can be used when evaluating other models.

Anamat File: anamat259dge_cr3curve_wCreepFactor.o
Input File: A1_cr3v1_rebar_259mod4ip1_dt_cr3_100m_temp.inp
Concrete Fracture Strain: 100e-6 in/in

4.1.2 Analysis Results

The radial strain at the end of the initial stressing step and after subsequent detensioning are shown in Figure 4-1 and Figure 4-2, respectively. The maximum radial strain at the end of the initial stressing step is 161.3e-6 in/in. The radial stress after initial stressing is shown in Figure 4-3 where local compressive loads are seen just on the inner side of the hoop tendons. The analysis (MSG file) indicates no cracking of the ANACAP concrete at this point in the analysis. The maximum radial strain at the end of the detensioning step is 161.1e-6 in/in but with a significant change in strain contour. The detensioning has resulted in a radial outward displacement near the region of the future concrete opening, as can be seen in Figure 4-4. The analysis (MSG file) indicates cracking of the ANACAP concrete has occurred at the end of the detensioning step (Number of elements with 1, 2, and 3 open cracks: 476,0,0). Since the radial strain is less than twice the fracture strain, cracking is believed to be occurring due to flexural stress (stemming from the effects of the detensioned tendons), concentrated near the future opening and the inner diameter (near the ring girder). Plots of the vertical strain are shown in Figure 4-5 to demonstrate this. Note that the vertical reinforcement controls this cracking.
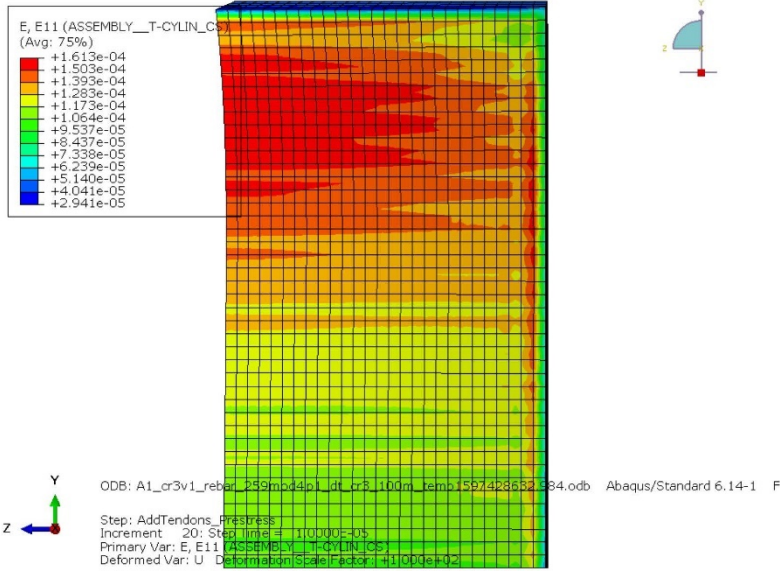
Figure 4-1 Concrete Radial Strain After Initial Stressing [A1]
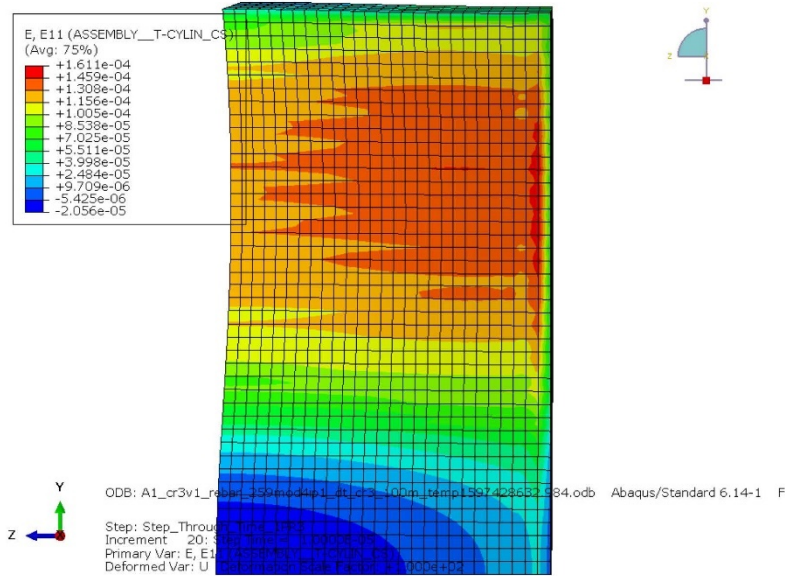
Figure 4-2 Concrete Radial Strain After Detensioning [A1]

S, S11 (ASSEMBLY__T-CYLIN_CS)
(Avg: 75%)
+9.655e+01
+0.000e+00
-8.333e+00
-1.667e+01
-2.500e+01
-3.333e+01
-4.167e+01
-5.000e+01
-5.833e+01
-6.667e+01
-7.500e+01
-8.333e+01
-9.167e+01
-1.000e+02
-4.556e+02

ODB: A1_cr3v1_rebar_259mod4ip1_dt_cr3_100m_temp1598389314.139.odb   Abaqus/Standard 6.14-1   Fri Au

Step: AddTendons_Prestress
Increment   20: Step Time =   1.0000E-05
Primary Var: S, S11 (ASSEMBLY__T-CYLIN_CS)
Deformed Var: U   Deformation Scale Factor: +1.000e+02

Figure 4-3 Concrete Radial Stress After Initial Stressing [A1]
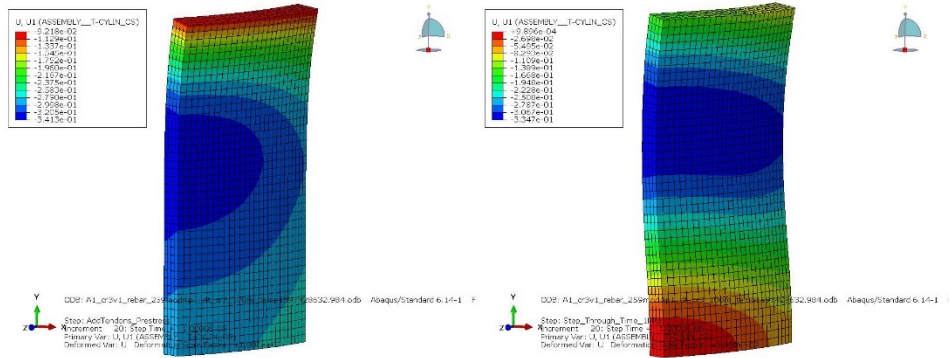
Figure 4-4 Radial Displacement After Initial Stressing (Left) and Detensioning (Right) [A1]
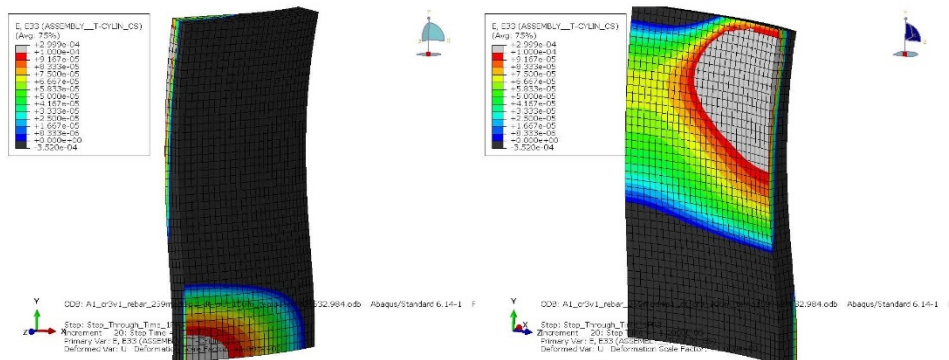
Figure 4-5 Vertical Strain (Z in Transformed Coordinate System) After Detensioning [A1]

An analogous model was assessed using the standard ANAMAT model (model 3) and showed identical results, giving confidence that the concrete creep model simplifies to the standard ANAMAT model when creep is turned off.

4.2   Case A2 – Baseline Case, With Creep

4.2.1 Description

The baseline configuration is assessed with the creep factor set to one (creep compliance per Figure 3-6Figure 3-6). The concrete fracture strain is set to 100e-6 in/in. The results from this baseline creep can be used when evaluating other models.

Anamat File: anamat259dge_cr3curve_wCreepFactor.o
Input File: A2_cr3v1_rebar_259mod4ip1_dt_cr3_100m_temp.inp
Concrete Fracture Strain: 100e-6 in/in

4.2.2 Analysis Results

The radial strain and number of elements with 1, 2, and 3 cracks (per the MSG file) are summarized in Table 4-2 at various steps. Associated radial strain contours are shown in Figure 4-6 and Figure 4-7. No cracking is observed after 30 years of creep (prior to detensioning). Since cracking is not seen in the MSG file prior to detensioning, the increase in radial strain prior to detensioning is attributed to the development of creep strain (as opposed to increased mechanical strain). During the detensioning process significant cracking occurs. Cracking is attributed to flexural stress (stemming from the effects of the detensioned tendons), concentrated near the future opening and the inner diameter (near the ring girder). Plots of the vertical strain are shown in Figure 4-8 to demonstrate this. Again, this cracking is controlled by the vertical reinforcement near the inner and outer surfaces of the containment wall. The total number of cracks during creep recovery remain unchanged, indicating that creep recovery is not causing additional cracks to form.   Note that the radial strain profile after detensioning when creep is included now resembles the hourglass type shape seen in the delamination cracking in the Crystal River containment (see Figure 1-1).

Table 4-2. Summary Results for A2

Step	Max Radial Strain (in/in)	MSG File Cracking
After Initial Stressing	161e-6	(0,0,0)
Before Detensioning	420e-6	(0,0,0)
After Detensioning	399e-6	Open: (1945, 398, 0) Closed: (34, 0, 0)
1250Hr After Detensioning	384e-6	Open: (1568 ,382, 0) Closed: (411, 16, 0)
5250Hr After Detensioning	379e-6	Open: (1298, 331, 0) Closed: (681, 67, 0)

Structural Integrity
Associates, Inc.

Figure 4-6 Radial Strain Before (Left) and After (Right) Detensioning [A2]
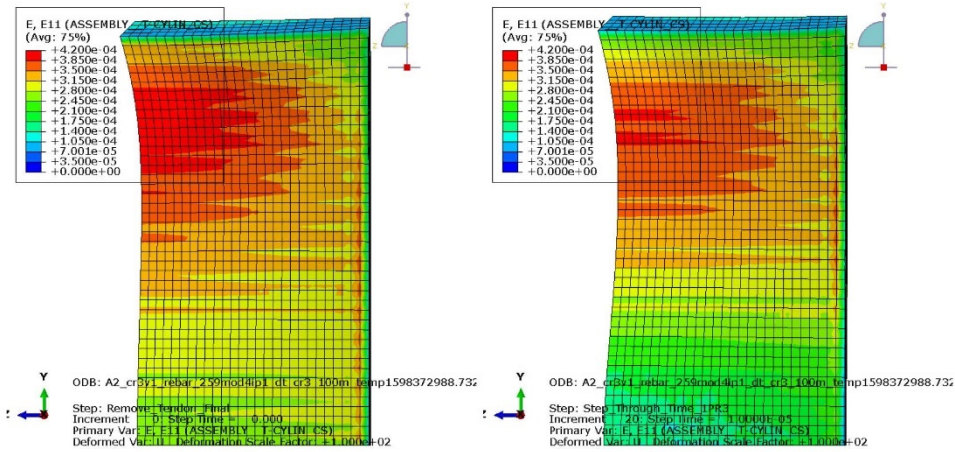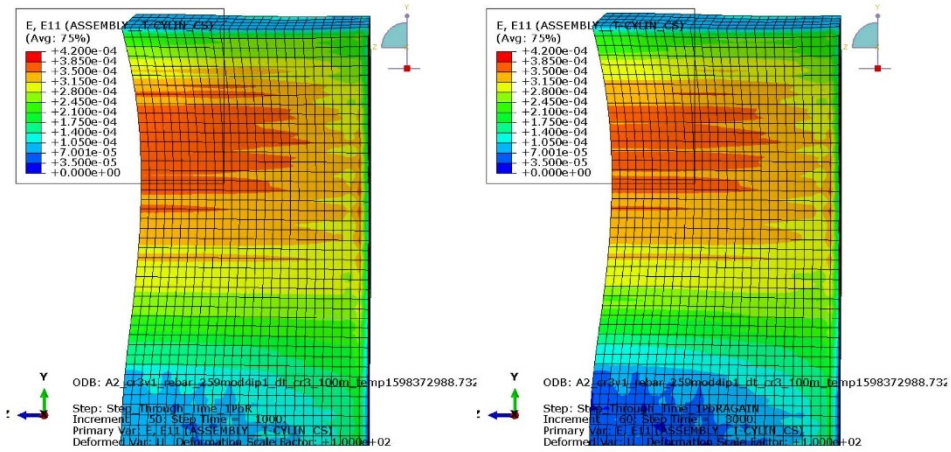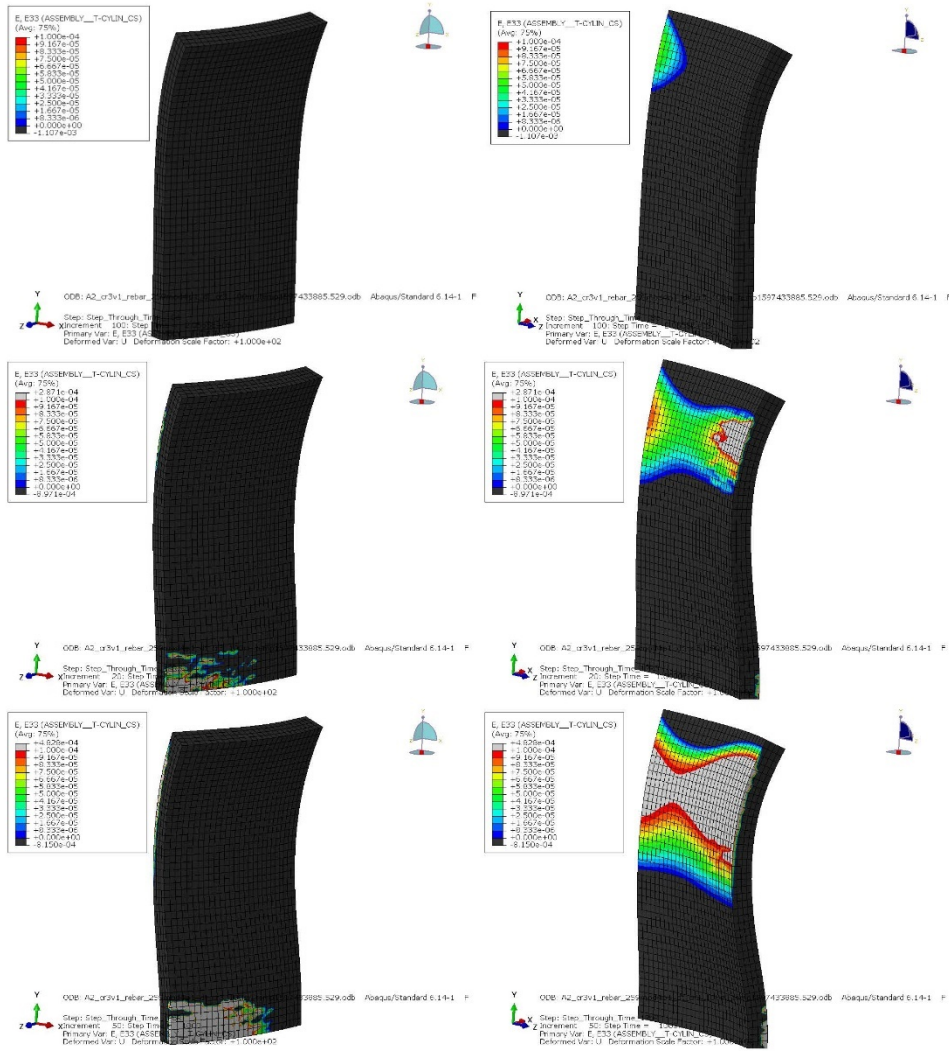

Figure 4-7 Radial Strain After 1250Hr (Left) and 5250Hr (Right) of Creep Recovery [A2]

Figure 4-8 Vertical Strain (Z in Transformed Coordinate System) Prior to (Top), Immediately After (Middle), and 1250 Hours After (Bottom) Detensioning [A2]

4.3 Case B1 – Delamination During Initial Tensioning

4.3.1 Description

In this analysis the ANACAP concrete tensile strain limit is iterated such that cracking of the containment wall occurs at the end of the initial tensioning phase (i.e. at 0 years). This assessment is performed to observe how the inclusion of a crack in the containment wall might propagate because of creep. A concrete tensile strain limit of 80e-6 in/in is used in this assessment to induce cracking.

Anamat File: anamat259dge_cr3curve_wCreepFactor.o
Input File: B1_cr3v1_rebar_259mod4ip1_dt_cr3_80m_temp.inp
Concrete Fracture Strain: 80e-6 in/in

4.3.2 Analysis Results

The analysis MSG file indicates that at the end of the tensioning phase/start of the creep phase 8441 open cracks have formed. Cracking occurs during the last increment of tendon stressing and quickly propagates at the outer diameter. The cracking appears to start near the highest radial strain. Cracking propagates from this location following the radial strain pattern seen in Figure 4-1. The radial strain shown in Figure 4-9 shows the crack propagating. Note that the delaminated nodes appear concentrated at the outer diameter of the structure. Figure 4-10 shows the evolution of radial displacement in an isometric view to emphasize the area of delamination. The analysis was discontinued prior to the creep steps as the structure has obviously failed due to tensioning. The simplified modeling used in this case has an inherent brittle failure mode since there is no alternative load path when mechanical loading causes delamination due to radial strains. This result also provides confidence that the modeling used is fully capable of capturing the delamination cracking if conditions warrant.
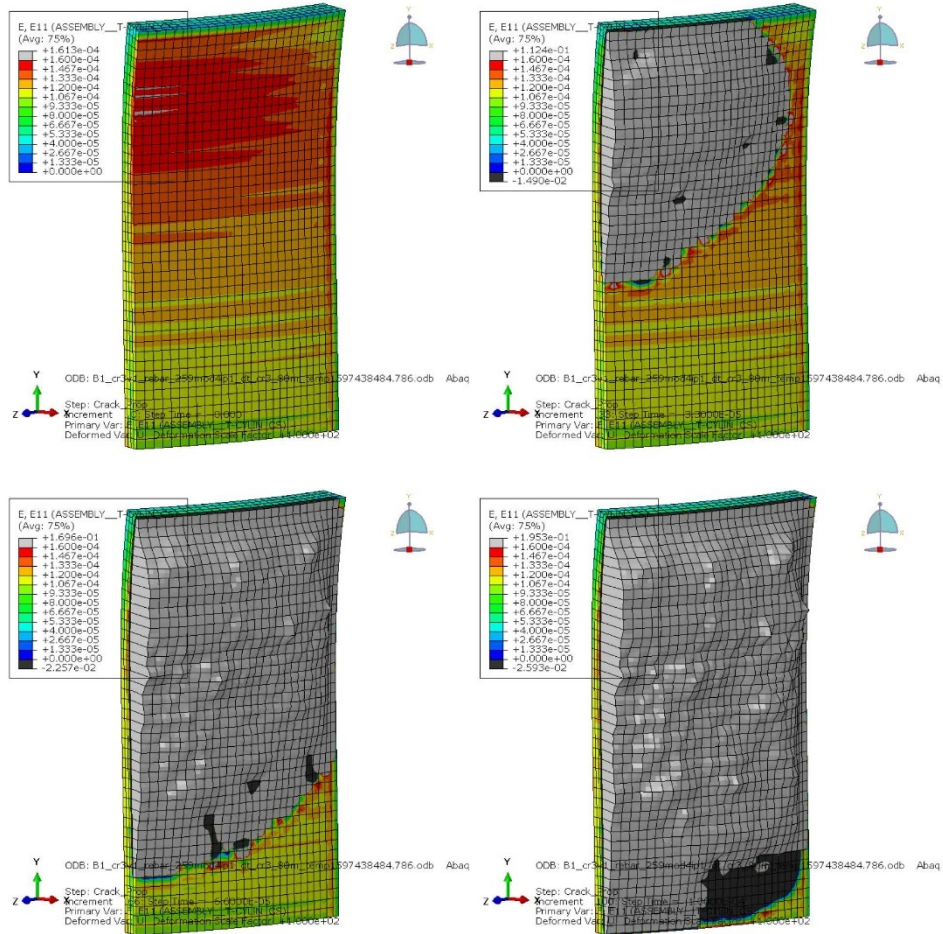
Figure 4-9. Crack Propagation (Radial Strain) at End of Initial Stressing [B1]

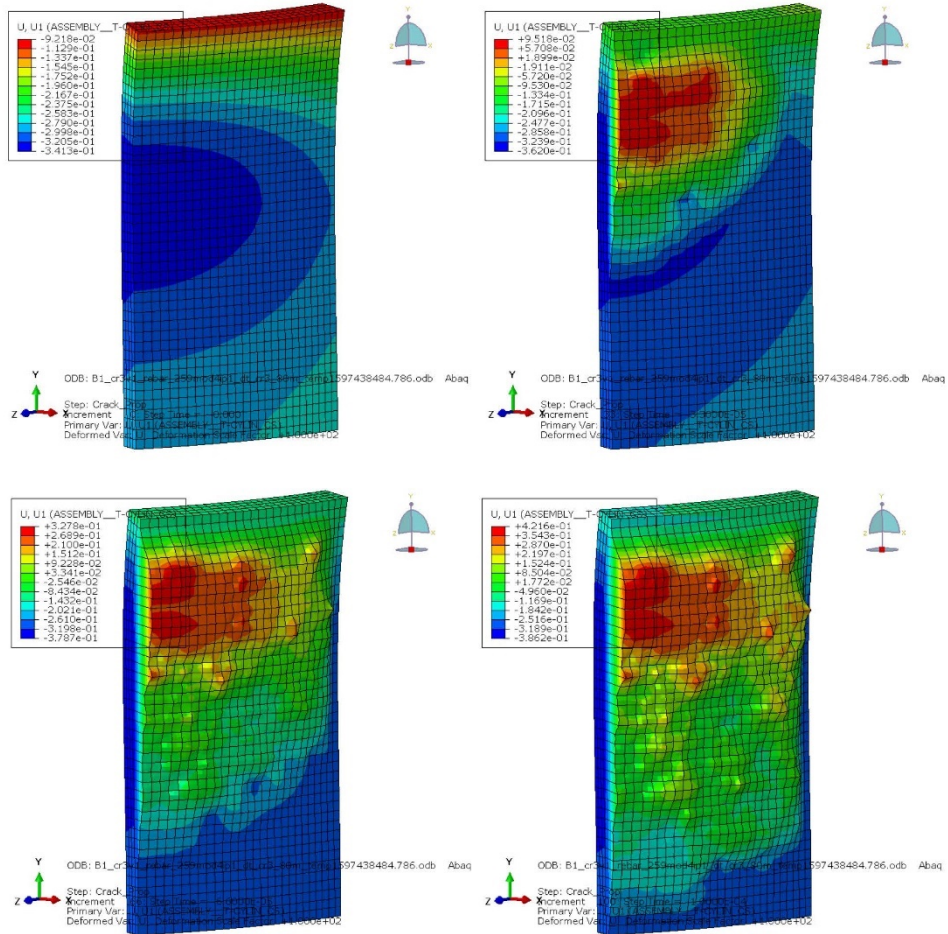Structural Integrity
Associates, Inc.

info@structint.com   1-877-4SI-POWER   structint.com

Figure 4-10. Radial Displacement at End of Initial Stressing [B1]

Structural Integrity
Associates, Inc.

info@structint.com   1-877-4SI-POWER   structint.com

4.4 Case B2 – Investigating Potential Delamination After Initial Tensioning

4.4.1 Description

In this analysis the ANACAP concrete tensile strain limit is set slightly higher than that in Case B1 to prevent delamination during initial tensioning. This assessment is performed to observe if a delamination crack will form due to creep or creep recovery when a low tensile strength concrete is assumed. A concrete tensile strain limit of 81e-6 in/in is used in this assessment.

Anamat File: anamat259dge_cr3curve_wCreepFactor.o
Input File: B2_cr3v1_rebar_259mod4ip1_dt_cr3_81m_temp.inp
Concrete Fracture Strain: 81e-6 in/in

4.4.2 Analysis Results

The radial strain and number of elements with 1, 2, and 3 cracks (per the MSG file) are summarized in Table 4-3 at various steps. Associated radial strain contours are shown in Figure 4-11 and Figure 4-12. Note that at the end of the initial stressing step 929 integration points are near cracking (>90% likelihood), although no cracking has occurred. After 250 hours of creep, only 41 integration points are near cracking, indicating that creep is reducing the likelihood of cracking. No cracking is observed prior to detensioning. Detensioning appears to cause the formation of flexural cracks near the future opening and inner diameter (near the ring girder). Approximately twice as many cracks form in Case B2 when compared to Case A2. This is attributed to the lower concrete fracture strain used in Case B2. It is not apparent that radial delamination has occurred. The total number of cracks observed during the creep recovery steps is not seen to change significantly, indicating crack propagation is not occurring.

Table 4-3. Summary Results for B2

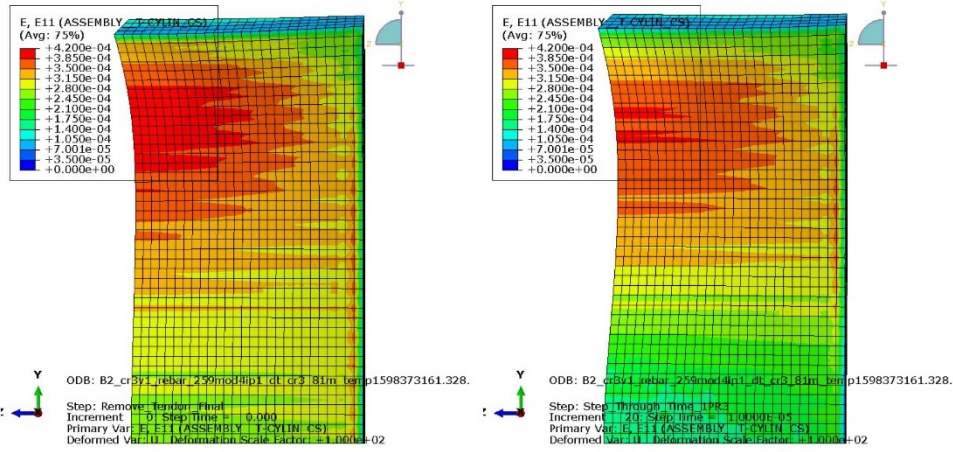| Step	Max Radial Strain (in/in)	MSG File Cracking
After Initial Stressing	161e-6	(0,0,0)
Before Detensioning	420e-6	(0,0,0)
After Detensioning	399e-6	Open: (3832, 653, 0) Closed: (133, 12, 0)
1250Hr After Detensioning	384e-6	Open: (2776, 607, 0) Closed: (1189, 58, 0)
5250Hr After Detensioning	379e-6	Open: (2378, 466, 0) Closed: (1587, 199, 0)

Figure 4-11 Radial Strain Before (Left) and After (Right) Detensioning [B2]
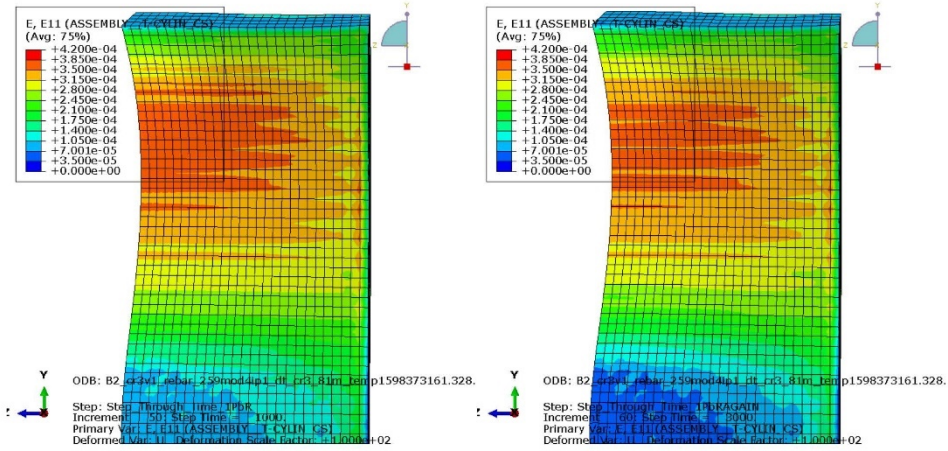

Figure 4-12 Radial Strain After 1250Hr (Left) and 5250Hr (Right) of Creep Recovery [B2]

4.5 Case B3 – Intentional Delamination After Initial Tensioning

4.5.1 Description

In this analysis a single truss element (defined as a No.9 rebar) is added into the model (Abaqus MODEL CHANGE after initial tensioning) near the largest radial strain (530in vertically from base of model, 28.5deg from centerline of the buttress). The truss element is 8in long and located entirely within an outer diameter concrete wall element. A +30deg temperature is applied to the truss element to induce radial cracking in the concrete (α_{rebar}=6.5e-6in/in/degF). This assessment is performed to observe how the formation of a crack after tensioning might propagate. This case is intended to assess the possibility that a delamination type crack has initiated over the operational history of the containment, perhaps due to scheduled SIT testing or other environmental events.

Anamat File: anamat259dge_cr3curve_wCreepFactor.o
Input File: B3_RA_cr3v1_rebar_259mod4ip1_dt_cr3_81m_temp.inp
Concrete Fracture Strain: 81e-6 in/in

4.5.2 Analysis Results

As temperature is applied to the truss element a compression force develops balanced by tension in the concrete. Quickly, however, a radial crack forms in the concrete and delamination begins to propagate. The radial strain (delamination) begins to induce tension in the truss element as the element now acts to prevent significant radial strain locally. When the truss element is removed from the model (post-radial cracking), the radial delamination begins to take a more uniform appearance. The radial strain, shown in Figure 4-13, shows the crack propagating. The analysis was discontinued prior to the creep steps as the structure has obviously failed. The radial strain and number of elements with 1, 2, and 3 cracks (per the MSG file) are summarized in Table 4-4 at various steps.

Table 4-4. Summary Results for B3

Step	Max Radial Strain (in/in)	MSG File Cracking
After Initial Stressing	161e-6	(0,0,0)
Peak Thermal Load on Truss Element	4826e-6	(180,0,0)
Prior to Creep Steps	0.1296	Open: (3383, 0, 0)
		Closed: (88, 0, 0)
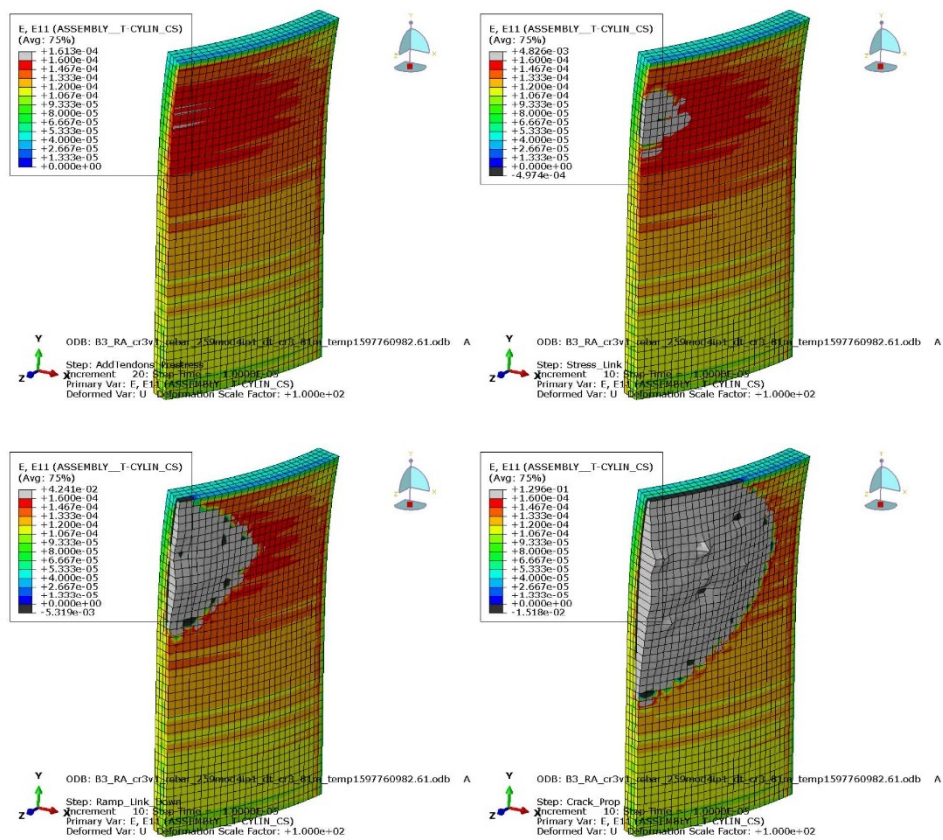
Figure 4-13. Crack Propagation (Radial Strain) at End of Initial Stressing (Top-Left) to Start of Creep Step (Bottom-Right) [B3]

4.6   Case B4 – Intentional Delamination After 6.5 Years

4.6.1 Description

In this analysis the single truss element defined in section 4.5.1 is "activated" 6.5 years after initial stressing. A +180deg temperature is applied to the truss element to induce radial cracking in the concrete. Note that this is a larger load than that required to induce cracking in Case B3. This is attributed to the reduction of mechanical strain due to creep. This assessment is performed to observe how the formation of this type of crack during operations might propagate after a period of creep.

Anamat File: anamat259dge_cr3curve_wCreepFactor.o
Input File: B4_RA_cr3v1_rebar_259mod4ip1_dt_cr3_81m_temp.inp
Concrete Fracture Strain: 81e-6 in/in

4.6.2 Analysis Results

The induced cracking at 6.5 years is minimal and appears concentrated near the truss element. After unloading and removing the truss element there are 34 open cracks (per the MSG file). No additional cracks form during the subsequent creep steps (~6.3 years). Due to the small region of high radial strains and the lack of widespread delamination, it is unclear if cracking is due to local delamination or a punching shear mode. The analysis was halted prior to the detensioning step. The radial strain and number of elements with 1, 2, and 3 cracks (per the MSG file) are summarized in Table 4-5 at various steps.

Table 4-5. Summary Results for B4

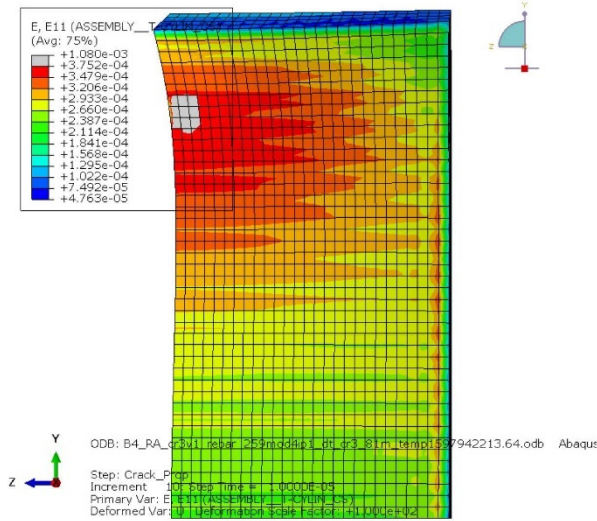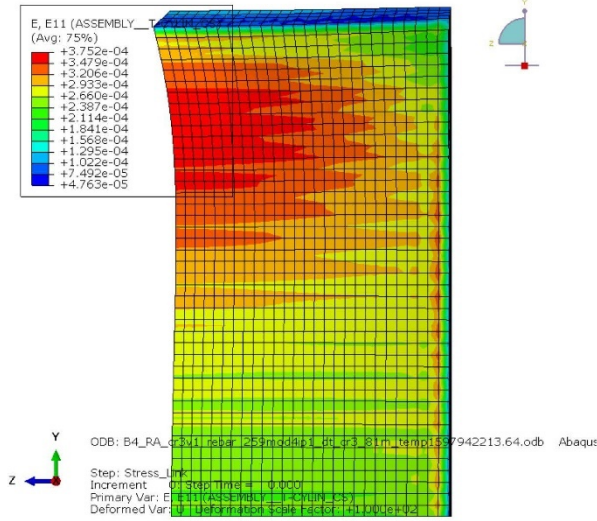| Step	Max Radial Strain (in/in)	MSG File Cracking
After Initial Stressing	161e-6	(0,0,0)
Removal of Truss Element	1080e-3	(34,0,0)
55500Hr After Removal of Truss Element	1619e-6	Open: (34,0,0)

Figure 4-14 Radial Strain Prior (Top) and After (Bottom) Truss Thermal Loading [B4]

4.7   Case B5 – Intentional Delamination Prior to Detensioning

4.7.1   Description

In this analysis the single truss element defined in section 4.5.1 is "activated" just prior to detensioning. A +210deg temperature is applied to the truss element to induce radial cracking in the concrete. Note that this is a larger load than that required to induce cracking in Case B3 or Case B4. This is attributed to the reduction of mechanical strain due to creep. This assessment is performed to observe how the formation of a crack during operations might propagate during detensioning.

Anamat File: anamat259dge_cr3curve_wCreepFactor.o
Input File: B5_RA_cr3v1_rebar_259mod4ip1_dt_cr3_81m_temp.inp
Concrete Fracture Strain: 81e-6 in/in

4.7.2   Analysis Results

The cracking induced by the truss element is minimal and appears concentrated near the truss element. After unloading and removing the truss element there are 17 open cracks (per the MSG file). Like Case B4, it is unclear if cracking is due to local delamination or a punching shear mode. There is no significant change in total radial strain adjacent to this region during the detensioning or creep recovery steps. The radial strain and number of elements with 1, 2, and 3 cracks (per the MSG file) are summarized in Table 4-6 at various steps.

Table 4-6. Summary Results for B5

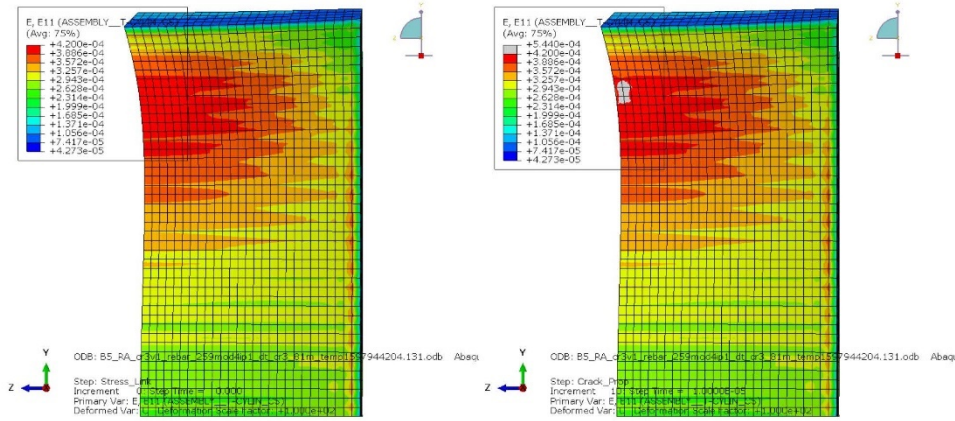| Step	Max Radial Strain (in/in)	MSG File Cracking
After Initial Stressing	161e-6	(0,0,0)
Removal of Truss Element	544e-6	(17,0,0)
After Detensioning	526e6	Open: (3850, 653, 0) Closed: (136, 12, 0)
1250Hr After Detensioning	584e-6	Open: (2794, 607, 0) Closed: (1192, 58, 0)

Figure 4-15 Radial Strain Prior (Left) and After (Right) Truss Thermal Loading [B5]
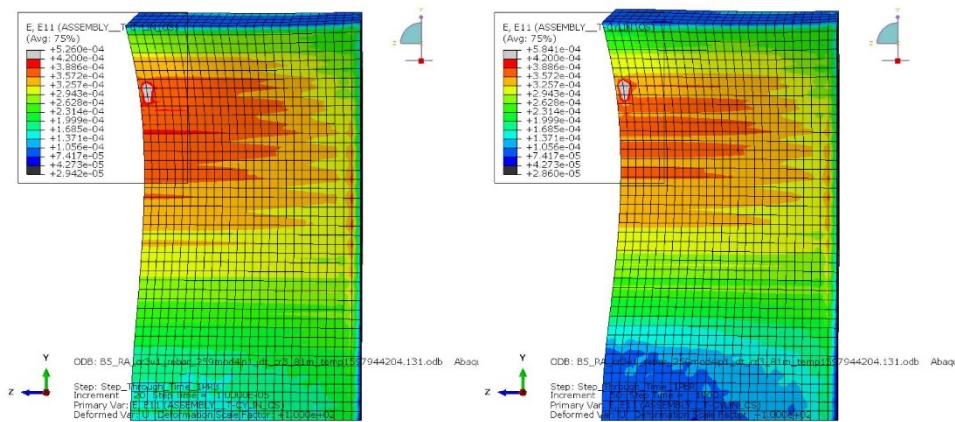

Figure 4-16 Radial Strain Immediately (Left) and 1250Hr (Right) After Detensioning [B5]

4.8   Case B6 – Intentional Delamination After Detensioning

4.8.1 Description

In this analysis the single truss element defined in section 4.5.1 is "activated" just after detensioning. A +300deg temperature is applied to the truss element to induce radial cracking in the concrete. This assessment is performed to observe how the formation of a crack after detensioning might propagate during the creep recovery steps.

Anamat File: anamat259dge_cr3curve_wCreepFactor.o
Input File: B6_TEST_RA_cr3v1_rebar_259mod4ip1_dt_cr3_81m_temp.inp
Concrete Fracture Strain: 81e-6 in/in

4.8.2 Analysis Results

The cracking induced by the truss element is minimal and appears concentrated near the truss element. After removal of the truss element only 17 cracks have been added, this is consistent with Case B5. Like previous cases, it is unclear if cracking is due to local delamination or a punching shear mode. There is no significant change in total radial strain adjacent to this region during the creep recovery steps and there is no increase in total cracks after 5250Hr, indicating crack propagation is not occurring. The radial strain and number of elements with 1, 2, and 3 cracks (per the MSG file) are summarized in Table 4-7 at various steps. Radial strain at various steps are shown in Figure 4-17.

Table 4-7. Summary Results for B6

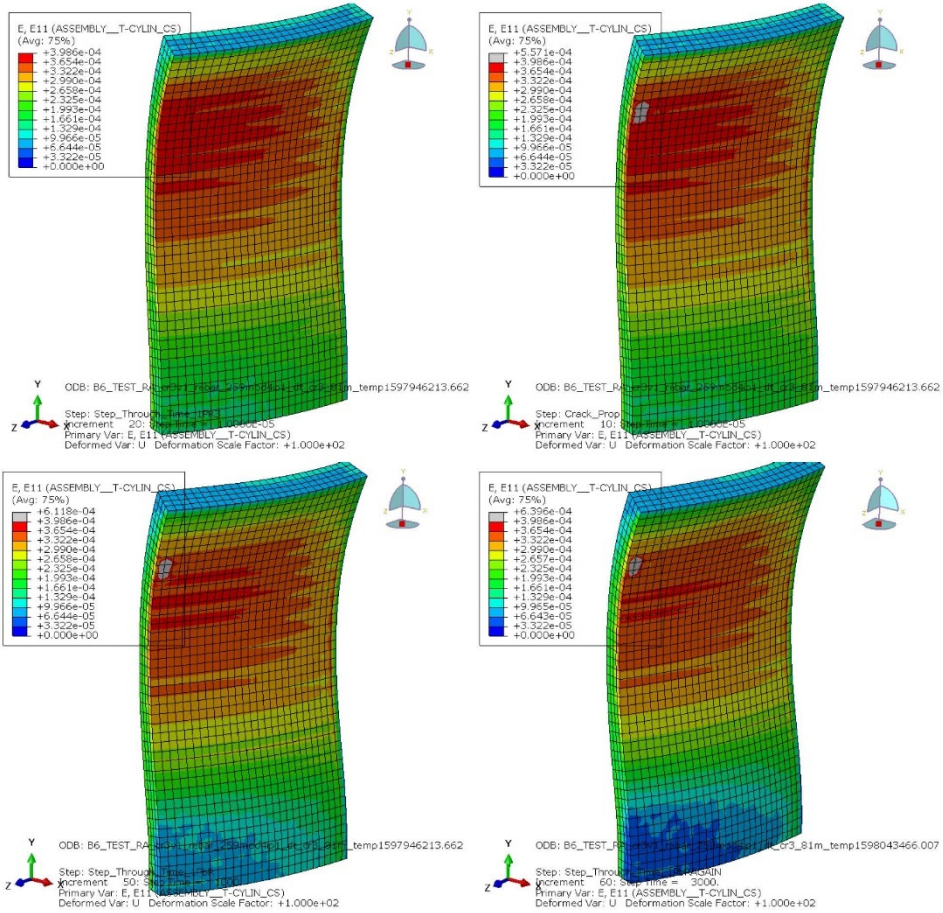| Step	Max Radial Strain (in/in)	MSG File Cracking
Before Detensioning	420e-6	(0, 0, 0)
After Detensioning	399e-6	Open: (3832, 653, 0)
		Closed: (133, 12, 0)
Removal of Truss Element	557e-6	Open: (3849, 653, 0)
		Closed: (133, 12, 0)
1250Hr After Detensioning	612e-6	Open: (2792, 607, 0)
		Closed: (1190, 58, 0)
5250Hr After Detensioning	639e-6	Open: (2395, 466, 0)
		Closed: (1587, 199, 0)

Figure 4-17 Radial Strain After Detensioning (Upper Left), Truss Thermal Loading (Upper Right), and After 1250Hr (Lower Left) and 5250Hr (Lower Right) of Creep Recovery [B6]

4.9 Case C1 – Differential Creep Compliance (0.5x & 1.0x)

4.9.1 Description

In this analysis, two different creep factors are applied to two different concrete element sets. The layer of finite elements on the outer diameter of the wall are assigned a creep factor of one while the remaining three layers of finite elements (through the wall thickness) are assigned a creep factor of one-half, see Figure 3-8. The concrete fracture strain is set to 81e-6in/in to maximize the probability of cracking after the initial tensioning step.

Anamat File: anamat259dge_cr3curve_wCreepFactor.o
Input File: C1_cr3v1_rebar_259mod4ip1_dt_cr3_81m_temp.inp
Concrete Fracture Strain: 81e-6 in/in

4.9.2 Analysis Results

The radial strain and number of elements with 1, 2, and 3 cracks (per the MSG file) are summarized in Table 4-8 at various steps. Associated radial strain contours are shown in Figure 4-18 and Figure 4-19.

No cracking is observed prior to detensioning. Detensioning appears to cause the formation of flexural cracks near the future opening and inner diameter (near the ring girder). It is not apparent that radial delamination has occurred. The total number of cracks observed during the creep recovery steps is not seen to change significantly, indicating crack propagation or delamination is not occurring. The maximum radial strain during the creep recovery steps is observed on the inner diameter, just below the ring girder.

Table 4-8. Summary Results for C1

Step	Max Radial Strain (in/in)	MSG File Cracking
After Initial Stressing	161e-6	(0,0,0)
Before Detensioning	346e-6	(0,0,0)
After Detensioning	389e-6	(2011, 772, 0)
1250Hr After Detensioning	446e-6	Open: (1770, 733, 0) Closed: (246, 39, 0)
5250Hr After Detensioning	458e-6	Open: (1509, 669, 0) Closed: (510, 103, 0)

info@structint.com   1-877-4SI-POWER   structint.com
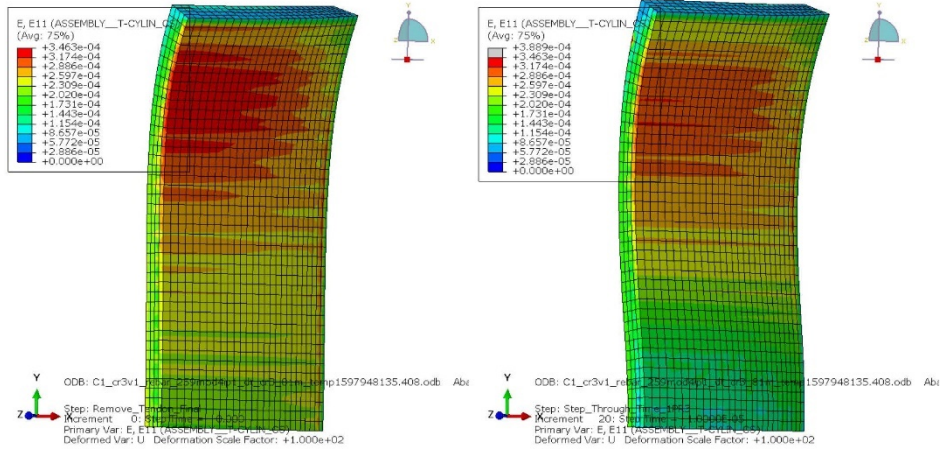
Structural Integrity Associates, Inc.

Figure 4-18 Radial Strain Before (Left) and After (Right) Detensioning [C1]
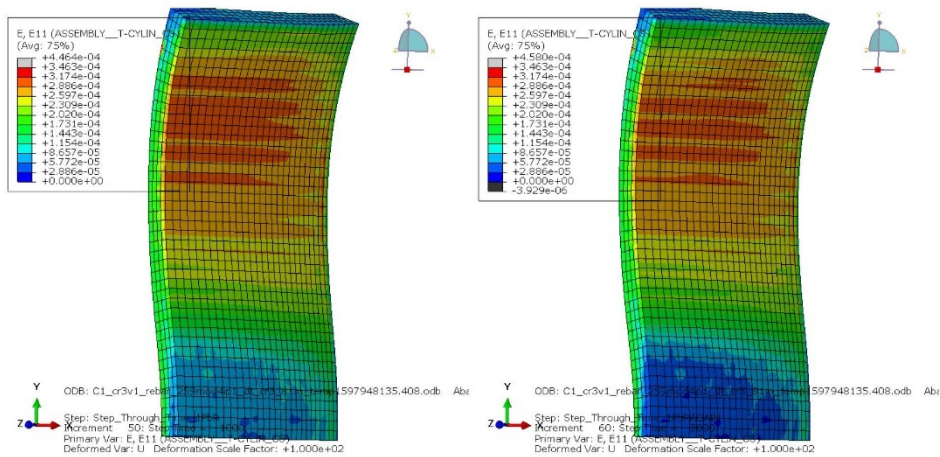

Figure 4–19 Radial Strain After 1250Hr (Left) and 5250Hr (Right) of Creep Recovery [C1]

4.10 Case C2 – Differential Creep Compliance (1.0x & 2.0x)

4.10.1 Description

In this analysis, two different creep factors are applied to two different concrete element sets. The layer of finite elements on the outer diameter of the wall are assigned a creep factor of two while the remaining three layers of finite elements (through the wall thickness) are assigned a creep factor of one, see Figure 3-8. The concrete fracture strain is set to 81e-6in/in to maximize the probability of cracking after the initial tensioning step.

Anamat File: anamat259dge_cr3curve_wCreepFactor.o
Input File: C2_cr3v1_rebar_259mod4ip1_dt_cr3_81m_temp.inp
Concrete Fracture Strain: 81e-6 in/in

4.10.2 Analysis Results

The radial strain and number of elements with 1, 2, and 3 cracks (per the MSG file) are summarized in Table 4-9 at various steps. Associated radial strain contours are shown in Figure 4-20 and Figure 4-21. No cracking is observed prior to detensioning. Detensioning appears to cause the formation of flexural cracks near the future opening and inner diameter (near the ring girder). Significantly more cracks are seen then in previous cases. This is attributed to the higher creep factor on the outer diameter concrete elements. It is not apparent that radial delamination has occurred. The total number of cracks observed during the creep recovery steps is not seen to change, indicating crack propagation is not occurring.

Table 4-9. Summary Results for C2

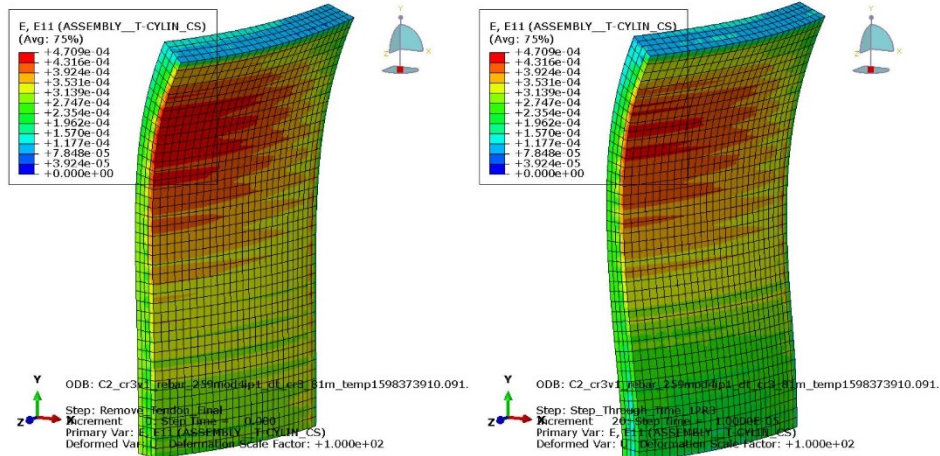| Step	Max Radial Strain (in/in)	MSG File Cracking
After Initial Stressing	161e-6	(0,0,0)
Before Detensioning	471e-6	(0,0,0)
After Detensioning	451e-6	Open: (6437, 1610, 0)
		Closed: (219, 9, 0)
1250Hr After Detensioning	431e-6	Open: (3775, 1450, 0)
		Closed: (2881, 169, 0)
5250Hr After Detensioning	425e-6	Open: (2871, 1325, 0)
		Closed: (3785, 294, 0)

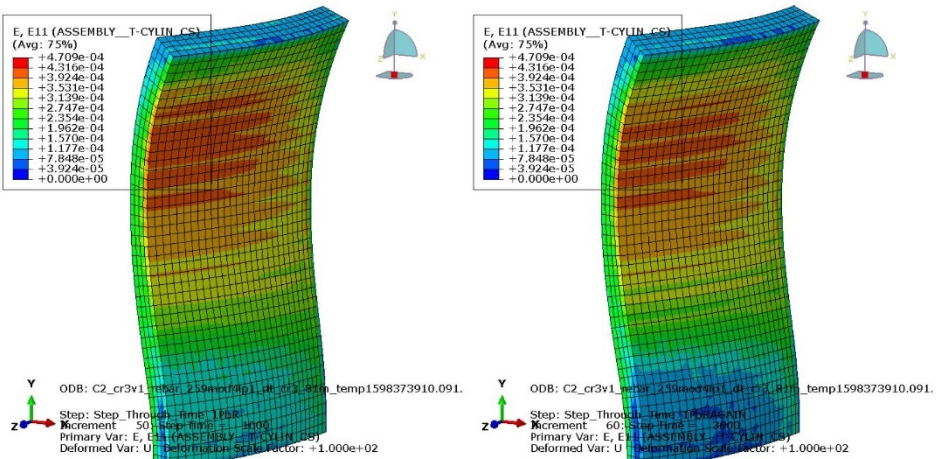Figure 4-20 Radial Strain Before (Left) and After (Right) Detensioning [C2]

Figure 4-21 Radial Strain After 1250Hr (Left) and 5250Hr (Right) of Creep Recovery [C2]

4.11 Case C3 – Differential Creep Compliance (1.0x & 0.5x)

4.11.1 Description

In this analysis, two different creep factors are applied to two different concrete element sets. The layer of finite elements on the outer diameter of the wall are assigned a creep factor of one-half while the remaining three layers of finite elements (through the wall thickness) are assigned a creep factor of one, see Figure 3-8. Three different concrete fracture strains are assessed: 81e-6in/in, 84e-6 in/in, and 90e-6 in/in.

Anamat File: anamat259dge_cr3curve_wCreepFactor.o
Input File: C3_cr3v1_rebar_259mod4ip1_dt_cr3_81m_temp.inp
Concrete Fracture Strain: 81e-6 in/in
Input File: C3_cr3v1_rebar_259mod4ip1_dt_cr3_85m_temp.inp
Concrete Fracture Strain: 85e-6 in/in
Input File: C3_cr3v1_rebar_259mod4ip1_dt_cr3_90m_temp.inp
Concrete Fracture Strain: 90e-6 in/in

4.11.2 Analysis Results

The original model (81e-6in/in) resulted in an initial crack forming after the first step of creep (2.5Hr) and not at the end of the initial stressing. The crack propagated into a delamination failure similar to case B1 (see Figure 4-9).

The model was then updated to a 90e-6 in/in fracture strain and re-analyzed. The MSG file indicates that during the initial creep steps the number of integration points with high cracking potential slowly climbs to a peak around 310 (occurring near 430Hrs into the creep assessment) before declining back to 0 after 10.3Yr.

The third model run used a concrete fracture strain of 85e-6in/in. This run's MSG file reports 0 cracks at the end of initial tensioning, but 326 integration points with high cracking potential. As the creep assessment progresses, the number of integration points likely to crack increases up to ~900 until the first crack forms 130Hr into the creep assessment. The crack propagates into the delaminated hourglass shape seen in previous assessments.

This result is unique as this is the first case where delamination can be directly attributable to creep. The lower creep factor applied to the exterior concrete elements, and higher creep factor

applied to the interior concrete elements, appears to cause a radial (mechanical) strain to form at the interface as the interior elements creep inward at a faster rate than the exterior elements.

The second model (90e-6in/in) MSG file was then revisited to track the evolution of crack formation during the creep recovery phase. The radial strain and number of elements with 1, 2, and 3 cracks (per the MSG file) are summarized in Table 4-10 at various steps. The total number of cracks observed during the creep recovery steps is not seen to change, indicating crack propagation is not occurring.

Table 4-10. Summary Results for C3 (90e-6in/in)

Step	Max Radial Strain (in/in)	MSG File Cracking
After Initial Stressing	161e-6	(0,0,0)
Before Detensioning	371e-6	(0,0,0)
After Detensioning	349e-6	Open: (3092, 49, 0) Closed: (8, 0, 0)
1250Hr After Detensioning	337e-6	Open: (2349, 49, 0) Closed: (751, 0, 0)
20250Hr After Detensioning	333e-6	Open: (1678, 46, 0) Closed: (1422, 3, 0)

4.12   Case C4 – Not Used

info@structint.com   1-877-4SI-POWER   structint.com

7-47

4.13 Case C5 – Differential Creep Compliance (0.5x & 3x)

4.13.1 Description

In this analysis, two different creep factors are applied to two different concrete element sets. The layer of finite elements on the outer diameter of the wall are assigned a creep factor of three while the remaining three layers of finite elements (through the wall thickness) are assigned a creep factor of one-half, see Figure 3-8. The concrete fracture strain is set to 81e-6in/in to maximize the probability of cracking after the initial tensioning step.

Anamat File: anamat259dge_cr3curve_wCreepFactor.o
Input File: C5_cr3v1_rebar_259mod4ip1_dt_cr3_81m_temp.inp
Concrete Fracture Strain: 81e-6 in/in

4.13.2 Analysis Results

The radial strain and number of elements with 1, 2, and 3 cracks (per the MSG file) are summarized in Table 4-11 at various steps. Associated radial strain contours are shown in Figure 4-22 and Figure 4-23.

The results of this analysis are like that of Case C1 and C2. No cracking is observed prior to detensioning. Detensioning appears to cause the formation of flexural cracks near the future opening and inner diameter (near the ring girder). It is not apparent that radial delamination has occurred. The total number of cracks observed during the creep recovery steps is not seen to change significantly, indicating crack propagation is not occurring.

Table 4-11. Summary Results for C5

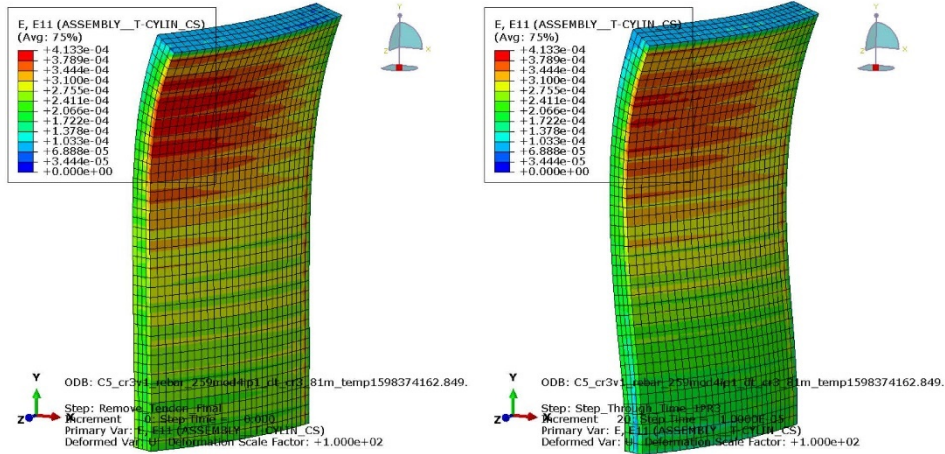| Step	Max Radial Strain (in/in)	MSG File Cracking
After Initial Stressing	161e-6	(0,0,0)
Before Detensioning	413e-6	(0,0,0)
After Detensioning	391e-6	Open: (4702, 1690, 0) Closed: (1, 1, 0)
1250Hr After Detensioning	380e-6	Open: (3162, 1649, 0) Closed: (1544, 42, 0)
5250Hr After Detensioning	377e-6	Open: (2416, 1594, 0) Closed: (2290, 97, 0)

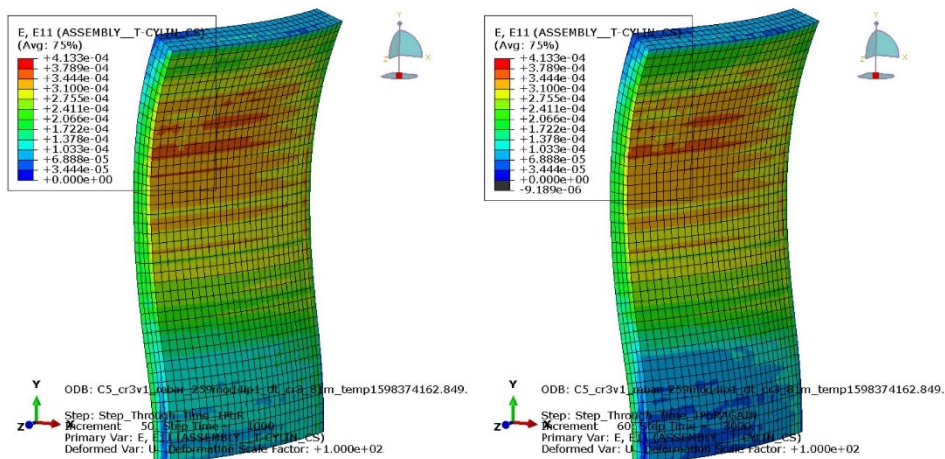**Figure 4-22 Radial Strain Before (Left) and After (Right) Detensioning [C5]**

Figure 4-23 Radial Strain After 1250Hr (Left) and 5250Hr (Right) of Creep Recovery [C5]

4.14   **Case D1 – Not Used**

4.15   **Case D2 – Not Used**

4.16   **Case D3 – Time Dependent Material**

4.16.1 Description

In this analysis, the concrete compressive strength is defined to be linearly time varying with a 100% increase in strength over 60 years (i.e. ~50% increase at time of detensioning). The concrete modulus is increased as a function of sqrt(f'c(t)). The concrete fracture strain is set to 133e-6in/in (within the ANAMAT) and is made time dependent, effectively increasing as a function of sqrt(f'c(t)). Both interior and exterior elements are assigned a creep factor of one.

Anamat File: anamat259dge_cr3curve_wCreepFactor_BRTIME50_ABQHR.o
Input File: D3_cr3v1_rebar_259mod4ip7_dt_cr3_81m_temp_BR50CF3.inp
Concrete Fracture Strain: 133e-6 in/in initial & time varying

4.16.2 Analysis Results

The radial strain and number of elements with 1, 2, and 3 cracks (per the MSG file) are summarized in Table 4-12 at various steps. Associated radial strain contours are shown in Figure 4-24 and Figure 4-25. The analysis indicates no concrete cracking, even after detensioning. This is attributed to the high initial, and time dependent, concrete fracture strain.

Table 4-12. Summary Results for D3

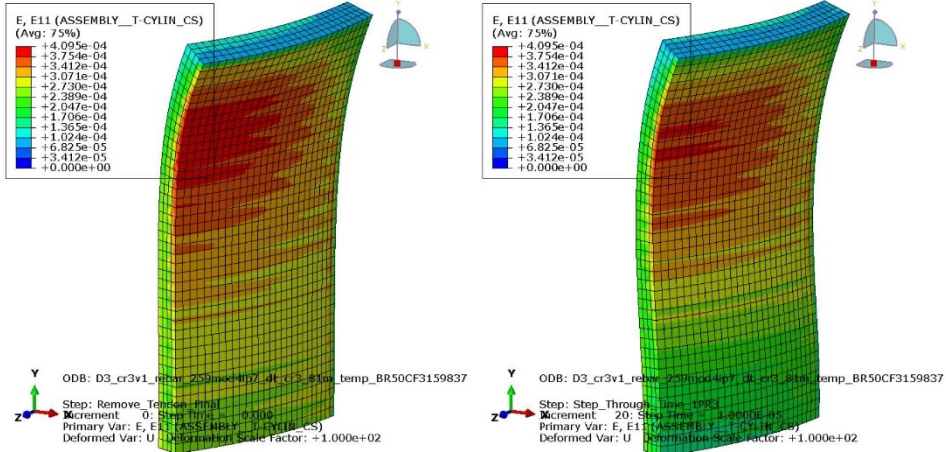| Step	Max Radial Strain (in/in)	MSG File Cracking
After Initial Stressing	161e-6	(0,0,0)
Before Detensioning	409e-6	(0,0,0)
After Detensioning	391e-6	(0,0,0)
1250Hr After Detensioning	375e-6	(0,0,0)
5250Hr After Detensioning	369e-6	(0,0,0)

Figure 4-24 Radial Strain Before (Left) and After (Right) Detensioning [D3]
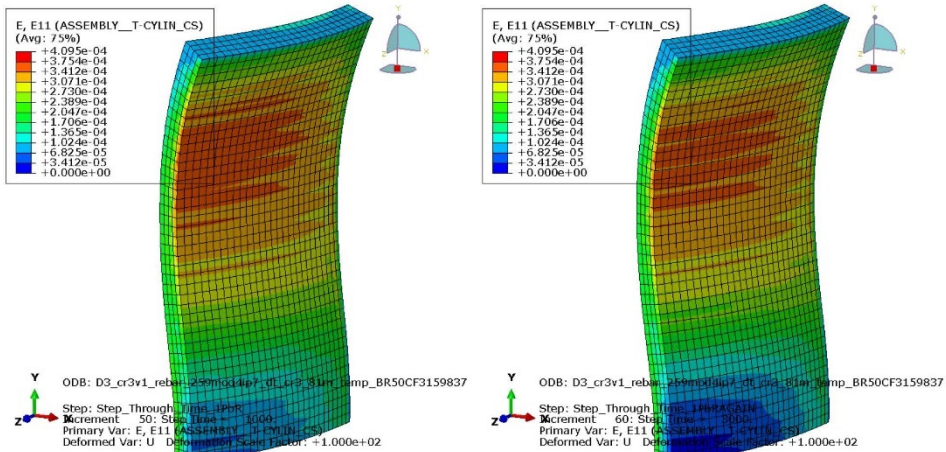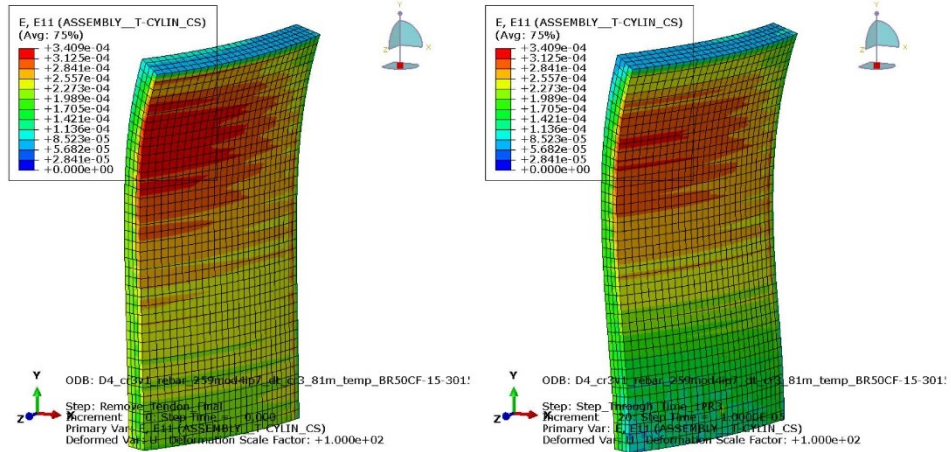

Figure 4-25 Radial Strain After 1250Hr (Left) and 5250Hr (Right) of Creep Recovery [D3]

4.17 Case D4 – Time Dependent Material, Differential Creep Compliance (0.5x & 1x)

4.17.1 Description

In this analysis, two different creep factors are applied to two different concrete element sets. The layer of finite elements on the outer diameter of the wall are assigned a creep factor of one while the remaining three layers of finite elements (through the wall thickness) are assigned a creep factor of one-half, see Figure 3-8. Time dependent material properties, as described in section 4.16.1 are used.

Anamat File: anamat259dge_cr3curve_wCreepFactor_BRTIME50_ABQHR.o
Input File: D4_cr3v1_rebar_259mod4ip7_dt_cr3_81m_temp_BR50CF-15-30.inp
Concrete Fracture Strain: 133e-6 in/in initial & time varying

4.17.2 Analysis Results

The radial strain and number of elements with 1, 2, and 3 cracks (per the MSG file) are summarized in Table 4-13 at various steps. Associated radial strain contours are shown in Figure 4-26 and Figure 4-27. Minimal cracking is observed. The total number of cracks observed during the creep recovery steps is not seen to change, indicating crack propagation is not occurring.

Table 4-13. Summary Results for D4

Step	Max Radial Strain (in/in)	MSG File Cracking
After Initial Stressing	161e-6	(0,0,0)
Before Detensioning	341e-6	(0,0,0)
After Detensioning	321e-6	Open: (389, 101, 0) Closed: (2, 0, 0)
1250Hr After Detensioning	317e-6	Open: (388, 101, 0) Closed: (3, 0, 0)
5250Hr After Detensioning	315e-6	Open: (360, 101, 0) Closed: (31, 0, 0)

Figure 4-26 Radial Strain Before (Left) and After (Right) Detensioning [D4]
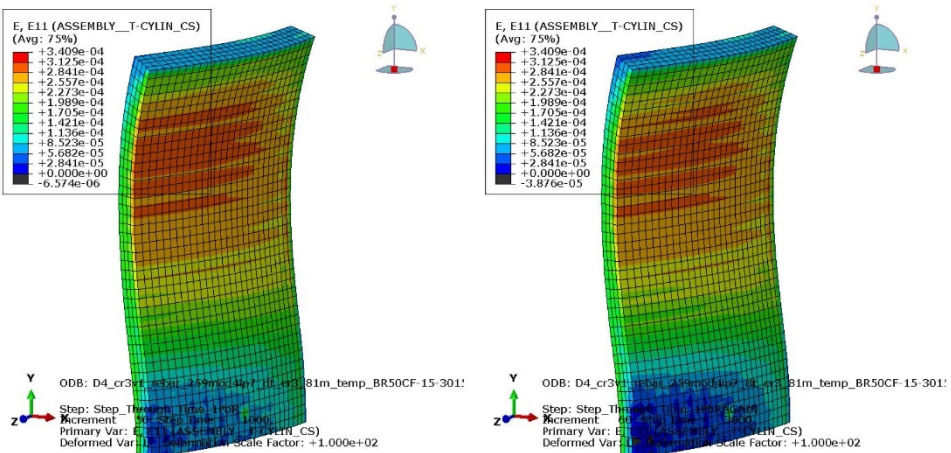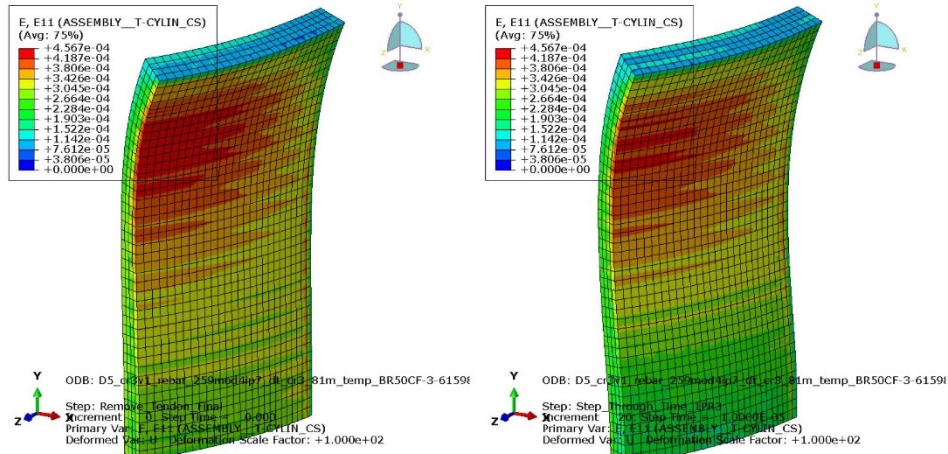

Figure 4-27 Radial Strain After 1250Hr (Left) and 5250Hr (Right) of Creep Recovery [D4]

4.18 Case D5 – Time Dependent Material, Differential Creep Compliance (1x & 2x)

4.18.1 Description

In this analysis, two different creep factors are applied to two different concrete element sets. The layer of finite elements on the outer diameter of the wall are assigned a creep factor of two while the remaining three layers of finite elements (through the wall thickness) are assigned a creep factor of one, see Figure 3-8. Time dependent material properties, as described in section 4.16.1 are used.

Anamat File: anamat259dge_cr3curve_wCreepFactor_BRTIME50_ABQHR.o
Input File: D5_cr3v1_rebar_259mod4ip7_dt_cr3_81m_temp_BR50CF-3-6.inp
Concrete Fracture Strain: 133e-6 in/in initial & time varying

4.18.2 Analysis Results

The radial strain and number of elements with 1, 2, and 3 cracks (per the MSG file) are summarized in Table 4-14 at various steps. Associated radial strain contours are shown in Figure 4-28 and Figure 4-29. It is not apparent that radial delamination has occurred. The total number of cracks observed during the creep recovery steps is not seen to change significantly, indicating crack propagation is not occurring.

Table 4-14. Summary Results for D5

Step	Max Radial Strain (in/in)	MSG File Cracking
After Initial Stressing	161e-6	(0,0,0)
Before Detensioning	457e-6	(0,0,0)
After Detensioning	440e-6	Open: (1812, 473, 0) Closed: (0, 0, 0)
1250Hr After Detensioning	420e-6	Open: (1573, 472, 0) Closed: (239, 1, 0)
5250Hr After Detensioning	413e-6	Open: (1165, 456, 0) Closed: (647, 17, 0)

Figure 4-28 Radial Strain Before (Left) and After (Right) Detensioning [D5]
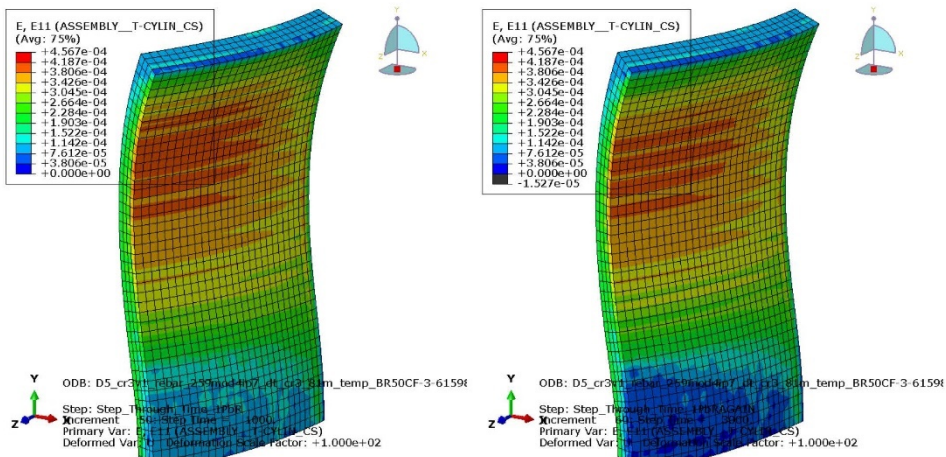

Figure 4-29 Radial Strain After 1250Hr (Left) and 5250Hr (Right) of Creep Recovery [D5]

4.19 Case Fb2 – Variation of Case B2

4.19.1 Description

This analysis serves as a variation of Case B2 with the following changes:

- The ring girder modulus is increased (to 16e6psi) to represent a stiffer boundary.
- The concrete fracture strain is defined as 81e-6 in/in
- The vertical tendons are not removed during the tendon removal stage.

Anamat File: anamat259dge_cr3curve_wCreepFactor.o
Input File: Fb2_cr3v1_rebar_259mod4ip1_dt_cr3_81m_temp.inp
Concrete Fracture Strain: 81e-6 in/in

4.19.2 Analysis Results

The radial strain and number of elements with 1, 2, and 3 cracks (per the MSG file) are summarized in Table 4-15 at various steps. Associated radial strain contours are shown in Figure 4-30 and Figure 4-31. Unlike previous cases, the radial strain increases during the detensioning process. This is attributed to (a) not removing the vertical tendons and (b) increased radial strain due to flexure (and the Poisson's effect) stemming from the removal of the horizontal tendons. Since this change in strain occurs over a short duration, it is not attributed to creep, and is thus interpreted as an increase in radial mechanical strain. The mechanical strain increase (~10e-6 in/in) does not appear sufficient to cause delamination in this particular case. The total number of cracks observed during the creep recovery steps is not seen to change, indicating crack propagation is not occurring. However, the creep recovery steps show an increase in total strain, which differs from previous results.

Table 4-15. Summary Results for Fb2

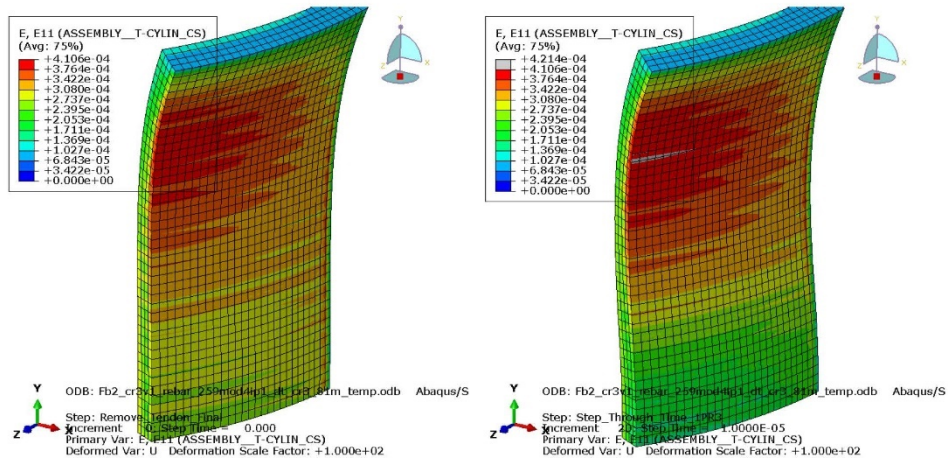| Step	Max Radial Strain (in/in)	MSG File Cracking
After Initial Stressing	162e-6	(0,0,0)
Before Detensioning	411e-6	(0,0,0)
After Detensioning	421e-6	Open: (2142, 0, 0) Closed: (141, 0, 0)
1250Hr After Detensioning	431e-6	Open: (951, 0, 0) Closed: (1332, 0, 0)
5250Hr After Detensioning	435e-6	Open: (249, 0, 0) Closed: (2034, 0, 0)

Figure 4-30 Radial Strain Before (Left) and After (Right) Detensioning [Fb2]
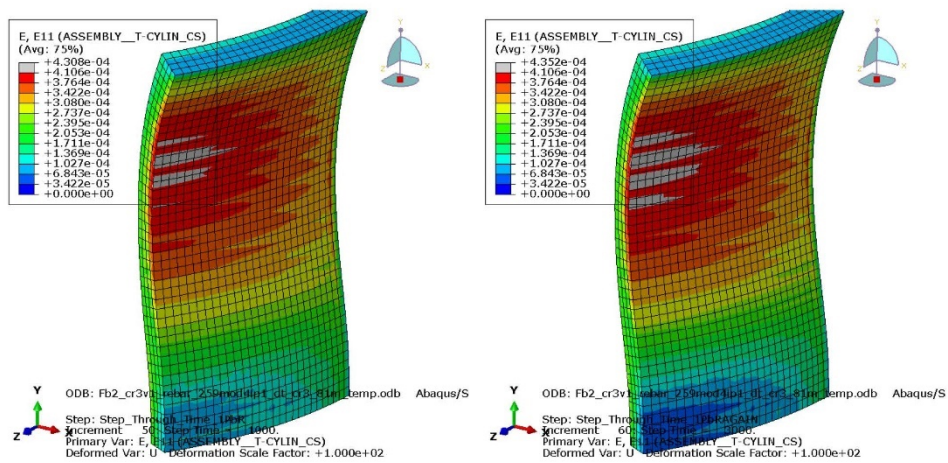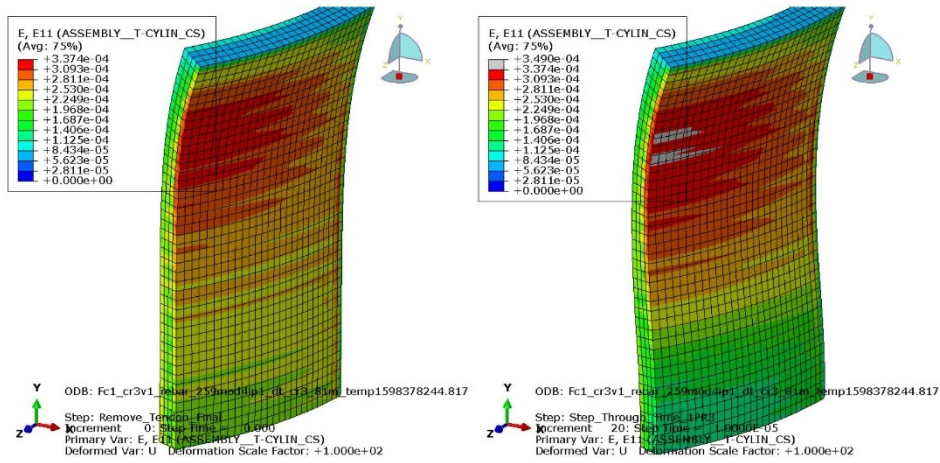

Figure 4-31 Radial Strain After 1250Hr (Left) and 5250Hr (Right) of Creep Recovery [Fb2]

4.20 Case Fc1 – Variation of Case C1

4.20.1 Description

This analysis serves as a variation of Case C1 with the following changes:

- The ring girder modulus is increased (to 16e6psi) to represent a stiffer boundary.
- The concrete fracture strain is defined as 81e-6 in/in
- The vertical tendons are not removed during the tendon removal stage.

Anamat File: anamat259dge_cr3curve_wCreepFactor.o
Input File: Fc1_cr3v1_rebar_259mod4ip1_dt_cr3_81m_temp.inp
Concrete Fracture Strain: 81e-6 in/in

4.20.2 Analysis Results

The radial strain and number of elements with 1, 2, and 3 cracks (per the MSG file) are summarized in Table 4-16 at various steps. Associated radial strain contours are shown in Figure 4-32 and Figure 4-33. Unlike previous cases, the radial strain increases during the detensioning process. This is attributed to (a) not removing the vertical tendons and (b) increased radial strain due to flexure (and the Poisson's effect) stemming from the removal of the horizontal tendons. Since this change in strain occurs over a short duration, it is not attributed to creep, and is thus interpreted as an increase in radial mechanical strain. The mechanical strain increase (~12e-6 in/in) does not appear sufficient to cause delamination in this particular case. The total number of cracks observed during the creep recovery steps is not seen to change, indicating crack propagation is not occurring. However, the creep recovery steps show an increase in total strain, which differs from previous results.

Table 4-16. Summary Results for Fc1

Step	Max Radial Strain (in/in)	MSG File Cracking
After Initial Stressing	162e-6	(0,0,0)
Before Detensioning	337e-6	(0,0,0)
After Detensioning	349e-6	Open: (1527, 0, 0)
1250Hr After Detensioning	356e-6	Open: (1254, 0, 0)
		Closed: (273, 0, 0)
5250Hr After Detensioning	359e-6	Open: (905, 0, 0)
		Closed: (622, 0, 0)

Structural Integrity
Associates, Inc.

info@structint.com   1-877-4SI-POWER   structint.com

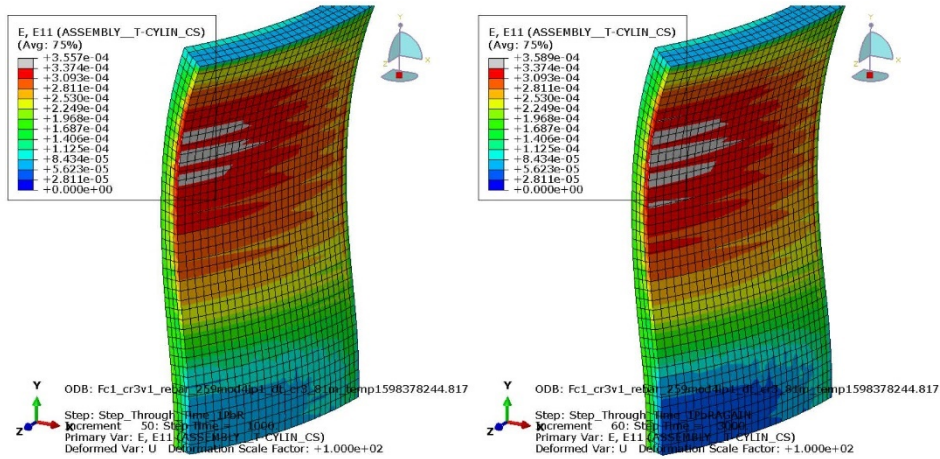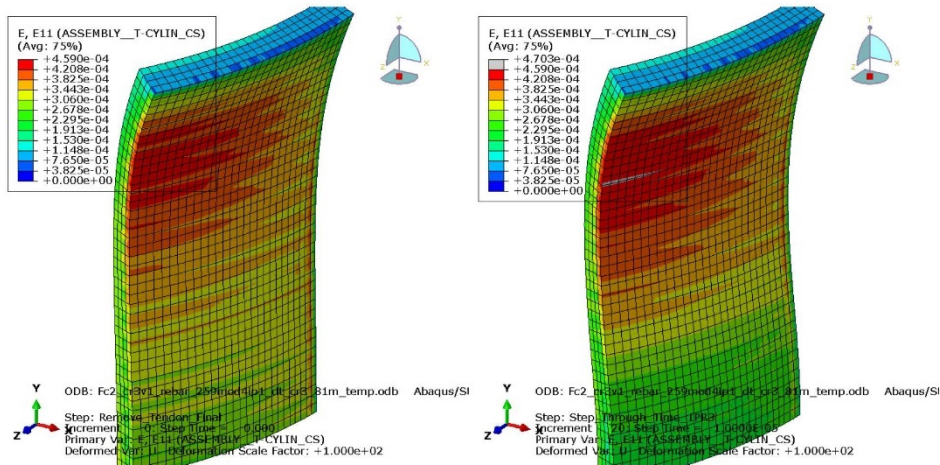**Figure 4-32 Radial Strain Before (Left) and After (Right) Detensioning [Fc1]**

Figure 4-33 Radial Strain After 1250Hr (Left) and 5250Hr (Right) of Creep Recovery [Fc1]

4.21 Case Fc2 – Variation of Case C2

4.21.1 Description

This analysis serves as a variation of Case C2 with the following changes:

- The ring girder modulus is increased (to 16e6psi) to represent a stiffer boundary.
- The concrete fracture strain is defined as 81e-6 in/in
- The vertical tendons are not removed during the tendon removal stage.

Anamat File: anamat259dge_cr3curve_wCreepFactor.o
Input File: Fc2_cr3v1_rebar_259mod4ip1_dt_cr3_81m_temp.inp
Concrete Fracture Strain: 81e-6 in/in

4.21.2 Analysis Results

The radial strain and number of elements with 1, 2, and 3 cracks (per the MSG file) are summarized in Table 4-17 at various steps. Associated radial strain contours are shown in Figure 4-34 and Figure 4-35. Unlike previous cases, the radial strain increases during the detensioning process. This is attributed to (a) not removing the vertical tendons and (b) increased radial strain due to flexure (and the Poisson's effect) stemming from the removal of the horizontal tendons. Since this change in strain occurs over a short duration, it is not attributed to creep, and is thus interpreted as an increase in radial mechanical strain. The mechanical strain increase (~11e-6 in/in) does not appear sufficient to cause delamination in this particular case. The total number of cracks observed during the creep recovery steps is not seen to change, indicating crack propagation is not occurring. However, the creep recovery steps show an increase in total strain, which differs from previous results.

Table 4-17. Summary Results for Fc2

Step	Max Radial Strain (in/in)	MSG File Cracking
After Initial Stressing	162e-6	(0,0,0)
Before Detensioning	459e-6	(0,0,0)
After Detensioning	470e-6	Open: (4384, 360, 0) Closed: (196, 0, 0)
1250Hr After Detensioning	482e-6	Open: (2199, 306, 0) Closed: (2381, 54, 0)
5250Hr After Detensioning	486e-6	Open: (1188, 231, 0) Closed: (3392, 129, 0)

Figure 4-34 Radial Strain Before (Left) and After (Right) Detensioning [Fc2]
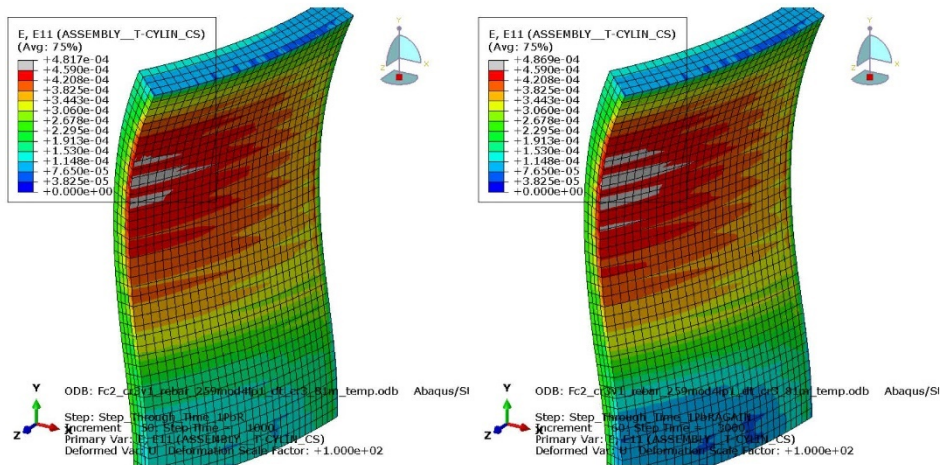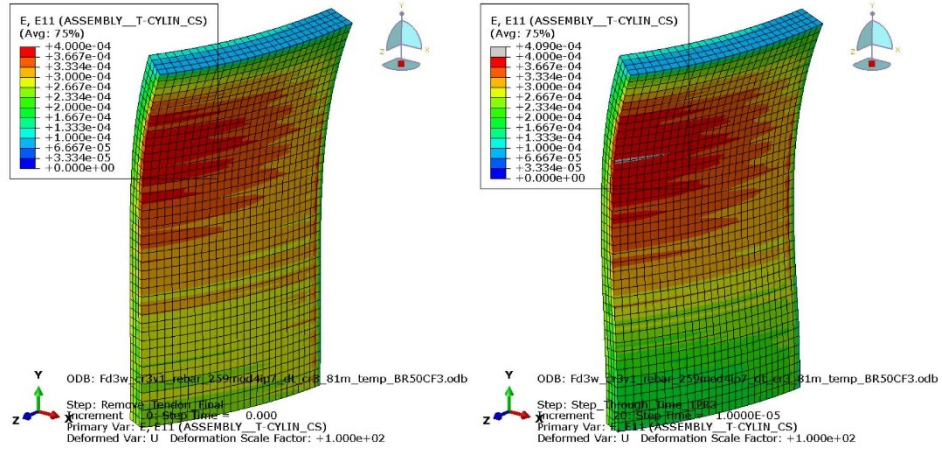

Figure 4-35 Radial Strain After 1250Hr (Left) and 5250Hr (Right) of Creep Recovery [Fc2]

4.22 Case Fd3w – Variation of Case D3

4.22.1 Description

This analysis serves as a variation of Case D3 with the following changes:

- The ring girder modulus is increased (to 16e6psi) to represent a stiffer boundary.
- The concrete fracture strain is defined as 81e-6 in/in
- The vertical tendons are not removed during the tendon removal stage.
- Only the ANACAP modulus is made time dependent. The modulus increases with time as described in Section 4.16.1. Other ANACAP properties (compressive strength, tensile fracture, etc.) are not time dependent.

Anamat File: anamat259dge_cr3curve_wCreepFactor_BRTIME50w_ABQHR_81m.o
Input File: Fd3w_cr3v1_rebar_259mod4ip7_dt_cr3_81m_temp_BR50CF3.inp
Concrete Fracture Strain: 81e-6 in/in

4.22.2 Analysis Results

The radial strain and number of elements with 1, 2, and 3 cracks (per the MSG file) are summarized in Table 4-18 at various steps. Associated radial strain contours are shown in Figure 4-36 and Figure 4-37. Unlike previous cases, the radial strain increases during the detensioning process. This is attributed to (a) not removing the vertical tendons and (b) increased radial strain due to flexure (and the Poisson's effect) stemming from the removal of the horizontal tendons. Since this change in strain occurs over a short duration, it is not attributed to creep, and is thus interpreted as an increase in radial mechanical strain. The mechanical strain increase (~9e-6 in/in) does not appear sufficient to cause delamination in this particular case. The total number of cracks observed during the creep recovery steps is not seen to change, indicating crack propagation is not occurring. However, the creep recovery steps show an increase in total strain, which differs from previous results.

Table 4-18. Summary Results for Fd3w

Step	Max Radial Strain (in/in)	MSG File Cracking
After Initial Stressing	162e-6	(0,0,0)
Before Detensioning	400e-6	(0,0,0)
After Detensioning	409e-6	Open: (2607, 0, 0) Closed: (124, 0, 0)
1250Hr After Detensioning	419e-6	Open: (1057, 0, 0) Closed: (1674, 0, 0)
5250Hr After Detensioning	423e-6	Open: (241, 0, 0) Closed: (2490, 0, 0)

7-62

Figure 4-36 Radial Strain Before (Left) and After (Right) Detensioning [Fd3w]
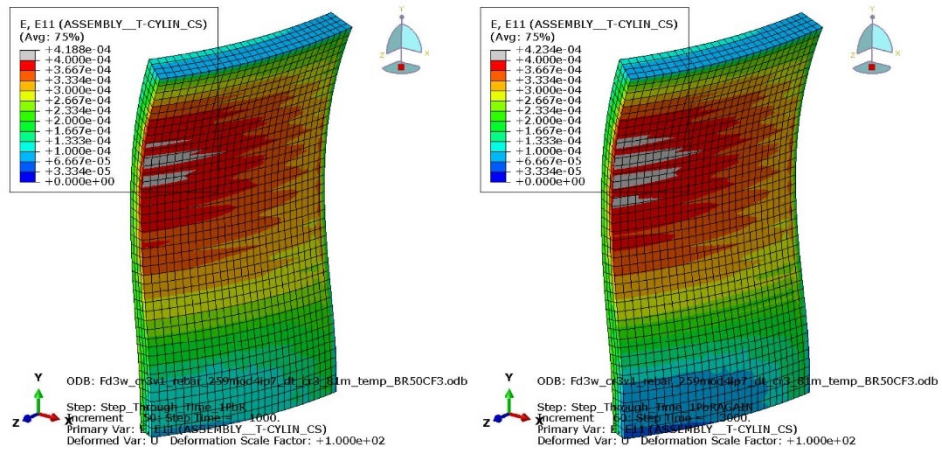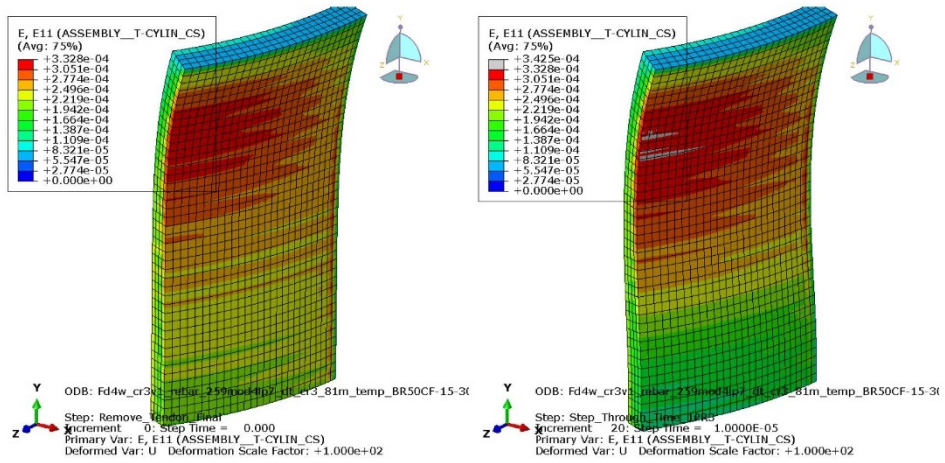

Figure 4-37 Radial Strain After 1250Hr (Left) and 5250Hr (Right) of Creep Recovery [Fd3w]

4.23   Case Fd4w – Variation of Case D4

4.23.1 Description

This analysis serves as a variation of Case D4 with the following changes:

- The ring girder modulus is increased (to 16e6psi) to represent a stiffer boundary.
- The concrete fracture strain is defined as 81e-6 in/in
- The vertical tendons are not removed during the tendon removal stage.
- Only the ANACAP modulus is made time dependent. The modulus increases with time as described in Section 4.16.1. Other ANACAP properties (compressive strength, tensile fracture, etc.) are not time dependent.

Anamat File: anamat259dge_cr3curve_wCreepFactor_BRTIME50w_ABQHR_81m.o
Input File: Fd4w_cr3v1_rebar_259mod4ip7_dt_cr3_81m_temp_BR50CF-15-30.inp
Concrete Fracture Strain: 81e-6 in/in

4.23.2 Analysis Results

The radial strain and number of elements with 1, 2, and 3 cracks (per the MSG file) are summarized in Table 4-19 at various steps. Associated radial strain contours are shown in Figure 4-38 and Figure 4-39. Unlike previous cases, the radial strain increases during the detensioning process. This is attributed to (a) not removing the vertical tendons and (b) increased radial strain due to flexure (and the Poisson's effect) stemming from the removal of the horizontal tendons. Since this change in strain occurs over a short duration, it is not attributed to creep, and is thus interpreted as an increase in radial mechanical strain. The mechanical strain increase (~10e-6 in/in) does not appear sufficient to cause delamination in this particular case. The total number of cracks observed during the creep recovery steps is not seen to change, indicating crack propagation is not occurring. However, the creep recovery steps show an increase in total strain, which differs from previous results.

Table 4-19. Summary Results for Fd4w

Step	Max Radial Strain (in/in)	MSG File Cracking
After Initial Stressing	162e-6	(0,0,0)
Before Detensioning	333e-6	(0,0,0)
After Detensioning	343e-6	Open: (1592, 0, 0)
1250Hr After Detensioning	349e-6	Open: (1198, 0, 0) Closed: (394, 0, 0)
5250Hr After Detensioning	353e-6	Open: (737, 0, 0) Closed: (855, 0, 0)

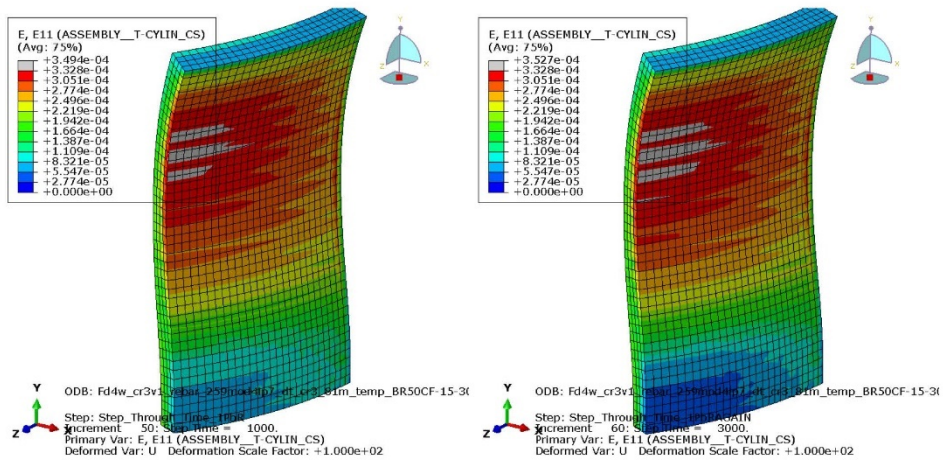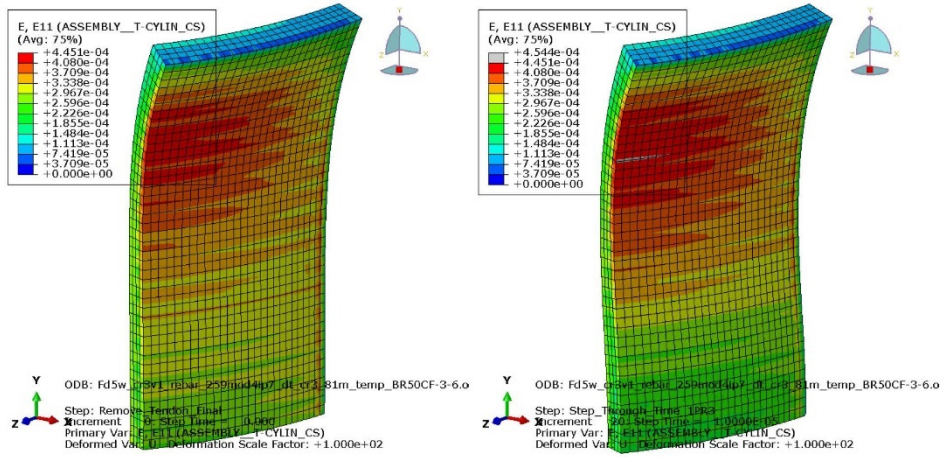**Figure 4-38 Radial Strain Before (Left) and After (Right) Detensioning [Fd4w]**

Figure 4-39 Radial Strain After 1250Hr (Left) and 5250Hr (Right) of Creep Recovery [Fd4w]

Structural Integrity Associates, Inc.

4.24 Case Fd5w – Variation of Case D5

4.24.1 Description

This analysis serves as a variation of Case D5 with the following changes:

- The ring girder modulus is increased (to 16e6psi) to represent a stiffer boundary.
- The concrete fracture strain is defined as 81e-6 in/in
- The vertical tendons are not removed during the tendon removal stage.
- Only the ANACAP modulus is made time dependent. The modulus increases with time as described in Section 4.16.1. Other ANACAP properties (compressive strength, tensile fracture, etc.) are not time dependent.

Anamat File: anamat259dge_cr3curve_wCreepFactor_BRTIME50w_ABQHR_81m.o
Input File: Fd5w_cr3v1_rebar_259mod4ip7_dt_cr3_81m_temp_BR50CF-3-6.inp
Concrete Fracture Strain: 81e-6 in/in

4.24.2 Analysis Results

The radial strain and number of elements with 1, 2, and 3 cracks (per the MSG file) are summarized in Table 4-20 at various steps. Associated radial strain contours are shown in Figure 4-40 and Figure 4-41. Unlike previous cases, the radial strain increases during the detensioning process. This is attributed to (a) not removing the vertical tendons and (b) increased radial strain due to flexure (and the Poisson's effect) stemming from the removal of the horizontal tendons. Since this change in strain occurs over a short duration, it is not attributed to creep, and is thus interpreted as an increase in radial mechanical strain. The mechanical strain increase (~9e-6 in/in) does not appear sufficient to cause delamination in this particular case. The total number of cracks observed during the creep recovery steps is not seen to change, indicating crack propagation is not occurring. However, the creep recovery steps show an increase in total strain, which differs from previous results.

Table 4-20. Summary Results for Fd5w

Step	Max Radial Strain (in/in)	MSG File Cracking
After Initial Stressing	162e-6	(0,0,0)
Before Detensioning	445e-6	(0,0,0)
After Detensioning	454e-6	Open: (5312, 437, 0) Closed: (220, 0, 0)
1250Hr After Detensioning	466e-6	Open: (2495, 322, 0) Closed: (3037, 115, 0)
5250Hr After Detensioning	471e-6	Open: (1278, 212, 0) Closed: (4254, 225, 0)

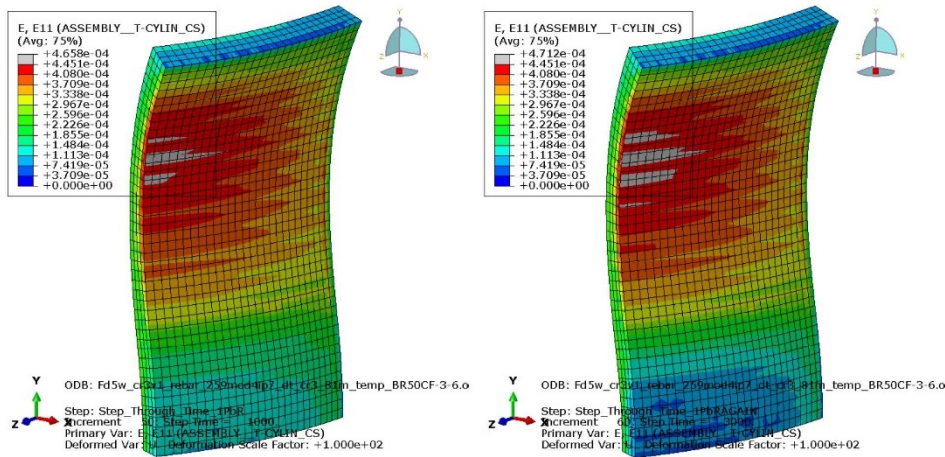**Figure 4-40 Radial Strain Before (Left) and After (Right) Detensioning [Fd5w]**

Figure 4-41 Radial Strain After 1250Hr (Left) and 5250Hr (Right) of Creep Recovery [Fd5w]

info@structint.com   1-877-4SI-POWER   structint.com

Structural Integrity Associates, Inc.

5 CONCLUSIONS AND OTHER CONSIDERATIONS

Twenty-one analysis variations were considered in this study. Variables considered included concrete fracture strain, creep compliance factors, differential creep, time dependent concrete material properties, and tendon removal sequence. Results were obtained from the Abaqus ODB file (i.e. strain magnitudes and contours) and the Abaqus MSG file (number of concrete cracks). Investigation of the MSG file was required as the ODB file does not present mechanical strain, which causes crack formation, but rather total strain. Subject to the assumptions and analysis steps described above, observations are summarized below:

a) The radial strain profile after detensioning is significantly different if creep is included in the analysis (Case A1 and A2) and the profile with creep better resembles the hourglass shape found in the delamination cracking at Crystal River.

b) A sufficiently large concrete fracture strain (capacity) is required during initial tendon stressing or delamination may occur (Case B1). Delamination, when it occurs, appears to follow the radial strain contour which is seen to be like that observed in actual delamination failures.

c) After initial stressing (during the initial creep steps), creep appears to reduce the radial (mechanical) strain resulting in a lower likelihood of delamination prior to detensioning (Case B2). However, if a local delamination is introduced just after initial tensioning (i.e. early in the creep analysis), there may still be sufficient mechanical strain (demand) to cause widespread delamination (Case B3).

d) Differential creep, with a lower creep factor assigned to the outer diameter causes a delamination failure to occur during the creep steps (Case C3). The outer diameter concrete elements appear to act as a displacement restraint, leading to the development of mechanical strain as the interior concrete elements creep inwards.

e) Removing the horizontal tendons while leaving the vertical tendons in place shows an increase in mechanical (radial) strain after detensioning and an increase in total radial strain during the creep recovery steps (the 'F' cases). The increase in total strain during the creep recovery steps may include an increase in mechanical strain but determining how much of the strain is mechanical is not currently feasible with the analyses performed in this study. The effects of creep coupled with the sequence and timing of tendon detensioning may play a role in exacerbating delamination cracking.

The 'F' cases indicate that first detensioning the hoop tendons results in an increase in mechanical (radial) strain and an increase in total (radial) strain during creep recovery. While the combination of parameter values used in these analyses did not result in delamination, the results do indicate that creep can play a role in developing mechanical strains that can cause delamination. If a local pre-existing delamination existed in the structure prior to detensioning,

perhaps stemming from ungrouted tendon ducts, SIT testing, or periodic tendon retensioning, it is reasonable to infer that this local delamination could have been subjected to increased strain during detensioning and creep recovery, causing the local delamination to propagate throughout the structure.

Recommended future studies include:

1. Investigation of inelastic, or unrecoverable, creep. Unrecoverable creep may result in a displacement restraint during creep recovery (analogous to what was observed in Case C3) which may lead to an increase in mechanical (radial) strain and a propensity for delamination. Since inelastic creep is generally not considered in a design basis or long-term performance assessments, its investigation may lead to important findings regardless if it is contributor to the observed delamination at Crystal River.
2. Further investigation of the 'F' cases, including assessing the structural response when a local delamination crack exists prior to detensioning.
3. Further investigation of various incremental detensioning scenarios.
4. Larger studies, which model a larger portion of the structure and use more refined material inputs, may also provide better insight since changing deformation restraint coupled with creep appears to influence the cracking potential.
5. Research on the propensity of interior concrete to experience higher autogenous creep rates than the exposed exterior concrete, and additional analysis cases to determine if similar conditions might lead to delamination cracking during detensioning.

Appendix A
Single Element Test Results – ANAMAT 259

Structural Integrity
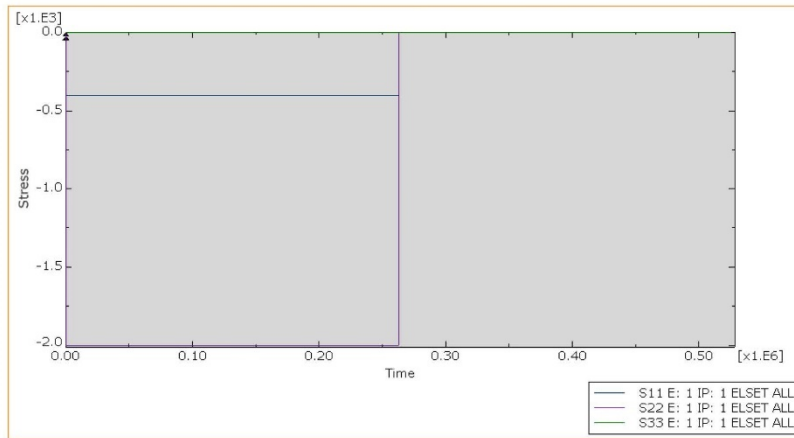Associates, Inc.

info@structint.com   1-877-4SI-POWER   structint.com

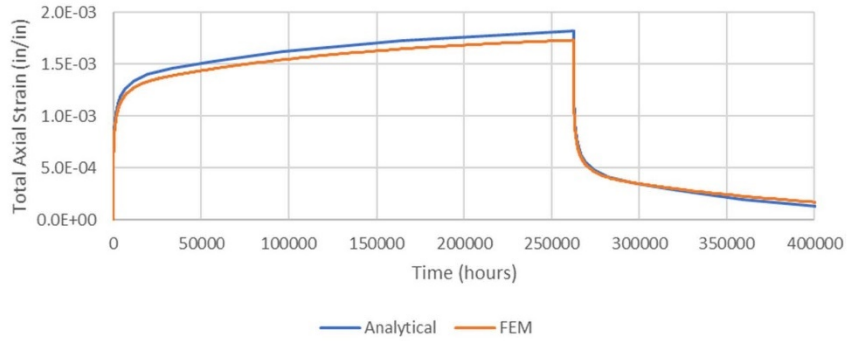A.1   *Unconfined*: Zero displacement on -X, -Z, and -Y faces. Pressure (2ksi compression) imposed on +Y face.

FEM strain and stress results are presented below. Note that the transverse directions (11 & 33) are seen to strain (expand laterally) due to the Poisson effect and no transverse stresses develop. The axial FEM results (22) are compared to analytical hand calculations and show excellent agreement.
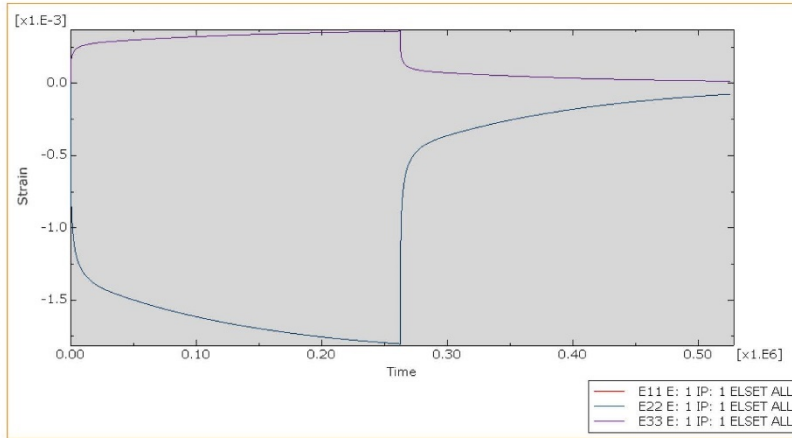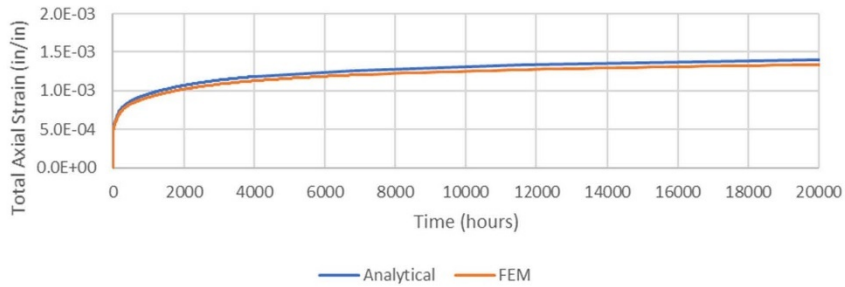

Figure A-1. Strain Results, Unconfined Model
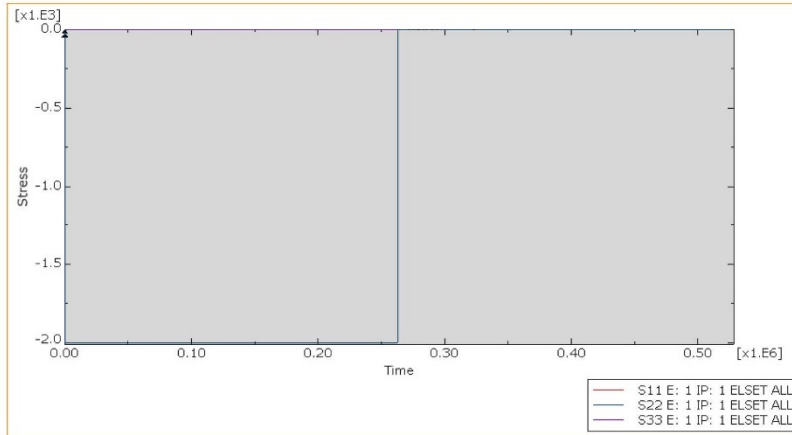
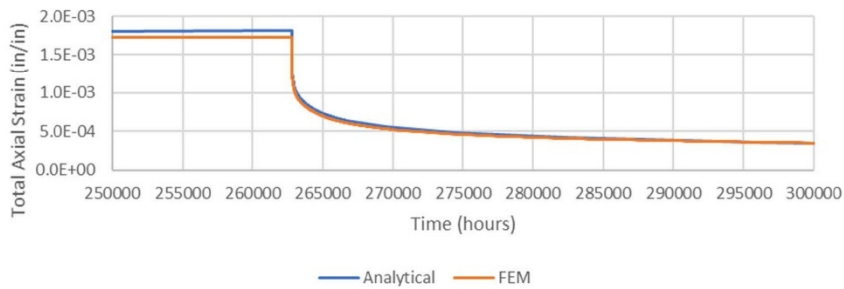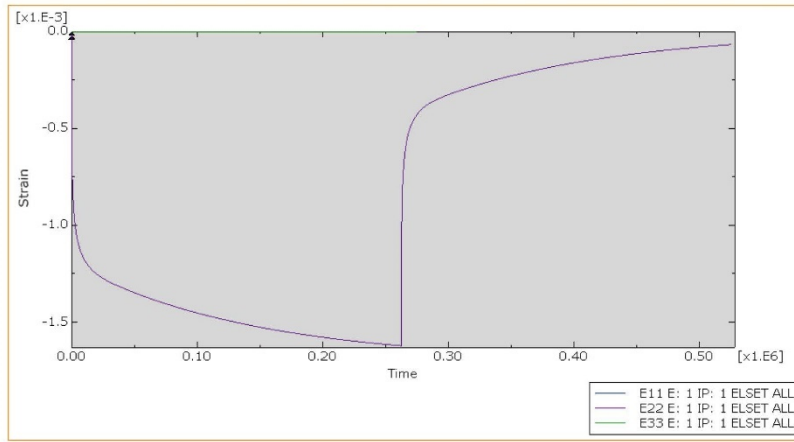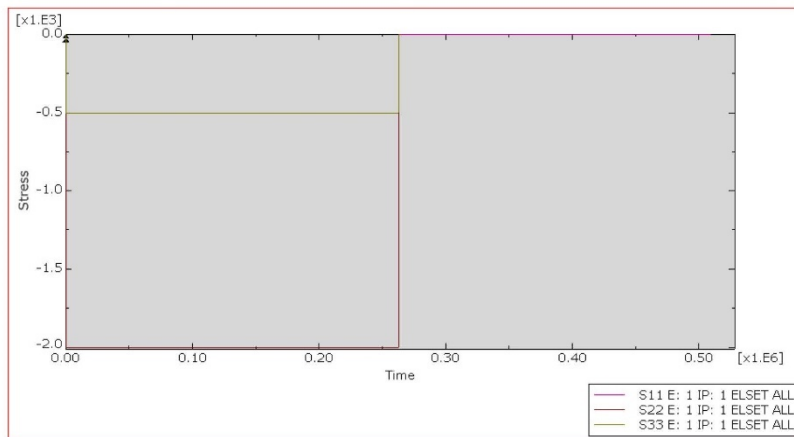**Figure A-2. Stress Results, Unconfined Model**
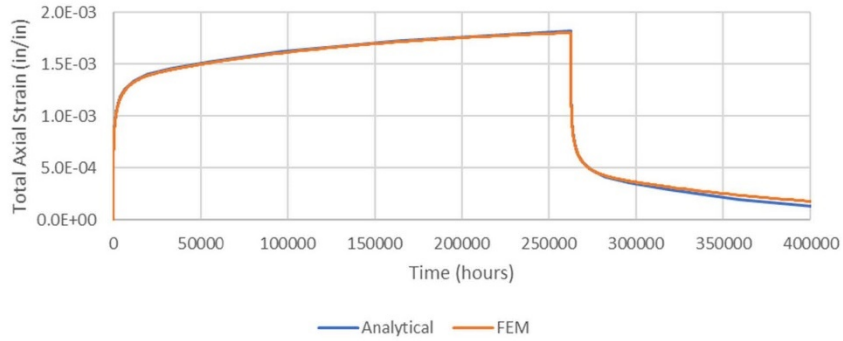
Initial Loading
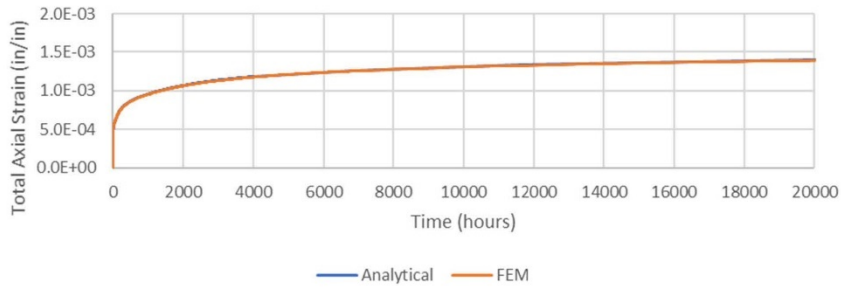
Unloading
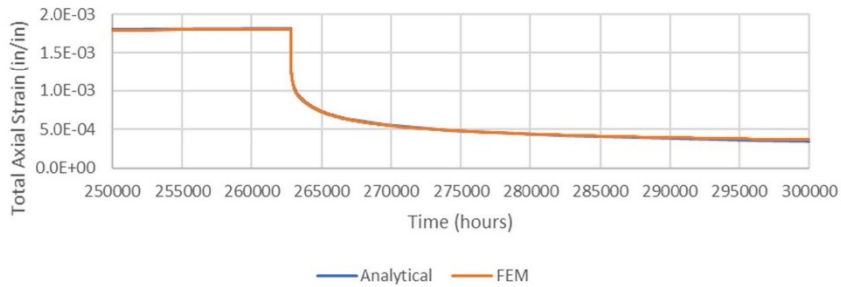
Figure A-3. Analytical vs. FEM Results, Unconfined Model

A.2   *Partially Confined*: Zero displacement on -X, +X, -Z, and -Y faces. Pressure (2ksi compression) imposed on +Y face.

FEM strain and stress results are presented below. Note that the unrestrained transverse direction (33) is seen to strain (expand laterally) due to the Poisson effect but the restrained (11) direction does not; corresponding confining stresses are seen to develop in the 11 direction. The axial FEM results (22) are compared to analytical hand calculations and show excellent agreement. The difference between the analytical and FE results is attributed to the confinement provided by the FEM boundary condition and the corresponding Poisson effects.
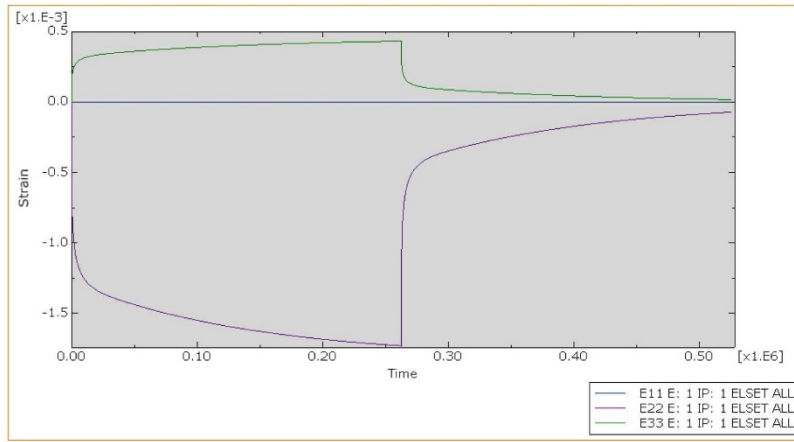
Figure A-4. Strain Results, Partially Confined Model

Figure A-5. Stress Results, Partially Confined Model

Structural Integrity
Associates, Inc.

info.structint.com ✉   1-877-4SI-POWER 📞   structint.com 🌐

Figure A-6. Analytical vs. FEM Results, Partially Confined Model

Structural Integrity
Associates, Inc.

info.structint.com ✉ 1-877-4SI-POWER ☎ structint.com 🌐

A.3 *Confined*: Zero displacement on -X, +X, -Z, +Z, and -Y faces. Pressure (2ksi compression) imposed on +Y face.
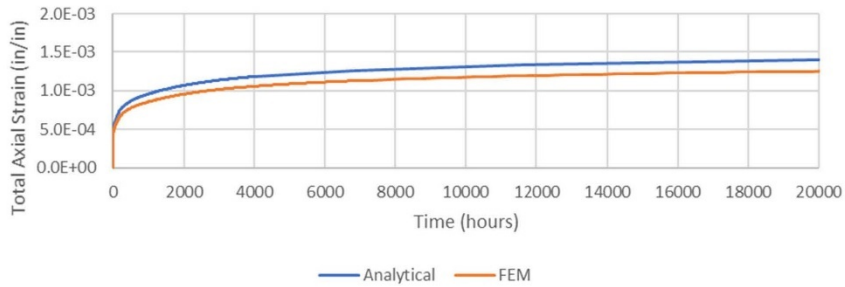
FEM strain and stress results are presented below. Note that both transverse directions (11 & 33) are restrained and experience no strain; corresponding confining stresses are seen to develop in both directions. The axial FEM results (22) are compared to analytical hand calculations and show excellent agreement. The difference between the analytical and FE results is attributed to the confinement provided by the FEM boundary condition and the corresponding Poisson effects.

Figure A-7. Strain Results, Confined Model

Figure A-8. Stress Results, Confined Model
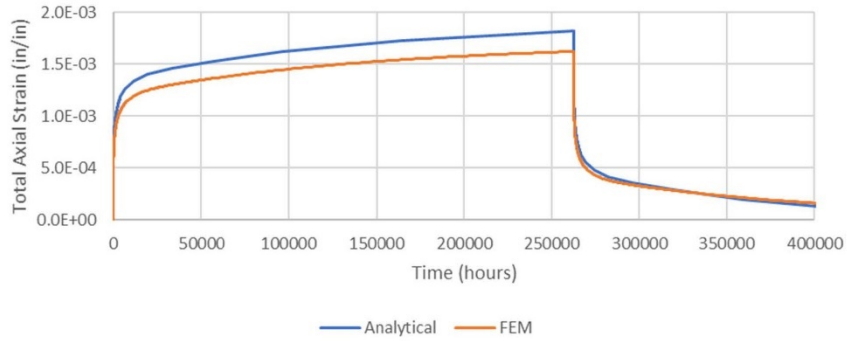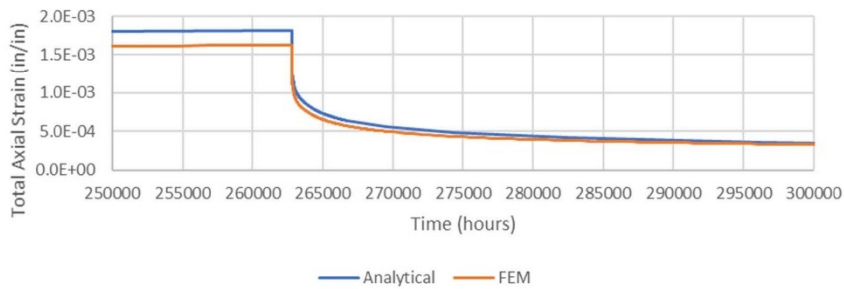
Initial Loading

Unloading

Figure A-9. Analytical vs. FEM Results, Confined Model

A.4 *Unconfined with Imposed Displacement.* Zero displacement on -X, -Z, and -Y faces. Impose 5e-4in displacement (equivalent to 2ksi compression) on +Y face.

FEM strain and stress results are presented below. The imposed axial strain results in a compressive stress of 2ksi which is seen to reduce over time due to creep. When the imposed displacement is removed (i.e. total 22 strain is set to zero), the resulting tensile mechanical strain is sufficient to crack the element at which point the stress and strain results diverge (the problem contains only a single finite element so cracking of the integration points leads to an unrestrained system).
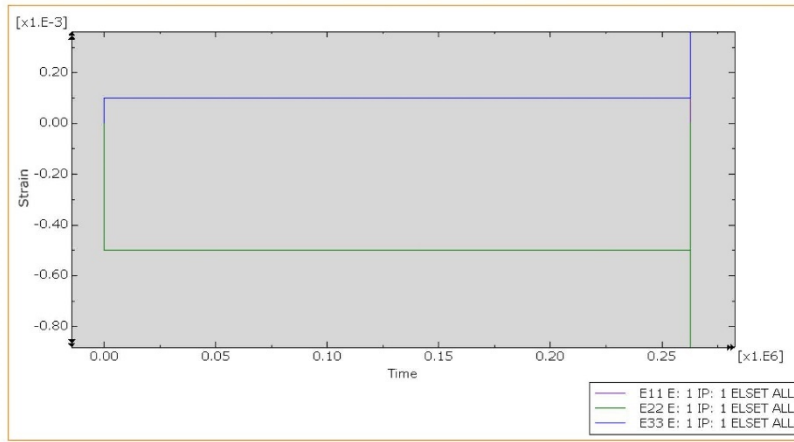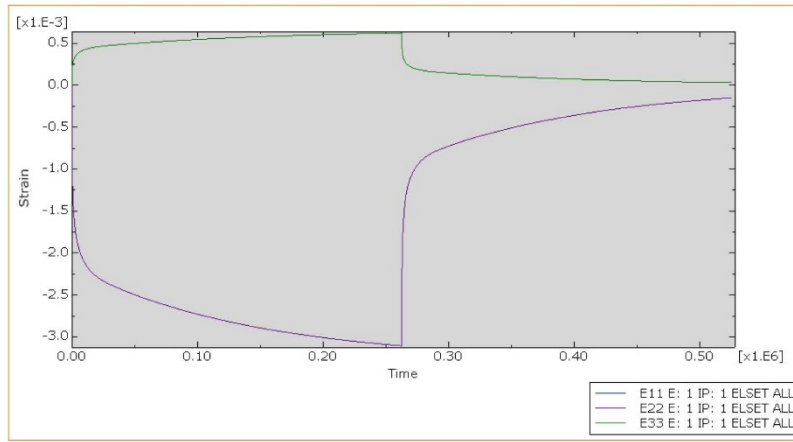

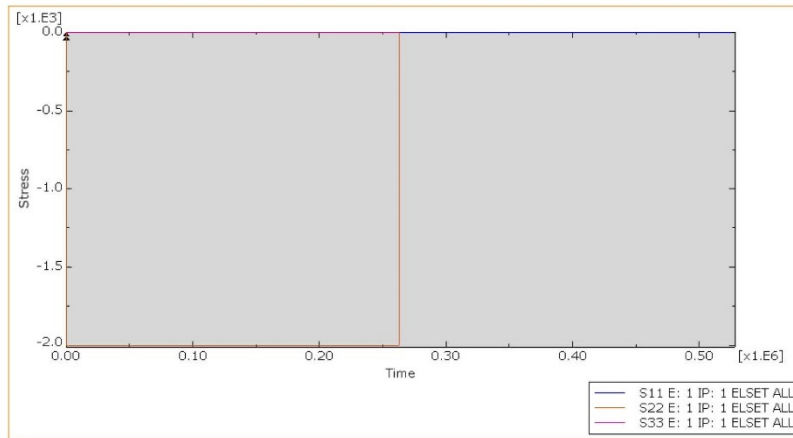Figure A-10. Strain Results, Unconfined Model, Imposed Displacement
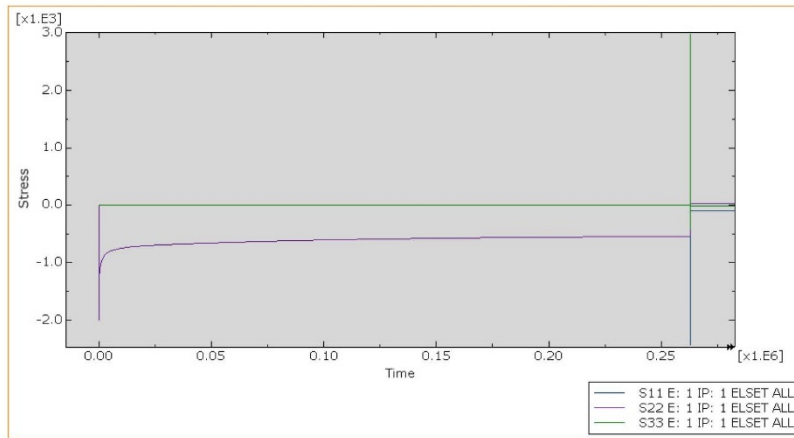
Figure A-11. Stress Results, Unconfined Model, Imposed Displacement

A.5 *Unconfined*: Zero displacement on -X, -Z, and -Y faces. Pressure (2ksi compression) imposed on +Y face. Creep Factor Doubled.
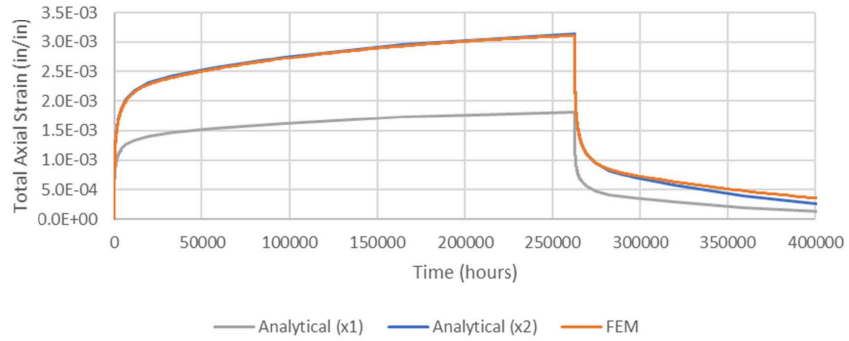
Some analyses may apply a creep factor the ANCAP model in order to include two different concrete constitutive models within the same analysis. This creep factor is defined within the input file and is passed into the ANAMAT user material model. This sample problem uses the unconfined model configuration and applies a factor of two (2) to the creep strains. The strain and stress results show the same general behavior as the original unconfined model, and demonstrates that the applied creep factor performs as intended.
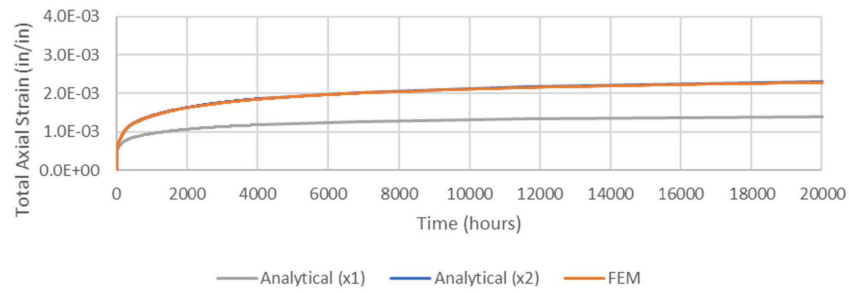

Figure A-12. Strain Results, Unconfined Model, 2x Creep Factor

Figure A-13. Stress Results, Unconfined Model, 2x Creep Factor

Structural Integrity
Associates, Inc.

info.structint.com   1-877-4SI-POWER   structint.com

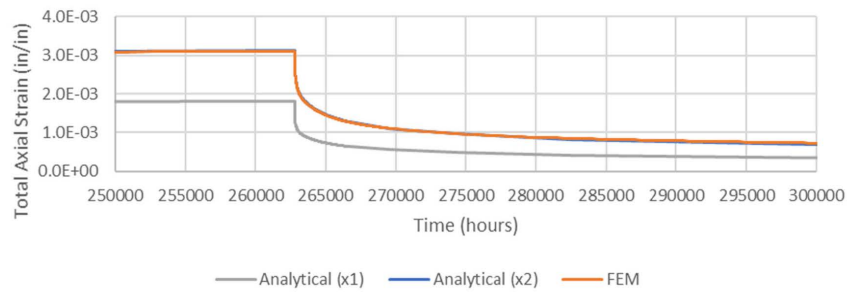7-78

Initial Loading

Unloading Loading

Figure A-14. Analytical vs. FEM Results, Unconfined Model, x2 Creep Factor

Structural Integrity
Associates, Inc.

info.structint.com 1-877-4SI-POWER structint.com